SPECT System Design Optimisation for a Simultaneous SPECT/MRI Clinical Scanner

Débora Sofia Almeida Silva Salvado

A dissertation submitted in partial fulfilment
of the requirements for the degree of
Doctor of Philosophy
in Medical Physics

Institute of Nuclear Medicine
Division of Medicine
University College London

April 26, 2017

I, Débora Sofia Almeida Silva Salvado, confirm that the work presented in this thesis is my own. Where information has been derived from other sources, I confirm that this has been indicated in the work.

I'm nothing.
I'll never be anything.
I can't wish I were anything.
Even so, I have all the dreams of the world in me.
– Fernando Pessoa

Abstract

The aim of this project was to optimize the design of a Single Photon Emission Computed Tomography (SPECT) insert based on high-resolution detectors and a high-sensitivity collimator, for a Magnetic Resonance Imaging (MRI) scanner, in order to perform simultaneous human brain SPECT/MRI and improve radionuclide-based therapies for glioma patients. The radionuclides of interest are ^{99m}Tc, ^{111}In and ^{123}I.

Specific emphasis was given to the collimator and overall system design, data simulation and performance assessment, which would feed directly into the European-funded INSERT project. The SPECT insert was to consist of a stationary system with SiPM-based photodetectors, insensitive to magnetic fields. Regarding the design, a number of system and collimator geometries were evaluated considering the restricted space in the MRI bore and the limited angular sampling. High sensitivity was prioritised over high spatial resolution, because of the clinical application. Gamma shielding design was also addressed.

Analytical calculations of system sensitivity and resolution, in addition to Monte Carlo simulations, were performed to compare various slit-slat and pinhole collimator designs.

A new collimator design was proposed: multi-mini-slit slit-slat (MSS) collimator. The MSS has multiple mini-slits, some of which are shared between adjacent detectors, and they are embedded in the slat component, allowing for longer slats in comparison to a standard slit-slat collimator.

The MSS design demonstrated to have the best overall performance, and the final system design consisted of a partial ring with 20 detectors.

A framework for geometrical calibration of the system was developed and assessed, utilising a single prototype detector equipped with a prototype collimator. This framework takes advantage of the specific collimator design to estimate geometrical parameters from independent measurements of calibration phantoms.

Experimental evaluation with tomographic acquisition of phantoms demonstrated the applicability of the new collimation concept, confirming the superiority of the MSS design over equivalent pinhole collimation.

Acknowledgements

I acknowledge funding support from Fundação para a Ciência e Tecnologia, Portugal, PhD grant SFRH/BD/88093/2012; the European INSERT collaboration, grant EC-FP7-HEALTH-305311; and the National Institute for Health Research, University College London Hospitals Biomedical Research Centre.

In addition, there are a number of people without whom I would not have made it this far.

First of all, I would like to thank my supervisors, Professor Brian Hutton and Dr. Kjell Erlandsson, not only for their share of knowledge, but also for their critical thinking, which allowed me to improve as a researcher.

Second, I would like to express my gratitude towards my INSERT colleagues/friends. Paolo Busca and Michele Occhipinti taught me everything about the INSERT electronics. I had useful discussions with Zoltan Nyitrai about practical system design; with Pieter van Mullekom, Coen Linskens and Jurgen Willems about collimator design and manufacturing; with Jan Rieger and Andre Kuhne about MR compatibility; with Irene de Francesco about clinical considerations. I also thank the whole collaboration for for providing the acquisition software, prototype collimators, and prototype detection module.

Third, I would like to thank everyone at the Institute of Nuclear Medicine, in particular the medical physics team and my lovely girls Ottavia Bertolli, Beverley Holman, Alaleh Rashidnasab, Yu-Jung Tsai and Vesna Cuplov. Ottavia and Beverley, I will always be thankful for your friendship and support.

A special thanks to Cláudia Lopes, André Ribeiro, João Monteiro and Rui Teixeira – my Portuguese support in London, to Maria João Bigode, Patrícia Ribeiro, Frederico Severo – my Portuguese support in Lisbon, and to my UCL Live Music Society friends, for making my time at UCL even better.

Finally, words cannot express my love, appreciation and gratitude towards my (extended) family, who have always been, and now more so, proud of me: Florin, mum and dad, grandparents, godparents, Chester/Oliveira/Curvelo/Santos/Silva/Coelho families... To you I dedicate my thesis.

Contents

List of Figures

List of Tables

List of Abbreviations

1D One-Dimensional

2D Two-Dimensional

3D Three-Dimensional

ADC Analogue to Digital Converter

APD Avalanche Photodiode

ASIC Application-Specific Integrated Circuit

B Back

BP Base Plate

CoG Centre of Gravity

COR Centre of Rotation

CoV Coefficient of Variation

CsI:Tl Caesium Iodide doped with Thallium

CT Computed Tomography

CZT Cadmium-Zinc-Telluride

DAQ Data Acquisition

DOI Depth of Interaction

FBP Filtered Back-projection

FE Front/End

FID Free Induction Decay

FOV Field of View

FT Fourier Transform

FWHM Full Width at Half Maximum

GUI Graphical User Interface

INSERT Integrated SPECT/MRI for enhanced stratification in radio-chemotherapy

L Lateral

L(Y)SO Lutetium-(Y)ttrium Oxyorthosilicate

LabVIEW Laboratory Virtual Instrument Engineering Workbench, Austin TX, USA

LEHR Low-Energy High-Resolution

LRF Light Response Function

MAP-EM Maximum A Posteriori Expectation Maximisation

MATLAB Matrix Laboratory, The Mathworks Inc., Natick MA, USA

MC Monte Carlo

MCX Micro Coaxial

ML Maximum Likelihood

MLEM Maximum Likelihood Expectation Maximization

MRI Magnetic Resonance Imaging

MSS Multi-mini-slit Slit-Slat

NEMA National Electrical Manufacturers Association

NUCFI Nuclear Fields, The Netherlands

OSEM Ordered Subsets Expectation Maximization

PET Positron Emission Tomography

PH_{mag} Single Pinhole with Magnification Factor M=4

PH_{min} Single Pinhole with Magnification Factor M=0.25

PMT Photomultiplier Tube

POLIMI Politecnico di Milano, Italy

PSF Point Spread Function

RF radio-frequency

ROR Radius of Rotation

SD Standard Deviation

SDD Silicon Drift Diode

SiPM Silicon Photomultiplier

SNR Signal to Noise Ratio

SPECT Single Photon Emission Tomography

SS_{min} Single Slit-Slat with Magnification Factor M=0.25

TE Echo Time

TR Repetition Time

Chapter 1

Introduction

1.1 Preamble

In recent years, there has been an increasing interest in the development of multi-modality medical imaging systems, especially those providing simultaneous acquisition. These systems have the potential to combine anatomical structure information, from imaging modalities such as Computed Tomography (CT) and Magnetic Resonance Imaging (MRI), with functional information, from Single Photon Emission Tomography (SPECT) and Positron Emission Tomography (PET). Moreover, when acquired simultaneously, images are intrinsically aligned, facilitating the image fusion process. Patient throughput and comfort are also key features of these types of systems, in which the total scan time can be reduced. This is especially important in the case of paediatric patients that might require anaesthesia.

At the end of the 1990s, the first clinical SPECT/CT (Blankespoor et al., 1996) and PET/CT (Beyer et al., 2000) scanners were introduced. The integration of CT with PET or SPECT instrumentation consisted of having both technologies side by side within the same gantry, and the patient moving through the system. Commercial systems were available soon after the prototype systems. The use of the CT image for attenuation correction of the emission data, in addition to having an anatomical reference, made the use of these systems common practice in Nuclear Medicine departments.

In the case of PET or SPECT integration with MRI, however, the design concept had to be totally reformulated, due to the incompatibility of detectors based on photomultiplier tubes (PMTs) with magnetic fields. After important technological advances, such as the development of magnetic-insensitive detectors, namely Avalanche Photodiodes (APDs) and silicon photomultipliers (SiPMs), the first clinical brain PET/MRI system was introduced (Schlemmer et al., 2008). Currently, there are two commercial systems for simultaneous whole-body PET/MRI, the Siemens Biograph mMR and the GE SIGNA PET/MRI. Regarding SPECT,

despite the advances in technology and studies showing the feasibility of SPECT/MR systems for preclinical use (Meier et al., 2011; Tsui et al., 2011b; Cai et al., 2014), a fully integrated clinical scanner has not yet been available.

1.2 Objectives

The aim of this thesis is to design a stationary SPECT system based on high-resolution detectors and a high-sensitivity collimator to insert in a commercially available MRI scanner, in order to perform simultaneous SPECT/MRI of the human brain. The main focus is therefore to understand the constraints and challenges in building such a system and optimise the design, especially of the collimator, in terms of clinical performance. Analytical calculations of resolution and sensitivity, Monte Carlo simulations of different system designs and experimental tests with prototype collimators will form the basis for the evaluation of different collimator configurations.

The output of this project will feed directly to an associated European grant: the INSERT project, which aims to improve radionuclide-based therapies for brain tumour (glioma) patients (see Chapter 3).

1.3 Motivation and Challenges

Gliomas are a type of tumour that arise from glial cells in the brain or spine. They make up 80% of all brain and central nervous system tumours and 30% of all malignant brain tumours (Goodenberger and Jenkins, 2012). There is high incidence of recurrence which makes patient management difficult, with no widely agreed standard of care (Wang and Jiang, 2013). A combined approach of surgery, radiotherapy, chemotherapy and antiangiogenic therapy is used as treatment options for these patients (Wang and Jiang, 2013). However, the prognosis is usually poor due to the nature of these tumours. Depending on the position of the tumour in the brain, complete removal may not be possible and high doses of radiotherapy may cause too much damage. But even when patients can go through radiotherapy treatment, the standard follow-up is anatomical imaging with MRI only, which can lead to inappropriate clinical decisions due to the pseudo-progression and pseudo-response phenomena observed in these patients (Hygino da Cruz et al., 2011; Khan et al., 2016). Disease progression or treatment response are assessed based on enhancement changes of the lesion area in the conventional MR image; however, contrast enhancement can be induced by inflammation, post-surgical changes or radiation necrosis, indistinguishable from tumour processes. Therefore, the combined use of SPECT and MRI would enable a better characterization of the tumour biology and potentially help in the estimation of internal radiation dose, towards a personalized radionuclide-based therapy and improvement of the treatment efficacy.

In addition, the simultaneous acquisition of SPECT and MRI images reduces errors in the co-registration process. Even if the co-registration errors for the simultaneous SPECT/MRI images were significantly smaller than those obtained for SPECT and MRI independent acquisitions, the co-registration between the two modalities could be difficult to achieve. In the presence of highly-targeted radionuclides, there might be a lack of common structures between the two images; hence the need for a simultaneous multi-modality system.

Other potential applications of a SPECT/MR system include Parkinson's disease and epilepsy, in which the additional anatomical and functional MR-based information to the already standard SPECT imaging can improve patient management.

The main challenges in developing a simultaneous SPECT/MRI system are the restricted space, MR-compatibility and the absence of rotation. The SPECT insert system has to fit inside the MR bore, and be able to accommodate the patient's head and MR-coil. This has a direct effect not only in the collimator design, but also on the detector technology which needs to support a compact design. All materials should be compatible with the magnetic fields, and the electromagnetic interference between the two systems minimised: the effects of high power radio-frequency pulses and rapidly switching gradient magnetic fields in the SPECT operation, and the effects of electromagnetic waves radiated by the SPECT electronics in the MR system. Rotation of the SPECT should be avoided to minimise the bulk and complexity of the collimation system, and possible artefacts in the MR operation, resulting in a system with limited angular sampling. However, a stationary system allows dynamic imaging and the estimation of kinetic parameters that can improve the study of physiological function, an advantage compared to conventional SPECT. Finally, the weight of the collimator and radiation shielding, which are usually made of heavy metals, is also of concern when designing such a system.

1.4 Outline of Thesis

In order to address the aforementioned objectives, this thesis is structured in the following manner:

- Chapter 2 presents the general scientific background in terms of SPECT and MR instrumentation and operation, and the design and integration of multi-modality systems. As the main focus of this thesis is to design a SPECT collimator, this chapter also includes a relevant literature review on collimator and system design.
- Chapter 3 summarises the scope of the INSERT project, in which the output of this thesis had a major contribution.
- Chapter 4 discusses the main challenges of designing a collimator for a SPECT insert for an MRI scanner, and sets the scene for the design of a final collimator and system

geometry.

- Chapter 5 presents a novel collimator for the SPECT insert system, based on the findings of the previous chapter and the detector technology advances within the INSERT project. Collimator and system design are also refined in the context of prototype collimators and the final INSERT system.
- Chapter 6 presents a framework for Monte Carlo simulations of different collimator designs using GATE, and uses those simulations to further evaluate and refine the final INSERT system design.
- Chapter 7 introduces the development of a platform to perform tomographic acquisitions with a prototype SPECT system.
- Chapter 8 combines an analytical and experimental framework for the development of a practical calibration procedure for a prototype SPECT system, and establishes the calibration protocol for the final INSERT system.
- Chapter 9 presents the experimental evaluation of the proposed collimator design, using a prototype system.
- Chapter 10 summarises the main conclusions and contributions of this thesis for the development of an MR-compatible SPECT insert, and highlights future areas for investigation.

Chapter 2

Background

This chapter overviews the technical background behind this thesis project, in which the main topics are SPECT, MRI, multi-modality systems and their design issues.

2.1 SPECT Imaging

In a SPECT scan, the patient is administered with a radiopharmaceutical. This compound is a pharmaceutically-active molecule labelled with a single-photon emitter, which emits gamma rays during radioactive decay. The pharmaceutically-active molecule is chosen on the basis of its preferential localization in a given organ, or its participation in a physiological process. The distribution of the radiopharmaceutical within the body generates radiation that can be detected and reconstructed by the SPECT system, to create a 3D tomographic image. Therefore, this 3D image yields functional information about biological processes, important to assess the patient's health state.

The main components of a conventional SPECT system, as first introduced by Anger (1958); Anger and Rosenthal (1959), included a collimator, a scintillation crystal coupled with an array of photomultiplier tubes (PMTs) and additional electronics for signal processing. But, in general, a SPECT system requires a converter of gamma-rays into electrical charge, readout electronics, and signal processing and estimation. The acquisition is focused on the field of view (FOV), which is the area to be imaged. In order to acquire sufficient information to reconstruct a tomographic image of the tracer activity distribution, different sets of 2D projection images are acquired at multiple angles, usually by rotation of the system around the patient.

Technological advances in detector materials, readout electronics and computing power originated new developments in the fields of radiation detection and collimation, with novel and dedicated SPECT systems for clinical and also pre-clinical use (Hutton, 2010; Peterson and Furenlid, 2011; Smith, 2013).

2.1.1 Photon Collimation

The first component that gamma-rays meet after being emitted by a phantom or patient is the collimator. The function of the collimator is to select preferentially gamma-rays travelling in a particular direction. Gamma-rays travelling in other directions will be absorbed or highly attenuated, due to the high density material of the collimator – usually lead or tungsten, 11.34 and 19.25 g.cm^{-3}, respectively. In addition, the more the gamma-rays deviate from the selected direction, the more they are attenuated by the collimator material, and the lower is the probability that those gamma-rays will reach the detector.

Properties such as distance from source position, and collimator thickness and hole size affect the efficiency of the collimator, and thus the overall sensitivity of the system. A detailed discussion on collimator design issues is given in Section 2.3.1 of this chapter.

Therefore the collimator design has an important role in the sensitivity of the system, which is defined by the fraction of emitted photons that are actually detected. In fact, the collimator is one of the most limiting factors in SPECT sensitivity, which is an underlying reason for poor quality images. Image quality is also governed by how well the system physically achieves the principle of correspondence between the direction of the gamma-ray emission and the point of detection.

Collimators may have different configurations, such as parallel-hole, convergent, divergent, pinhole, slit-slat, but they all exhibit a trade-off between efficiency, resolution and FOV. Therefore different collimator schemes may be advantageous depending on the application (Freed et al., 2008; Goorden et al., 2009; Metzler et al., 2010; van Audenhaege et al., 2011). Many developments in collimator design for small animal imaging are applied in small FOV imaging, such as cardiac SPECT, or even translated to clinical imaging.

2.1.1.1 Parallel-Hole Collimator

The parallel-hole collimator is the most commonly used collimator in SPECT imaging, and it is made of arrays of parallel holes and septa (Figure 2.1, left). These holes can have different shapes, lengths and diameters, according to the application of the collimator.

With parallel-hole collimation, only photons travelling nearly perpendicular to the detector surface can pass through the collimator. The longer the septa and the smaller the hole diameter, the smaller the acceptance angle of the emitted gamma-rays, i.e. only gamma-rays travelling closer to the detector's normal will be accepted, improving resolution. However, more photons are attenuated, reducing sensitivity. On the other hand, for larger holes and shorter septa, sensitivity improves, but spatial resolution deteriorates. Equation 2.1 and Equation 2.2 also show this relationship between resolution R and geometric efficiency g, respectively, and the hole diameter d and length l, and septa thickness t. Spatial resolution also gets worse with increasing distance h from the collimator to the source. In a conventional

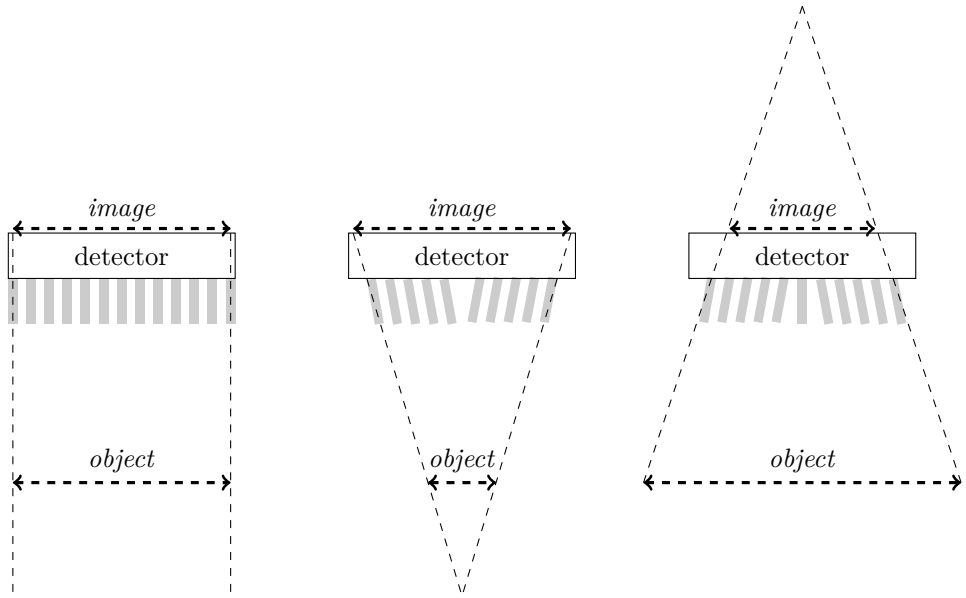

Figure 2.1: Diagrams of the geometry of conventional collimators: parallel-hole (left), converging (centre) and diverging (right). The projection through the collimator is represented in dashed lines.

camera, sensitivity is in the order of 10^{-4} for a resolution of $8-12$ mm at a 10 cm distance.

$$R_{\mathrm{PAR}} = \sqrt{d^2 \frac{(h+l)^2}{l^2} + R_i^2} \tag{2.1}$$

$$g_{\mathrm{PAR}} = \frac{d^4}{4\pi l^2 (d+t)^2} \tag{2.2}$$

2.1.1.2 Converging and Diverging Collimators

Another type of collimation is obtained with arrays of non-parallel holes.

Converging collimators (Jaszczak et al., 1979) have radially converging holes that focus on a point beyond the source plane (Figure 2.1, centre). The advantage of these collimators is that they offer magnification, improving resolution, specially for objects smaller than the detector.

In contrast, diverging collimators (Muehllehner, 1969) have radially diverging holes that focus on a point behind the detector plane (Figure 2.1, right). These collimators offer an extended FOV at the expense of minification of the object.

Equation 2.3 and Equation 2.4 give the resolution and sensitivity for converging and diverging collimators, where R_i is the detector's intrinsic resolution; d, l and t are the hole's diameter, length and thickness; k is a factor that accounts for the hole shape; h is the distance from the source to the collimator; f is the focal length, i.e. the distance from the focal point to the collimator; m is the magnification factor ($m = f/h$). For diverging collimators, the

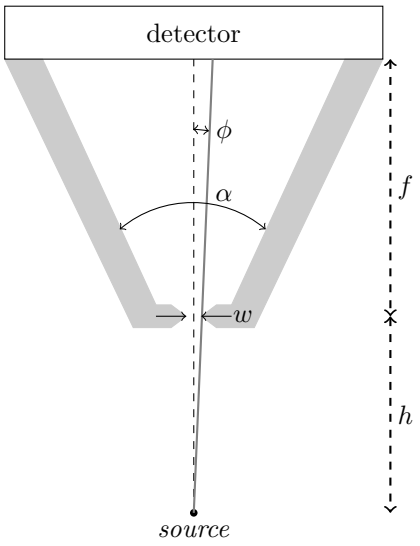

Figure 2.2: Diagram of the pinhole collimator geometry (grey) and corresponding geometric parameters (see Table 2.1). The aperture shows the detail of the knife edge.

focal length takes a negative value and the magnification factor is actually a minification factor, meaning that $m < 1$.

$$R = \sqrt{d^2 \frac{(h+l)^2}{l^2} + \left(\frac{R_i}{m}\right)^2} \tag{2.3}$$

$$g = k \frac{d^4}{l^2(d+t)^2} \left(\frac{f}{f-h}\right), \begin{cases} f < 0 & \text{diverging} \\ f > 0 & \text{converging} \end{cases} \tag{2.4}$$

One drawback of both types of collimation is image distortion, because the magnification factor varies with the distance from the source to the collimator. Therefore different source planes correspond to different distances. However, this is normally accounted for during reconstruction.

2.1.1.3 Pinhole Collimator

The pinhole collimator (Anger, 1952) has the shape of a cone or trapezoid, usually with a knife-edge aperture placed at the end (Figure 2.2). The collimator's geometric parameters are described in Table 2.1. As gamma-rays pass through the pinhole aperture which is smaller than the imaging object, the projected image is inverted in the detector plane.

One advantage of pinhole collimators is that the image is magnified when the distance from the source to the pinhole is smaller than the collimator's focal length, i.e. the distance between the aperture and the detector (Beekman and van der Have, 2007). This is particularly useful to overcome constraints imposed on resolution by the detector's intrinsic response in high-resolution applications. However, the image can also be minified, if the distance to

Table 2.1: Geometric parameters of the pinhole collimator.

Parameter	Description
w	Pinhole aperture width
ϕ	Angle between the incident ray and the pinhole normal
f	Pinhole focal length (projected onto the pinhole normal)
h	Pinhole distance to the object (projected onto the pinhole normal)
m	Magnification factor ($m = f/h$)
N	Total number of pinholes
R_i	Detector's intrinsic resolution
α	Full acceptance angle (pinhole opening angle)

the object is larger than the focal length, as expressed in Equation 2.5. Because of these magnification effects, pinhole collimators have a limited FOV and therefore they are usually used for imaging of small organs that can be positioned close to the collimator.

$$I = \frac{f}{h} O \begin{cases} f > h, & \text{magnification} \\ f < h, & \text{minification} \end{cases} \tag{2.5}$$

The geometric efficiency of the pinhole collimator is given by Equation 2.6 (Mallard and Myers, 1963). Sensitivity increases for objects close to the pinhole, i.e. small distance h. Another way to improve sensitivity is to have a multi-pinhole design (Vogel et al., 1978; Schramm et al., 2003), in which multiple apertures replace the single pinhole plane, since geometric efficiency is increased by a factor proportional to the number of pinholes N and their overlap in the object FOV (Barrett and Hunter, 2005). However the pinhole projections cannot overlap on the detector surface. Otherwise there will be uncertainties in the detection of the emission point, degrading the collimator's resolution and introducing artefacts.

$$g_{\text{PIN}} = k \frac{w^2}{4\pi h^2} \sin^3\theta,\ k = \begin{cases} \pi/4 & \text{circular hole} \\ 1 & \text{square hole} \end{cases} \tag{2.6}$$

In addition, resolution is also good at close distances to the object (Equation 2.7).

$$R_{\text{PIN}} = \sqrt{\left(w\frac{h+f}{f}\right)^2 + \left(\frac{R_i}{m}\right)^2} \tag{2.7}$$

Equation 2.6 and Equation 2.7 assume an ideal pinhole aperture, having infinitely attenuating edges. But in reality, gamma-rays will penetrate through the knife-edge edges affecting the pinhole's aperture, and subsequently resolution and sensitivity. In order to calculate an effective aperture size that accounts for penetration, there are two approaches. The first is obtained considering that the effective aperture size w_e is the aperture of an ideal pinhole w passing the same number of photons as the real pinhole (Smith and Jaszczak, 1997; Metzler et al., 2001). The so called sensitivity-effective pinhole diameter is given by Equation 2.8 (Paix, 1967)). The second approach is obtained considering that the effective

aperture size is the aperture of an ideal pinhole w that has the same geometric resolution as the total resolution of the real pinhole, due to both geometry and septal penetration (Accorsi and Metzler, 2004; Metzler and Accorsi, 2005). As resolution depends on the direction of measurement, the resolution-effective pinhole diameter is given by two different expressions for the parallel and perpendicular directions, Equation 2.9 and Equation 2.10, respectively. Considering the centre of the aperture as the origin of XYZ axes, the parallel direction would be along the Y axis and the perpendicular, along the X axis. These resolution-effective diameters are more suitable for predicting the FWHM of the pinhole's PSF than the sensitivity-effective diameter (Metzler and Accorsi, 2005). When considering the FWHM, the parameter ΔL_k is calculated by Equation 2.11.

$$w_{e,S} = \sqrt{w\left(w + \frac{2}{\mu}\tan\frac{\alpha}{2}\right) + \frac{2}{\mu^2}\tan^2\frac{\alpha}{2}} \tag{2.8}$$

$$w_{e,R\parallel} = w + \Delta L_k\left(\tan^2\frac{\alpha}{2} - \cot^2\theta\right)\cot\frac{\alpha}{2}\sin\theta \tag{2.9}$$

$$w_{e,R\perp} = \sqrt{\left(w + \Delta L_k\tan\frac{\alpha}{2}\sin\theta\right)^2 - \Delta L_k^2\cos^2\theta} \tag{2.10}$$

$$\Delta L_k = \Delta L_{0.5} = -\frac{\ln 0.5}{\mu} = \frac{\ln 2}{\mu} \tag{2.11}$$

One disadvantage of pinhole collimation is the axial blurring and object truncation with a circular orbit due to incomplete sampling at the edges of the FOV (Metzler et al., 2003), as there is not sufficient information to unambiguously reconstruct the image without artefacts. This effect is reduced as the radius of rotation of the collimator is increased; however sensitivity and spatial resolution decrease – both are influenced by the increase of h. A solution is then to acquire in a helical or spiral orbit, which allows for a decreased radius of rotation in addition to reduced axial blurring.

Many studies have been developed in the area of pinhole collimation in brain and small-animal SPECT. Rogulski et al. (1993) optimised multi-pinhole collimator geometry for an ultra-high resolution (2 mm) brain SPECT system, showing that improvements in detector resolution can lead to both improved spatial resolution and counting efficiency, when compared to parallel-hole imaging. Beekman and Vastenhouw (2004) evaluated a new design for a stationary small-animal SPECT system: highly focusing multi-pinhole collimator with gold apertures to reduce septal penetration, and focused columnar crystals and non-overlapping projection views to reduce parallax errors due to DOI variations. Freed

et al. (2008) presented an adaptive design for a small-animal SPECT system with single pinhole collimation. The idea was that design optimisation can be performed specifically for a given subject or task, evaluating parameters such as FOV, resolution and sensitivity for feedback adjustment. Although neat, the mechanical design behind it is more difficult to manage in a clinical setting. Goorden et al. (2009) proposed an analytical model for the design of a high-resolution and high-sensitivity full ring multi-pinhole brain SPECT system. They found that the trade-off between resolution and sensitivity has the form $S \propto R^2$ and that performance is improved for large detector-to-collimator distances or detectors with high intrinsic resolution (R_i <0.2 mm). Nillius and Danielsson (2010) discussed the theoretical bounds for multi-pinhole SPECT design and showed that maximum sensitivity is obtained when the detector is orthogonal to the optical axis. van Audenhaege et al. (2011) designed a non-rotating brain SPECT system with a tungsten multi-pinhole collimator. The obtained sensitivity was four times lower than a dual-head system with LEHR parallel-hole collimator, but it was able to achieve a 4 mm-resolution instead of 6-8 mm. Parallax effects were reduced with truncating pinholes so that the opening angle is smaller, and a shutter mechanism was used to simulate the rotational movement in order to obtain sufficient angular views. In the context of small animal imaging, Branderhorst et al. (2011) designed a static system for targeted imaging with optical sliders, an automatic movable bed, and exchangeable collimators. The sequence of bed positions is automatically calculated after choosing the organ of interest from the optical images. Targeted imaging allows an increased count yield from the region of interest, which is important for dynamic imaging, increased throughput or decreased radiation dose. Metzler et al. (2012) designed a stationary pinhole system with rectangular apertures for cardiac animal imaging. The collimator cylinder contained two adjacent FOVs: a small one for high resolution imaging (0.4 mm and high magnification) and a large one for scout imaging. Regarding the issue of system compactness, Lin and Meikle (2011) designed a two-detector system based on asymmetric pinholes and truncated projections, allowing for system compactness. Complete sampling is achieved with circular rotation of the detector heads. Deprez et al. (2013) introduced the lofthole – a circular aperture with a rectangular entrance/exit, to avoid overlapping projections on the detector or the use of extra shielding. Finally, to tackle imaging with high-energy radionuclides, Goorden et al. (2013) designed a system with clusters of pinholes. Each cluster samples the whole FOV with several small opening angles, increasing the path length for the incident photon so that penetration is decreased. van der Have et al. (2016) optimized the previously mentioned system for *in vivo* ^{131}I mouse SPECT imaging. They modelled edge penetration and DOI to compensate for the distance- and energy-dependent pinhole sensitivity.

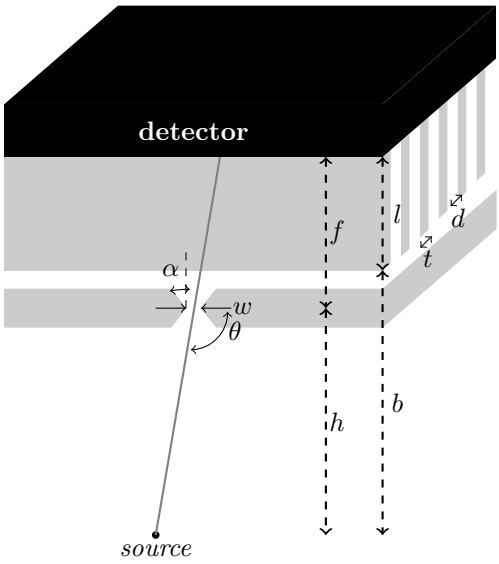

Figure 2.3: Diagram of the slit-slat collimator geometry (grey).

Table 2.2: Parameters of the slit-slat collimator.

Parameter	Description
w	Slit aperture width
t	Slat septa thickness
h	Slit distance to the object (projected onto the slit normal)
N	Total number of slits
b	Slat distance to the object (projected onto the slat-gap normal)
θ	Angle between the incident photon and the aperture slit plane
f	Slit focal length (projected onto the slit normal)
μ	Attenuation coefficient of the collimator material
R_i	Detector's intrinsic resolution
k	Fraction of the peak (usually 0.5 for FWHM)
m	Magnification factor ($m = {}^{f}/_{h}$)
α	Full acceptance angle (slit opening angle)
d	Slat septa spacing
l	Slat septa length

2.1.1.4 Slit-Slat Collimator

The slit-slat collimator (Rogers et al., 1982, 1984, 1988) combines two types of collimation: pinhole collimation in the transaxial direction ruled by the slit, and parallel-hole collimation defined in the axial direction ruled by the slats. The slit aperture extends along the axial direction of the detector and the parallel septa, called slats, extend in the opposite direction of the detector and until the slit plane (Figure 2.3).

Table 2.2 shows all the parameters that need to be defined in order to fully characterize a slit-slat collimator.

As for pinhole collimation, high sensitivity is obtained for points near the slit. In addition, multiple slits also provide increased sensitivity. Another advantage of having multi-slits

in the slit plane is that multiple, non-overlapping transverse copies of the object can be obtained and sensitivity increases.

In contrast to multi-pinhole collimators, the use of axial slats provides independent axial slices, which achieve complete sampling with a circular orbit around the object being imaged. Also slit-slat collimation provides an enlarged axial FOV, at the expense of loss in axial resolution due to no axial magnification.

In the transaxial direction, slit magnification is given by the ratio between the focal length and the distance to the object (Table 2.2), improving system resolution. However as magnification increases, the FOV decreases because FOV $= {}^{D}/_{m}$, for the same detector size D. Therefore a compromise must be made between high resolution (high magnification) and large FOV (low magnification).

The geometric efficiency of the slit-slat collimator, a key point for the system's sensitivity, is given by Equation 2.12 (Metzler et al., 2010), which can be seen as the combination of the geometric efficiency equation's for parallel-hole (Equation 2.2) and pinhole (Equation 2.6) collimation. Similarly Equation 2.13 and Equation 2.14 give the resolution for the transaxial and axial directions (Metzler et al., 2006), respectively, due to the different type of collimation in each direction.

$$g_{\mathrm{SS}} = N\frac{wd^2}{4\pi lh(d+t)}\sin^3\theta \tag{2.12}$$

$$R_{tr_{\mathrm{SS}}} = \sqrt{\left(w\frac{h+f}{f}\right)^2 + \left(\frac{R_i}{m}\right)^2} \tag{2.13}$$

$$R_{ax_{\mathrm{SS}}} = \sqrt{\left(d\frac{b+l}{l}\right)^2 + R_i^2} \tag{2.14}$$

In practice, there will be penetration through the collimator (see Section 2.3.1.1), which affects the sensitivity and resolution of the system. This can be seen as having different slit apertures and septa thickness in the collimator, so that the amount of detected photons will be different. In order to account for penetration, slat length l and slit aperture w on resolution and sensitivity formulae have to be replaced by effective lengths and apertures (Accorsi and Metzler, 2004; Accorsi et al., 2008). Equation 2.15, Equation 2.16 and Equation 2.17 show expressions for effective slat length l_{eff}, sensitivity-effective slit-width w_{eff_g} and resolution-effective slit-width w_{eff_R}, respectively.

$$l_{eff} = l - \frac{2}{\mu} \tag{2.15}$$

$$w_{e,S} = w + \frac{1}{\mu}\left(1 - \cot^2\frac{\alpha}{2}\cot^2\theta\right)\sin\theta\tan\frac{\alpha}{2} \tag{2.16}$$

$$w_{e,R} = w - \frac{\ln k}{\mu}\sin\theta\cot\frac{\alpha}{2}\left(\tan^2\frac{\alpha}{2} - \cot^2\theta\right) \tag{2.17}$$

In terms of applications, this type of collimation has been suggested for small FOV imaging, such as for human brain, cardiac and breast imaging, in which the use of multiple slits in the transaxial direction is advantageous. Mahmood et al. (2009) compared three multi-slit-slat system designs, Asymmetric Rotating Collimator, Asymmetric Rotating Detector and Symmetric Rotating Collimator, for human brain imaging. Both mixed multiplexing and non-multiplexing data can be acquired with these designs, which has potential to improve reconstructed image quality (Mahmood et al., 2008, 2010). The latter design had the best performance in terms of system sensitivity at an average resolution of 6 mm. Metzler et al. (2007) assessed multi-slit-slat collimation for cardiac SPECT, and concluded that it offers improved sensitivity at the same resolution of single slit-slat, ultra-high resolution parallel-beam and ultra-high resolution fan-beam collimation, over a large range of torso widths. Kau and Metzler (2012) optimized slit-slat and multi-slit-slat collimators for breast imaging and determined that optimising sensitivity is more important than angular range of the camera head, when aiming for improved image quality. Also, multiple slits improve contrast recovery for the chest-wall and centre lesions in comparison to a single slit-slat collimator. In general, all mentioned studies came to the same conclusion, that the slit aperture has to be placed as close to the object as possible for optimal utilization.

2.1.2 Photon Detection

After being collimated, the photons of interest have to be detected and collected for image formation. In that sense, it is important that detectors have a good performance in terms of efficiency, spatial resolution, energy resolution, uniformity, count rate, robustness/stability, and ultimately they should have a reasonable cost.

Efficiency relates to the detector's capacity of actually detecting the photons of interest. The detector has to convert the emitted photons into useful electrical signals, so efficiency will be affected by the detector's density, size, thickness and composition, its distance from the source, absorption, scatter and the energy of the photons. The better the efficiency, the better the count statistics. Energy resolution refers to the detector's ability to correctly estimate the energy of the detected photons. A detector with good energy resolution provides better energy spectra and the possibility to better distinguish between different photopeaks. Therefore energy windowing can be applied to remove scatter and characteristic X-rays, improving image quality. Although the collimator and reconstruction algorithm also contribute for

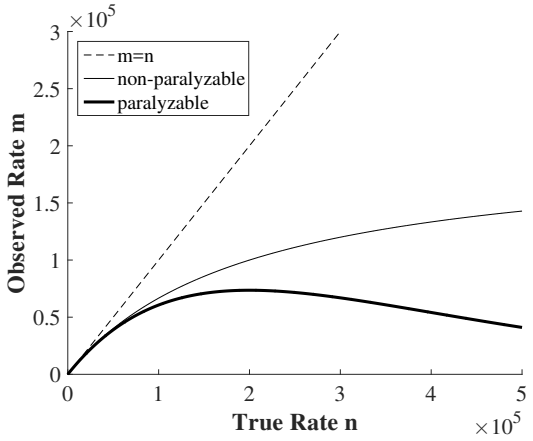

Figure 2.4: Effect of the true count rate on the observed count rate under the assumption of either a paralyzable or non-paralyzable detector for a dead time of 5 μs.

the final image resolution, the detector's spatial resolution has to be good to ensure that there is enough spatial information about the photon's interactions. Similarly the detection of these interactions throughout the detector has to be uniform, independent of location and time. This means that a stable power and bias supply has to be provided during acquisition. Detectors should have a sufficient count rate such that data can be collected within a reasonable time. However the count rate is affected by the dead time of the detector – the time during which the detector is unable to respond to a new event that would normally produce a count. Detector's dead time can follow a non-paralyzable or a paralyzable model. In the first, dead time is fixed and any events taking place during this time are lost. In the latter, the dead time is extendible and it depends on the actual count rate, i.e. any events taking place during this time are lost and they restart the dead time, prolonging the paralysis of the detector. The relation between the observed m and the true n count rates is given by Equation 2.18 for the non-paralyzable model and Equation 2.19 for the paralyzable model, where τ is the dead time.

$$m = \frac{n}{1 + n\tau} \tag{2.18}$$

$$m = ne^{-n\tau} \tag{2.19}$$

Generally the detection process can be divided into three steps: conversion, readout and estimation.

Conversion occurs when gamma-rays interact in a certain medium and can be subsequently converted into an electrical signal. Within the 30-250 keV energy range of most SPECT studies (Peterson and Furenlid, 2011), the two main possible interactions are photoelectric absorption and Compton scatter. The latter will contribute to image quality

degradation.

The scintillation crystal converts gamma photons into visible light, having a light output which is proportional to the absorbed energy. Scintillation properties, along with crystal thickness, size and shape contribute for a specific detection efficiency, energy resolution and spatial resolution.

The photodetector is responsible for converting visible light into an electrical signal, which is digitized by the readout electronics. These are also responsible for estimating the energy of the incident photons and the interaction location.

There are different types of detectors, which will be presented in the next sections.

2.1.2.1 Photomultiplier Tubes with Scintillation Detectors

In a conventional SPECT system, a large-area and continuous NaI(Tl) scintillator crystal is coupled to an array of photomultiplier tubes (PMTs).

PMTs convert light photons into a measurable electric signal. When the light photons generated in the scintillation crystal hit the photocathode, electrons are emitted to the vacuum space of the PMT. A focusing grid directs them to the first dynode, which absorbs those electrons and emits more electrons in the direction of the second dynode, amplifying the signal at each dynode until the signal reaches the anode. The pulse integration is then proportional to the crystal's absorbed energy.

Information on the energy deposited by a photon interaction is obtained by summing the signal amplitudes of all PMTs, while spatial information is extracted based on linear combinations of the distribution of signals across the array of PMTs.

However, PMTs are sensitive to magnetic fields, which alter the trajectory of the electrons during the amplifying process. For MR-compatible alternatives, solid state readouts have been proposed.

2.1.2.2 Solid State Devices

In solid state photodetectors, when a photon travelling through silicon is absorbed, its energy is transferred to a bound electron, causing the electron to move from the valence band to the conductive band – an electron-hole pair is created. If subjected to a reverse bias, an electric field is generated, which causes holes to be accelerated to the anode and electrons to the cathode. When the electric field is very strong, the charge carriers kinetic energy is sufficient to create secondary charge pairs through a process called impact ionization. Therefore a single absorbed photon can trigger a self-perpetuating ionization cascade within the volume subjected to the electric field. This is the working principle of Avalanche Photodiodes (APDs), which operate with high reverse bias voltages (Renker, 2006). These devices are small and compact, and insensitive to magnetic fields. However, the output signal is always the same and independent of the number of absorbed photons, hence there is no information about the

Table 2.3: Summary of the main features of the different detector techonologies [source: GmbH (2017)].

	PMT	**APD**	**SiPM**
Quantum Efficiency	25-40%	80%	80%
Single Photon Resolution	✓	×	✓
Operating Voltage	1000-3000 V	100-500 V	20-40 V
Gain	10^4-10^9	30-300	10^5-10^7
Insensitivity to Magnetic Field	×	✓	✓
Miniaturization	×	✓	✓
Production Costs	medium	low	low

magnitude of the photon flux. In addition, APDs show a trade-off between noise and timing.

An alternative technology to overcome the proportionality issue is the Silicon Photomultiplier (SiPM) detector. SiPMs consist of an array of Geiger mode avalanche photodiodes (Herbert et al., 2006; Eckert et al., 2010). At reverse bias higher than the breakdown voltage, the silicon becomes conductive, amplifying the signal into a measurable electric current. The size of the output pulse depends on the number of microcells that fire, providing an output signal that is proportional to the number of incident photons, provided each microcell on average sees less than one photon. These devices combine the compactness and low bias voltages of APDs with the high gain and stability of PMTs. Table 2.3 summarizes the main differences of the aforementioned technologies.

Cadmium-Zinc-Telluride (CZT) solid state detectors convert gamma photons directly into an electric pulse at room temperature, without the need for scintillation crystals and Anger electronics. Due to the direct conversion, CZTs have better energy and spatial resolution in comparison to photodetectors. However, these devices exhibit a low-energy tail, which results in poorer detection efficiency within the energies of interest for radionuclides like ^{99m}Tc and ^{57}Co.

2.1.3 Image Reconstruction

The process of obtaining a SPECT image is based on the acquisition of 2D projections of a 3D volume to reconstruct a contiguous stack of 2D slices of the distribution of activity. The main problem with the reconstruction process is that an infinite number of tracer distributions can yield the same projection. Otherwise stated, photons emitted at different depths, but along the same direction, are detected by the same detector. Since the distance travelled by the photon is not known, the amount of information given by only one projection is insufficient to reconstruct an image. However, the number of possible solutions reduces and becomes more alike as the number of angular positions of the detector in relation to the object increases.

Assuming that the distribution of emitted counts f in the FOV is known, as well as a projection operator or system matrix H, the distribution of the detected counts g is given by Equation 2.20, with a term for noise:

$$g = Hf + n \tag{2.20}$$

In the reconstruction process, the system of equations described in Equation 2.20 must be solved to find f, given the measured data g, system matrix H and an unknown term for noise n. Two main approaches can be used to solve this system of equations – analytic and iterative reconstruction algorithms.

Analytic methods typically attempt to find a direct mathematical solution for the inverse problem that is the reconstruction process, estimating the inverse of a formula that represents the image formation process. Thus, solutions can be computed very quickly and efficiently. However, the resulting images may contain some artefacts due to the fact that attenuation and noise are not suitably accounted for.

On the other hand, iterative reconstruction methods rely on a criterion that is used to select the best estimation of the true image and an algorithm that repetitively attempts to estimate this solution. Usually this is accomplished by statistical estimation methods and probabilistic models that include factors for noise, detector response characteristics, scatter and attenuation.

In the next sections, there is a brief description of one analytic reconstruction algorithm – Filtered Backprojection (FBP) –, and two iterative reconstruction algorithms – Maximum Likelihood Expectation Maximization (MLEM) and Ordered Subsets Expectation Maximization (OSEM).

2.1.3.1 Filtered Backprojection

The backprojection operator, obtained by the inversion of the Radon Transform, can be defined mathematically by:

$$f(x,y) = \int_0^{\pi} g(s,\theta)\mathrm{d}\theta,\ s = x\cos\theta + y\sin\theta \tag{2.21}$$

where f is the activity distribution, g is the distribution of the detected counts along projection s taken at angle θ.

As Equation 2.21 suggests, the reconstructed image represents the accumulation (integral) of ray-sums of the object projections acquired over π radians. In the backprojection process, each measured *bin* value is attributed to all pixels that project onto that *bin*, and not only to pixels where the source is, because its location is not known. This process is repeated for as many angles as those acquired, to obtain the reconstructed image. However, the resultant image is blurred due to the fact that the backprojection operation is not the exact inverse of the projection operation. In order to solve this problem, usually a ramp filter is applied first, and then projection data are backprojected – Filtered Backprojection (FBP). The ramp

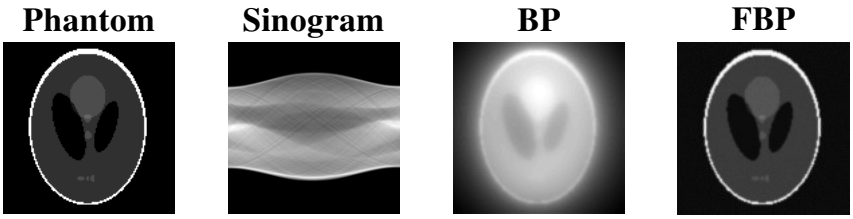

Figure 2.5: FBP reconstruction of a numerical phantom (left). The sinogram shows the projection data, and the two following images the backprojection without (BP) and with (FBP) the filter.

filter gives a weight proportional to the frequency of each sinogram's component, reducing the amplitude of the low frequency components. As a result, image noise increases due to the enhancement of high-frequency components. One way to correct for this effect is to combine the ramp filter with a low-pass filter, such as the Shep-Logan filter. Therefore, high frequencies are attenuated, while maintaining low frequencies, improving the image quality. However, the selection of the cutoff frequency for this filter is not trivial. A low cutoff value may smooth the reconstructed image, resulting in blurred details and a loss in spatial resolution, while a higher cutoff value may increase the amount of image noise. Thus, there is a trade-off between noise reduction and spatial resolution.

Usually the reconstruction process is performed in the frequency domain instead of the spatial domain, using the central section theorem. This theorem states that the 2D Fourier Transform (FT) of the activity distribution of a tomographic image can be seen as the 1D FT of a projection view of that image taken at a specific angle. Therefore the reconstruction process is easy to implement (Figure 2.5), and the algorithm is fast. First the 1D FT of each projection profile – acquired data – is calculated. Then, in the frequency domain, these data are multiplied by a ramp filter combined with a smoothing filter. The inverse FT is computed, hence filtered data return to the spatial domain. The next step is to backproject these data in order to obtain an estimate of the measured activity distribution.

Note that in a real SPECT system, the number of acquired projections is finite. This angular sampling influences the reconstruction process. When the number of angular projections is low, the reconstructed image will present streak artefacts (Figure 2.6). But, as more projection angles are added to the reconstruction process, the better is the resulting estimation of the real activity distribution (Figure 2.6). However the FBP method assumes angular symmetry of projections, a linear and shift-invariant system and it does not incorporate a noise model.

2.1.3.2 Maximum Likelihood Expectation Maximization

Proposed by Shepp and Vardi (1982) for Emission Tomography, MLEM is an iterative reconstruction method based upon the Poisson statistical nature of the radioactive decay.

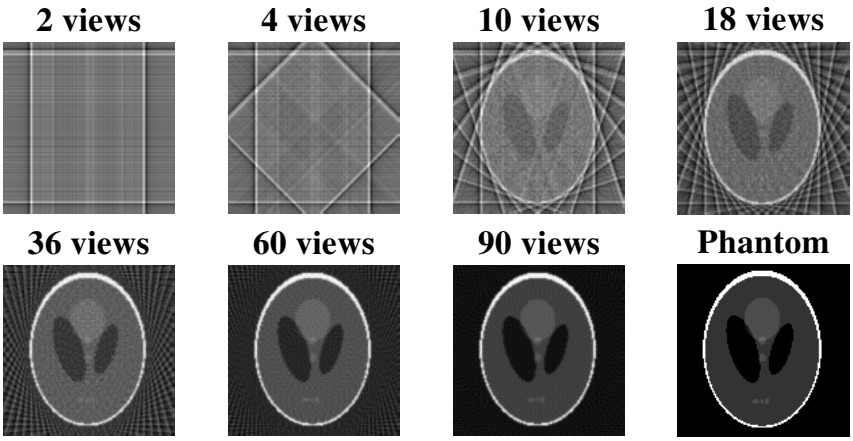

Figure 2.6: Effect of the number of viewing angles in FBP. On the right inferior corner, the original image is shown (phantom). All the remaining images correspond to FBP-reconstructed images using different numbers of views. Streak artefacts disappear with a higher number of views.

Unlike FBP, MLEM is more robust since it comprises models of the physics of SPECT imaging that account for system spatial resolution, attenuation and scatter effects, and collimator septa penetration.

The main goal of the method is to find the best estimate of the activity distribution given the measured projection data. Therefore, the algorithm is divided into two steps: the expectation step and the maximization step. In the first step, it estimates the mean number of detected counts f given the mean number of projection counts p using the likelihood function based on the Poisson distribution. Typically the logarithm function is applied to simplify calculations – log-likelihood function. Then, the second step is to find an estimate of the detected counts that makes the measured outcome most likely, given the projection data. Now, assuming that the detector D is divided into d units, and the object to reconstruct B is divided into b boxes or voxels, the current estimate of f, $\hat{f}^{[k+1]}$, is given as a function of the previous estimate $\hat{f}^{[k]}$ by Equation 2.22:

$$\hat{f}^{[k+1]}(b) = \hat{f}^{[k]}(b) \frac{1}{\sum_{d=1}^{D} p(b,d)} \sum_{d=1}^{D} \frac{n^*(d)}{\sum_{b'=1}^{B} \hat{f}^{[k]}(b') p(b',d)} p(b,d) \tag{2.22}$$

where $n^*(d)$ is the number of counts detected in each detector unit d and $p(b,d)$ is the probability or system matrix, which describes the probability of each emission from voxel b be detected in the detector unit d. This matrix can capture depth-dependent resolution, position-dependent scatter in the patient, and depth-dependent attenuation.

Evaluating Equation 2.22, it is possible to conclude that MLEM is a series of projection and backprojection operations. In each iteration k, the new image estimate $\hat{f}^{[k+1]}$ is obtained projecting the previous image $\hat{f}^{[k]}$ and comparing it with the measured projection by taking

the ratio between them; the resulting correction factor is then backprojected and used to update the current estimated image (Bruyant, 2002).

The selection of the Poisson distribution as the premise for the detection measurements ensures that convergence is achieved, even though several iterations are needed to reach it. Prior knowledge can be used to introduce constraints in the model capable of accelerating the convergence of the algorithm or to improve image quality. Moreover, the Poisson formula yields a statistically consistent estimate, with good noise properties, and imposes non-negative pixel values, which is in agreement with the assumption that activity cannot physically have a negative value.

A disadvantage of MLEM is the level of noise, which increases as the number of iterations increases. In the MLEM algorithm, noise is correlated with the signal, i.e. noise amplitude is lower than in high count regions, typically leading to an improved image quality compared to FBP in those regions. In order to solve this, one of two approaches may be taken: regularization, which includes control of the difference between neighbouring pixels throughout the reconstruction process, and post-reconstruction filtering, for example with a Gaussian filter. Either one will reduce the noise level in the reconstructed image (Hutton et al., 1997).

2.1.3.3 Ordered Subsets Expectation Maximization

This iterative reconstruction method has the same concept of projecting and back-projecting as the MLEM. However, instead of using the whole set of projection data to update the reconstructed image, it uses subsets of projection data. These subsets have an equal number of non-contiguous projections. For example, considering a SPECT acquisition of 64 projections and a total number of 8 subsets, each subset would have 8 projections distributed accordingly: the first subset would be 1, 9, 17, 25, 33, 41, 49, 57, the second subset 5, 13, 21, 29, 37, 45, 53, 61, and so on, to obtain more information.

The fact that the OSEM algorithm uses subsets of the total projection data instead of all data makes it much faster than MLEM. For an m number of subsets, OSEM needs only n iterations to get close to the same point of convergence as MLEM at $m \times n$ iterations (King et al., 2004). This is the main benefit of OSEM: the degree of acceleration increases with the number of subsets. However, the disadvantage in relation to MLEM is that it is not guaranteed to converge to the maximum likelihood solution (Tong et al., 2010). In addition, for systems with limited angular sampling, there might be insufficient data per subset, making OSEM impossible to use.

Post-filtering needs to be applied as in the case of MLEM. Furthermore, attention must be provided to the degree of acceleration. Sometimes noisy images appear after a single iteration, since the algorithm has already reached a point of convergence equivalent to many

iterations. This issue can be solved using a larger subset size in order to reduce the degree of acceleration (Hutton et al., 1997). As a consequence, the stopping point of this algorithm is now equivalent to a smaller number of iterations.

2.1.4 System Calibration

In the previous section, SPECT image reconstruction was discussed. The presented methods rely on the knowledge of the system matrix, which models the photon transport in the patient and SPECT system. Each element of this matrix gives the expected amount of detected photons given the activity distribution. Therefore the system matrix is highly dependent on the 3D model of the detector-collimator geometry.

Manufacturing errors may lead to significant deviations from the theoretical system design, and therefore from the model. In the case where system modelling errors occur, artefacts will appear in the reconstructed images (Vunckx et al., 2008; Nuyts et al., 2009). Therefore precise geometric calibration of SPECT cameras is essential to obtain the real geometry of the system and a good reconstructed image.

One way of calibrating a SPECT system is to estimate the system matrix. The system matrix can be determined using direct methods or indirect methods.

Direct methods consist in the direct measurement of each element of the system matrix (Furenlid et al., 2004). This is a long procedure, as it requires scanning a point source through the whole FOV, with enough counts to obtain the PSF for each aperture of the collimator. Variations of this method include measuring the position-sensitive PSFs in a limited number of points that sample the FOV, and interpolate for the remaining positions (van der Have et al., 2008). Interpolation has also been suggested in cases where a higher spatial resolution is needed (Chen et al., 2005). These methods are highly accurate and well-suited for stationary systems, because the geometry is more stable. However, the duration of the scanning process can become too long in order to acquire high statistical data at all the necessary grid points of the FOV, making them impractical in a clinical setting. For example, in the geometrical calibration of FastSPECTII (Chen et al., 2005), it took 24 hours to scan a grid of $64,000$ measuring points, 1 mm pitch, over the FOV. Using a similar procedure of PSF estimation from point source measurements, Miller et al. (2012) have suggested a method of generating the system matrix on the fly during reconstruction on graphics hardware, in order to tackle memory problems. In addition, these methods require sophisticated positioning tools, that might not be available or compatible with a magnetic field, in the case of hybrid systems. Finally, the actual SPECT system might be in a state of ongoing optimization, in which case the calibration procedure would have to be re-performed at each modification.

Indirect methods consist in the modelling of the system matrix as a function of geometric parameters. This can be achieved estimating a specific set of parameters by comparing

measured projection data from a set of point sources with some reference projection dataset.

For pinhole collimators, most indirect calibration methods are based on Bequé et al. (2003), which states that a pinhole aperture can be fully geometrically described by seven parameters: focal length f, electronic shifts e_u and e_v caused by drift of the detector hardware, mechanical offset m between the detector central ray and the rotation axis, distance d along the central ray between the focal point and the rotation axis, tilt ϕ and twist ψ of the aperture place in relation to the detector plane. With this knowledge, projections from point sources can be analytically calculated and fitted to measured ones in order to estimate the actual geometry of the collimator. An optimization of the method suggested the use of three non-collinear point sources with know relative distances (Bequé et al., 2005). Examples of application of this calibration method include: calibration of a variable-radius SPECT system for small animal imaging (Pino et al., 2011); calculation of a pinhole camera's system matrix with Monte Carlo simulations (Aguiar et al., 2014).

Several authors have suggested modifications to Bequé et al. (2003) method. For multi-pinhole cameras, Metzler and Patil (2005) proposed a definition of ROR that varies as a function of gantry angle and devised a method of measuring this parameter with a laser system. In addition, they proposed a new parameter – the axial offset of each aperture relative to the first one (Metzler and Jaszczak, 2006). Calibration was achieved by fitting of the point source projection centroids. For cameras with independent rotation of detectors and pinholes, DiFilippo (2008) proposed a method of full calibration with four point source projection data acquired over 360^o, and a rapid calibration after collimator repositioning with two point source projection data acquired over 180^o. For a hybrid system, a multi-pinhole SPECT-CT, Cao et al. (2009) showed how the use of *a priori* information from the CT can simplify the calibration procedure. El Bitar et al. (2013) proposed a description of the calibration parameters as a function of the SPECT detector viewing angle, in order to set up a flexible detector response function look-up table. Especially for MC simulations, this meant that the investigation of new designs did not require new MC runs. DiFilippo et al. (2006) suggested a real-time calibration of (multi-)pinhole systems using the method in Bequé et al. (2005), four point sources of a different radionuclide from the one administered to the animal, and energy windowing to separate point source data and emission data.

In the case of slit-slat collimators, calibration is similar to that of pinhole cameras. As evidenced by Ma et al. (2007), slit-slat calibration in the transaxial direction is a particular 2D case of the pinhole calibration. They were able to determine COR, slit position, and tilt and twist of the slats using projection data from one rotating point source. However, they later investigated the method for multiple slits and showed projections from one point source are insufficient for calibration, thus the use of more point sources and their relative positions, and *a priori* knowledge of the ROR greatly improves calibration accuracy (Ma et al., 2009).

Metzler et al. (2005, 2010) presented a method to estimate transverse mechanical shifts and axial electronic shifts, assuming tilt and twist are negligible, and focal length and RoR can be obtained separately. The study showed calibration is possible with a single point source, obtaining projection data at various viewing angles with a rotating camera. A recent study for slit-slat collimators and pixelated crystals showed the use of the full shape of the PSF instead of the centroid for the least squares fit provides improved slat calibration (Deng et al., 2011).

2.2 MR Imaging

Magnetic Resonance Imaging (MRI) is a non-invasive medical imaging technology that uses non-ionising radiation to provide structural images of the human body with high spatial resolution and high soft-tissue contrast, namely T_1 and T_2 weighted sequences. Physiological information can also be obtained with specific MRI sequences, such as diffusion weighted imaging, functional MRI, spectroscopy, arterial spin labelling, and others (Jackson et al., 1997; Bitar et al., 2006; Lu et al., 2005).

MRI is based on the magnetic effects of certain nuclei, especially that of hydrogen due to its abundance in water and fat, which makes up most of the human body. The hydrogen nucleus has a single proton (positively charged particle) that spins around its axis, resulting in a magnetic field. This spin will align with an external magnetic field B_0 and precess at a frequency given by the Larmor equation (Equation 2.23):

$$\nu_0 = \frac{\gamma}{2\pi} B_0 \tag{2.23}$$

where γ is the gyromagnetic ratio.

In equilibrium, all spins are precessing out of phase and aligned with B_0, resulting in a net magnetic moment in the z direction called longitudinal magnetization M_z. When an excitation pulse is applied, the spins start precessing in phase in the transverse plane, moving the net magnetic moment to that plane: M_{xy}. After the removal of the RF pulse, the spins will loose energy to the environment in a process called relaxation. With time, the spins dephase, returning to equilibrium. This results in a loss of M_{xy} and the generation of the Free Induction Decay signal (FID). The FID is what is measured as the MRI signal: the precessing signal in the transverse plane.

There are two types of relaxation: T_1 and T_2. The first refers to the recovery of the net magnetization into M_z through spin-lattice interactions. The latter refers the decay of the net magnetization in the transverse plane by spin-spin interactions. Different tissues experience T_1 relaxation at different rates, allowing for signal differentiation in the MR image.

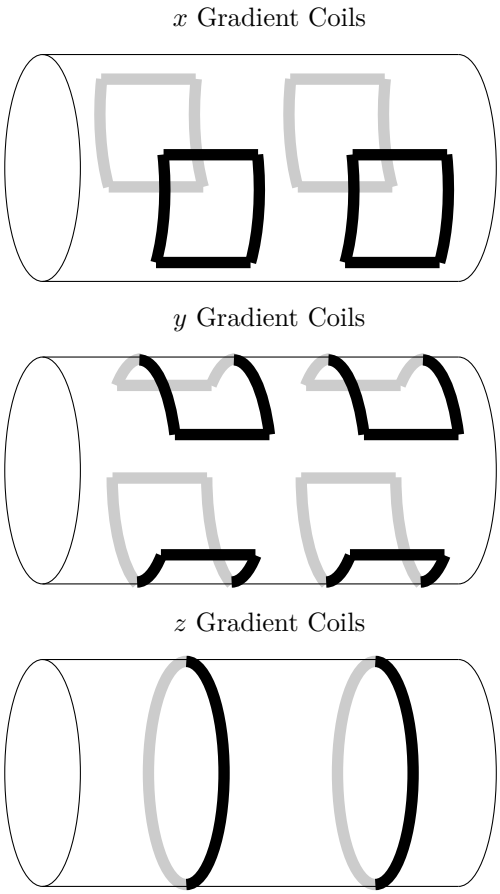

Figure 2.7: Diagram of the main MRI components. The gradient coils create a varying magnetic field from left to right (x), top to bottom (y) and head to toe (z). The main magnet (cylinder) provides a uniform magnetic field.

2.2.1 Instrumentation

The basic hardware components of MRI systems are the magnet, the gradient coils, the RF coil, shimming coils and a general purpose computer (Figure 2.7). In addition, magnetic shielding is provided by shielding coils, which reduce the magnetic field where it is not necessary, and a Faraday cage, which is incorporated in the scanning room to block RF interference from and to outside.

The magnet is a series of loops of superconducting material that is kept at a very low temperature, around 4 ^{o}K, using liquid helium or nitrogen. Its electric current generates a uniform and static magnetic field called B_0.

The gradient coils generate a linear variation in the magnetic field along the x, y and z directions, allowing for the frequency, phase and slice encoding of the MR signal.

The RF coil transmits the excitation pulse and/or receives the corresponding echo, i.e. the MR signal. There are different types of coils: body coils, head coils and surface coils (Figure 2.8). The latter are usually small and restricted to a specific area of the patient for

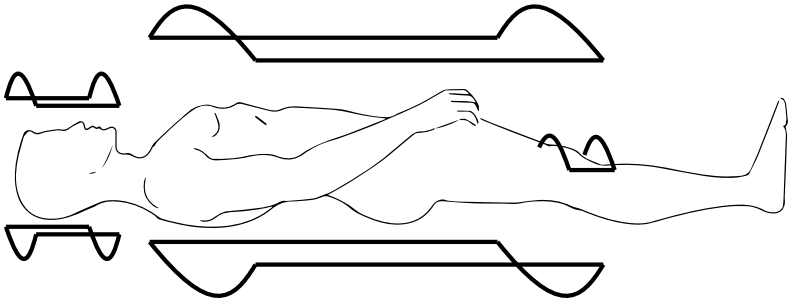

Figure 2.8: Diagram of the different types of RF coils: head, body and surface (e.g. knee) coils.

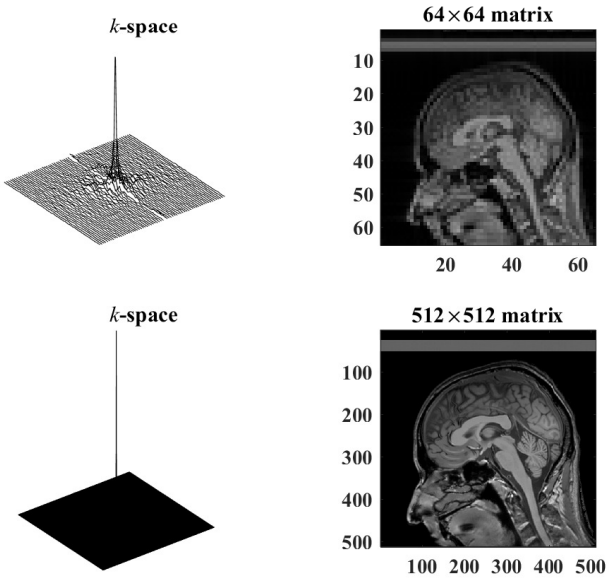

Figure 2.9: Illustration of the effect of the amount of the k-space (left) that is filled and the corresponding reconstructed MR image (right).

improved SNR due to their increased magnetic sensitivity; whilst the others are big enough to provide a uniform RF field.

The shimming coils provide auxiliary magnetic fields to obtain good B_0 homogeneity.

Finally, the computer serves two main purposes: to control the data acquisition and pulse generator, and to process and display the image.

2.2.2 Image Reconstruction

The acquired frequency signal encodes spatial information, therefore image reconstruction is based on the Fourier transform. The centre of k-space corresponds to low spatial frequencies, i.e. image structure, whilst the outer part corresponds to high spatial frequency, i.e. details of the image. The Fourier transform is applied to the k-space to decode spatial information into an image.

Image quality depends on the amount of the k-space that is filled; more complete filling results however in longer acquisitions (Figure 2.9). Furthermore, the signal-to-noise ratio in MRI is given by Equation 2.24:

$$SNR = \frac{FOV_x}{N_x} FOV_y \Delta z \sqrt{\frac{NEX}{N_y BW}} \tag{2.24}$$

where FOV is the size of the field of view and N is the size of the matrix, in the x and y directions; δz is the slice thickness, NEX is the number of excitations, and BW is the bandwidth. Therefore, SNR increases with:

- bigger voxel sizes, but resolution decreases;
- a higher number of excitations, but the acquisition time also increases;
- a stronger and more homogeneous magnetic field.

2.2.3 Safety

Safety is a very important issue when referring to MRI systems. The main problems arise from the static magnetic field, the magnetic gradients and the RF pulses (Hartwig et al., 2009).

One of the major problems of the static magnetic field relates to ferromagnetic materials, which are strongly subjected to attractive and rotational forces that project those materials to the bore entrance and the magnet itself. This can result in a serious harm of both the patient and medical staff, in addition to damage of any hardware in the travelled path. Therefore, there is a 5 G line limit that defines the safe level of static magnetic field exposure in every room with an MRI system installed. To date no biological hazards to humans have been identified from exposure to high static magnetic fields, apart from fields higher than 2 T which in some cases can cause sensory effects like nausea, vertigo and metallic taste (Schenck, 2000; Kangarlu and Robitaille, 2000).

Magnetic gradients induce an electric field in the patient, which may result in peripheral nerve and muscle stimulation, causing discomfort to the patient (Vogt et al., 2004). Also, the patient should be correctly positioned and not form a loop at any time to reduce the risk of induced current burns (Lipton, 2013). Rapid switching of the gradients generates significant acoustic noise, that should not surpass 140 dB for adult patients.

Regarding the RF pulses, deposition of energy may lead to overheating of localised body tissue resulting in burns. Therefore the patient's specific absorption rate should remain as low as possible.

Another concern is the effect of gradient fields and RF pulses on implanted devices, especially active ones such as pacemakers and cochlear implants, which can vary from movement or dislodgement, to dysfunction, and even damaging of the device.

In order to reduce the aforementioned risks, patients should undergo appropriate screening, with safety questionnaires, and equipment subjected to the magnetic field should be labelled according to their MR safety: safe, conditional or unsafe (Lipton, 2013).

Finally claustrophobia could be another source of patient discomfort, or even selection criteria, due to the closeness of the gantry and surface coil.

2.3 Multi-Modality Systems

SPECT is a functional imaging modality that uses radio-labelled pharmaceuticals to study biological processes. The emitted gamma-radiation is externally detected to generate a 3-dimensional (3D) image of the radioactive tracer distribution, which correlates with cellular function. However, limited anatomical information can be depicted, making it difficult to accurately localize disease.

The combination of functional (MRI, PET, SPECT) and anatomical imaging (MRI, CT) has potential for improved diagnostic value. Hence the development of multi-modality systems, specially with simultaneous acquisition, has been the focus of research in the field of medical imaging in recent years. Examples of such devices are PET/CT (Beyer et al., 2000), SPECT/CT (Schillaci, 2005), and more recently PET/MRI (Judenhofer et al., 2008). In the latter case, fully simultaneous acquisition is now commercially available (Drzezga et al., 2012; Levin et al., 2016).

Simultaneous acquisition of SPECT and MR images offers several advantages compared to just being able to combine functional and morphological information and have their correlation in space and time. Because both scans are acquired at the same time, the overall scanning time is reduced. Co-registration errors are smaller due to the intrinsic registration between the two modalities. The MRI scan can be used to facilitate compensation for motion and correction for partial volume effects in the SPECT image. Additionally, SPECT provides the possibility to target different biomarkers using multiple radionuclides simultaneously, and to label compounds with either diagnostic or therapeutic radionuclides. Therefore it has potential to estimate internal radiation dose, important for the treatment plan of personalised radionuclide-based therapies. Moreover there are several advantages of using MRI instead of CT: it provides improved soft tissue contrast, no additional ionizing radiation is given to the patient, and there is the possibility to use different MRI sequences to obtain functional information, which can be combined with that obtained with SPECT providing complementary information. However MRI does not give directly the information required for attenuation correction of the SPECT images. The main problems lie in the fact that MRI cannot distinguish well between bone and air, neither measure density variations within the lung (Cherry, 2009).

Some pre-clinical SPECT/MRI systems have been developed (Goetz et al., 2008; Breton

et al., 2007), although these are not truly integrated. They rely on a single pinhole SPECT camera adjacent to a low-field MR system, 0.1 T, such that the small animal can be imaged sequentially.

Meng et al. (2007) presented ultra-high resolution MR-compatible detectors, which were tested in a small animal system with pinhole collimation and point source phantoms. Preliminary experimental results were presented by Tan et al. (2009) and Hamamura et al. (2010) to show the feasibility of SPECT/MR, although they did not solve the problem of angular sampling. In the first, the SPECT system had to be moved in and out of the MR system and rotated around the object, and in the latter the object was rotated. For these systems, the importance of modelling the geometric response function of the pinhole in the reconstruction process has been shown by Xu et al. (2010).

More recently, studies addressing simultaneous SPECT/MRI have shown the feasibility of these multi-modality systems for preclinical use (Meier et al., 2009, 2011; Tsui et al., 2011b,a; Cai et al., 2012; Cai et al., 2014). These stationary SPECT inserts use cylindrical multi-pinhole collimation and two or more angularly offset detector rings. In contrast to Meier et al. (2011); Tsui et al. (2011a) , which use layers of tungsten, Cai et al. (2012); Cai et al. (2014) proposes a casted tungsten tube with platinum-iridium alloy pinhole inserts, with 300 μm and 500 μm diameters. When scanning a point source phantom with 37 MBq of ^{99m}Tc for 30 minutes, they are able to resolve sources 350 μm apart.

Regarding clinical SPECT-MRI, van Audenhaege et al. (2013); van Audenhaege et al. (2015) have designed a stationary multi-pinhole collimator for a brain SPECT insert based on four rings of thirty-four 32×32 mm digital SiPMs ($R_i = 0.5$ mm) coupled with a 2 mm-thick monolithic LYSO crystal. The tungsten powder collimator consisted in eight rings of twenty-four 0.62 mm pinholes. Pinhole rings are rotated relative to one another to improve angular sampling and separated with slats to avoid overlap of projections in the axial direction. Simulations showed a volume sensitivity of 395 cps.MBq^{-1} for a target resolution of 7.2 mm at the centre of the cylindrical FOV (220 mm-diameter, 124 mm-height).

2.3.1 System Design Issues

The important parameters when designing a SPECT system are sensitivity, resolution, field of view and sampling completeness. However, it is not possible to optimise all of them at the same time.

Collimator efficiency is defined as the fraction of gamma-rays reaching the collimator that actually pass through it to project the object onto the detector. Collimator resolution refers to the sharpness or detail of the image projected onto the detector. The more gamma-rays that reach the detector, the less specific they are, because of the uncertainty associated to their emission origin. As a result, resolution gets worse. In contrast, to improve the photon's

direction of incidence and therefore resolution, a greater fraction of gamma-rays are absorbed in the collimator, decreasing sensitivity. This is referred to as the sensitivity-resolution trade-off and consequently it is not possible to optimise both simultaneously.

Regarding sampling completeness, usually rotation of the SPECT system is needed to acquire a sufficient number of angular views or projections. This allows a good reconstruction of the 3D volume images but requires accurate calibration of the system acquisition, which may be difficult due to motion. Stationary systems, on the other hand, are more stable over time, but angular sampling may be limited (Beekman and van der Have, 2007).

A great effort is also put in the development of pre-clinical or small-animal SPECT imaging systems. These allow the acquisition of *in vivo* high resolution SPECT images and the performance of quantitative biodistribution studies, important for example for the study of pharmacokinetics and development of new drugs. In addition, they play an important role in the development of animal models of human diseases and act as a testing ground for new collimator and detector technologies.

Although many system and collimator developments start at a pre-clinical level because of easy access for testing, some strategies may not be feasible to scale up to clinical systems. Small-animal systems need to achieve higher intrinsic spatial resolution, while maintaining or improving sensitivity. In addition, some pre-clinical systems have rotation of the animal instead of the system, which is difficult in clinical settings, with the exception of the Cardius camera, Digirad (Babla et al., 2006).

Regarding the design of hybrid systems, integration can be achieved via proximity of the two modalities, development of an insert, or full re-design of the new system (van Holen et al., 2013; van Holen and Vandenberghe, 2013). Especially in the case of simultaneous operation, further technological challenges arise, namely magnetic compatibility and MR safety (see Section 2.2.3). For example, when placed in a gradient magnetic field, the collimator may be conductive and generate eddy currents. These eddy currents distort the gradient field, introducing artefacts in the MRI images (Graf et al., 2005). Samoudi et al. (2015) proposed a numerical model to investigate eddy currents in tungsten collimators. These can be reduced to residual eddy currents using different ring arrangements of the collimator units and introducing gaps with electrical insulating material between each unit. On the other hand, MRI can interfere with SPECT electronics; hence the use of semiconductor detectors has been proposed (Wagenaar et al., 2006; Hamamura et al., 2010).

In conclusion, different design strategies are applied depending on the target application for the SPECT system, if the system is for clinical or pre-clinical use, and its integration with another imaging modality. Furthermore, septal penetration and parallax effects, which deteriorate image quality, can also be taken into account when designing the collimator and system.

2.3.1.1 Septal Penetration

One important issue in the collimator design is septal penetration. It refers to gamma-rays that are not absorbed and can penetrate the collimator. For a parallel-hole collimator, it means that gamma-rays can cross from one hole into another and be detected. Similarly, for the pinhole collimator, the effective aperture size may change due to penetration of high-energy gamma-rays. This affects the targeted resolution and sensitivity.

If the collimator septa is too thin, the collimator becomes transparent to high-energy gamma-rays and a background image is added to the desired image. This results in loss of image contrast, which may affect the diagnosis. So the higher the energy of the photons emitted by the radioisotopes, the thicker the collimator septa have to be to reduce penetration. On the other hand, as the collimator gets thicker, the detection efficiency gets smaller. For example, for parallel-hole collimation, thicker septa corresponds to smaller available detection area. Therefore the desirable septal thickness needs to be as small as possible so that the occupied detector surface is small, and such that the collimator efficiency is high. For pinhole collimation, the use of channel-edge apertures has been proposed, instead of knife-edge. van der Have and Beekman (2006) simulated both types of aperture edges using Geant 4 Monte Carlo (Agostinelli et al., 2003) and they determined the penetration contribution for ^{99m}Tc, ^{123}I and ^{125}I. Channel-edge pinholes had a lower penetration fraction of perpendicularly-incident photons compared to knife-edge; however, this advantage was not true for higher angles of incidence. In addition, independent of the incident angle, sensitivity was lower for channel-edge in relation to knife-edge, resulting in lower imaging performance.

In practice, a level of 5% of septal penetration is usually chosen, because no thickness of any material is sufficient to stop all gamma-rays (Sorenson and Phelps, 1987). This is achieved by using materials with a large attenuation coefficient, i.e. materials of high atomic number and high density. However, the attenuation coefficient of the collimator material also depends strongly on the gamma-ray energy of the photons emitted by the radioisotopes used in the imaging process. Therefore it is the maximum gamma-ray energy that should be considered for the determination of an adequate septal thickness.

2.3.1.2 Multiplexing and Parallax

Multiplexing is a phenomenon related to the ambiguity in the origin of the projected gamma-rays. For example, when imaging with a multi-pinhole collimator, overlap between the projected gamma-rays through the pinholes onto the detector surface might occur. Consequently there will be uncertainty about which pinhole the detected gamma-rays came through. This means that the photons are less specific and carry less information about the object being imaged (Barrett and Hunter, 2005). As a result, the image quality deteriorates, although sensitivity might improve due to the multiple pinholes.

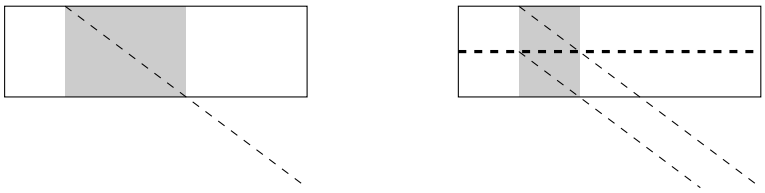

Figure 2.10: Parallax error (left) and improvement (right) using DOI information. The photon path is represented by the dashed line, and the uncertainty in the detection point by the grey area. The thick dashed line divides the crystal in two halves.

Parallax errors relate to the uncertainty of how deep gamma-rays penetrate the scintillation crystal or sensitive volume before causing ionization and being detected. The detector will attribute each gamma-ray to a different ray path and this information will be used later for image reconstruction. For gamma-rays hitting the crystal perpendicularly or in a near-to-perpendicular direction, the uncertainty associated with the detection point is very small. However for particularly acute incident angles of the gamma-rays onto the crystal, the interaction can take place in a large range of depths in the crystal, leading to an erroneous detection direction (Figure 2.10). Furthermore parallax can lead to multiplexing and consequently poor image quality. For a slit-slat collimator, parallax is worse for small distances from the slit plane to the object, leading to parallax blur which can severely affect the resolution (Metzler et al., 2006).

A solution to reduce parallax effects is to use a thin crystal, but then only a small fraction of gamma-rays can be detected, or use the information about the photon's depth of interaction to reduce the error in the localisation of the photon's path and improve resolution (Vandeghinste et al., 2011).

Chapter 3

The INSERT Project

Due to the close proximity of the topics discussed in this thesis and the European project INSERT, this chapter summarizes the achieved technical developments and the status of the INSERT system at the time of writing.

3.1 Introduction

The acronym INSERT stands for *IN*tegrated *S*PECT/MRI for *E*nhanced stratification in *R*adiochemo*T*herapy. As the name suggests, the research project aims to develop, test, and validate a SPECT insert for commercially available MRI scanners, in order to acquire simultaneously SPECT and MR images of the brain and improve personalized treatment of glioma patients[1].

The project is funded by the Seventh Framework Programme of the European Commission for 4 years, from March 2013 to February 2017. The consortium has the collaboration of several European institutions: University College London, Politecnico di Milano, Nuclear Fields, Mediso, Università Vita-Salute San Raffaele, Fondazione Bruno Kessler, Università degli Studi di Milano, CROmed, MRI.TOOLS GmbH and CF consulting.

3.2 System Design

The purpose of the grant is to manufacture a pre-clinical and a clinical system: the pre-clinical system will be installed and tested at Ospedale San Raffaele, Milan, Italy, and the clinical system at the Macmillan Cancer Centre, University College London Hospital, London, United Kingdom.

The animal system will allow the development of appropriate technical knowledge to overcome the challenges of producing such a simultaneous, multi-modality system, and to evaluate animal models of the disease. Once that is achieved, the technology will be translated to the clinical system, which aims to perform a pilot study involving glioma patients.

[1] http://www.insert-project.eu/

Table 3.1: Photopeak energies of the radionuclides of interest for the INSERT project.

Radionuclide	Photopeak Energy [keV]
^{99m}Tc	140
^{111}In	171
	245
^{177}Lu	113
	208
^{123}I	159
^{131}I	365

For the pre-clinical system, the FOV is set to 2 cm transaxially and 2 cm axially, imaged by a complete ring of ten 5×5 cm detection modules and a 3×3 multi-pinhole collimator. The full system should fit within a maximum diameter of 20 cm, which corresponds to the internal diameter of the MRI bore. A specific transmit/receiver coil will be designed for use in the 3 T Ingenia, Philips (Amsterdam, The Netherlands). The foreseen radionuclides of interest are ^{99m}Tc, ^{123}I, ^{111}In, ^{177}Lu and ^{131}I. The photopeak energies of these radionuclides are indicated in Table 3.1.

Regarding the clinical system, the FOV is set to a cylindrical shape of diameter 20 cm and height 9 cm, and imaged by 5×10 cm detection modules. The full system will consist of a ring of detection and collimation modules that should fit within a maximum diameter of 59 cm, which corresponds to the internal diameter of the 3 T Biograph mMR, Siemens (Munich, Germany). The collimator design is based on multi-slanted holes to allow for compactness and sensitivity maximisation; details are given in the following chapters of this thesis. For the clinical system, the radionuclides of interest are ^{99m}Tc, ^{111}In and ^{123}I.

Both systems have the same architecture design of a stationary system, in which the main MR-compatible components are the following:

- gamma-radiation detection modules based on the well-established Anger logic, with a single and continuous Caesium Iodide doped with Thallium (CsI:Tl) scintillation crystal and light readout;
- front-end electronics implemented in a dedicated ASIC and DAQ board to process and digitise the light readout;
- cooling strategy to lower the temperature of the photodetectors;
- tungsten collimator that maximises sensitivity;
- shielding for gamma energies higher than the highest photopeak of the radionuclides of interest;
- dedicated transmit/receiver RF coil to optimise the MR signal.

Table 3.2: Specifications for the development of an MR-compatible clinical and pre-clinical SPECT system.

	Clinical System	**Pre-clinical System**
SPECT	same FOV for SPECT and MRI	same FOV for SPECT and MRI
	simultaneous operation	simultaneous operation
	cylindrical FOV: ⌀=20 cm, h=9 cm	cylindrical FOV: ⌀=2 cm, h=2 cm
	stationary system	stationary system
	MRI bore ⌀59 cm	MRI bore ⌀70 cm
	minification at FOV centre	magnification at FOV centre
	ring geometry	ring geometry
Collimator	based on multi-slant-hole	based on multi-pinhole
	maximise sensitivity	maximise sensitivity
	target R=[8-10] mm at FOV centre	target R=[0.8-1] mm at FOV centre
	tungsten material or equivalent	tungsten material
Detector	max. 30 gamma detector modules	max. 10 gamma detector modules
	CsI:Tl scintillators	CsI:Tl scintillators
	5×10 cm 72-channel readout	5×5 cm 36-channel readout
	125-270 keV energy range	100-400 keV energy range
	intrinsic R=1 mm	intrinsic R=1 mm
	target En_{res}=10 % at 140 keV	target En_{res}=10 % at 140 keV
RF Coil	target patient aperture: 28 cm	target animal aperture: 4 cm
	match isocentre with SPECT	match isocentre with SPECT
	resonance frequency=123 MHz	resonance frequency=123 MHz

In terms of performance, the aim is to maximise sensitivity for a target resolution of 0.8-1 mm and 8-10 mm, for the pre-clinical and clinical systems, respectively. Furthermore, the target energy resolution is 10 % at 140 keV, to allow dual-radionuclide acquisition. All the specifications and characteristics of both systems are summarised in Table 3.2.

3.2.1 Detection Module

The detection module consists of a scintillation crystal, light readout, heat sink and front-end electronics.

A monolithic slanted CsI:Tl crystal was chosen as the scintillation crystal for the INSERT. This crystal has a high light yield, contributing for improved spatial and energy resolution of the photodetector. Preliminary tests on CsI:Tl samples showed a good intrinsic resolution, 5-6 %, and an absorption efficiency of 95 % at 140 keV for a thickness of 8 mm. However, the decay time is long compared to other crystals, which can affect the count rate capability of the detector.

Regarding the light readout, SDDs were first considered for the INSERT, however these detectors require a working temperature of -20^{o}C, which could be very difficult to implement in such a compact system. Furthermore, SiPMs were emerging as a feasible technology, requiring only moderate cooling for optimal performance. Therefore a SiPM-based readout was chosen for the INSERT systems. In this case, the CsI:Tl crystal is also a suitable option because of crystal's emission spectrum agrees with the quantum efficiency of the silicon

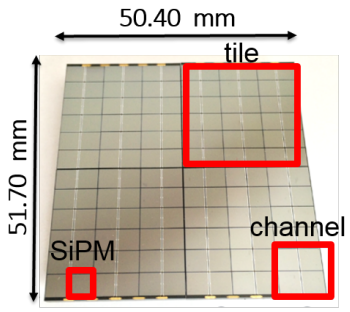

Figure 3.1: Pre-clinical SiPM readout: distinction between single SiPM and SiPM tiles. [Courtesy of POLIMI]

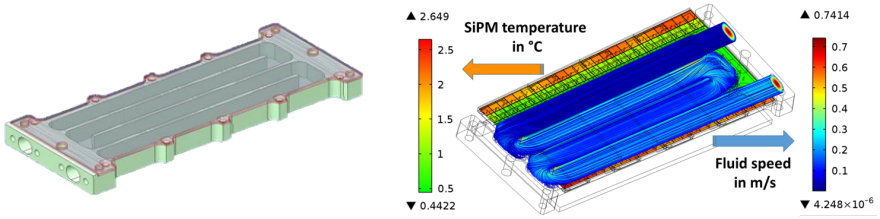

(a) (b)

Figure 3.2: Cooling block: (a) photo of the unassembled block and (b) plot of the temperature distribution in the SiPM tiles, for a simulation with a fluid speed distribution as shown in the serpentine pathway. [Courtesy of MEDISO]

detector. For the pre-clinical system, each module is read out by 12×12 SiPMs, i.e. 4 SiPM tiles with an array of 6×6 SiPMs (Figure 3.1), whereas, for the clinical system, each module is read out by 24×12 SiPMs – 8 SiPM tiles. Note that each SiPM contains 1600 APDs. Qualification of the produced tiles showed a photon detection efficiency of 40 %, an excess noise factor of 1.2, and dark count rate of 200 kHz.mm^{-2} at 550 nm and 4 V of over-voltage.

The heat sink consists of a thermally conductive plastic block, that allows cooled fluid to circulate through a serpentine pathway (Figure 3.2). This design maintains a uniform temperature distribution in the area corresponding to the SiPM tiles, in order to lower their temperature. The cooling fluid is a mixture of water and glycol that is pumped by an external recirculating cooler.

Finally, the front-end electronics were designed specifically for the INSERT. A dedicated 36-channel ASIC was developed for low-energy gamma imaging. Each ASIC reads out 4 SiPM tiles. The electronics board that contains the ASICs also provides mechanical support for the other components of the detection module, namely SiPMs and cooling block. The analogue DAQ board was designed to minimise signal corruption from the MR RF pulses and switching gradients. Both boards have a compact design to compensate for the space restrictions inside the MR bore.

The final design of the detection module for both systems is shown in Figure 3.3.

In terms of performance, measurements were performed with a ^{57}Co source at 0 ^{o}C

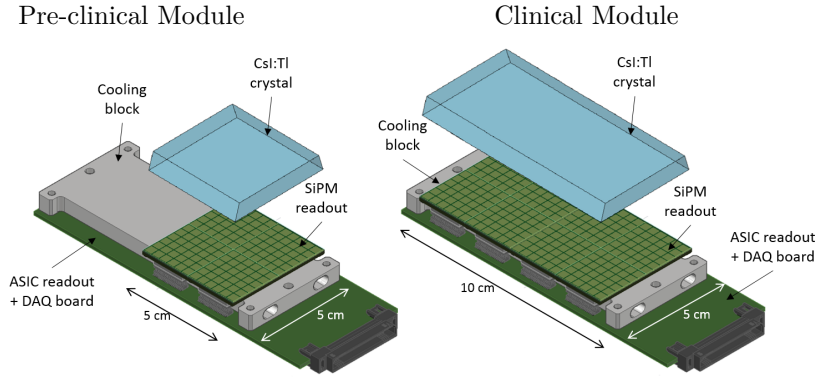

Figure 3.3: Detection module: pre-clinical and clinical designs, that apply the same electronics technology. [Courtesy of POLIMI]

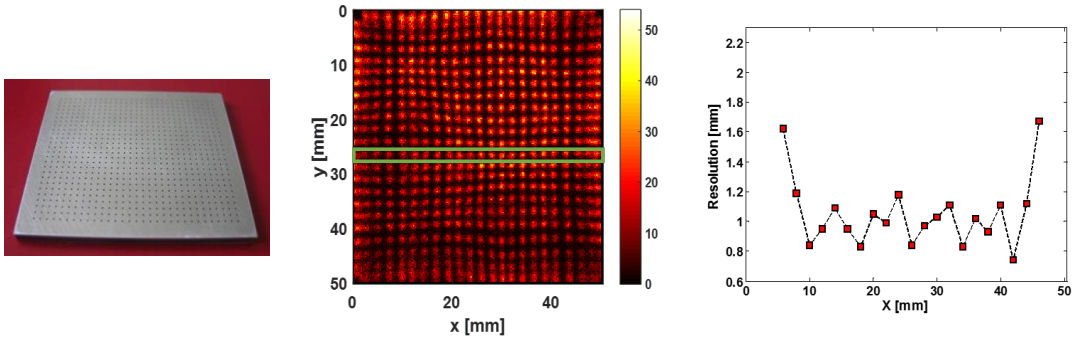

Figure 3.4: Intrinsic resolution study. Lead plate with a hole grid used on top of the 5×5 cm detection module (a). Planar projection data from a ^{57}Co source irradiation with the lead plate (b). FWHM resolution for the spots in the profile evidenced in the planar projection (c). [Courtesy of POLIMI]

and the pre-clinical detection module. The energy spectrum was obtained for a uniform irradiation (Figure 3.5). Analysis of the photopeak showed a 14 % energy resolution at FWHM of the ^{57}Co photopeak. In addition, a planar projection was obtained with an irradiation through a lead plate positioned on top of the crystal. The 2 mm-thick lead plate consisted of a grid of 0.5 mm holes with a 2 mm pitch. Analysis of the FWHM of each hole projection showed an average intrinsic resolution of 1 mm, with slight degradation at the edges of the detection module (Figure 3.4).

3.2.2 Collimator

The collimator design has three main limitations: the restricted space inside the MR bore, the limited angular sampling due to the stationary constraint, and the manufacturing material that has to be MR-compatible. The performance target is to maximise sensitivity, to be able to better evaluate metabolic and functional information of a previously detected tumour.

For the pre-clinical system, the collimator is based on multi-pinhole design, with a moulded tungsten epoxy frame and 3D-printed tungsten inserts for the pinhole apertures

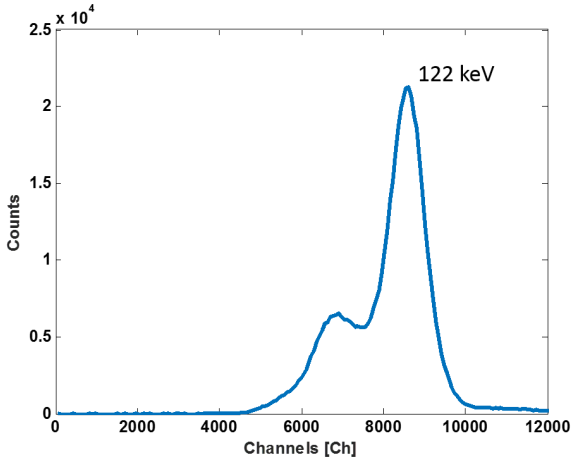

Figure 3.5: Energy spectrum from a ^{57}Co source irradiation. The highest peak corresponds to the photopeak. [Courtesy of POLIMI]

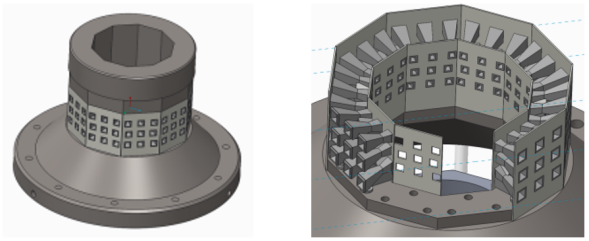

Figure 3.6: General design (left) and aperture detail (right) of the multi-pinhole collimator for the pre-clinical system. [Courtesy of MEDISO]

(Figure 3.6). For the clinical system, the design will rely on slit-slat collimation. In contrast to animal imaging, the imaging FOV is bigger than the detectors, therefore minification will occur. However this can be traded-off with the high intrinsic resolution of the detectors, in order to obtain a reasonable system resolution. Further details on the specific design of the collimator for the clinical system is given on Chapter 5.

3.2.3 RF Coil

Dedicated RF coils have to be designed and manufactured for both pre-clinical and clinical systems.

The main reasons for developing these coils are the restricted space inside the MR bore and the impossibility of using the body coil of the MR system. Standard RF coils would require a bigger space, which has to be compromised for the design of the SPECT system and better patient comfort. Considering that the SPECT electronics would be damaged by the RF pulses from the body coil, the designed RF coil has to be both a transmit/receive coil to compensate for that.

Other design considerations include the use of materials that do not highly attenuate gamma radiation, the tuning of the resonance frequency to 123 MHz for 3 T systems, and

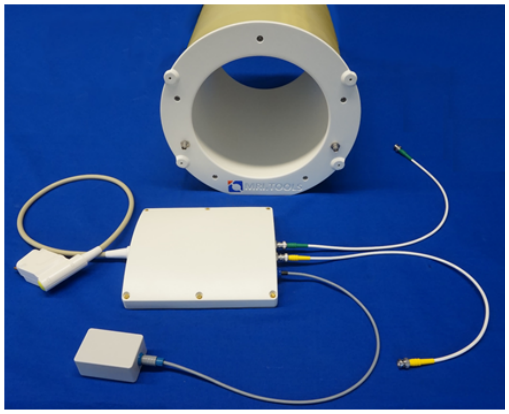

Figure 3.7: Final manufactured RF coil for the clinical INSERT system. [Courtesy of MRI.TOOLS]

the alignment of the isocentre of the SPECT and MR systems. Finally, in order to operate the coils in the respective MR systems, adequate interface and connectors will have to be produced. However, this might require proprietary information.

The final RF coil for the clinical INSERT system is shown in Figure 3.7. This coil is a result of compromised design and therefore does not cover the whole brain axially – 11 cm axial FOV. The patient aperture size is 26.5 cm.

3.3 MR Compatibility

The main issues related to MR-compatibility arise from the static magnetic field, the rapidly switching gradients and the high power RF transmit/receiver coils. Important compatibility considerations had to be taken into account in order to design a SPECT system that could be inserted inside the MRI bore, and operated simultaneously with the MRI.

Firstly, samples of materials were tested inside an MRI system, for components such as the collimator, fixation parts and wires. Additionally, special attention was given to the components shape that could generate eddy currents: looped structures were minimised and large surfaces slotted.

Secondly, the full system mechanics and geometry were constrained by the available space inside the MRI bore.

Finally, regarding the compatibility of the electronics, the process was an iterative one, with a loop of testing and compatible-design improvement. A detector box was developed (Figure 3.8) not only to be able to test a working detection module inside an MRI system, but also to perform planar SPECT experiments. The black plastic box provides stability, light shielding and an insulated environment for the detection module. Also, a bench device was developed to simulate the magnetic gradients in a controlled and localised manner (Figure 3.9). Hence magnetic-sensitive areas of the electronic boards could be mapped and their design improved (Montagnani et al., 2016).

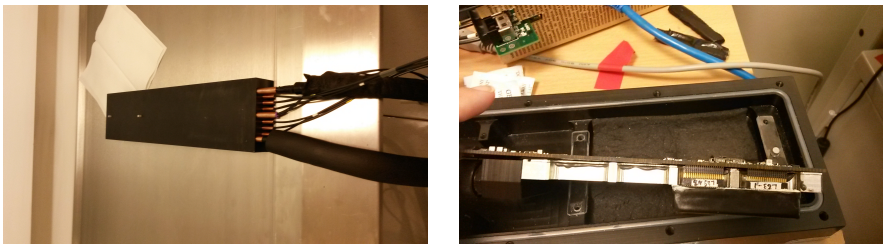

(a) (b)

Figure 3.8: Detector box set-up for experimental tests: closed (a) and open (b) box. The ASIC and DAQ boards, cooling block and scintillation crystal with SiPM readout sit inside the box, which has holes that allow the passing through of pipes and wires for signal transmission, cooling and power supply.

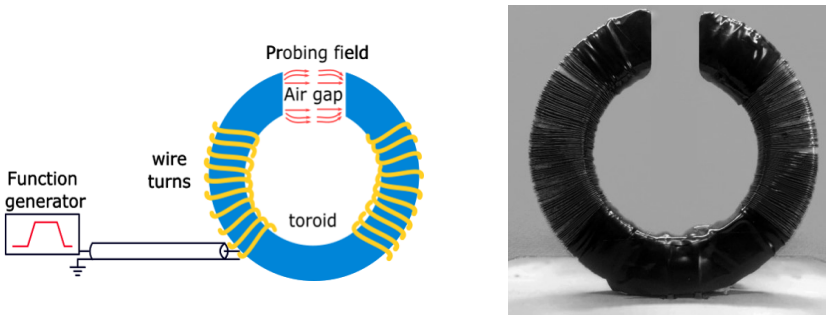

(a) (b)

Figure 3.9: Magnetic probe schematic design (a) and final device (b). [Courtesy of POLIMI]

3.4 Pre-clinical and Clinical Evaluation

As explained in Chapter 1, an effective response to treatment biomarker is an unmet need in glioma imaging and treatment.

In order to identify an early biomarker, a pre-clinical model of glioma was established, from a human-derived cell line that can be grown in mice. Non-invasive investigation on glioma models treated with temozolomide, before and after radio/chemo-therapy, showed the reduction of ^{99m}Tc-MIBI uptake can be used as a treatment efficacy biomarker, whilst MR-based features can be used as a tumour growth marker. These results point out the utility of a multi-parametric system, such as the INSERT.

The ultimate goal is to evaluate these findings with simultaneous SPECT/MR acquisition of the murine models, using the pre-clinical SPECT insert.

Clinically, the aim is to set up a pilot study with glioma patients to assess the clinical value of the INSERT system. Therefore, a protocol will have to be designed to submit for ethical approval. However, pre-clinical and clinical evaluation of the identified biomarkers are highly dependent on the availability of the planned SPECT systems.

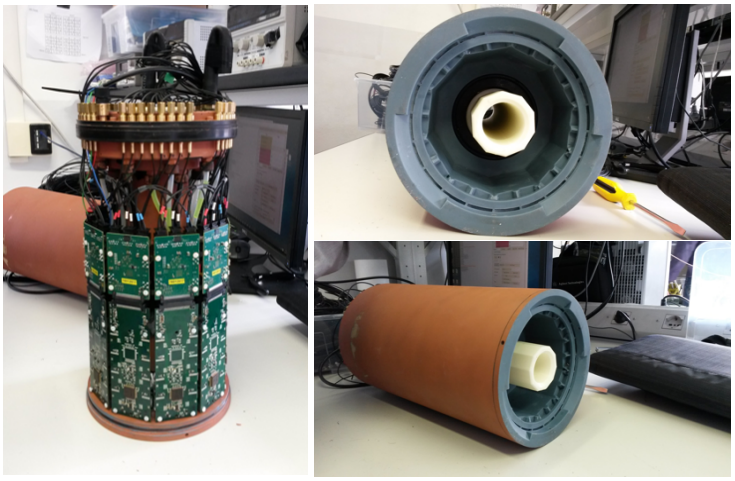

Figure 3.10: Final pre-clinical system fully assembled: with (right) and without (left) housing. Collimator is absent; it will fit between the detectors cover (grey) and the coil (white).

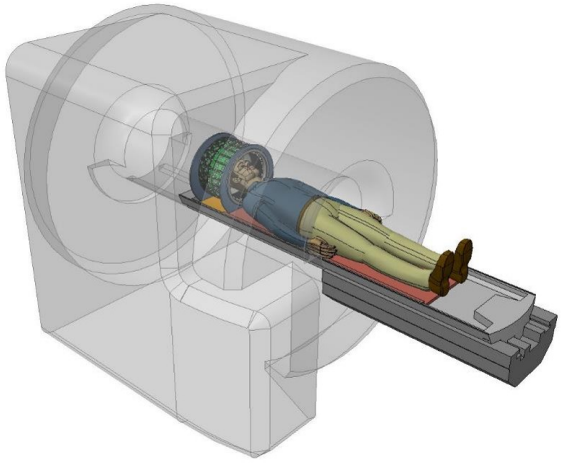

Figure 3.11: Diagram of the envisioned SPECT insert for simultaneous SPECT/MR imaging of the human brain. [Courtesy of MEDISO]

3.5 Summary

The objective of the INSERT project was to develop and manufacture two SPECT insert systems: a pre-clinical system for mouse/rat brain imaging and a clinical system for human brain imaging. The approach was to develop production techniques, MR-compatible detector technology and system design for the pre-clinical system, that could be later extended for the design and manufacture of the clinical system. Similarly, in terms of biological application, the aim was to investigate glioma models in mice with the pre-clinical system, to guide the investigation of glioma treatment in humans with the clinical system.

However, this was quite a challenging project within the proposed time-frame. Due to unforseen delays, the pre-clinical system only finished assembly in February 2016, one year before the official end date of the project. This system is depicted in Figure 3.10.

Regarding the clinical system (Figure 3.11), the housing and all individual components were produced by February 2017, but qualification and assembly as a full system had to be carried out afterwards. As a result, the clinical system will only be ready for testing and evaluation with phantoms, as a stand-alone SPECT, after the submission of this thesis.

Chapter 4

System Design for a Human Brain SPECT Insert

This chapter discusses design issues of a SPECT insert for an MR system, in order to perform simultaneous SPECT/MR imaging of the human brain.

4.1 Introduction

A simultaneous SPECT/MR system could provide combined functional (SPECT and MRI) and morphological information (MRI), correlated in space and time. SPECT provides the possibility to target different biomarkers using multiple radionuclides simultaneously, and to label compounds with either diagnostic or therapeutic radionuclides. Therefore it has the potential to estimate internal radiation dose, important for the treatment planning of personalised radionuclide-based therapies. On the other hand, MRI provides the spatial resolution for accurate localisation, but also functional information by applying various MRI pulse-sequences.

Some pre-clinical SPECT/MRI systems have already been developed (Breton et al., 2007; Goetz et al., 2008), although these systems are not truly integrated. More recently, studies addressing simultaneous SPECT/MRI have shown the feasibility of these multi-modality systems for preclinical use (Hamamura et al., 2010; Meier et al., 2011; Tsui et al., 2011a,b; Cai et al., 2014).

The objective of this chapter is to discuss a preliminary design of a SPECT insert for a clinical MRI system in order to perform simultaneous brain SPECT/MR imaging in humans. Regarding the starting point for the detector technology, it is assumed that each detector unit of the double-ring insert will consist of an 8 mm-thick CsI:Tl crystal and SiPM-based readout of size $50 \times 50 \times 13.69$ mm, insensitive to magnetic fields, with expected intrinsic resolution of 0.8 mm and a dead space of 5 mm around the edge (Busca et al., 2014b).

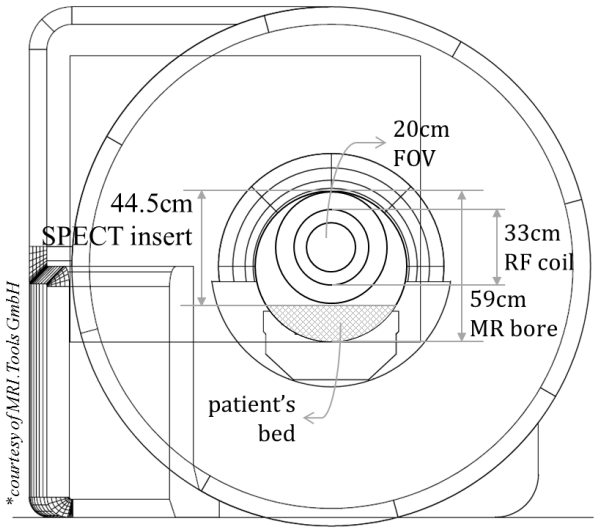

Figure 4.1: Technical sketch of the mMR system installed at the UCL Hospital, London. Annotations show the maximum available space for different components of the SPECT insert. [Adapted from MRI.TOOLS]

Compactness is needed due to the limited space inside the MR bore, whose internal diameter is 59 cm. The external diameter of the SPECT insert must be less than 44.5 cm because it will be positioned on top of the patient bed and the internal diameter should not be less than 33 cm to accommodate the patient head and the MRI receive/transmit coil (Figure 4.1). The system has to be stationary for practical reasons and to minimise interference with the MRI system. Stationary multi-pinhole systems have been investigated previously by several groups (Rowe et al., 1993; Furenlid et al., 2004; Beekman and Vastenhouw, 2004; Xu et al., 2010; van Audenhaege et al., 2013; Cai et al., 2014).

For what concerns the SPECT system, the main limitations in the development of the collimator are:

- the restricted space due to the fact that the SPECT has to fit inside the MRI bore and the patient aperture has to accommodate the patient's head and coil;
- the limited angular sampling because the SPECT cameras are stationary;
- the trade-off between sensitivity and spatial resolution, the improvement of one results in the degradation of the other.

For the INSERT, the aim is to maximise sensitivity, while maintaining a spatial resolution close to 10 mm, figure similar to state of the art resolution for conventional SPECT. From a biological point of view and considering that the system main objective is not lesion detection, improving sensitivity is more important than resolution, specially for brain imaging, in which tracer uptake is restricted by the blood brain barrier. Given the target resolution, the design issues will be addressed in the following sections.

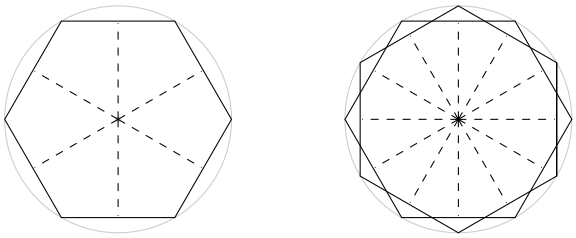

Figure 4.2: Diagram of the angular sampling for matched (left) and mismatched (right) detector rings. Dashed lines correspond to the number of angular views. NB: Only six detectors are shown here for clarity.

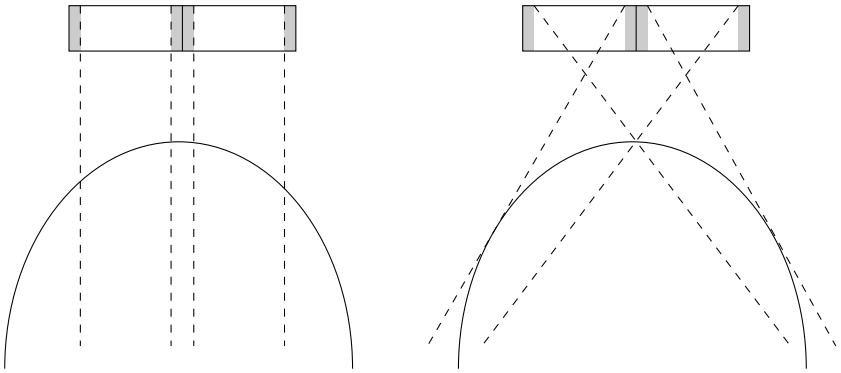

Figure 4.3: Illustration of the detector's dead area (shaded area). The dashed lines represent the axial projection in the object domain of the single-pinhole (right) and the slit-slat (left) collimators.

4.2 Methods

The slit-slat collimator was included in the evaluation due to its suitability for brain imaging (Metzler et al., 2006; Mahmood et al., 2009). This collimator provides two different types of collimation in the transaxial and axial directions. In most applications of slit-slat collimators, there is magnification in the transaxial direction defined by the slit. In the INSERT system, the distance between the collimator and the detector is small so that the SPECT insert can fit inside the MRI system and the imaging FOV is large in comparison to the detector size. Hence minification will occur in the projections space; however the system can benefit from the detector's high intrinsic resolution to compensate for this effect. In order to improve sensitivity, also multi-slit configurations of the slit-slat collimator were evaluated, and compared to analogous multi-pinhole collimator configurations.

In order to improve angular sampling with pinhole collimators, the two detector rings were rotated by half the detector-size. This mismatched configuration of the detector rings doubles the number of views as each detector ring can cover the entire axial FOV (Figure 4.2). For multi-slit slit-slat configurations with parallel slats, each ring covers only half of the imaging FOV, resulting in a small axial gap due to the 5 mm dead area at the edge of the detectors (Figure 4.3) and a smaller axial FOV compared to multi-pinhole systems:

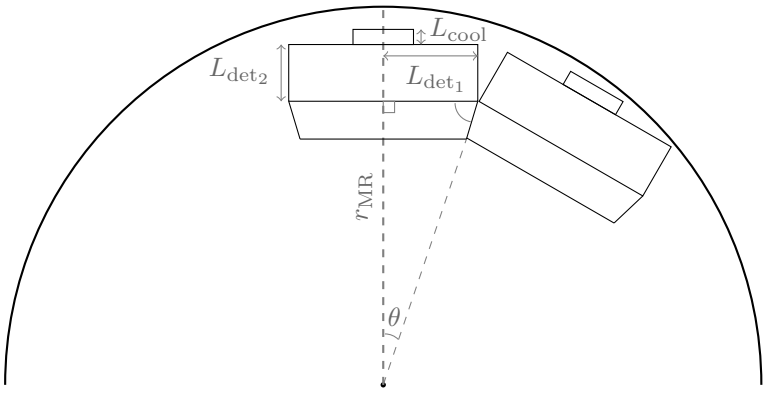

Figure 4.4: Partial diagram of a detection ring. The outer circumference represents the MR bore opening, and the boxes represent the scintillation crystal, detector and cooling system, from inside to outside. L_{det_2} and L_{cool} are the heights of the detector and the cooling system, respectively; r_{MR} is the maximum outer radius of the SPECT insert; L_{det_1} is half of the detector width and θ is half the angle covered by one detector. Dimensions are given in mm (figure not to scale).

an ellipsoidal imaging FOV of size 20×20×15 cm was assumed for the pinhole collimators due to the diverging geometry and a cylindrical FOV of size 20×20×10 cm for the slit-slat collimators. Note that for multi-pinhole configurations, the axial gap is not a problem because the whole FOV is projected onto each detector. Additionally the use of half-pinholes or half-slits to improve angular sampling is proposed. These half apertures have only half the projection area of a complete pinhole/slit and are shared between adjacent detectors in a ring. Therefore, in practice, the two halves form a complete pinhole/slit when the detectors are arranged in a ring configuration.

However, the use of pinholes and slits for collimation can introduce parallax errors due to photons incident at an oblique angle with respect to the crystal. These can be reduced using depth-of-interaction (DOI) information. This aspect was explored using minimal DOI information to assess its impact on system performance. For DOI, it is assumed that the crystal's first and second half can be differentiated, i.e. there are two separate detector-layers based on the distribution of the scintillation light. In that case, the associated detection-position uncertainty can be reduced (see Figure 2.10 of Chapter 2, Section 2.3.1.2).

Geometrical optimisation was performed using the inequality in Equation 4.1 to obtain the maximum number of detectors N in a ring that fits between the patient bed and MRI bore.

$$\sqrt{L_{\text{det}_1}^2 + \left(\frac{L_{\text{det}_1}}{\tan\theta} + L_{\text{det}_2}\right)^2} < r_{\text{MR}},\ N \in \mathbb{N} \tag{4.1}$$

where L_{det_2}=8 mm is the height of the detector; L_{det_1}=25 mm is half of the detector width;

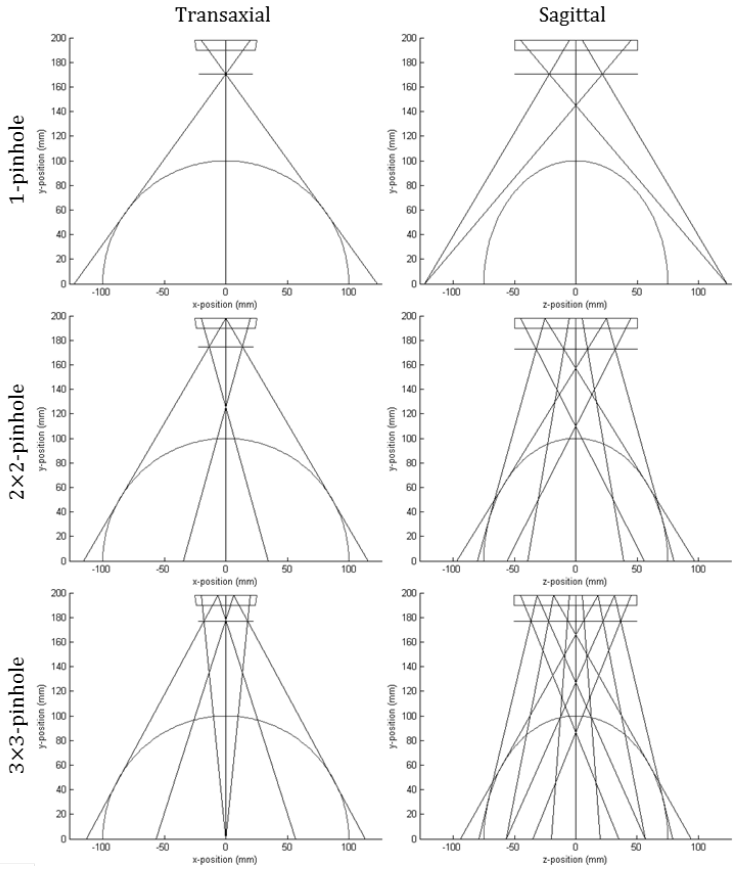

Figure 4.5: Diagrams of the multi-pinhole collimator configurations with single (1st row), 2×2 (2nd row) and 3×3 (3rd row) pinholes per detector, for transaxial (left) and sagittal (right) views. The lines from the back of the crystal correspond to the projection of the pinholes FOV. The half circle/ellipse corresponds to the object FOV.

r_{MR}=445/2 is the maximum outer radius of the SPECT insert in order for it to fit inside the MR bore; and $\theta = \pi/N$ is half the angle covered by one detector (Figure 4.4). Solving for N, a maximum of 25 detectors per ring is obtained.

Figures 4.5 and 4.6 show possible configurations of multi-pinhole and multi-slit slit-slat collimators, respectively, for the SPECT insert, with two rings of 25 detectors each. Figures 4.7 and 4.8 show the collimator configurations that apply the half pinhole/slit concept: the 5+2·½-pinhole and the 1+2·½-slit slit-slat, respectively. Because they have half-pinholes or half-slits, the 5+2·½-pinhole and 1+2·½-slit configurations can be considered intermediate between the 2×2- and 3×3-pinhole and 2- and 3-slit slit-slat collimators, respectively. One advantage of these configurations in comparison to the 2×2-pinhole and 2-slit ones is that they make better use of the central part of the detectors. With the 2×2-pinhole and the 2-slit slit-slat collimators, the centre of the detectors, which is the best part, would be used to image the edges of the object FOV, where there is usually not much activity. In addition, the slit-slat configurations have extended slats - extending from the scintillation crystal to the RF

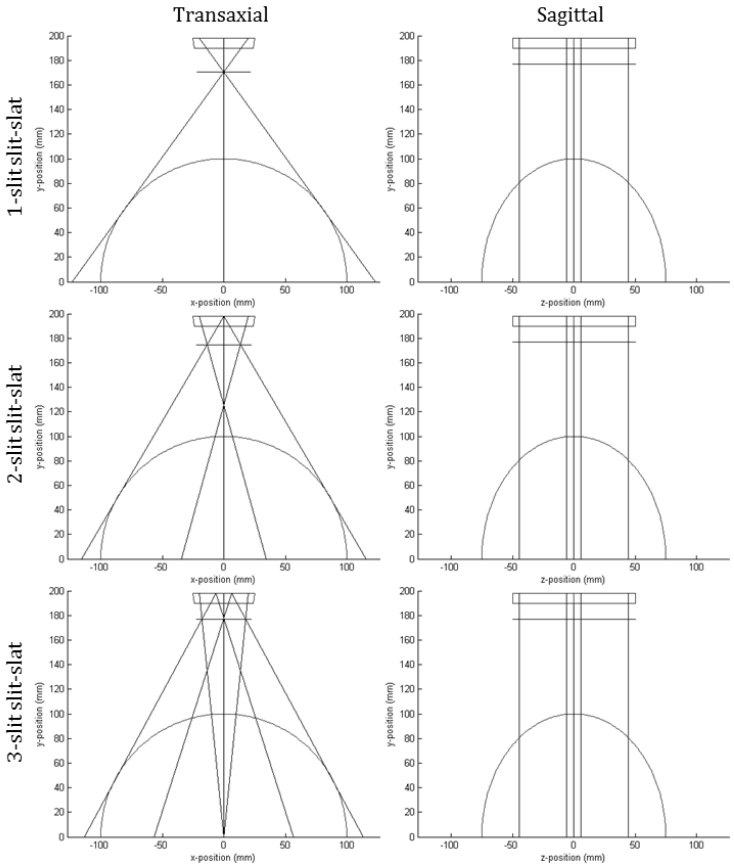

Figure 4.6: Diagrams of the multi-slit slit-slat collimator configurations with 1 (1st row), 2 (2nd row) and 3 (3rd row) slits per detector, for transaxial (left) and sagittal (right) views. The lines from the back of the crystal correspond to the projection of the slits FOV. The collimator slats are parallel, hence they correspond to straight projections in the sagittal view. The half circle/ellipse corresponds to the object FOV.

coil. As the resolution is fixed in both directions, the slat spacing can be increased, improving sensitivity. When the slat spacing increases, the shielding effect of the slats decreases, leading to higher sensitivity for the same acceptance angle.

For all collimator configurations, the geometric efficiency for a given voxel i, pinhole/slit j and detector k was calculated using Equation 4.2 (Mallard and Myers, 1963; Metzler et al., 2010) for the pinhole and slit-slat collimators, respectively. The parameters are the following: h is the distance to the collimator aperture; ϕ is the angle between the incident ray and the pinhole plane; θ is the angle between the incident ray and the aperture slit plane; d is the slat spacing; t is the slat thickness; and l_{Eff} is the slat length corrected for septal penetration. The pinhole/slit aperture w is calculated according to the target resolution with resolution-effective formulae and corrected for septal penetration with sensitivity-effective formulae (Accorsi and Metzler, 2004; Metzler and Accorsi, 2005; Accorsi et al., 2008), considering a tungsten collimator ($\mu = 3.3976$ mm^{-1} at 140.5 keV). Calculations were performed for an intrinsic resolution of the detector of $R_i = 0.8$ mm and different target resolutions $R_t = \{10, 11, 12\}$ mm

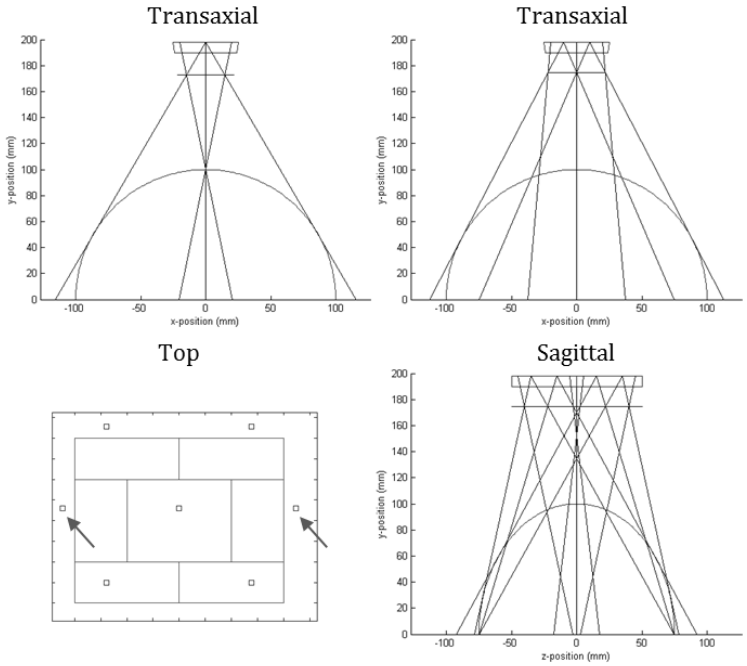

Figure 4.7: Diagram of the 5+2·½-pinhole collimator. The top row shows transaxial views through the 2-pinhole plane (left) and the 1+2·½-pinhole plane (right), the bottom left row, the top view, and the bottom right, the sagittal view. In the top view, each big rectangle corresponds to each aperture's (small square) detector FOV. The half-pinholes are highlighted by the arrows. There is a gap between the projected FOVs of the square pinholes and the detector edges which corresponds to the dead space.

at the centre of the FOV, as well as a target resolution of $R_t = 10$ mm and different intrinsic resolutions $R_i = \{0.6, 0.8, 1.0\}$ mm, for a double ring of 25 detectors each. Note that for slit-slat configurations, transaxial and axial resolutions were matched to achieve the same target resolution in both directions. The efficiency was averaged over an ellipsoidal volume δ of size 13×18×13 cm, as shown in Equation 4.2.

$$g = \frac{1}{\delta N} \sum_{i \in \delta} \sum_{k \in N} \sum_{j \in n} g_{i,j,k} \text{ , where}$$

$$g_{i,j,k} = \begin{cases} \frac{w_{g_{Eff}}^2}{4\pi h^2} \sin^3 \phi \,, & \text{pinhole (square hole)} \\ \\ \frac{d^2 w_{g_{Eff}}}{4\pi l_{Eff} h(d+t)} \sin^3 \theta \,, & \text{slit-slat} \end{cases} \tag{4.2}$$

Noise-free data were simulated with 0.8 mm R_i and 10 mm R_t and projected using an angular blurring approach (Bousse et al., 2013a). It can be described as analytical blurring of the line integrals within a cone of response, based on an angular point spread function, allowing for the modelling of a range of collimators by simply changing a weighting function. Four different phantoms were simulated to evaluate uniformity, axial and transaxial

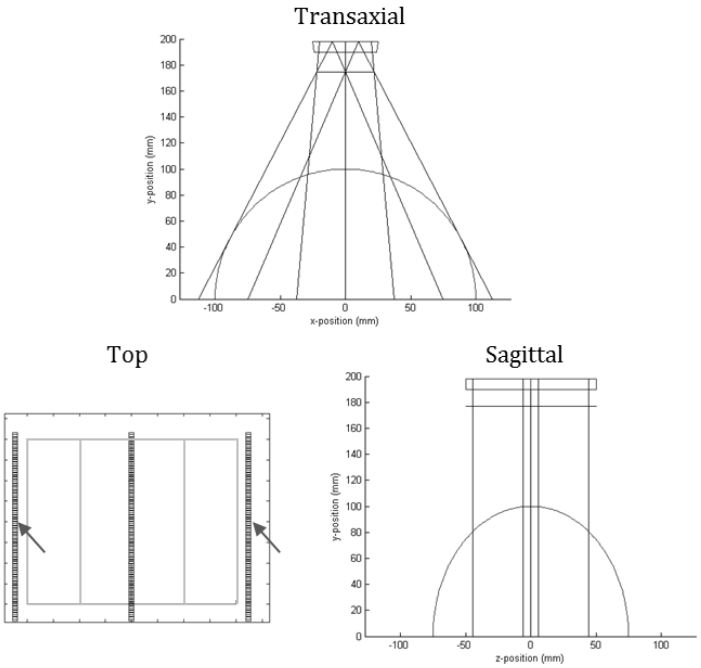

Figure 4.8: Diagram of the 1+2·½-slit slit-slat collimator. The top row shows a transaxial view, the bottom left, the top view, and the bottom right, the sagittal view. In the top view, the shaded areas correspond to the slit or half-slit; the half-slits are highlighted by the arrows. The big rectangles are the aperture's detector FOV.

sampling issues, and a realistic activity distribution: one phantom with a uniform distribution (Figure 4.9(a)); a Defrise phantom with alternating hot and cold transaxial slices of 6.25 mm thickness (Figure 4.9(b)); a Derenzo phantom with six segments with hot rod-sources of diameters 6, 7, 8, 9, 10, 11 mm (Figure 4.9(c)). All phantoms had an overall ellipsoidal shape with dimensions of 18×18×13.5 cm. Data were simulated with and without DOI information, corresponding to whether the interaction took place in the first or second half of the crystal, so as to investigate how useful this information could be. Neither attenuation nor scatter was included in the simulations. Images were reconstructed using the OS-EM algorithm (Hudson and Larkin, 1994), based on the same projection algorithm. The reconstruction parameters for each phantom are shown in Table 4.1 and the specific collimator parameters in Tables 4.3 and 4.2. The reason for not including noise was to better illustrate sampling artefacts.

Simulations were also performed with a Zubal brain phantom (Zubal et al., 1994) (Figure 4.19 - top row), corresponding to a 30 min acquisition, with 5.5×10^6 counts for the 5+2·½-pinhole and 8.6×10^6 for the 1+2·½-slit slit-slat collimator. Attenuation was included, but no DOI information. Images were reconstructed with 400 iterations of ML-EM. For the noisy simulations, Poisson distributed data were generated based on the forward-projected mean values and smoothed post-reconstruction with a 6 mm 3D Gaussian filter.

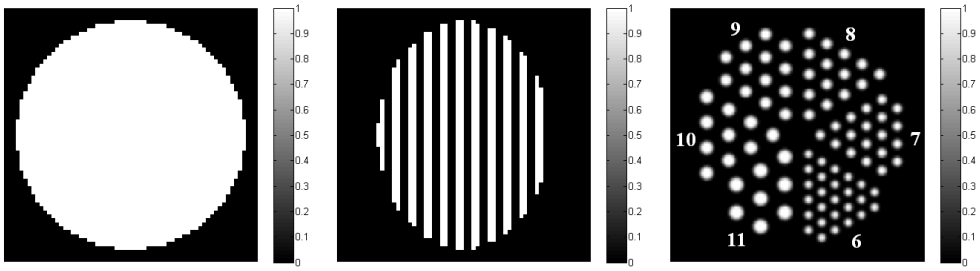

(a) Uniform (b) Defrise (c) Derenzo

Figure 4.9: Geometric phantoms: transaxial section of the (a) uniform phantom, axial section of the (b) Defrise phantom with alternating hot-cold transaxial 6.25 mm-thick compartments, and transaxial section of the (c) Derenzo phantom with 6 to 11 mm hot rod sources.

Table 4.1: Reconstruction parameters for each type of phantom.

Phantom	Phantom matrix size	Phantom voxel size (mm)	Image matrix size	Image voxel size (mm)	Number of iterations	Number of subsets
Uniform	64	3.125	64	3.125	200	5
Defrise	64	3.125	64	3.125	500	5
Derenzo	100	2	64	3.125	400	5
Zubal	90	2.2	64	3.125	400	1

Table 4.2: Geometric parameters of the slit-slat collimator designs for R_t=10, R_i=0.8 mm. Parameters legend: f is focal length, d is slat spacing, t is slat thickness, l is slat length, w is slit aperture, p is slit position, α is slit opening angle, and tr is transaxial direction.

Configuration	**2-slit**	**1+2·½-slit**	**3-slit**
f [mm]	25.32	23.25	20.77
d [mm]	1.29	1.29	1.29
t [mm]	0.3	0.3	0.3
l [mm]	24.9	24.9	24.9
w [mm]	0.68	0.55	0.28
p_{tr} [mm]	-14.83	-22.06	-17.90
	14.83	0	0
		22.06	17.90
α_{tr} [°]	42	22	34
	42	47	36
		22	34

Table 4.3: Geometric parameters of the pinhole collimator designs for R_t=10 and R_i=0.8 mm. Parameters legend: f is focal length, w is pinhole aperture, p is pinhole position, α is pinhole opening angle, subscripts tr and ax refer to transaxial and axial directions, and subscript 1 and 2 refer to each detector ring.

Configuration	**2×2**	**5+2·½**	**3×3**
f [mm]	25.32	23.25	20.77
w [mm]	0.68	0.55	0.28
p_{tr_1}; p_{ax_1} [mm]	-14.83;-15.63	-13.62;-22.65	-17.90;-18.47
	14.83;-15.63	13.62;-22.65	0;-18.47
	-14.83; 7.03	-22.06; -02.94	17.90;-18.47
	14.83; 7.03	0; -02.94	-17.90; -02.62
		22.06; -02.94	0; -02.62
		-13.62; 15.06	17.90; -02.62
		13.62; 15.06	-17.90; 11.6
			0; 11.6
			17.90; 11.6
α_{tr_1}; α_{ax_1} [°]	42;41	46;34	34;34
	42;41	46;34	36;34
	42;43	22;35	34;34
	42;43	47;35	34;35
		22;35	36;35
		46;35	34;35
		46;35	34;35
			36;35
			34;35
p_{tr_2}; p_{ax_2} [mm]	-14.83;-07.03	-13.62;-15.06	-17.90;-11.60
	14.83;-07.03	13.62;-15.06	0;-11.60
	-14.83; 15.63	-22.06; 02.94	17.90;-11.60
	14.83; 15.63	0; 02.94	-17.90; 02.62
		22.06; 02.94	0; 02.62
		-13.62; 22.65	17.90; 02.62
		13.62; 22.65	-17.90; 18.47
			0; 18.47
			17.90; 18.47
α_{tr_2}; α_{ax_2} [°]	42;43	46;35	34;35
	42;43	46;35	36;35
	42;41	22;35	34;35
	42;41	47;35	34;35
		22;35	36;35
		46;34	34;35
		46;34	34;34
			36;34
			34;34

4.3 Results

Figures 4.10 and 4.11 show the average geometric efficiency for different pinhole and slit-slat configurations, at different target resolutions and intrinsic resolutions of the detectors, respectively. The 2×2-pinhole and 2-slit slit-slat configurations achieve the highest efficiency, for the range of target and intrinsic resolutions shown. Comparing each pinhole configuration with the corresponding slit-slat, the latter achieves higher efficiency. For the 3×3-pinhole and 3-slit slit-slat configurations, there is no efficiency value for an intrinsic resolution of 1.0 mm and a target resolution of 10 mm because it is not possible to obtain a real aperture.

Figures 4.12 and 4.13 show the reconstructed images simulated with and without DOI

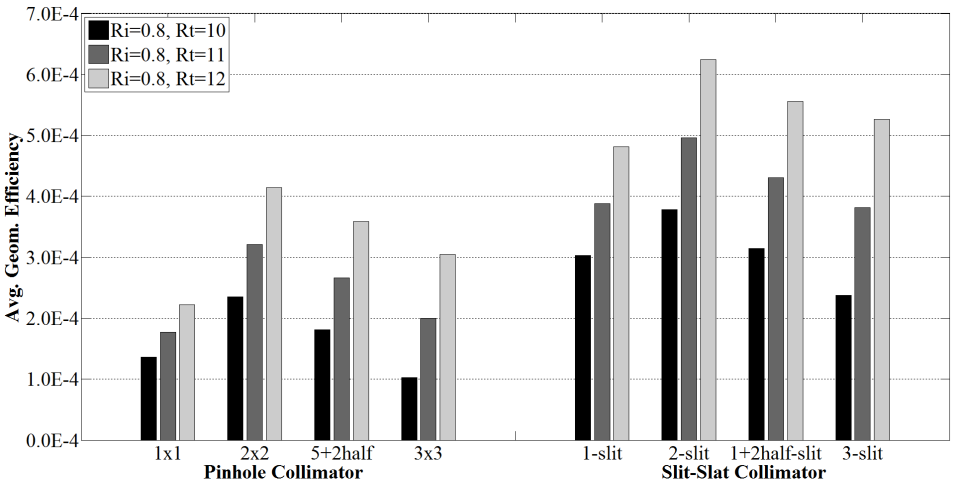

Figure 4.10: Plot of the average geometric efficiency G at a fixed intrinsic resolution $R_i = 0.8$ mm for different pinhole and slit-slat configurations and different target resolutions $R_t = \{10, 11, 12\}$ mm.

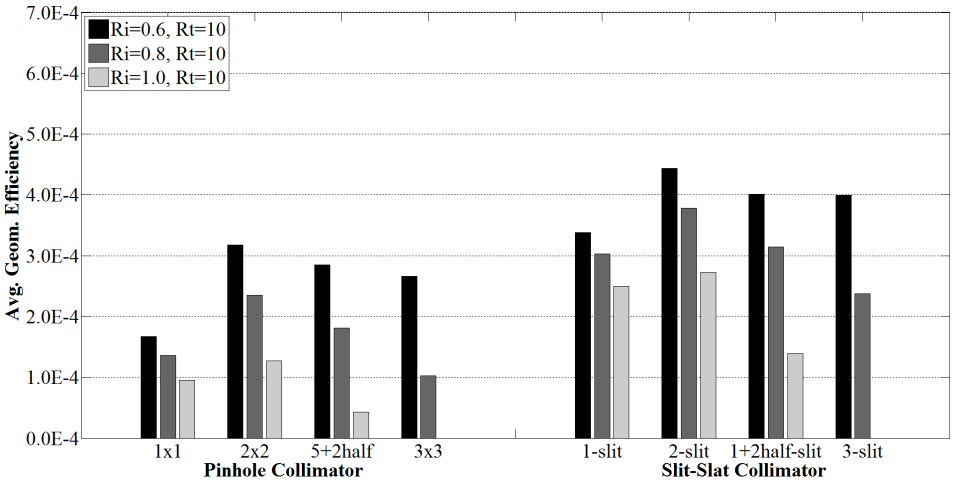

Figure 4.11: Plot of the average geometric efficiency G at a fixed target resolution $R_t = 10$ mm for different pinhole and slit-slat configurations and different intrinsic resolutions of the detector $R_i = \{0.6, 0.8, 1\}$ mm.

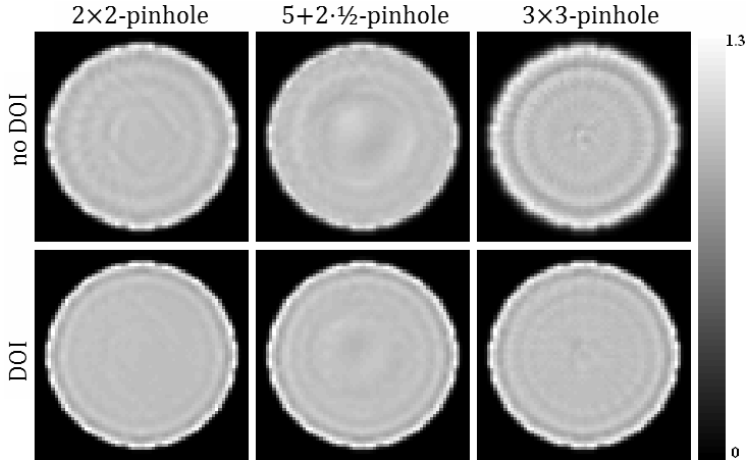

Figure 4.12: Reconstructed images for the uniform phantom simulated with different configurations of the pinhole collimator (each column), with (bottom row) and without (top row) DOI information.

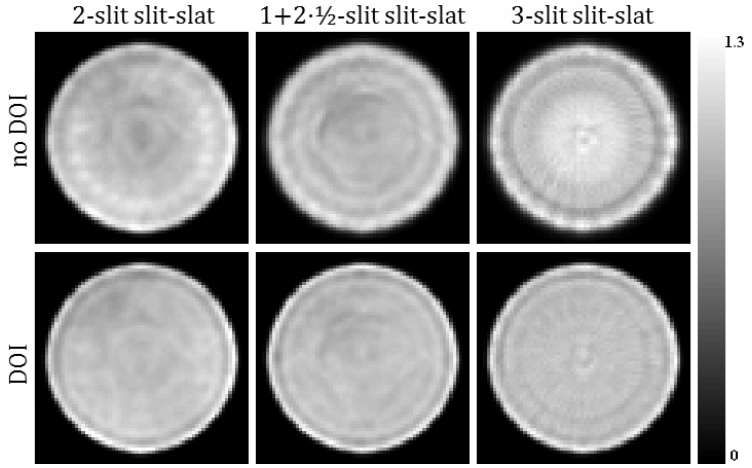

Figure 4.13: Reconstructed images for the uniform phantom simulated with different configurations of the slit-slat collimator (each column), with (bottom row) and without (top row) DOI information.

information for the uniform phantom with the different multi-pinhole and multi-slit slit-slat collimator configurations, respectively. These images are averaged over 50 mm axially for display purposes. They show ring and streak artefacts, that are improved when including the DOI information. Ring artefacts near the edges of the phantom are due to the classic Gibbs-effect, related to resolution recovery during reconstruction. The results for the single-pinhole and single-slit slit-slat collimators are not shown due to lack of sampling information for the reconstruction. They also have the lowest efficiency of all the collimator configurations and are therefore excluded from all the phantom simulations.

In order to quantitatively compare the different reconstructions with the uniform phantom, Figure 4.14 shows the coefficient of variation (CoV) for each collimator configuration. The inclusion of the DOI information improves significantly the reconstructed uniformity

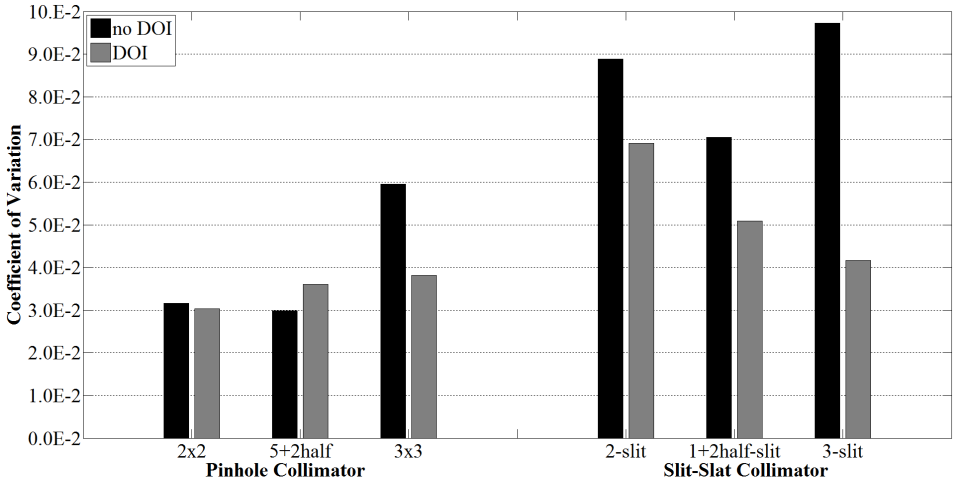

Figure 4.14: Plot of the coefficient of variation CoV of the uniform phantom for different pinhole and slit-slat configurations, including and excluding the DOI information from the simulation.

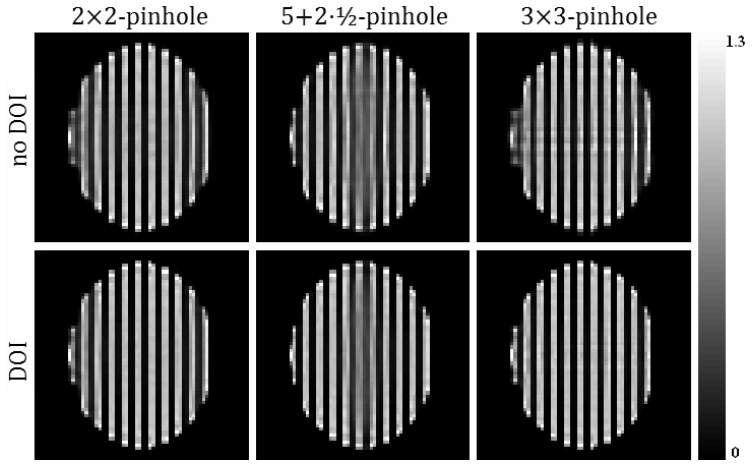

Figure 4.15: Reconstructed images for the Defrise phantom simulated with different configurations of the pinhole collimator (each column), with (bottom row) and without (top row) DOI information.

in the case of the multi-slit slit-slat collimators. With DOI, the uniformity improves with increasing number of slits due to improved angular sampling. The deterioration in uniformity for the 3-slit collimator without DOI is due to an increased amount of cross-talk, related to the parallax effect. For the multi-pinhole configurations, the effect of including the DOI information is not obvious. The angular sampling is better with the pinhole collimators due to the angular offset of the two rings, which results in better uniformity compared to the slit-slat collimators. An improvement with DOI can be seen for the 3×3-pinhole collimator for the same reason as above.

Figures 4.15 and 4.16 show the reconstructed images simulated with and without DOI information for the Defrise phantom, with different multi-pinhole and multi-slit slit-slat configurations, respectively. These images are averaged over 6.25 mm transaxially for display

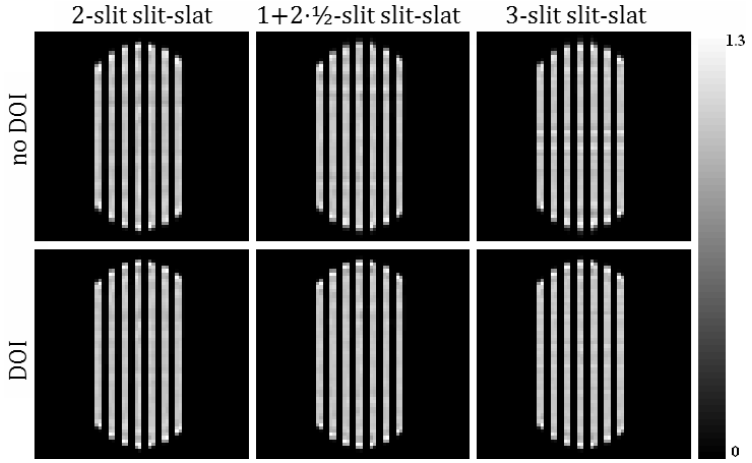

Figure 4.16: Reconstructed images for the Defrise phantom simulated with different configurations of the slit-slat collimator (each column), with (bottom row) and without (top row) DOI information.

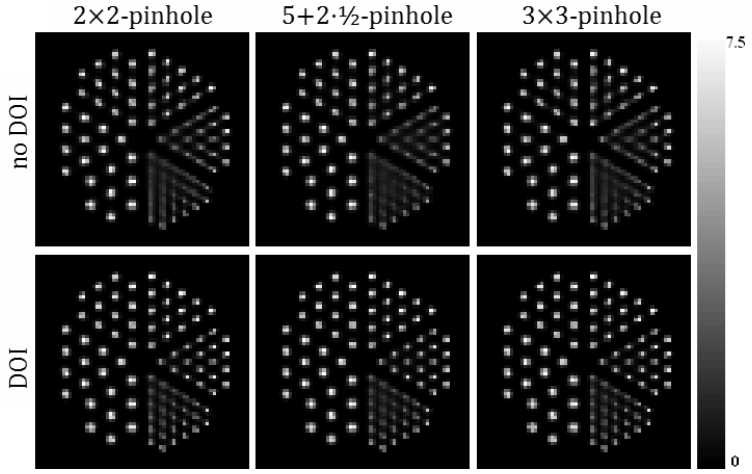

Figure 4.17: Reconstructed images for the Derenzo phantom simulated with different configurations of the pinhole collimator (each column), with (bottom row) and without (top row) DOI information.

purposes. The contrast between hot and cold compartments is slightly larger for the slit-slat configurations when compared to the pinhole ones. With the 5+2·½-pinhole collimator, increased blurring is seen at the centre of the phantom, in between the two rings. However, the inclusion of the DOI information in the reconstruction appears to reduce this blurring.

Figures 4.17 and 4.18 show the reconstructed images simulated with and without DOI information for the Derenzo phantom, with different multi-pinhole and multi-slit slit-slat configurations, respectively. These are averaged over a section of 50 mm axially. For all configurations, 7 mm rods can be distinguished in the reconstructed images. In general, the pinhole collimators give better resolution, due to better angular sampling. The images simulated with DOI information present better resolution.

The reconstructed images for the simulations with the Zubal phantom are shown in

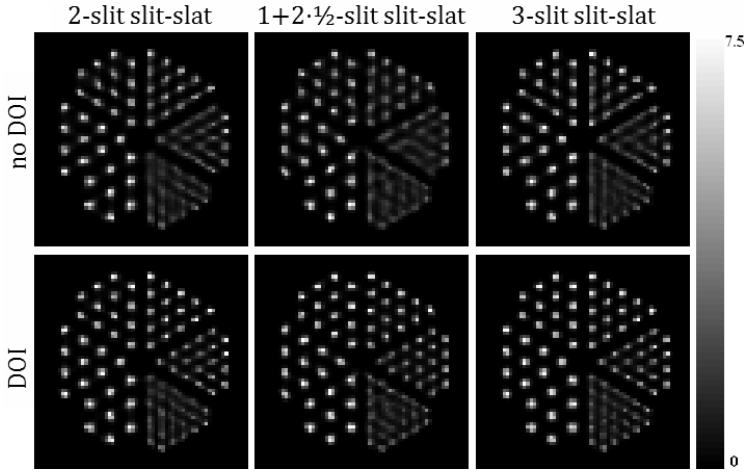

Figure 4.18: Reconstructed images for the Derenzo phantom simulated with different configurations of the slit-slat collimator (each column), with (bottom row) and without (top row) DOI information.

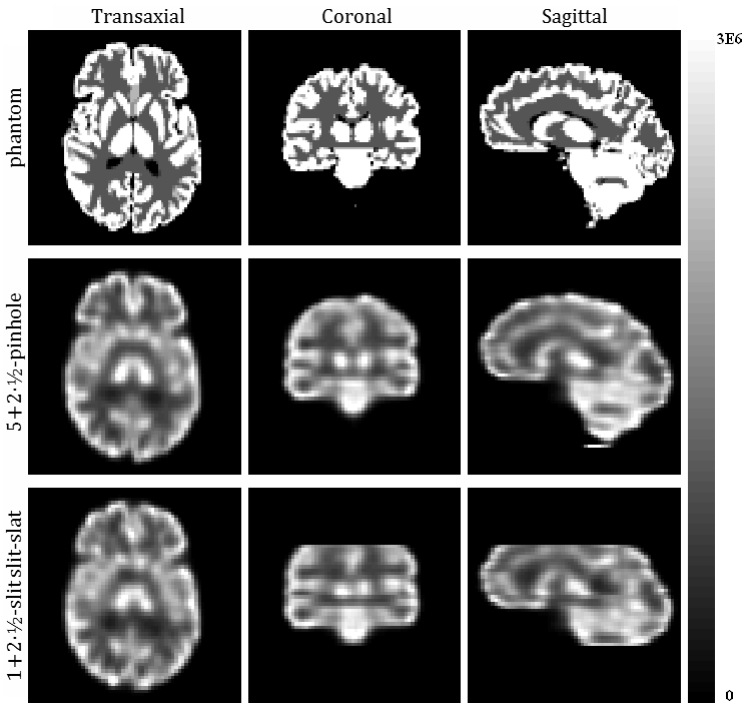

Figure 4.19: Reconstructed images for the Zubal brain phantom simulated with the 1+2·½-slit slit-slat (bottom row) and 5+2·½-pinhole (middle row) collimators and excluding DOI information. The top row shows the brain phantom for comparison. Each column corresponds to a different anatomical plane.

Figures 4.19 and 4.20, for the noise-free and noisy simulations. For the noise-free simulations, the reconstruction for the 5+2·½-pinhole shows slightly better transaxial and coronal images, specially in terms of structural definition and left-right symmetry, due to improved angular sampling. In the axial direction, the reconstructions with both collimators are comparable, even though the axial FOV is smaller for the 1+2·½-slit slit-slat. For the noisy simulations,

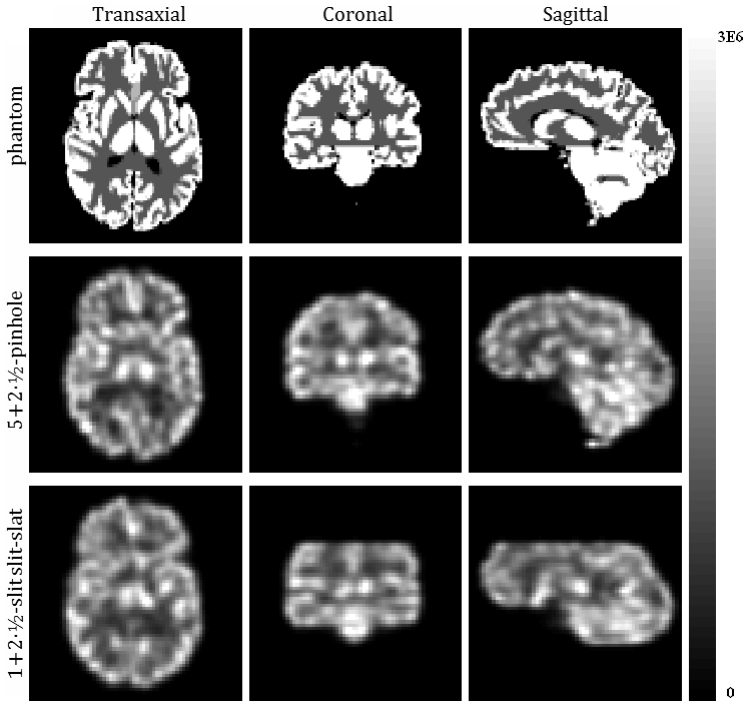

Figure 4.20: Reconstructed images for the Zubal brain phantom simulated with noise and the 1+2·½-slit slit-slat (bottom row) and 5+2·½-pinhole (middle row) collimators and excluding DOI information. The top row shows the brain phantom for comparison. Each column corresponds to a different anatomical plane.

the 1+2·½-slit slit-slat image shows slightly less variability due to better statistics, although it is difficult to draw a definite conclusion.

4.4 Discussion

Figures 4.10 and 4.11 show that improved efficiency is obtained for collimator configurations with multiple slits or pinholes when compared to the single-aperture configurations. Meaningful comparison with state-of-the-art SPECT systems is difficult as these utilise collimators designed to provide a compromise between sensitivity and resolution, e.g. for the Mediso Nucline X-Ring-4R 4-head SPECT, with LEHR collimators, resolution is better than 7 mm with a sensitivity of 2.7×10^{-4} cps.Bq^{-1}. The proposed SPECT insert design can achieve similar sensitivity, albeit with a target resolution of 10 mm, but fitting within the MRI bore.

When the target resolution of the system is relaxed from 10 to 12 mm FWHM, there is a gain in sensitivity of about 30 % (Figure 4.10). Furthermore, as the intrinsic resolution of the detectors improves, so does the efficiency due to bigger pinhole/slit apertures, for the target resolution of the SPECT insert. The gain ranges between 10-30 %, depending on the collimator configuration, and intrinsic and target resolutions. Hence the lowest possible intrinsic resolution should be aimed for, which can also compensate for the minification. For all combinations of intrinsic and target resolutions, the slit-slat collimators achieve

higher efficiency than the corresponding pinhole configurations. Note that with the slit-slat collimators, there is a reduction in sensitivity between the two detector rings due to the axial gap, but it does not reach zero.

Comparing the different multi-pinhole systems and the different multi-slit slit-slat systems, it would seem that the 2×2-pinhole and the 2-slit systems provide the best overall performance, in terms of sensitivity (Figure 4.10), uniformity (Figure 4.14) and resolution (Figure 4.15-4.18). However, there is a disadvantage with these designs from a practical point of view - the centre of the detector is used to image the edges of the object FOV and vice-versa. In practice, the performance of a detector tends to deteriorate towards the edges, so this is a sub-optimal situation. Therefore these designs should be avoided, and the 5+2·½-pinhole and 1+2·½-slit slit-slat designs favoured. These have better sensitivity than the 3×3-pinhole and 3-slit designs, respectively, and better uniformity in the absence of DOI.

Comparing the multi-pinhole to the multi-slit slit-slat collimators, the former gives better reconstructed uniformity and transaxial resolution, while the latter gives better axial resolution and higher sensitivity. The pinhole configurations have extended axial FOV but there is a risk of artefacts due to activity in incomplete sampled areas.

For the brain phantom (Figure 4.19), reconstructions with the 5+2·½-pinhole collimator are slightly superior when compared to the 1+2·½-slit slit-slat, in terms of symmetry and accuracy of the activity distribution. However, the difference is reduced in the presence of noise due to the higher sensitivity of the slit-slat collimator (Figure 4.20). For the slit-slat collimator, the reduced axial FOV may be a problem for tracers which require a reference region in the cerebellum, unless it is possible to reposition the patient in relation to the collimator's FOV.

In the INSERT system, the angular sampling is limited by the total number of detectors: 50 for the pinhole configurations and 25 for the slit-slat collimators, as each ring covers only half of the imaging FOV. This results in some degradation of image quality compared to a rotating system, where 128 projections are usually acquired over 360 degrees.

Regarding the use of DOI information, reconstructed images show reduced artefacts and improved uniformity in geometric phantoms. Although the difference is small for the brain phantom, the inclusion of the DOI information shows some potential for implementation within the INSERT project. Another way of improving image quality would be to incorporate MR-based anatomical priors in the reconstruction algorithm (Nuyts, 2007; Chan et al., 2009; Bousse et al., 2010; Vunckx et al., 2012; Kazantsev et al., 2012).

4.5 Conclusion

The main goal of this chapter was to discuss collimation design issues for a simultaneous SPECT/MRI brain scanner, using high-resolution detectors and prioritising sensitivity over

spatial resolution.

Many of the constraints in the development of such collimators have been addressed, mainly the restricted space in the MRI bore and the angular sampling. Different types of multi-pinhole and multi-slit slit-slat collimators were designed and compared in terms of performance. Additionally new concepts of collimation were proposed to improve angular sampling: the half-pinhole and half-slit.

The rotation of one ring in regards to the other is a simple solution for improved angular sampling for the multi-pinhole systems. The use of DOI information has the potential to improve the reconstructed image quality.

Comparing the multi-pinhole and multi-slit slit-slat collimators, the former gives better reconstructed uniformity and transaxial resolution, while the latter gives better axial resolution and sensitivity. Regarding individual configurations, the 2×2-pinhole and 2-slit slit-slat designs achieved relatively high sensitivity, but would have the disadvantage of a sub-optimal utilisation of the detector area. As a result, the 5+2·½-pinhole and 1+2·½-slit slit-slat designs are preferable. However, these are preliminary collimator designs based on initial expected detector performance for the INSERT system. Final design of the collimator will have to be adjusted according to realistic detector performance (see Chapter 5).

Chapter 5

INSERT System Design based on Novel Collimation: the MSS Collimator

This chapter discusses further the design of collimator prototypes and the final collimator and insert SPECT system, for simultaneous SPECT/MR imaging, taking into consideration the technological advances of the INSERT project.

5.1 Introduction

The main aim of this work is to design a high sensitivity collimator for a SPECT insert for an MRI system, in order to perform simultaneous SPECT/MR imaging of the human brain. The clinical system will consist of small, high-resolution and MR-compatible photodetectors, with 8 mm-thick CsI:Tl scintillation crystals and SiPM readout. In contrast to the specifications in the previous chapter, each detection module will consist of one long scintillation crystal with 4×2 SiPM tiles and two ASICs to read out an area of 100×50 mm instead of two of 50×50 mm. Furthermore, advances in the detector development indicate an expected intrinsic resolution of 0.8 mm and energy resolution of 12 % (Busca et al., 2014a; Occhipinti et al., 2014). With this new detector design, there is no axial gap and new collimator configurations can be explored to improve angular sampling.

Due to the fact that the SPECT insert has to accommodate an MR coil and fit inside the MRI bore when positioned on top of the patient bed, there is restricted space for the collimator. The external diameter of the SPECT insert has to be less than 44.7 cm, to fit inside the bore of the clinical MRI scanner (Biograph mMR, Siemens), and the internal diameter should not be less than 33 cm, to leave enough space for the MRI coil between the SPECT collimator and the patient opening. In addition, rotation of the SPECT system will be avoided to reduce the interference between the two systems. However, with a stationary system, angular sampling will be limited.

In the next sections, different collimation options will be proposed and the final collimator and system design will be refined, within the context of the INSERT project.

5.2 New Collimation Design and Assessment

In the previous chapter, the use of multi-pinhole and multi-slit slit-slat collimators was investigated for the INSERT system, and the concept of half-aperture was introduced for optimal utilisation of the detector area.

A pinhole collimator is characterised by the aperture size and the focal length, which may lead to magnification or minification of the object depending on the distance to the collimator. In general, the use of multi-aperture systems leads to increased sensitivity, although it depends on the amount of overlap in the object FOV. One disadvantage of pinhole collimation is the presence of axial blurring and artefacts at the edges of the FOV due to incomplete sampling (Metzler et al., 2003).

The conventional slit-slat collimator combines two types of collimation: pinhole collimation in the transaxial direction defined by the slit, and parallel-hole collimation in the axial direction defined by the slats. The slit aperture extends along the axial direction of the detector and the parallel septa, called slats, extend in the opposite direction, from the detector surface to the slit collimator. In contrast to pinhole collimation, the use of axial slats provides independent axial slices, which achieve complete sampling with a circular orbit around the object being imaged. Also slit-slat collimation provides an enlarged axial FOV, at the expense of loss in axial resolution due to no axial magnification. Finally, multiple slits can be accommodated in the transaxial direction to increase sensitivity.

Therefore, the objective is to design a multiple-aperture collimator for a stationary system with 25 detectors, maximising system sensitivity for a target resolution of 10 mm. Based on pinhole and slit-slat collimation and the updated specifications of the detection modules, novel collimation designs are introduced, for improved angular sampling and performance.

5.2.1 Methods

Two new concepts for slit-slat collimation were introduced: the interior slit and the mini-slit. With an interior slit to the slat component of the collimator, the slit aperture is located between the slats. This new design provides the possibility of having longer slats extending beyond the slit plane. As the resolution is fixed in both transaxial and axial directions, the slat spacing can be increased, resulting in a sensitivity gain. So the main advantage is allowing minification without compromising the slat length and maximising the use of space to optimise sensitivity. The mini-slit is a short section of the slit component, and therefore arrays of mini-slits can be used to cover the object FOV with one detector, in

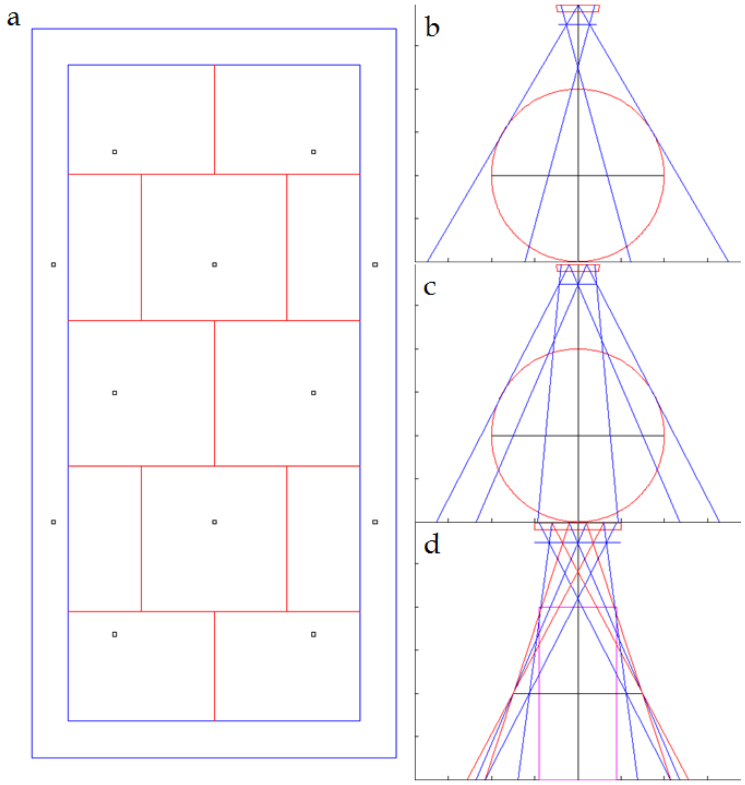

Figure 5.1: Geometry of the 8+4·½-pinhole collimator: top view through the aperture plane (a), transaxial view through the 2-pinhole (b) and 3-pinhole (c) plane, axial view (d). The projected area for each pinhole is highlighted in red. On the right hand side diagrams, the collimator's FOV coverage can be depicted.

contrast to the normal continuous slit in a standard slit-slat collimator. In order to improve angular sampling, each mini-slit array is also misaligned with the adjacent one. Finally, the half-aperture design is also included for the mini-slit arrays at the transaxial edges of the collimator. This new collimator design will be referred to as the multi-mini-slit slit-slat (MSS) collimator.

For the new detector design, three different configurations for each type of collimation (pinhole and slit-slat) were compared: 4×2-, 8+4·½- and 5+10·½-pinhole, and 2-, mini- and 1+2·½-slit slit-slat collimator. Each configuration corresponds to the number of pinholes or slits that project to one detector. Note that ½-pinholes or ½-slits refer to apertures that are shared between two adjacent detectors in the ring configuration. All configurations cover a 20×20×9 cm cylindrical FOV and avoid multiplexed data at the back of the crystal.

Figure 5.1 shows the geometry of the 8+4·½-pinhole collimator. The layout of the MSS collimator is shown in Figure 5.2. Along the axial direction, each collimator has alternating sections of 2 pinholes/mini-slits and 1+2·½pinholes/mini-slits.

Geometric efficiency was calculated using analytical equations for efficiency, which take into account septal penetration, for the pinhole and slit-slat collimators (Accorsi and Metzler,

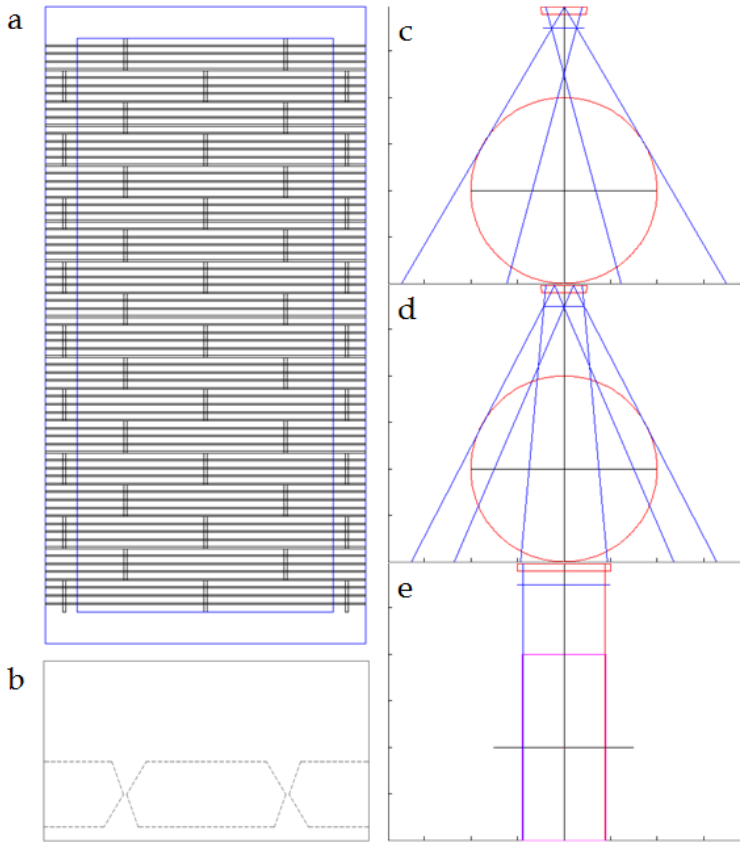

Figure 5.2: Geometry of the MSS collimator: top view through the aperture plane (a), slat detail with the interior slit (b), transaxial view through the 2-mini-slit (c) and 3-mini-slit (d) plane, axial view (e). On the right hand side diagrams, the collimator's FOV coverage can be depicted.

2004; Metzler et al., 2006; Accorsi et al., 2008; Novak et al., 2008). The efficiency was averaged over the FOV. The parameters for each collimator configuration were determined so as to achieve a target resolution of 10 mm FWHM at the centre of the FOV, in both transaxial and axial directions. The aperture angle was calculated such that there was no overlap between the FOVs from the collimator apertures at the back of the crystal to avoid multiplexing.

Noise-free simulations were performed for three digital phantoms – uniform, Derenzo and Defrise –, using a projection algorithm based on angular blurring (Bousse et al., 2013a). Attenuation was included in the simulation, but not scatter. Images were reconstructed using the MLEM algorithm based on the same projector.

5.2.2 Results

The bar chart in Figure 5.4 shows the average analytical geometric efficiency, for the different collimator configurations. For each collimation type, highest efficiency is obtained for the 4×2-pinhole collimator, 2.8×10^{-4}, and for the 2-slit slit-slat collimator, 3.8×10^{-4}; efficiency

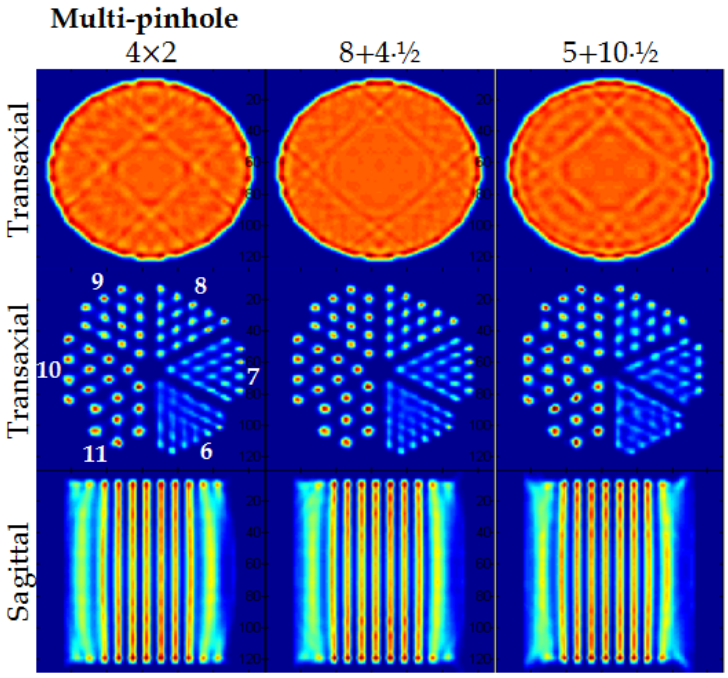

Figure 5.3: Reconstructed images for the uniform (top row), Derenzo (middle row) and Defrise (bottom row) phantoms simulated with different multi-pinhole collimator configurations.

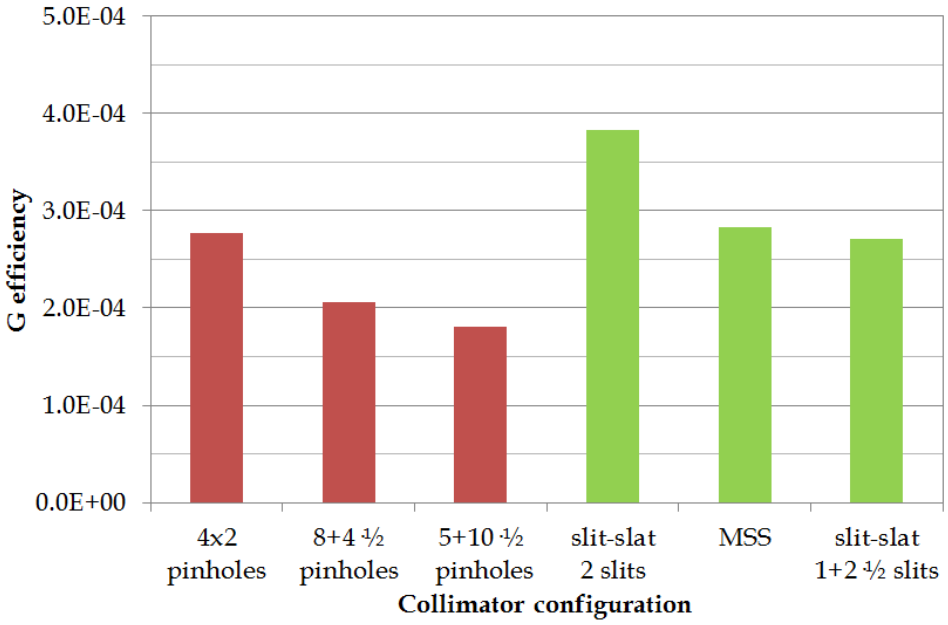

Figure 5.4: Analytical geometric efficiency for different multi-pinhole and slit-slat collimator designs.

decreases with a higher number of apertures, because focal length decreases and the object-collimator distance increases.

For the noise-free simulations, Figure 5.3 and Figure 5.5 show the transaxial slices of the reconstructed images for the uniform and Derenzo phantoms, and sagittal slices of the

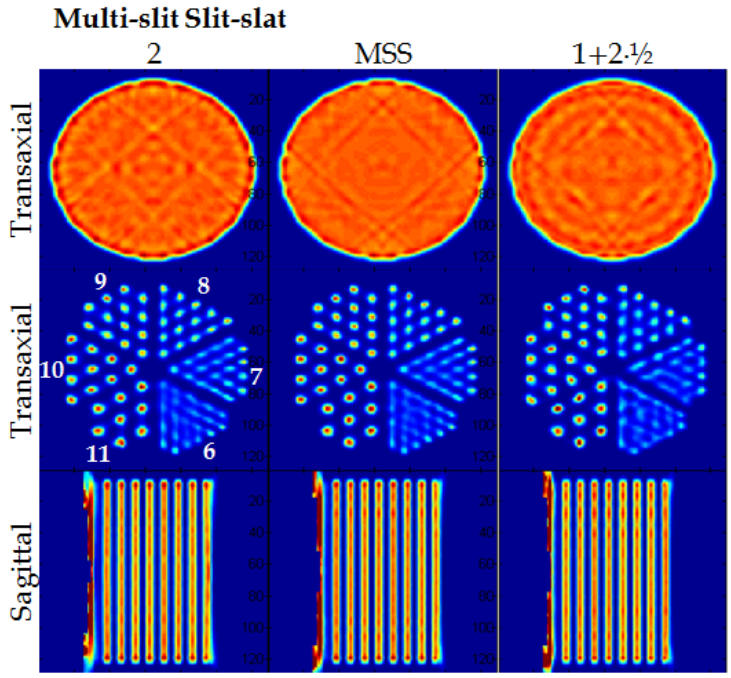

Figure 5.5: Reconstructed images for the uniform (top row), Derenzo (middle row) and Defrise (bottom row) phantoms simulated with multi-slit slit-slat collimator configurations.

reconstructed images for the Defrise phantom, for the multi-pinhole and multi-slit slit-slat configurations, respectively.

The 8+4·½-pinhole collimator provides better transaxial uniformity when compared to the other multi-pinhole configurations (Figure 5.3 – centre top image), although some artefacts due to limited angular sampling are still visible. In addition, it is possible to distinguish the 7 mm rods of the Derenzo phantom with this collimator (Figure 5.3 – centre middle image), even though the target resolution was 10 mm. For all pinhole configurations, extensive blurring is observed at the edges of the Defrise phantom, as well as non-uniform activity (Figure 5.3 – bottom images).

Regarding the simulations with the multi-slit slit-slat configurations, the reconstructed images for the MSS collimator show reduced sampling artefacts in the uniform phantom, as compared to the other two configurations (Figure 5.5 – centre top image). Also in the reconstructed image of the Derenzo phantom, with this collimator, it is possible to distinguish the 7 mm rods (Figure 5.5 – centre middle image).

5.2.3 Discussion

In terms of geometric efficiency, the multi-slit slit-slat designs achieve higher efficiency when compared to the multi-pinhole collimators.

Regarding the noise-free simulations, they show better performance for the MSS and 8+4·½-pinhole collimators in comparison to the other configurations. The 8+4·½-pinhole

collimator achieves slightly better transaxial resolution, and reduced angular sampling artefacts in the uniform phantom, when compared to the MSS collimator. In contrast, the MSS collimator achieves better axial resolution and uniform axial coverage as shown by the Defrise phantom results. As expected, the 8+4·½-pinhole collimator shows artefacts at the edges of the axial FOV due to incomplete sampling.

There is no clear indication of which collimator design can provide the best performance for the INSERT system, therefore prototypes of these two collimator configurations will be built (see next Section), with the objective of conducting an experimental evaluation. Moreover, evaluation with Monte Carlo simulations of these collimator designs will be addressed in the next Chapter.

5.3 Design of Prototype Collimators

Given the purpose of these collimator prototypes, the design problem is slightly different from the full system collimator design adopted in the previous section. The objective here is to adapt each design for testing with a single prototype detector, ensuring a good correspondence between prototype and final system. Moreover, dimension tolerances have to be determined, without compromising system performance; materials have to be tested for density, purity and MR-compatibility; and feasibility of the design in terms of manufacture has to be assessed. Finally, the whole process will also allow NUCFI to develop a framework for the production of the final collimator for the INSERT system.

Regarding this topic, my role was to work closely with NUCFI in order to produce the final technical drawings for each prototype collimator using Autodesk, Inc. software (Mill Valley, California, U.S.A.) and to discuss manufacturing ideas and specifications.

5.3.1 Methods

As a general indication, for the prototype collimators, the manufactured collimator corresponds to a single collimator module, it has to be self-supported and include extra shielding, and the weight is not a concern. Taking this into account, the design and engineering of the prototype collimators are as follows.

For the ring configuration, each collimator module can be seen as a trapezoidal prism, with the base face smaller than the top face, which interfaces with the scintillation crystal. Figure 5.6 shows a transaxial representation of the MSS collimator and crystal in a ring configuration, for a 1+2·½-slit section. This representation would be very similar for the 8+4·½-pinhole collimator, at the 1+2·½-pinhole section, because the slit and pinhole collimations are the same in the transaxial direction.

For both prototype collimators, the half-aperture has to be preserved, as the lateral collimator modules will be absent. Therefore, the main transaxial dimension was increased

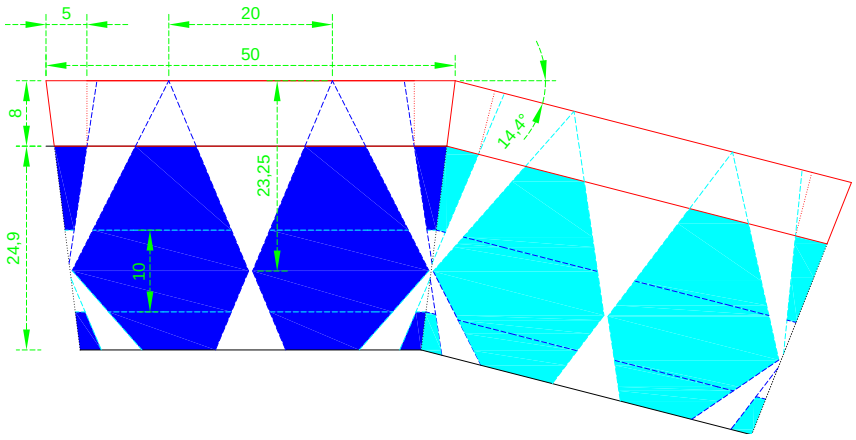

Figure 5.6: Technical sketch of the MSS collimator and scintillation crystal in a ring configuration. Each slat is represented with filled in colour and its internal slit highlighted by the dashed lines. Dimensions are given in mm.

to accommodate the projection of the half-aperture in the object side of the collimator and to provide extra shielding to the aperture. Moreover, as the trapezoidal prism shape is unnecessary, both top and base faces can have the same dimensions. Diagrams on Figure 5.7 show how this can be achieved.

In terms of manufacturing, for the MSS collimator, because the slit component is interior to the slat component, the collimator can be set up along the axial direction with interleaved plates, as a stack of attenuating layers of material. Each layer is independent and can have a different configuration allowing for the creation of the mini-slits. Copper rods were chosen to bolt the collimator together, as the use of glue would introduce large tolerances in the collimator dimensions and it could not be strong enough to hold the collimator together, namely for the final system. The prototype MSS collimator will have total dimensions of 100×64×24.9 mm. For the 8+4·½-pinhole collimator, only the pinhole apertures have to be defined, therefore a block with the same dimensions of the MSS prototype is not necessary. The idea for this collimator is to have the walls of each pinhole and a bottom plate with area 100×64 mm and 3 mm thickness to shield the crystal in the regions outside the apertures. Figure 5.8 shows the final agreed design for each collimator prototype, with a tolerance of 0.0295 mm. This tolerance was calculated based on a variation of 10±0.2 mm for the target resolution and assuming an intrinsic resolution of 0.8 mm.

Regarding MR-compatibility, all the materials used in the production of the prototype collimators, such as tungsten samples and rods, were tested inside a 3 T MRI system. After manufacturing, each prototype collimator was also tested for displacement force in the MR bore, susceptibility effects and eddy currents. These tests were performed by MRI.TOOLS in Berlin. In addition, the MSS prototype collimator was also scanned at UCL's Biograph mMR to check for temperature changes due to gradient switching and eddy currents. A fast

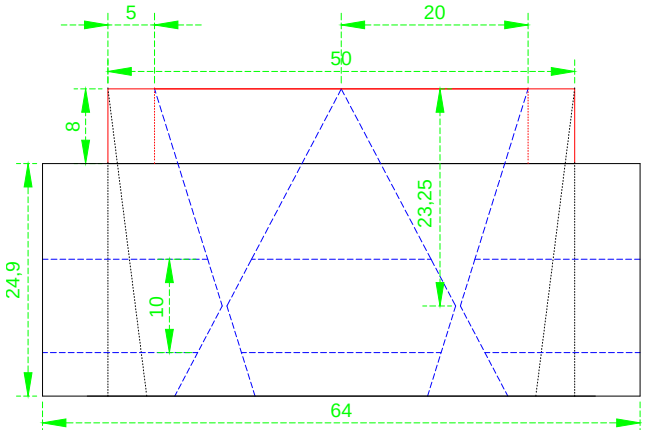

(a) 2-slit-array plane. The slit aperture is 0.49 mm.

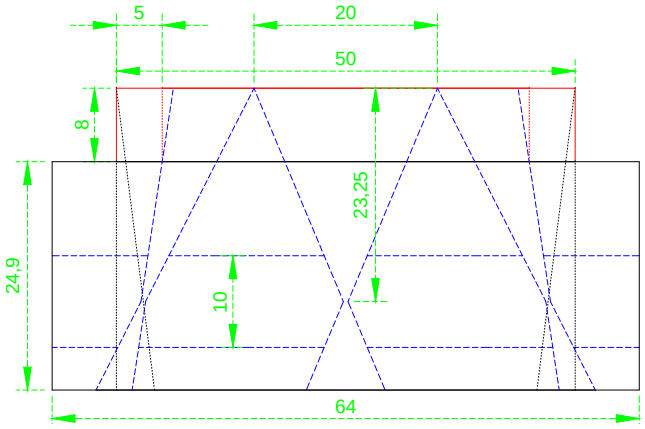

(b) 3-slit-array plane. The aperture for the central slit is 0.49 mm and 0.53 mm for the half-slits.

Figure 5.7: Diagrams of the prototype MSS collimator with dimensions in mm. The detail of the slat is shown in black, the crystal in red and the projection of the slits in blue.

gradient echo sequence, 3 ms TE, 4.5 ms TR, matrix size 256×256, FOV 15×15 cm, with rapid switching gradients, was selected to scan an MR quality control phantom, with the prototype collimator 15 cm off centre. The temperature was monitored real-time with a fibre optic probe glued to the collimator.

5.3.2 Results and Discussion

Figure 5.9 shows the manufactured prototype collimators. Both collimators are 99.5 % tungsten, with density 17 g.cm^{-3}. The MSS collimator was manufactured from cut tungsten plates and weighs 2.85 kg, whilst the 8+4·½-pinhole collimator was produced by laser sintering from tungsten powder. In fact, finding a suitable tungsten powder proved to be quite challenging, as well as the use of laser sintering for the required pinhole design. Quality control analysis of the post-manufacture square holes showed they were not uniform, with a maximum measured hole tolerance of 0.026 mm (Figure 5.10).

As for the MR-compatibility testing, MRI.TOOLS reported that the MSS prototype

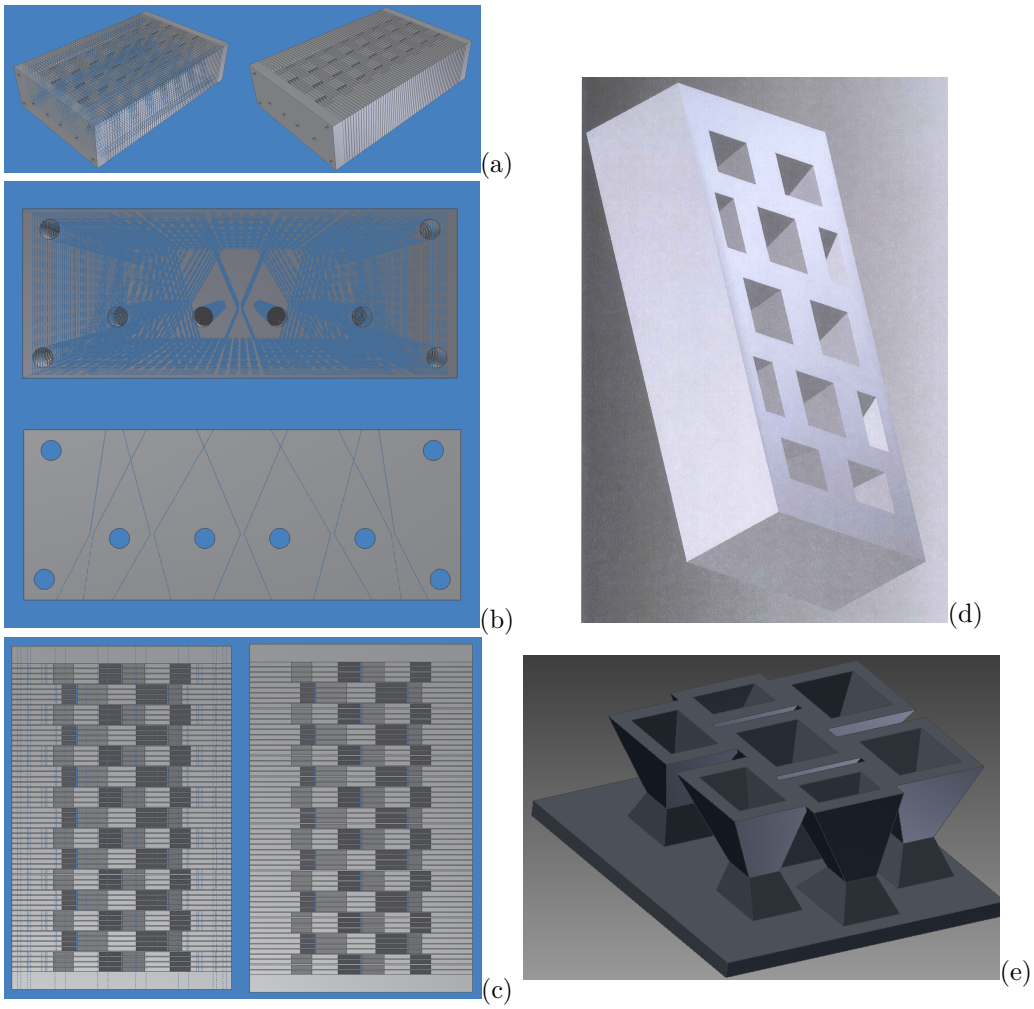

Figure 5.8: Technical drawings of the final prototype collimators: (a) perspective, (b) top/bottom and (c) front/back views of the MSS prototype collimator, (d) perspective view of the 8+4·½-pinhole prototype collimator without weight reduction, and weight reduction concept applied to half of the pinhole prototype collimator. [Adapted from NUCFI]

collimator showed no displacement force when subjected to the static magnetic field; the analysis of the FID for the different acquisition set-ups, gradients and delays between the gradient and the RF pulse showed no strong or major changes, suggesting eddy currents are somewhat minimised by the specific sandwich-type design; and the susceptibility tests showed the collimator module causes inhomogeneities in the magnetic field, however these could be compensated by optimising the shimming. Similarly, tests with the 8+4·½-pinhole prototype collimator showed negligible eddy currents and inhomogeneities in the main magnetic field that can be mitigated by shimming. Regarding the temperature test with the MSS prototype collimator, no temperature increase was observed in the probe's monitor, and at the end of the scan the collimator was cold to the human touch.

To summarise, both collimator prototypes were successfully designed, manufactured and tested for MRI-compatibility. These designs, however, reflect the need for weight optimisation

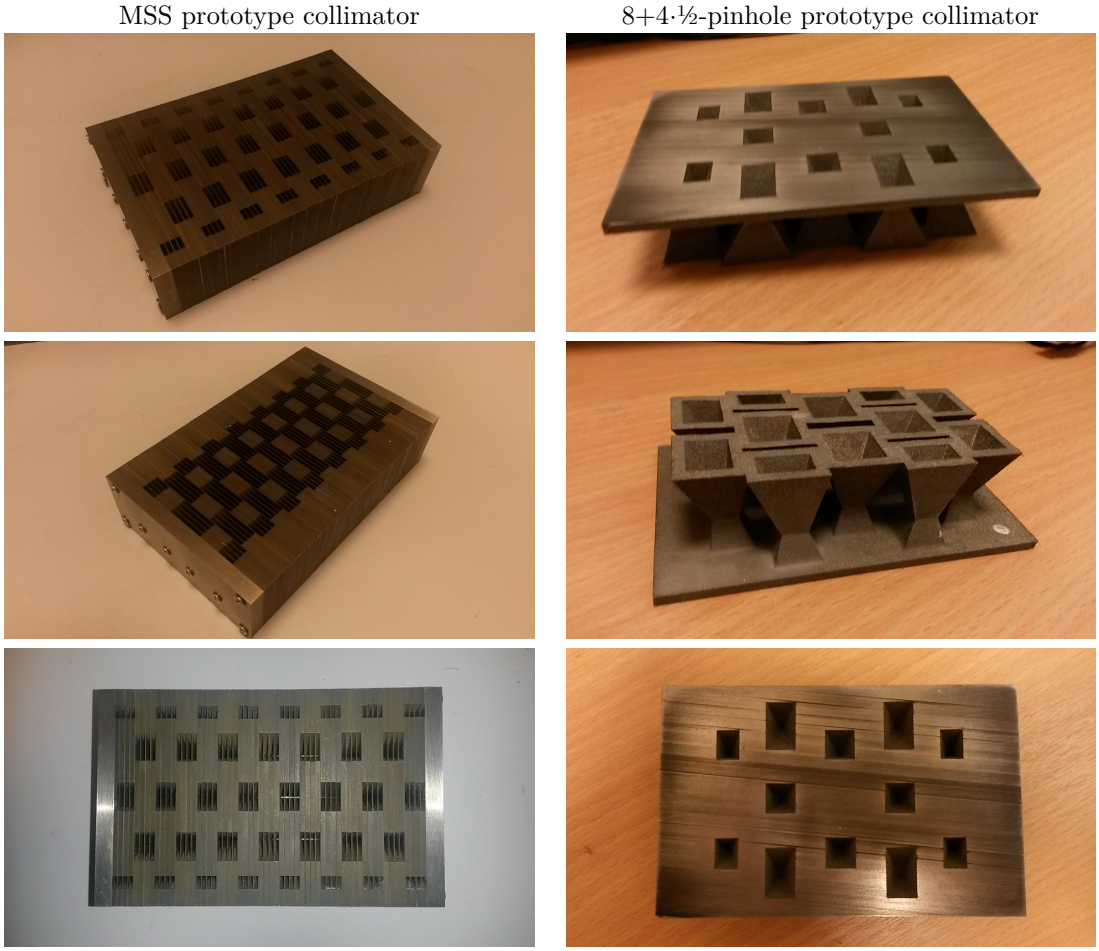

Figure 5.9: Manufactured prototype collimators. For both collimators, the side with bigger apertures corresponds to the detector side, and the one with smaller ones to the object side.

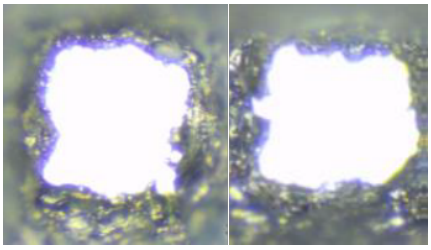

Figure 5.10: Zoomed in picture of two "square" holes in the 8+4·½-pinhole prototype collimator. [Courtesy of NUCFI]

for the final system collimator, because of the load on the MR patient bed and gantry. For example, regarding the MSS design, a rough estimation of the full-ring collimator weight can be obtained multiplying the single-module weight by the total number of collimator modules, which gives 71.25 kg. For the full system weight, one also has to consider the system's casing, electronics, cooling blocks, scintillation crystals and shielding. Furthermore, eddy currents and magnetic field inhomogeneities are still a concern in the case of the final system. Firstly,

the collimator modules will form a complete ring, which can act as an electrical conductor in the presence of gradient magnetic fields, interfering with the MR acquisition. Secondly, it is difficult to predict from the compatibility tests with only a single collimator module how big the inhomogeneities created by the final collimator and system will be. On top of this, the human head also introduces inhomogeneities, which has not been accounted for during the tests. Regardless of the source of the magnetic field inhomogeneities, it is unknown what inhomogeneity the scanner can actually compensate for.

5.4 Final System Design Refinement

In the previous sections, a new collimation design was discussed, as well as the design and manufacturing of prototype collimators. It is clear that the MSS collimator is the best compromise for the final INSERT system: there is complete axial sampling, high sensitivity, low MR interference and relatively easy manufacturing. Therefore, in this section, the collimator and system design will be adjusted according to the final dimensions and performance of the components.

Characterisation measurements with the clinical photodetectors indicated an achievable intrinsic resolution of 1 mm, instead of the 0.8 mm referred before, which could imply recalculating the collimator apertures. However, that would have resulted in lower sensitivity. Therefore the aperture dimensions were kept the same, assuming that, with resolution modelling in the reconstruction, a target resolution of 10 mm at the centre of the FOV is still achievable. Additionally, when assembled in a ring geometry, the detectors require a 2 mm gap between them due to the holding frame, and a 4.5 mm axial gap between the crystal and the detector side of the collimator for safety of the components and to accommodate the system cover, tolerances and heat expansion. Consequently, the position of the half-slit apertures and the thickness of the collimator need to be adjusted to account for these dimension changes. With such constraints, the 25-detector is no longer feasible, and hence the system geometry had to be revised too.

In the next sections, the system and collimator geometry will be refined for the final INSERT system.

5.4.1 Methods

5.4.1.1 System Geometry

The possibility of using a partial ring geometry with 20 detector modules, instead of a 24-detector full ring, was investigated in view of the new space constraints.

The main advantage of this geometry is a better utilisation of the available space inside the MRI bore. Given that the system needs to be positioned on top of the patient bed, a full ring geometry would only allow an outer diameter of 330 mm for the MRI coil and the space

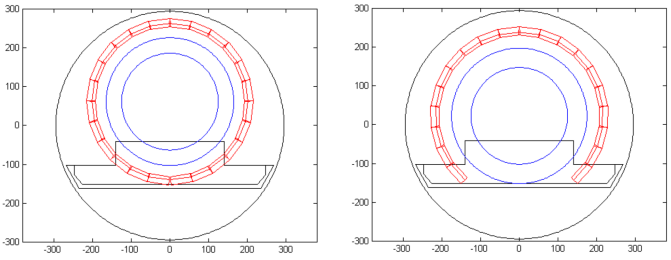

Figure 5.11: System geometry options: full ring design with 24 detector modules (left) and partial ring design with 20 detector modules (right). The outer circle corresponds to the MRI bore, the red rectangles to the detectors and the horizontal polygon to the patient bed.

for the top detectors would be very restricted. On the other hand, with a partial ring design, the outer diameter of the MRI coil could be increased to 350 mm, and the working margins for the space around the detector system would be bigger. Technically, patient positioning would be easier too, as the patient head would be less raised from the existing MR patient bed.

From an imaging point of view though, the drawback of having a partial ring system is that it does not provide full angular sampling of the brain, which degrades image quality. Nonetheless these limitations might be mitigated by the use of prior information, namely MRI data, in the reconstruction algorithm. Therefore the impact of using MR-derived anatomical priors was also investigated.

Simulations were performed for both ring geometries as in Figure 5.11 by forward-projecting an analytical cylindrical phantom using an algorithm based on angular blur-ring (Bousse et al., 2013a). The phantom consisted of 48 spherical inserts in 3 different planes (Figure 5.12). The spheres had a 15 mm diameter and the sphere-to-background ratio was 5. Attenuation was included, but not scatter. Noise-free and Poisson-noise projection data were reconstructed with MLEM, and with MAP-EM with a smoothing prior and an anatomical prior, based on segmentation of the true object to simulate the MR-based prior. Data from the full ring system were reconstructed with 400 iterations, and those from the partial ring system, with 400-1600 iterations.

Reconstructed image quality was assessed with contrast-recovery and coefficient of variation (CoV). CoV was calculated in the background region, and contrast-recovery was calculated as the average of the bottom 3×2 spheres divided by the top 3×8 spheres.

5.4.1.2 Collimator Refinement

The MSS collimator design was refined for the final system collimator, taking into account the partial ring design with 20 detection modules, the 1 mm intrinsic resolution, and the final components dimensions: 51.7 mm detector width and 8 mm crystal thickness. For safety reasons and space for housing, two gaps had to be incorporated into the system design:

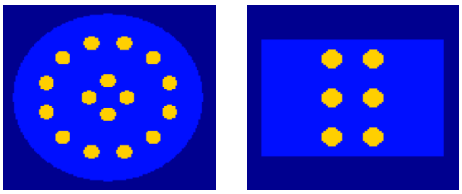

Figure 5.12: Transaxial (left) and coronal (right) views of the analytical phantom with 48 spheres with a diameter of 15 mm.

2 mm between adjacent crystals and 4.5 mm between crystal and collimator. Considering a cylindrical FOV of 200 mm diameter and 90 mm height, each collimator module should project to a maximum of 40 mm by 90 mm detector FOV measured at the back of the crystal, which excludes 5 mm at the edges of the detector where performance deteriorates.

The fundamental distances to get the final collimator dimensions were the following: distance from the centre of the scanner and back of the crystal is 215 mm; distance from the centre of the scanner and back of the collimator is 202.5 mm; each detection module occupies an angle of 14.24099 ^{o}; collimator thickness is 26.5 mm, to allow for a patient opening diameter of 350 mm. Therefore the collimator focal length is 28.49039 mm, measured as the distance between the mini-slits aperture plane and the back of the crystal. The slit angulations are defined by the projection at the back of the crystal and in the FOV, avoiding multiplexing.

For the 2-slit sections, each aperture has a dimension of 0.75021 mm and it is located at ±14.96905 mm, measured transaxially on each side of the centre of the collimator module. The opening at the detector side of the collimator is defined by connecting the central point of the slit aperture to the point where the central ray meets the back of the crystal, and to ±20 mm measured transaxially from the central point of the back of the crystal. When projecting these angulations to the patient side, it should mean that the lines tangent to the FOV are projected to the centre of the crystal and the top centre point of the FOV is projected to ±20 mm at the back of the crystal. This defines the opening at the patient side.

For the 1+2·½-slit sections, the central slit has a dimension of 0.75021 mm and it is located transaxially at the centre of the collimator module. The opening at the detector side of the collimator is defined by connecting the central point of the slit aperture to ±10 mm measured transaxially from the central point of the back of the crystal. The opening at the patient side has the same angulation. The ½-slits have half the size of the central slit and they are located at ±23.29876 mm measured transaxially on each side of the central ray of the collimator module. These positions should match the point between two consecutive collimator modules, at the focal distance. For the angulations, let's consider the ½-slit on the left-hand side. The opening at the detector side of the collimator is defined by connecting the central point of the whole slit aperture, i.e. at -23.29876 mm, to -10 mm and -20 mm

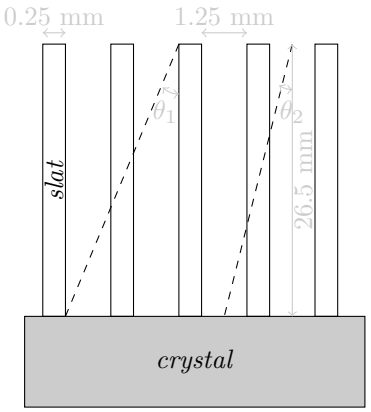

Figure 5.13: Diagram of the axial collimation to investigate septal penetration. The dashed lines correspond to two cases in which incident gamma photons would be wrongly detected.

measured transaxially from the central point at the back of the crystal. The opening at the patient side sits in the adjacent left collimator module and below the focal plane. Its angulation is the projection of the lines aforementioned. The opening at the patient side, which sits below the left-hand side ½-slit, belongs to the projection of the right-hand side ½-slit of the collimator module on the left side. For the ½-slit located at +23.29876 mm, the openings are just a mirrored version of the ones just described.

Along the axial direction, the collimator module is divided into 15 mini-slit sections, that interlock 2-slit sections with 1+2·½-slit sections. Each different mini-slit section consists of 4 slats with a thickness of 0.25 mm each, and a centre-to-centre spacing of 1.5 mm. This means that each mini-slit section is 6 mm long and the 15 sections add up to 90 mm, to cover the whole detection module axially.

The collimator was designed considering ^{99m}Tc imaging, however the use of ^{111}In and ^{123}I is also envisioned. Therefore, septal penetration was investigated for the corresponding photopeaks, analytically. To illustrate the effect, two angles of incidence θ_1 and θ_2 were chosen, which represent paths with minimum attenuation (Figure 5.13). The percentage of gamma photons that penetrate through the tungsten slats was calculated as a function of their energy for these two cases.

In order to reduce the total weight of the collimator, and therefore the load on the MR patient bed, the design of the tungsten parts that form the slit apertures of the MSS collimator was replaced by a hollow-part design. Basically, only material more than 5 mm from the slit aperture was removed, such that a penetrating photon from outside the slit FOV always encountered 10 mm of collimator material. This would be enough to shield photon energies up to 245 keV, which is the second photopeak of ^{111}In. The concept is illustrated in Figure 5.14.

Finally, integration of the new system geometry and final collimator with the rest of

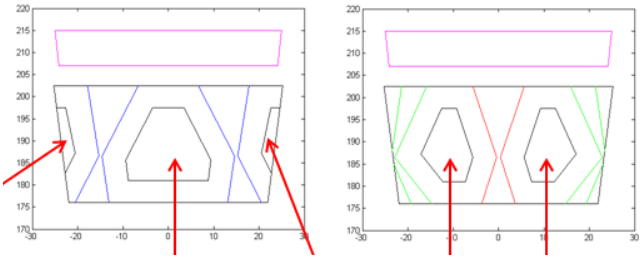

Figure 5.14: Weight reduction concept by removal of the collimator material between the mini-slit apertures, as indicated by the red arrows for the 2-mini-slit sections (left) and the 1+2·½-mini-slit sections (right).

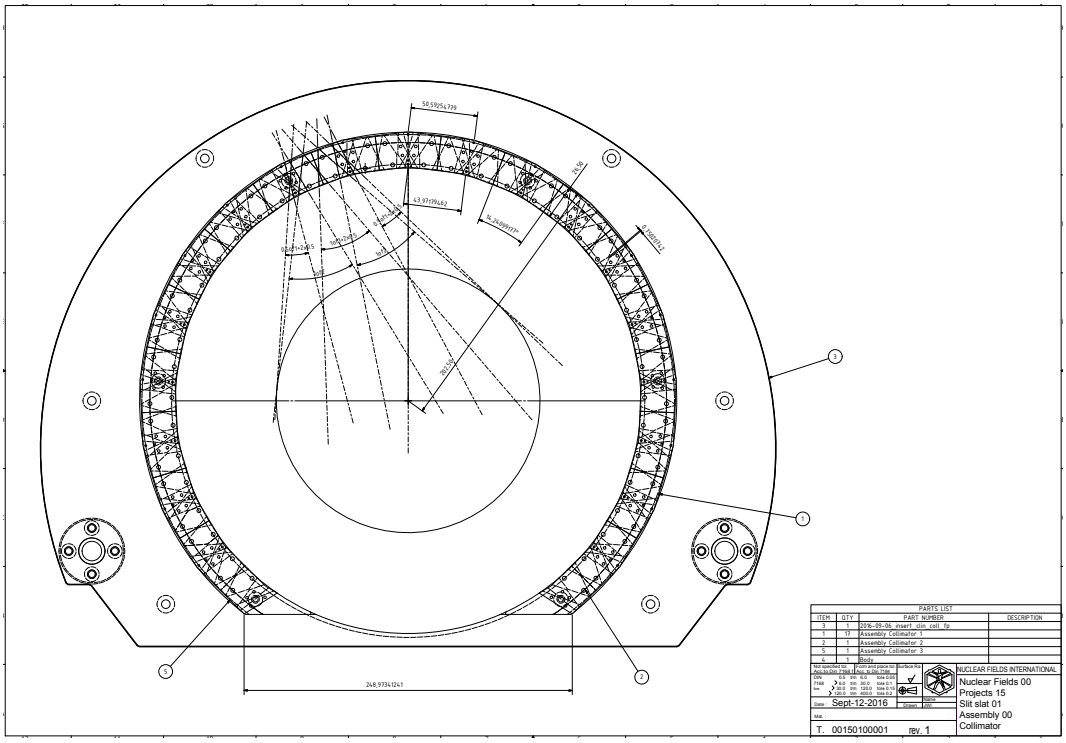

Figure 5.15: Technical drawing of the integration of the partial ring system with the MSS collimator. The central circle corresponds to the FOV. [Courtesy of NUCFI]

the components was performed in collaboration with MEDISO and NUCFI, and the final technical drawings were obtained for the full INSERT system with a MSS collimator and a partial ring geometry (Figure 5.15). These include positioning and support pins and rods, that keep the collimator design within margin and in the correct place in relation to the detector ring.

5.4.2 Results and Discussion

Figure 5.16 shows transaxial views of the reconstructed images of the analytical spheres phantom simulated with a full and partial ring. For the noise-free simulations, resolution deteriorates in the lower spheres due to the absence of the detectors. As expected, there is

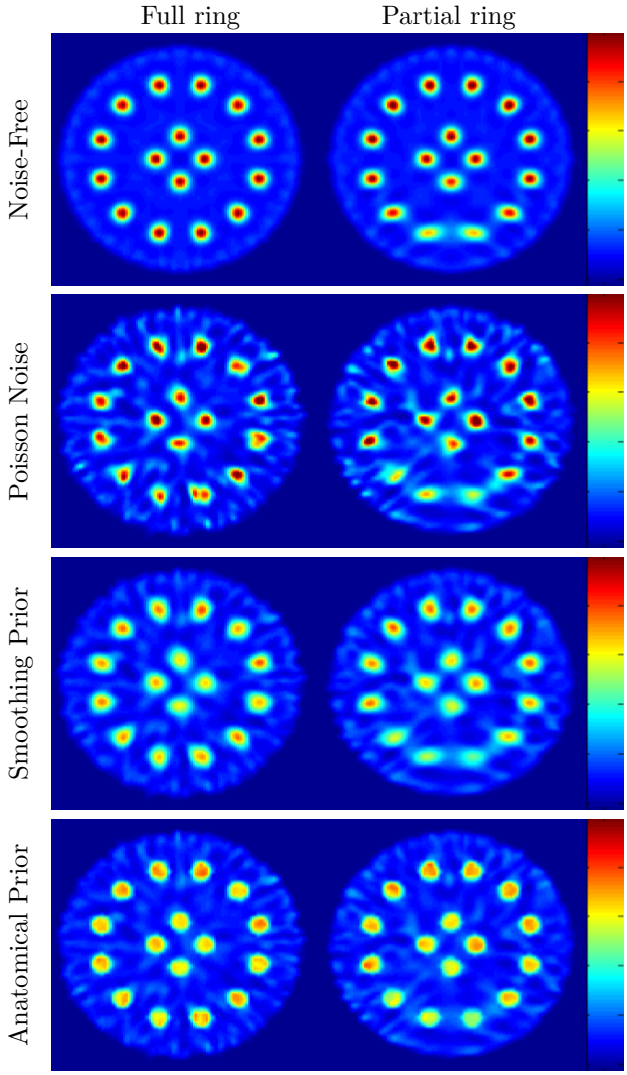

Figure 5.16: Transaxial view of the reconstructed images of the cylindrical phantom for the full ring (left) and partial ring (right) designs, for simulations without noise, with Poisson noise, applying a smoothing prior and an anatomical prior (top to bottom).

no degradation in the axial direction (Figure 5.17).

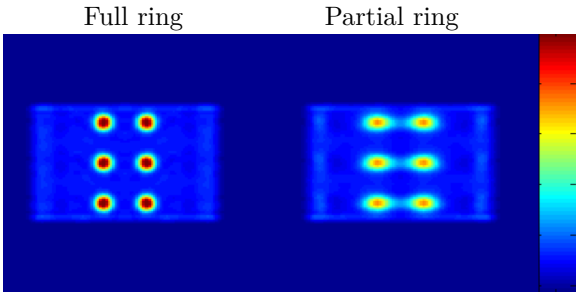

Figure 5.17: Axial view of the noise-free reconstructed images of the cylindrical phantom through the lowest two spheres, for the full ring (left) and partial ring (right) designs.

Table 5.1: Quantitative analysis of the reconstructed images. Contrast recovery and background CoV are given for 400-1600 iterations.

	Contrast Recovery [%]	**Background CoV** [%]
Noise-free	77-84	-
Noisy	78-85	28-56
Smoothing prior	78-80	22-28
Anatomical prior	85-89	20-25

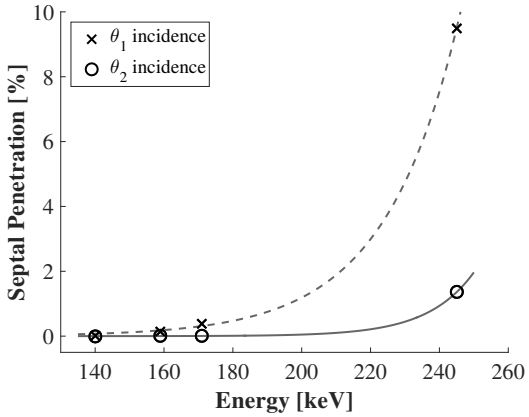

Figure 5.18: Percentage of septal penetration as a function of energy of the incident gamma photons. The two curves correspond to the two angles of incidence.

With noise, resolution degradation is slightly more pronounced, specially for a higher number of iterations, which have a higher background CoV. However, the noise amplification is lower using a high number of iterations of MAP-EM with regularisation. Images reconstructed with a smoothing prior and anatomical prior have lower spheres with better definition and contrast, when compared to the reconstruction without priors. In fact, the anatomical prior gives better image quality in comparison to the smoothing prior, resulting in very little visual difference between the full ring and partial ring simulations. This is especially relevant for the INSERT system, because the anatomical prior can be derived from the MR image, which will be acquired simultaneously with the SPECT.

Quantitatively, analysing Table 5.1, the background CoV values show regularisation reduces the background variability, i.e. noise. Furthermore, the use of the anatomical prior achieves greater contrast when compared to the smoothing prior. And finally contrast is enhanced for a higher number of iterations – higher contrast recovery, but so is noise – higher background CoV, therefore resolution improvement is limited.

Regarding the septal penetration, the plot in Figure 5.18 shows that the percentage of penetrating photons in the two worst-case scenarios studied is below 10 % up to 250 keV. However, for energies above 250 keV, penetration is high as it increases exponentially, with a negative impact on image quality.

Finally, the complete housing structure for the detection ring, collimator and coil is

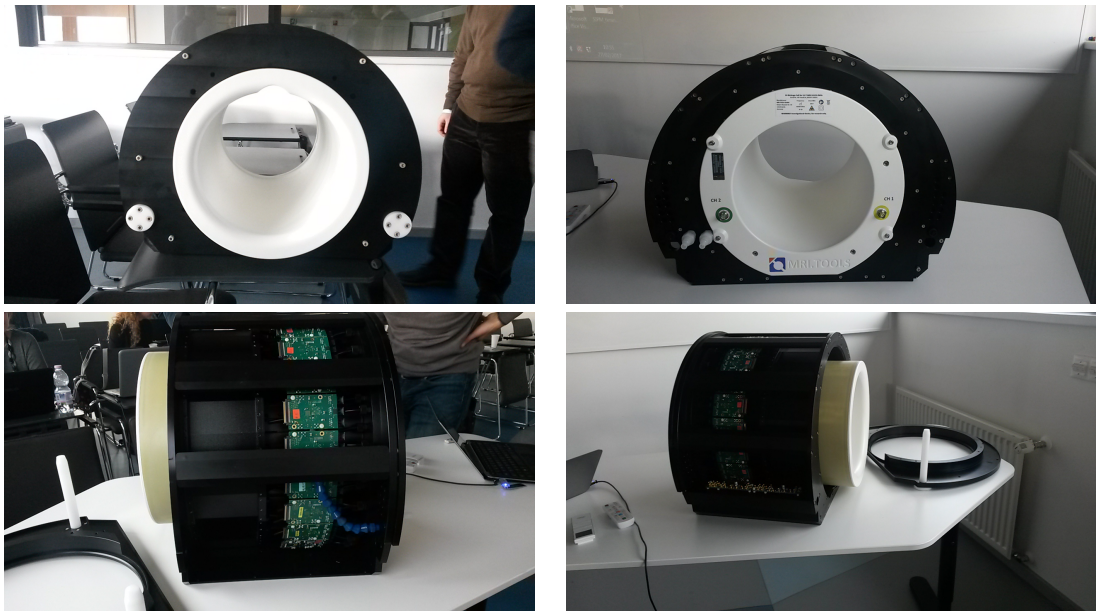

Figure 5.19: Final clinical INSERT system: housing structure (black), MR coil (white), and DAQ boards (green). Detection modules and collimator absent.

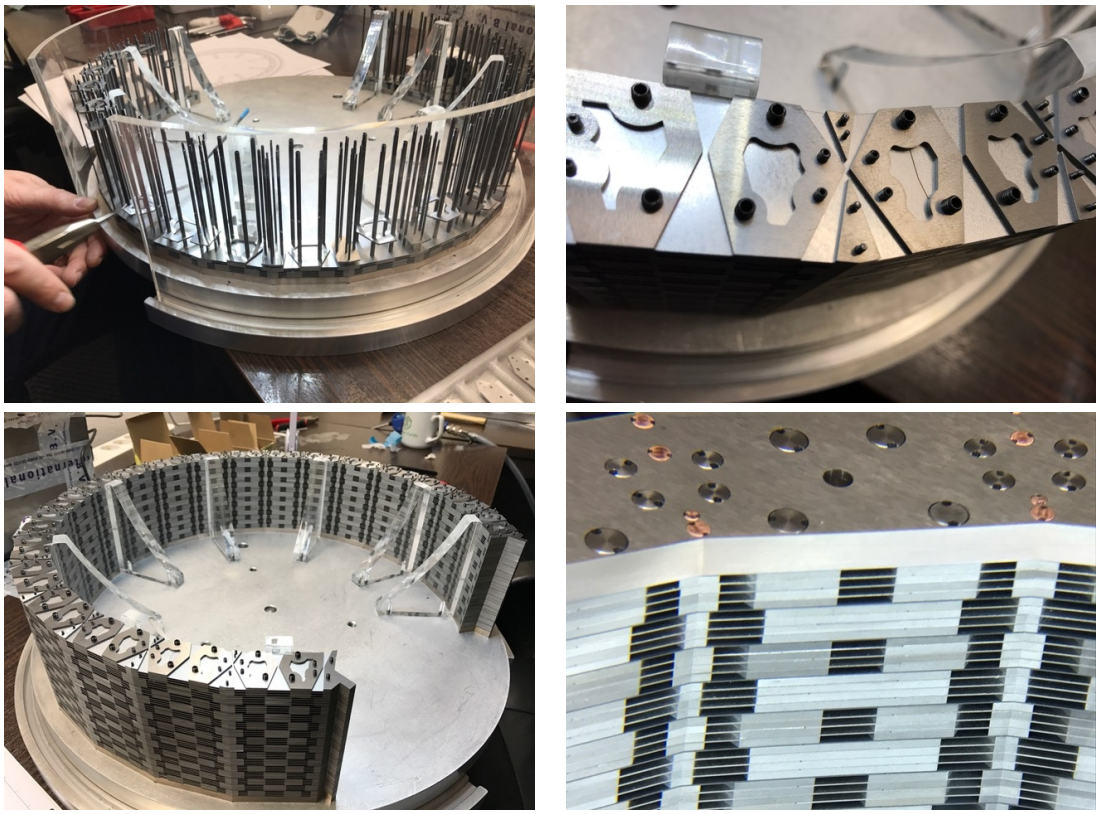

Figure 5.20: Final MSS collimator for the INSERT system: during assembly and in complete form. [Courtesy of NUCFI]

shown in Figure 5.19. Some components are mounted on the structure, such as the DAQ boards in green and the head coil in white. The size of the system is an indication of its portability, and restricted design and patient aperture. Due to the coil design without apertures and the actual components of the system, this system poses a higher risk of patient claustrophobia. Note that this will be installed inside the bore of the Biograph mMR, Siemens. Separately, the manufactured MSS collimator is shown in Figure 5.20, where the sandwich-type design is more perceptible. The full collimator consists of thousands of tungsten pieces that were mounted on the vertical rods, and fixed in place by positioning pins and the bottom and top plates of tungsten, which also act as shielding. The detail of the hollow design for weight reduction of the collimator is also observable.

5.5 Conclusion

A new concept of collimation was proposed, based on the MSS design and high-resolution detectors. Equivalent multi-pinhole collimators were also designed. These designs address the space constraints and limited angular sampling of a compact stationary SPECT insert for an MRI system, in order to perform simultaneous SPECT/MR of the human brain.

The MSS and 8+4·½-pinhole collimators showed the best performance in analytical simulations, and they were further developed as prototype tungsten collimators for experimental testing with a single prototype detector.

However, in comparison with the 8+4·½-pinhole design, the proposed MSS collimator showed higher efficiency, uniform axial coverage, high compactness, negligible interference with the MR operation, and easy manufacture. Therefore, the MSS collimator was the selected design of choice for the INSERT system.

Lastly, the final collimator was refined according to the final system geometry: a partial detector ring. This new geometry was suggested to allow more space for the MR head coil and patient opening, and to relax the space constraints for the system's components in general. Investigation of the effects of the system geometry in image quality showed that mainly transaxial resolution was reduced in the lower part of the FOV, where the detectors are missing. Nevertheless axial resolution was not affected. As the main objective for the INSERT system is not lesion detection, but treatment follow-up, the patient's head can be positioned into the FOV accordingly. Hence the partial ring geometry is a good compromise in terms of patient comfort, space for the components, and system performance.

Despite all the topics addressed in this Chapter, finalisation of the INSERT system is not complete. The impact of high energy photons has to be studied, a calibration method developed and the performance of the collimator evaluated. These topics will be addressed in the next chapters.

Chapter 6

Monte Carlo Evaluation of Different Collimator, Ring and Shielding Designs for the INSERT System

This chapter explores the Monte Carlo method to obtain realistic simulations of the INSERT system and evaluate its design and performance.

6.1 Introduction

The Monte Carlo method is a statistical technique used to approach scientific problems difficult to solve analytically, providing a numerical solution. Random numbers are generated and utilised to simulate random events, such as the radioactive decay.

One advantage of Monte Carlo simulations in Nuclear Medicine is that these simulations allow the record of radiation transport through different media – tissues, being able to compute dose, scatter, attenuation, among others (Bolch, 2010).

GATE is an open source software[1] for simulation of pre-clinical and clinical scans in emission tomography, transmission tomography and radiation therapy (Jan et al., 2004). This software is based on C++ and Geant4, but it uses macros to actually run the code in order to be more user-friendly.

The main components described in the macro file – `.mac` – relate to the specific simulation that is being set up and they can be summarised into visualisation and verbosity; geometry description; digitizer description; physics description; initialization; source description; output set-up; and experiment set-up. This is also the order in which they should be referred.

The geometry of the imaging system follows a tree diagram, in which each daughter volume has to be fully enclosed in the upper volume called the mother volume. All volumes

[1] http://www.opengatecollaboration.org/

are contained in the world, which is the maximum upper volume. For each volume, there is flexibility to set up different geometries, such as box, trapezoid, or sphere, and different dimensions, materials and positions. All dimensions are given in relation to an axis centred in the mother volume. Similarly, the phantom can be defined analytically using the volume geometries referred previously, or it can be defined voxel-by-voxel. For the latter, both emission and attenuation volumes have to be provided. Hence, more realistic phantoms can be simulated using this approach, however the running time of the simulation is longer. In the description of the digitizer chain, parameters for blurring, energy of reference – usually the radioisotope's photopeak – and energy threshold can be defined according to the experiment. Finally, the output of interest is projection data, which can be obtained defining the pixel size, pixel number and projection plane accordingly in the simulation file. Projection data can be saved in `.root` or `.sin` and `.hdr` files. The number of generated projections will depend on the number of rotations (*time slices*), the rotation speed, and the number of cameras.

The objective here is to describe the set up of parametrizable GATE simulations of the INSERT system, in order to investigate the system geometry, design, and performance with realistic simulations.

6.2 Methods

GATE provides scripts to simulate the tomographic acquisition of a conventional SPECT system, consisting of large detectors and parallel-hole collimators. However, the INSERT system consists of a ring of small detectors with a multi-mini slit-slat (MSS) collimator (Chapter 5). Therefore the geometry of the system in the simulation scripts had to be modified accordingly. Additionally, as the objective is to evaluate different system configurations in order test and assess the system acquisition and design, a parametrizable simulation approach will be developed.

The following sections discuss the geometry set-up of the different components of the INSERT system, as well as the simulation of the system as a SPECT camera to investigate different aspects of the system design and performance.

6.2.1 Set Up of the Geometry

The 3D volumes that can be utilised to describe the INSERT system components are mainly slanted trapezoids. In GATE, this is achieved with the generic trapezoid volume called `trap`. Table 6.1 indicates the parameters that have to be defined in GATE, in order to obtain a specific geometry and dimension of the trapezoid.

Assuming that the trapezoid's forward and backward faces have coordinates $A_{1,2,3,4}$ and $B_{1,2,3,4}$, respectively (Figure 6.1), one can generalise the angular parameters θ, ϕ, α_1

Table 6.1: Parameters that define the geometry and size of a generic trapezoid volume in GATE.

Symbol	Description
`Dx1`	Half x length of the side at $y = -$`Dy1` of the face at $-$`Dz`
`Dx2`	Half x length of the side at $y = +$`Dy1` of the face at $-$`Dz`
`Dx3`	Half x length of the side at $y = -$`Dy2` of the face at $+$`Dz`
`Dx4`	Half x length of the side at $y = +$`Dy2` of the face at $+$`Dz`
`Dy1`	Half y length at $-$`Dz`
`Dy2`	Half y length at $+$`Dz`
`Dz`	Half z length (height)
`Theta`	Polar angle of the line joining the centres of the faces at $\pm$`Dz`
`Phi`	Azimuthal angle of the line joining the centres of the faces at $\pm$`Dz`
`Alp1`	Angle with respect to the y axis from the centre of the side (at $-$`Dz`)
`Alp2`	Angle with respect to the y axis from the centre of the side (at $+$`Dz`)

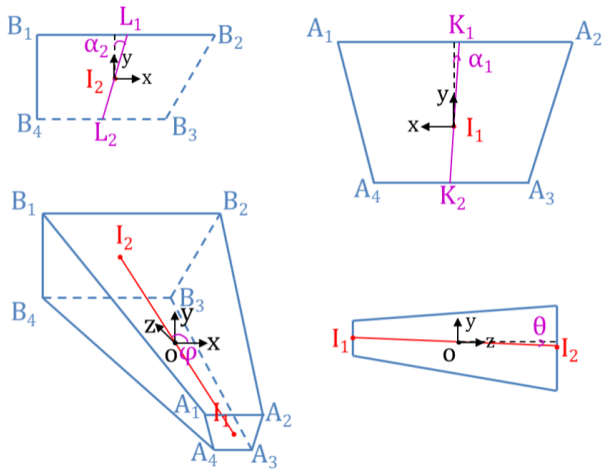

Figure 6.1: Arbitrary trapezoidal volume defined by coordinates A_i and B_i, in the axes with origin O. I_1 and I_2 are the geometric centre of the forward and backward faces, respectively. K_i and L_i are the centre points of the parallel sides on the forward and backward faces, respectively. The angular parameters are α_2, α_1, ϕ, and θ.

and α_2 using Equations 6.1, 6.2, 6.3 and 6.4:

$$\theta = \arccos \frac{\overrightarrow{I_1 I_2} \cdot \overrightarrow{e_z}}{\|\overrightarrow{I_1 I_2}\|} \tag{6.1}$$

$$\phi = \arccos \frac{\overrightarrow{I_1 I_2} \cdot \overrightarrow{e_y}}{\overrightarrow{I_1 I_2} \cdot \overrightarrow{e_x}} \tag{6.2}$$

$$\alpha_1 = \arccos \frac{\overrightarrow{K_2 K_1} \cdot \overrightarrow{e_y}}{\|\overrightarrow{K_2 K_1}\|} \tag{6.3}$$

$$\alpha_2 = \arccos \frac{\overrightarrow{L_2 L_1} \cdot \overrightarrow{e_y}}{\|\overrightarrow{L_2 L_1}\|} \tag{6.4}$$

The calculation of the trapezoid's parameters was implemented in a MATLAB function,

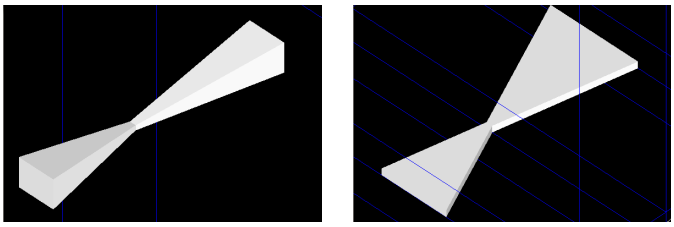

(a) (b)

Figure 6.2: Collimator apertures as defined in GATE for (a) pinhole and (b) mini-slit configurations.

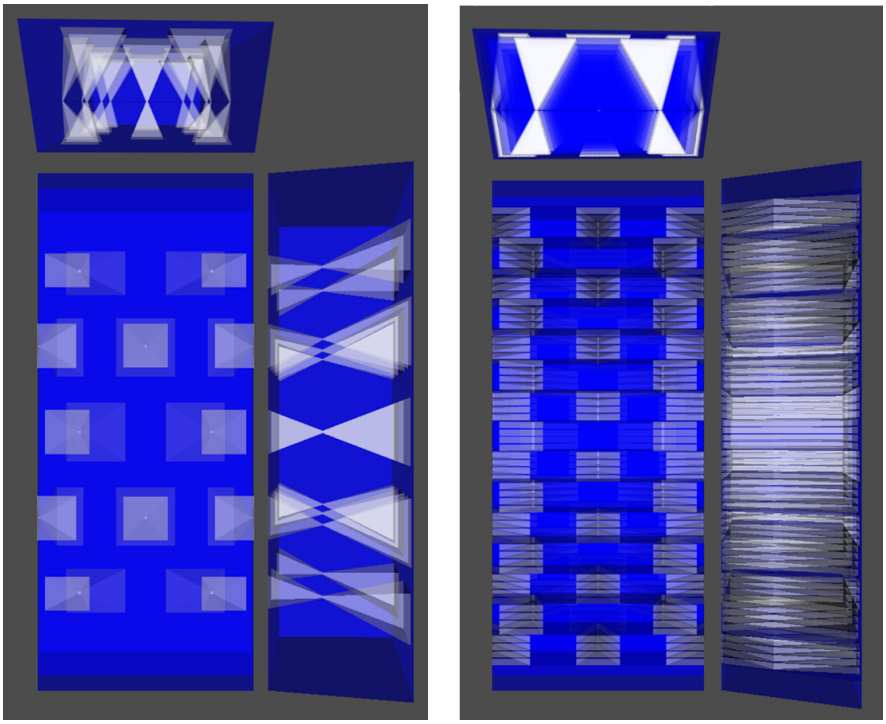

(a) (b)

Figure 6.3: Geometry of the 8+4·½-pinhole (a) and MSS (b) collimator modules in GATE. Attenuating material is represented in blue, and the pinholes/mini-slits, in white. The top figure corresponds to a transaxial view, the bottom left, to an axial view, and the bottom right, to a lateral view of the collimator module – each one in perspective. For the MSS, each mini-slit has four slats (the blue lines within the mini-slit apertures).

taking into account the position and dimension of the respective system component, and their relationship with the GATE's parameters previously described. Similarly, the implementation was extended to other geometries, such as sphere, box and cylinder. For practicality, the function outputs `.mac` files that can be used directly by GATE.

In order to simulate the full INSERT system geometry using the volumes described above, each camera was defined as a detection module (`SPECThead`) and a collimator module (`collUnit`), and both were repeated in a ring configuration.

Regarding the collimator, each module consists of two attenuating volumes, above and below the focal plane, where the apertures are inserted, i.e. air volumes. Each aperture is

Figure 6.4: Transaxial view of the detection module geometry in GATE. From top to bottom: the cooling block, the silicon layer and the CsI crystal represented in light blue, yellow and grey, respectively. Between each detection module in the ring configuration, there is attenuating material represented in dark blue.

defined by two `trap` volumes with different angulations and dimensions: one to define the aperture projection at the object side and the other, at the detector side (Figure 6.2).

For the 8+4·½-pinhole collimator, each pinhole is defined individually according to the specific design. The final geometry of the collimator module is depicted in Figure 6.3-a.

In the case of the MSS collimator, each module can be sub-divided into two different sections that repeat along the axial direction, one with 2 mini-slits and one with 1+2·½mini-slits. These apertures are similar to the pinhole ones, but axially two of the lateral trapezoid faces are parallel instead of divergent (e.g. in Figure 6.2-b). This allows for the set-up of the parallel slats in the axial direction, as each aperture is repeated with an axial gap within each mini-slit. The complete collimator module geometry is shown in Figure 6.3-b.

As for the detection ring, each module consists of a trapezoidal block of CsI, corresponding to the slanted scintillation crystal, and two rectangular blocks of silicon and water, which correspond to the SiPMs and cooling block, respectively. The geometry of a single detection module is shown in Figure 6.4.

Further simulated modules include gamma shielding components and an MRI bore. However, these will be discussed in more detail in the corresponding simulation studies in the following sections.

On the whole, the geometry architecture of the INSERT system with the 8+4·½-pinhole collimator and the MSS collimator is summarised in the block-diagrams of Figures A.1 and A.2 of the Appendix A.

6.2.2 Set Up of the Simulations and Data Analysis

A general framework of GATE simulation set-up and analysis was developed, based on parametrizable GATE scripts. The system geometry files were generated in MATLAB according to the design specifications: full or partial ring, and 8+4·½-pinhole or MSS collimator for a target resolution. Extra volumes such as shielding and phantoms could also be generated, as well as *source* `.mac` files according to the specified imaging radioisotope. In GATE, the handling of these files was performed via shell scripting and a main `.mac` file to run the simulation. Analysis of the output data was performed in ImageJ, ROOT or

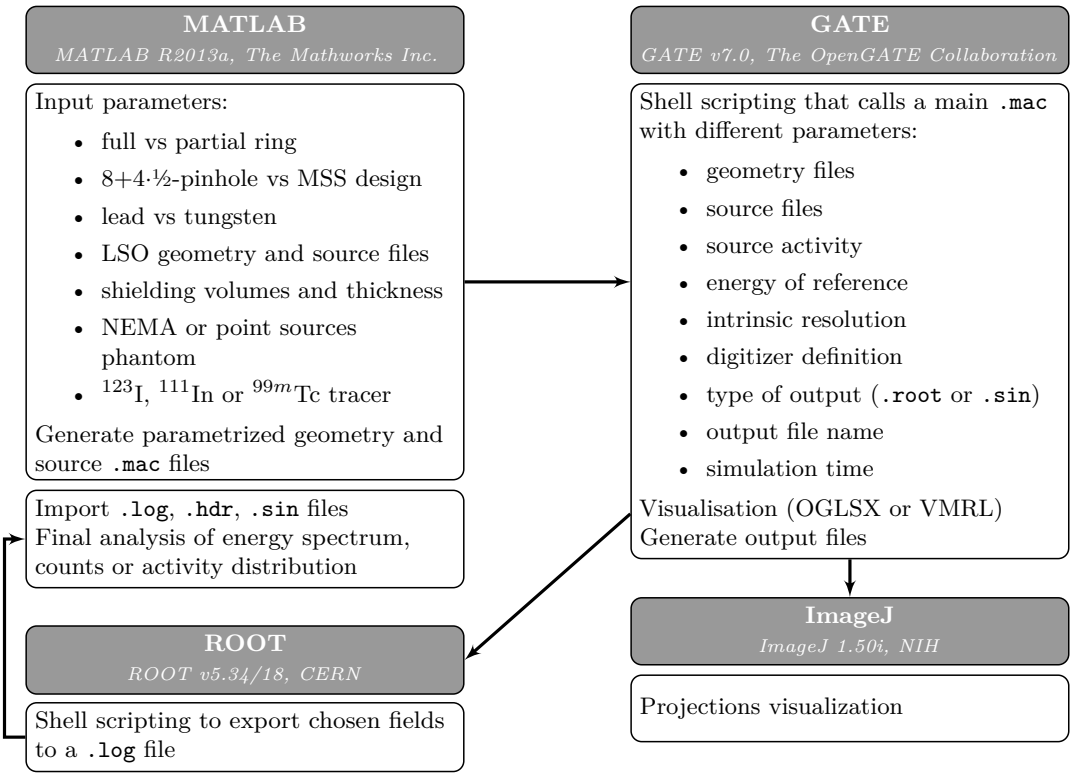

Figure 6.5: Overview of the implemented general framework for the set-up and analysis of parametrized GATE simulations.

MATLAB. An overview of this framework is shown in Figure 6.5.

Three main studies were performed in GATE. Firstly, to evaluate the system design, simulations of the INSERT system were performed with a 8+4·½-pinhole and MSS collimator, for a full and partial ring design. Secondly, the shielding design was assessed with a specific set of simulations of the INSERT system with a partial ring geometry and the MSS collimator. Finally, system performance was evaluated with simulations of the INSERT with final system and shielding design.

6.2.2.1 Investigation on System Design

Regarding the collimator design, simulations were performed with a complete ring of 24 detector modules for both the 8+4·½-pinhole and the MSS collimators, designed for a target resolution of 10 mm at the centre of the FOV (Figure 6.6). The simulations were run for both a point source with 1.6 MBq of ^{99m}Tc activity and a cylindrical phantom, the size of the FOV 200 mm diameter×90 mm height, with the same activity and no attenuation. The acquisition time was set to 10 minutes, the energy window to the photopeak range of 126-154 keV, and the projection output to 160×360 pixels of size 0.25×0.25 mm.

Resolution in the projection space was calculated as the FWHM of the Gaussian fit in the x and y directions of the point-source planar projection data. In the x direction, the

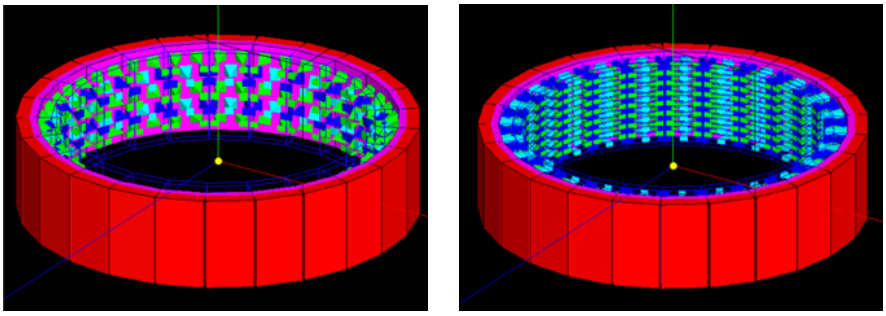

(a) (b)

Figure 6.6: Geometry of the INSERT system with the 8+4·½-pinhole (a) and the MSS (b) collimators in the GATE simulations to evaluate resolution. The central spot (yellow) corresponds to the point source, magnified for visualisation purposes. These system geometries were the same for the simulations with the cylindrical source.

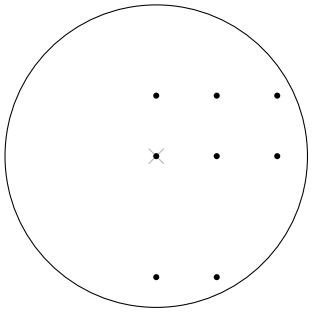

Figure 6.7: Transaxial diagram of the point source positions in the FOV for the GATE simulations with a partial and a full INSERT ring geometry. The bottom part corresponds to the region without detectors for the partial ring design. The cross marks the centre and the circle, the edge, of the FOV.

FWHM was multiplied by the minification factor to obtain the resolution figure, as there is minification in the transaxial direction due to the mini-slit/pinhole apertures. The same is applicable in the y direction for the simulations with the 8+4·½-pinhole collimator, but not with the MSS collimator because this has the slats in the axial direction, and thus no minification. Note that for this collimator, the y resolution was obtained as the FWHM of the Gaussian fit of a set of projected consecutive mini-slits in the axial direction.

Sensitivity was determined as the total detected counts divided by the total emitted gammas of the cylindrical phantom simulation.

As discussed in Chapter 5, a partial ring geometry was adopted for the final INSERT system design, with 20 detector modules. This design was a compromise between performance and patient comfort. In order to assess this design, point-source simulations were performed for eight different positions in the FOV (Figure 6.7), with both the full and partial ring designs equipped with the 8+4·½-pinhole and MSS collimators. The point sources were located at (0,0), (40,0), (80,0), (0,40), (40,40), (80,40), (0,-80) and (40,-80) mm in the transaxial plane. For each combination of ring geometry and collimator type, three different

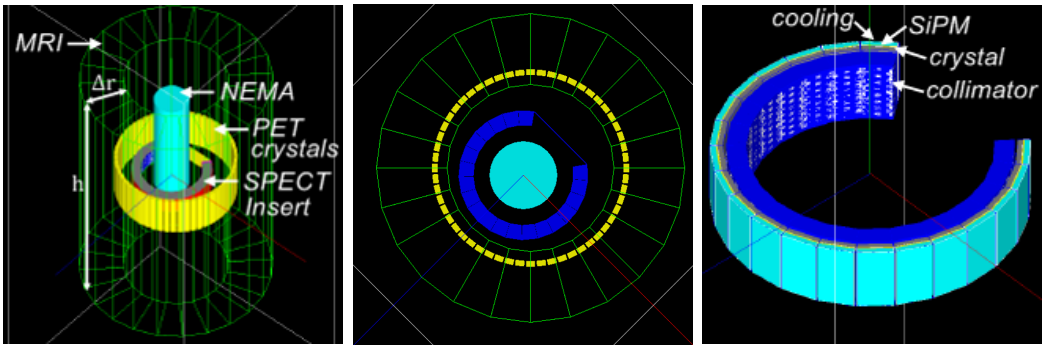

(a) (b) (c)

Figure 6.8: Configuration of the system set-up used in GATE: (a) perspective and (b) axial views of the whole system, and (c) detail of the INSERT part.

intrinsic resolutions of the detection module were assumed: 1.0, 1.2 and 1.4 mm.

Projection data with added analytical uniform background were reconstructed with 200 iterations of the ML-EM algorithm with resolution recovery and a back-projector based on angular blurring (Bousse et al., 2013a). Resolution was estimated as the FWHM in the x and y (transaxial), and z (axial) directions by fitting a rotated 3D Gaussion function to the reconstructed point source images.

6.2.2.2 Investigation on Shielding Design

Considering that the INSERT system will be installed in a PET/MR system, the Siemens Biograph mMR (Delso et al., 2011), there might be some backscatter in the bore, specially due to the high energy gamma photons. In addition, the PET LSO crystals have intrinsic activity (Ott, 2012) due to the presence of ^{176}Lu, which emits photons at 88.4 keV, 201.8 keV and 306.8 keV (Yao et al., 2008). These photons can then be detected by the INSERT and degrade image quality, if appropriate shielding is not in place. Furthermore, some of the radionuclides of interest for the INSERT system have high energy gammas, namely ^{111}I and ^{123}I. For the latter, there is a small percentage, around 3 %, of emission probability of gamma photons in the range of 248-784 keV. These gammas will have high penetration and contribute to high noise.

The objective of this study was to assess and evaluate the need for gamma shielding of the detection units, analogous to the one in a standard gamma camera, in order to minimise the backscatter due to activity in the patient outside the FOV and the LSO intrinsic activity interference.

When setting up the simulations in GATE, three main volumes were defined with specific attenuating media: the MRI system, the INSERT and a NEMA phantom (Figure 6.8). The MRI system was set up as a cylindrical aluminium volume, with a thickness of 250 mm and a length of 1594 mm, and 56 blocks of LSO in a ring configuration to mimic the PET crystals

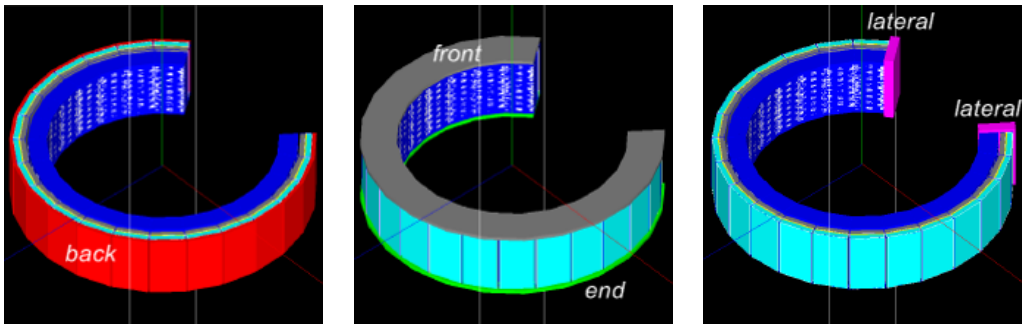

(a) (b) (c)

Figure 6.9: Shielding design for the INSERT system: (a) back (b) front and end, (c) lateral shield volumes in red, grey and magenta, respectively.

ring of the PET/MR system. Each block had a size of $20\times32\times256$ mm^3 and a ^{176}Lu-based activity of 45 kBq, amounting to a total intrinsic activity for the ring of 2.5 MBq. The INSERT system was defined as a partial ring of 20 detection modules with a MSS collimator, as previously described. The NEMA phantom was defined as a water cylinder with a radius of 102 mm and a length of 700 mm.

In regards to the shielding, three lead shielding volumes with variable thickness t were set up: front and end (FE), back (B), and lateral (L) shield, as depicted in Figure 6.9. FE shield reduces the interference of photons from out-of-field activity. B shield reduces interference from backscatter and LSO intrinsic activity. Finally, L shield reduces detector edge effects. A base plate (BP) was also simulated to emulate the system support plate.

Four sets of simulations were performed with a ^{123}I-filled NEMA phantom with 185 MBq of activity:

- variable thickness FE $t_{\mathrm{FE}} = \{0,5,6,10,15\}$ mm and remaining shield volumes thickness fixed $t_{\mathrm{B}} = 6$ mm, $t_{\mathrm{L}} = 15$ mm, $t_{\mathrm{BP}} = 3$ mm (an extra simulation with different F and E shields thickness, $t_{\mathrm{F}} = 6$ mm and $t_{\mathrm{E}} = 2$ mm, was also performed);
- variable thickness B $t_{\mathrm{B}} = \{0,2,3,4,6\}$ mm and remaining shield volumes thickness fixed $t_{\mathrm{FE}} = 15$ mm, $t_{\mathrm{L}} = 15$ mm, $t_{\mathrm{BP}} = 3$ mm;
- variable thickness L $t_{\mathrm{L}} = \{0,1,3,5,10,15\}$ mm and remaining shield volumes thickness fixed $t_{\mathrm{FE}} = 15$ mm, $t_{\mathrm{B}} = 6$ mm, $t_{\mathrm{BP}} = 3$ mm;
- variable thickness BP $t_{\mathrm{BP}} = \{0,1,2,3\}$ mm and remaining shield volumes thickness fixed $t_{\mathrm{FE}} = 15$ mm, $t_{\mathrm{B}} = 6$ mm, $t_{\mathrm{L}} = 15$ mm.

The same set of simulations was also performed for a ^{111}In-filled NEMA phantom.

All simulations were run for 1-second acquisition time. This is a short acquisition time when compared to practice, but it is enough to obtain the energy spectrum and it reduces the simulation time significantly. In the case of ^{123}I, only two photopeaks were modelled

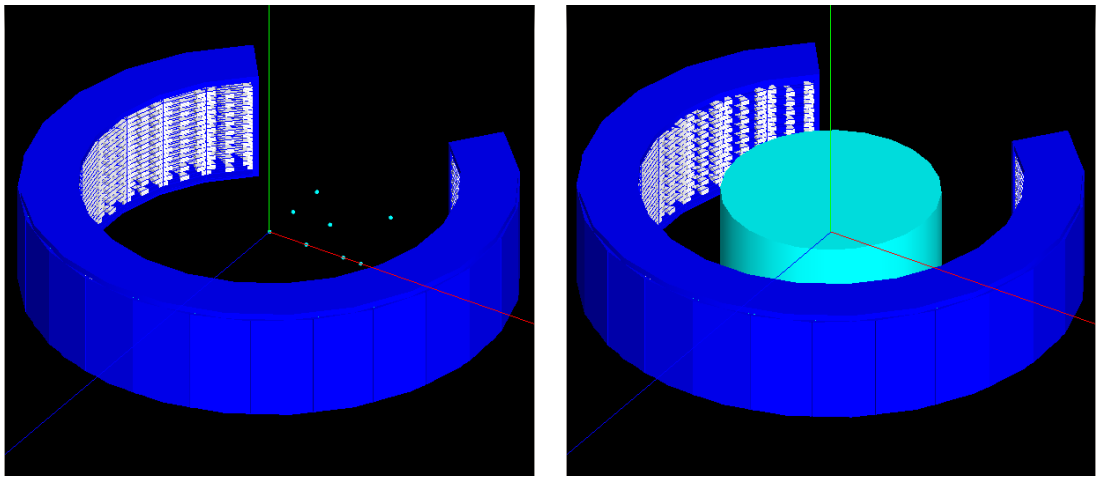

(a) (b)

Figure 6.10: Configuration of the GATE simulation geometry with the point sources (a) and the cylinder source (b) for the final INSERT system design.

to further simplify the simulation, 159 keV (83%) and 529 keV (3%) to account for the high-energy photon contribution.

The obtained energy spectra and detected counts distribution were compared for all cases, to select the most suited shielding configuration for the INSERT.

With the final design of shielding, the effects of the LSO intrinsic activity were assessed comparing non-shielded to shielded INSERT system. Furthermore, a simulation with ^{99m}Tc was also performed to obtain the energy spectrum for this radionuclide.

6.2.2.3 Investigation on System Performance

A last set of simulations was performed with the final system and shielding design.

Simulations of the INSET were performed for eight ^{99m}Tc point sources at different positions in the FOV (Figure 6.10-a): (0,0), (40,0), (80,0), (40,-40), (0,-80), (80,-80), (99,0) and (0,-40) mm in the transaxial plane. Each point source had an activity of 2 MBq, and it was acquired for 10 minutes.

Additionally a simulation with a cylinder the size of the FOV, 200 mm diameter and 90 mm height, was performed for a 10-minute acquisition and an activity of 10 MBq without attenuation (Figure 6.10-b).

For each point-source planar projection, resolution was calculated as the FWHM of the Gaussian fit in the transaxial and axial directions, and point-source sensitivity was determined as the total detected counts divided by the gamma photons emitted during the simulation. Volume sensitivity was estimated in a similar fashion using the cylindrical phantom simulation.

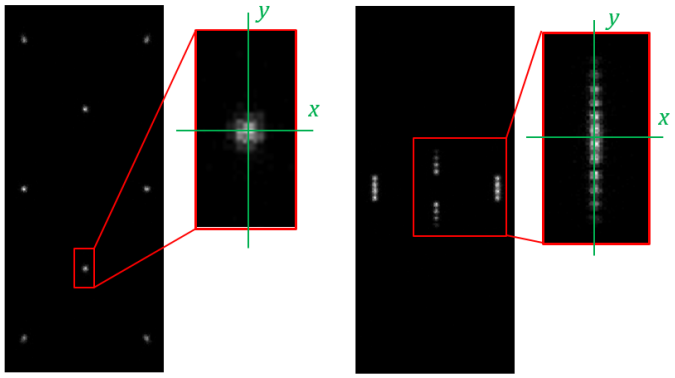

(a) (b)

Figure 6.11: Projection data obtained with the GATE simulation of the INSERT with the 8+4·½-pinhole (a) and the MSS (b) collimator, for a point source at the centre of the FOV. The zoomed box shows the projection through one of the pinholes in (a) and through three consecutive mini-slits in (b).

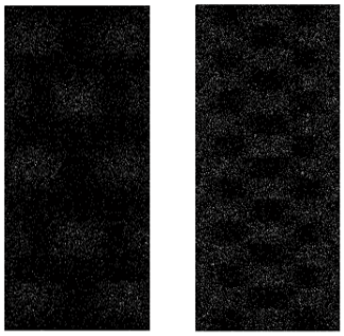

(a) (b)

Figure 6.12: Projection data obtained with the GATE simulation of the INSERT with the 8+4·½-pinhole (a) and the MSS (b) collimator, for a cylindrical source of activity at the centre of the FOV.

6.3 Results

6.3.1 Investigation on System Design

Figures 6.11 and 6.12 show the planar projection data for simulations with a point source positioned at the centre of the FOV and a cylindrical phantom, respectively, acquired with the 8+4·½-pinhole and MSS collimators.

For the point-source simulation with the 8+4·½-pinhole collimator, each full-pinhole views the centre of the FOV, where the point source is located, therefore its projection is repeated eight times in the image. In contrast, the half-pinholes view only the edges of the FOV, so there is no projection data related to these apertures.

For the point-source simulation with the MSS collimator, the point source is projected through four mini-slits. Due to the presence of the slats and the high intrinsic resolution of the detection modules, the projection has gaps in the axial direction.

Table 6.2: Average resolution (R) and efficiency (g) for the MSS and the 8+4·½-pinhole collimators obtained analysing the projection data of the GATE simulations.

	MSS	**8+4·½-pinhole**
R (*x* direction)	11.0	10.8
R (*y* direction)	10.5	12.2
g	2.8×10^{-4}	1.3×10^{-4}

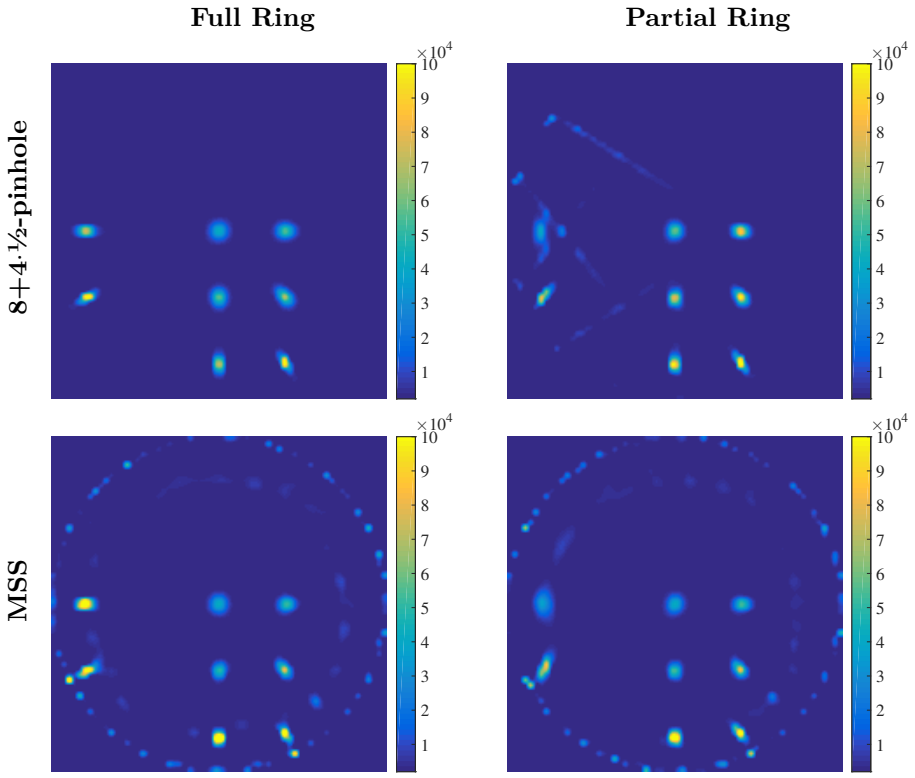

Figure 6.13: Transaxial view of the reconstructed images from the point source GATE simulations with a full (left column) and partial (right column) ring geometry of the INSERT system, with the 8+4·½-pinhole (top row) and MSS (bottom row) collimators and an intrinsic resolution of 1 mm.

For the simulation with the cylindrical phantom, data are projected through the three 2-pinhole sections and the two 1+2·½-pinhole sections of the 8+4·½-pinhole collimator. Similarly, data are projected through the eight 1+2·½-mini-slit sections and the seven 2-mini-slit sections of the MSS collimator.

Resolution and sensitivity figures estimated from the planar projection data for the two collimator designs are shown in Table 6.2. Resolution is in agreement with the target of 10 mm and sensitivity is higher with the MSS collimator when compared to the one obtained with 8+4·½-pinhole collimator.

Regarding the simulations with a set of eight point sources in the FOV, the reconstructed images for an intrinsic resolution of 1 mm and each ring geometry and collimator design simulated are shown in Figure 6.13. The two point sources on the left-hand side of the

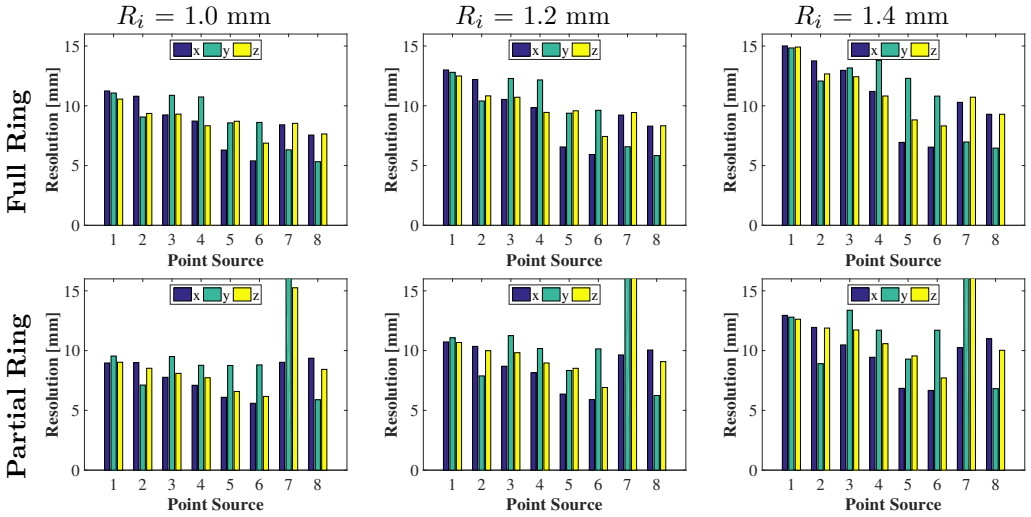

Figure 6.14: Resolution of the reconstructed point sources for the INSERT system simulations with a full (top row) and partial (bottom row) ring geometry and the 8+4·½-pinhole collimator. Each column corresponds to a simulation with a different intrinsic resolution of the detection module: 1.0, 1.2 and 1.4 mm from left to right.

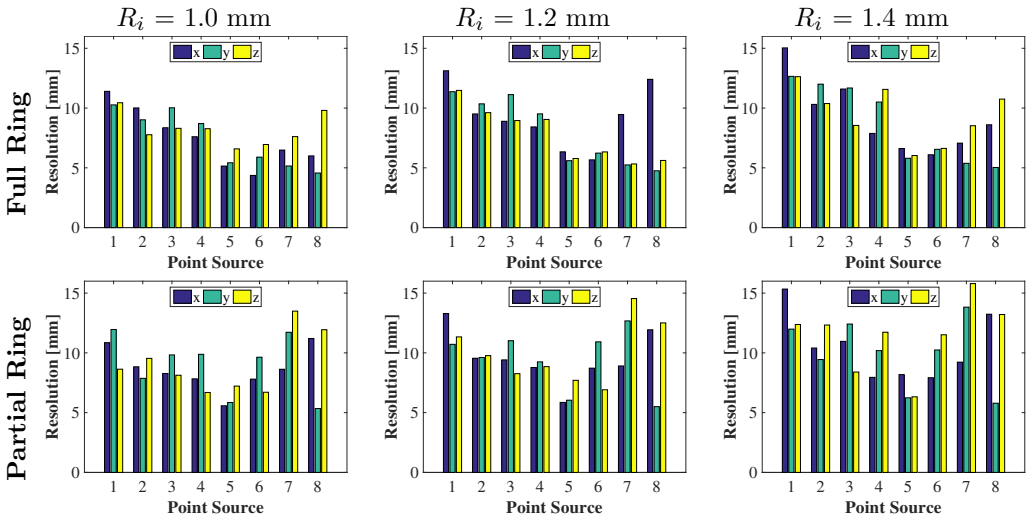

Figure 6.15: Resolution of the reconstructed point sources for the INSERT system simulations with a full (top row) and partial (bottom row) ring geometry and the MSS collimator. Each column corresponds to a simulation with a different intrinsic resolution of the detection module: 1.0, 1.2 and 1.4 mm from left to right.

reconstructed image have degraded resolution than the other six point sources, for the simulations with the partial ring geometry. These two point sources correspond to the region where the detectors are absent in the ring configuration. In general, these images show artefacts possibly due to crosstalk or absence of crystal shielding.

The results from the quantitative analysis are shown in Figures 6.14 and 6.15. The plots show the resolution in the x, y and z directions, for each point source and the different combinations of assumed intrinsic resolution, ring geometry and collimator design. Resolution

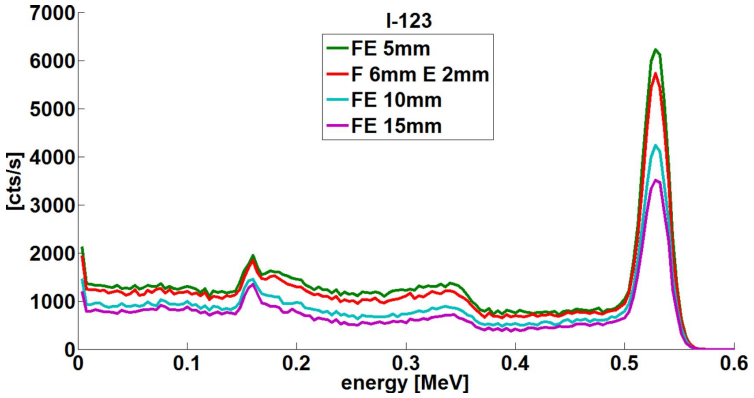

Figure 6.16: Energy spectra obtained with ^{123}I for simulations with variable FE shield thickness.

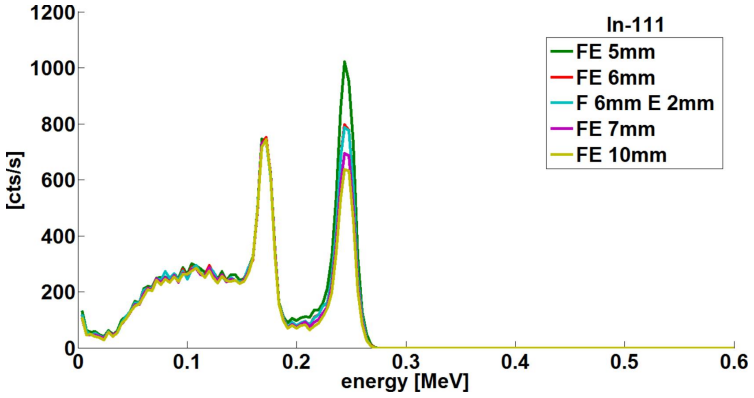

Figure 6.17: Energy spectra obtained with ^{111}In for simulations with variable FE shield thickness.

improves from the centre of the FOV towards the edge (point source 1 to 6). However, at the edge of the FOV where the detectors are missing for the partial ring design, resolution is affected by artefacts. Resolution behaviour is very similar for both collimator designs, and it degrades for increasing intrinsic resolution.

6.3.2 Investigation on Shielding Design

Figures 6.16, 6.18 and 6.26 show the energy spectra obtained with a source of ^{123}I for simulations with variable FE, B and BP thickness, respectively. The different colours correspond to a different thickness of the shielding. For viewing purposes, i.e. different scale, the spectrum for simulations without shielding is not shown. Figures 6.17, 6.19 and 6.27 show the energy spectra for the same simulations with variable shield thickness as described previously, but a source of ^{111}In.

Figures 6.20, 6.22 and 6.24 show the planar, transaxial and edge-detector count-distribution plots for ^{123}I simulations with variable FE, B and L thickness, respectively. Each blue dot corresponds to the position of the detected event. Peak 1 and 2 refer to the radionuclide photopeak, 159 keV and 529 keV. Figures 6.21, 6.23 and 6.25 show the corresponding count-distribution plots for the same simulations as described previously and

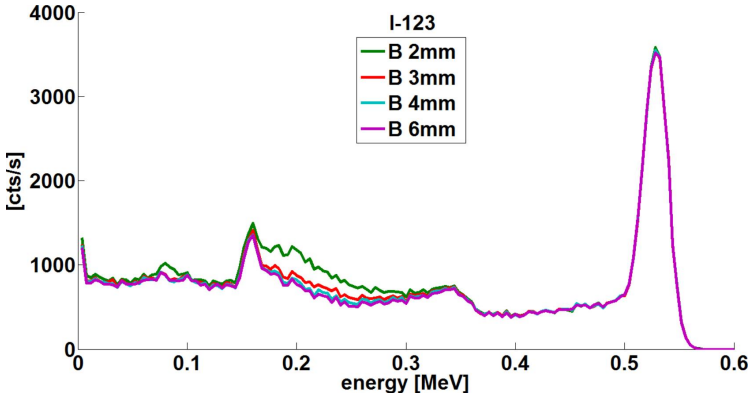

Figure 6.18: Energy spectra obtained with ^{123}I for simulations with variable B shield thickness.

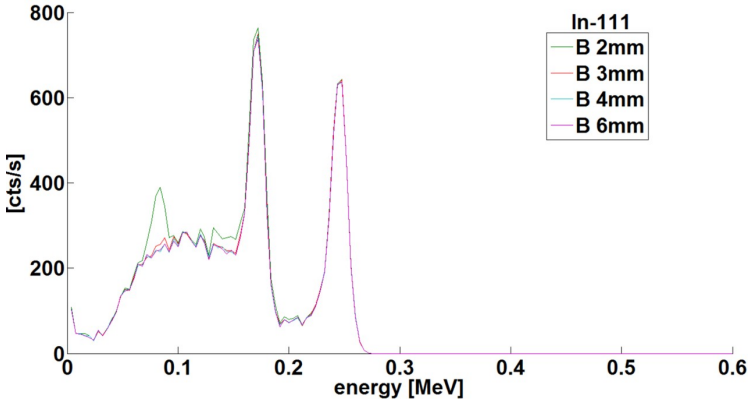

Figure 6.19: Energy spectra obtained with ^{111}In for simulations with variable B shield thickness.

a source of ^{111}In. In this case, peak 1 refers to 171 keV and peak 2 to 245 keV.

Figure 6.28 shows the energy spectra for simulations of the PET ring with ^{176}Lu and the INSERT system with and without the final shielding design.

Figure 6.29 shows the energy spectra obtained with simulations of the INSERT system with the final shielding design and ^{99m}Tc, ^{123}I and ^{111}In sources. The peaks corresponding

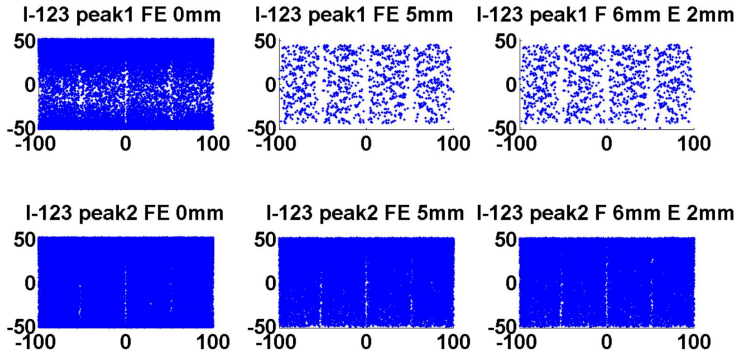

Figure 6.20: Distribution of counts along four detectors in the ring obtained with ^{123}I for simulations with variable FE shield thickness.

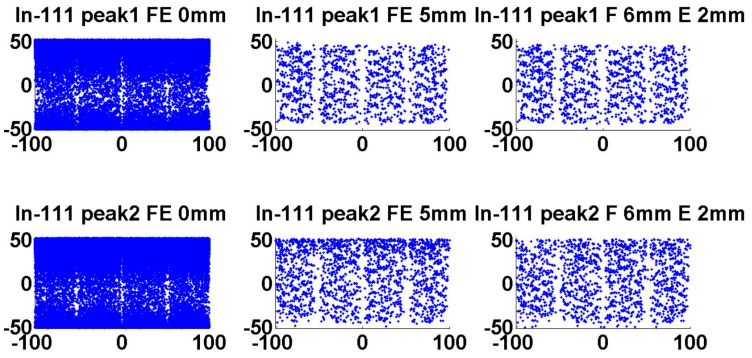

Figure 6.21: Distribution of counts along four detectors in the ring obtained with ^{111}In for simulations with variable FE shield thickness.

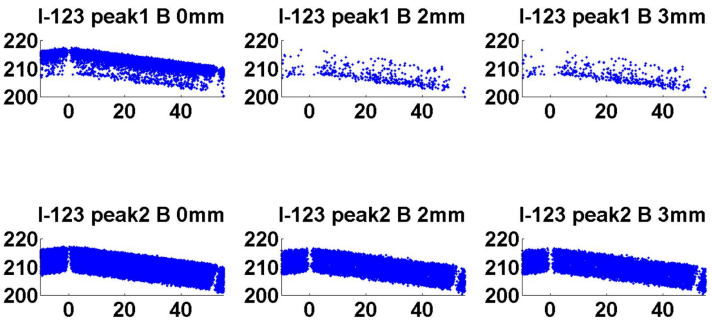

Figure 6.22: Transaxial distribution of counts along one detector in the ring obtained with ^{123}I for simulations with variable B shield thickness.

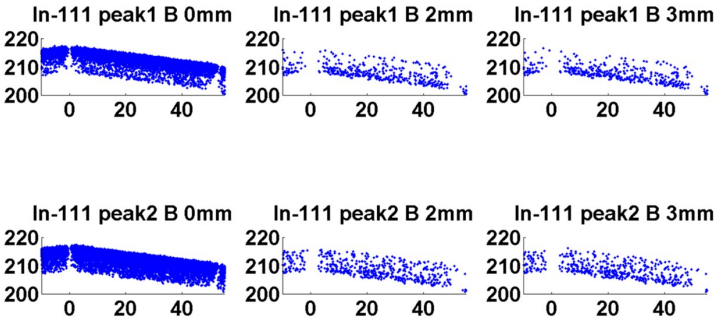

Figure 6.23: Transaxial distribution of counts along one detector in the ring obtained with ^{111}In for simulations with variable B shield thickness.

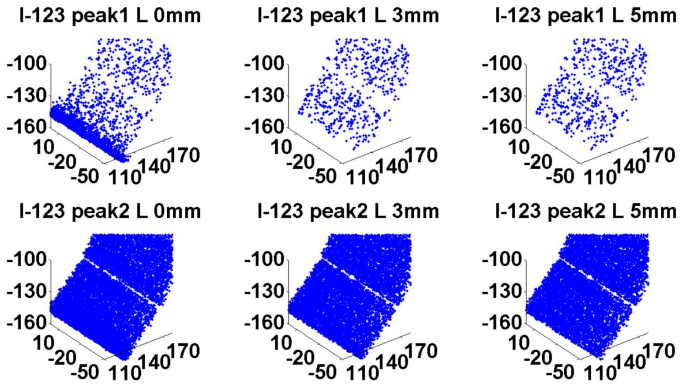

Figure 6.24: Distribution of counts along the edge-detector of the partial ring obtained with ^{123}I for simulations with variable L shield thickness.

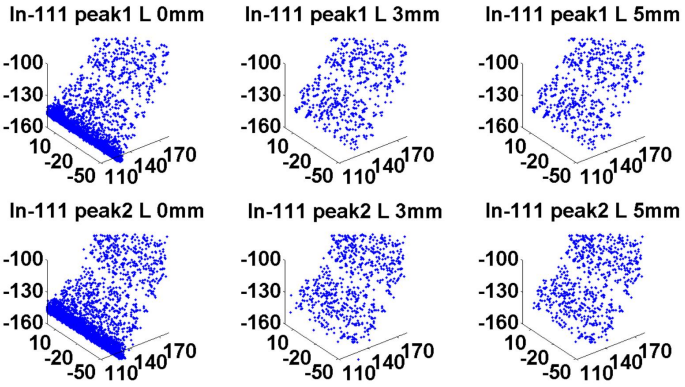

Figure 6.25: Distribution of counts along the edge-detector of the partial ring obtained with ^{111}In for simulations with variable L shield thickness.

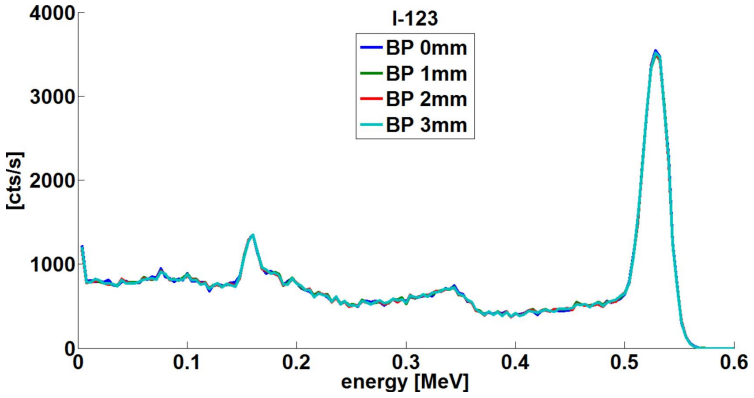

Figure 6.26: Energy spectra obtained with ^{123}I for simulations with variable BP shield thickness.

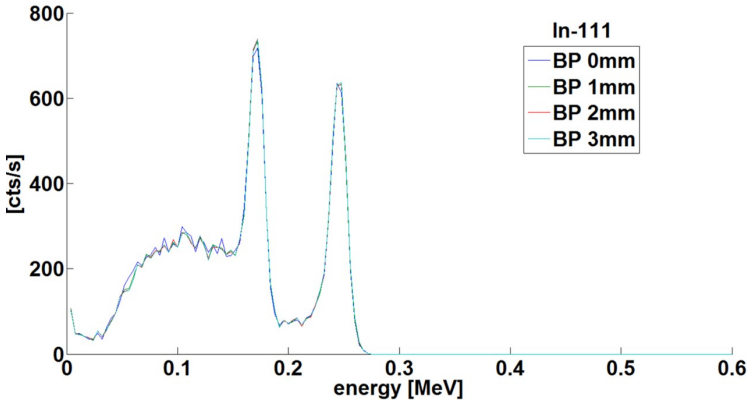

Figure 6.27: Energy spectra obtained with ^{111}In for simulations with variable BP shield thickness.

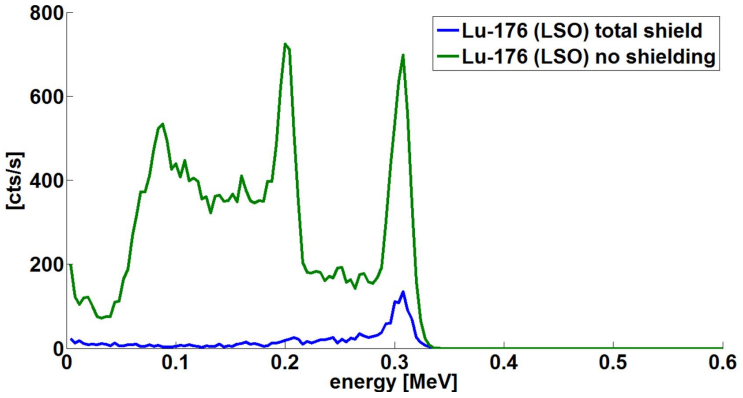

Figure 6.28: Energy spectra obtained for simulations of the INSERT system with the PET crystals present (^{176}Lu) and no source, with and without shielding.

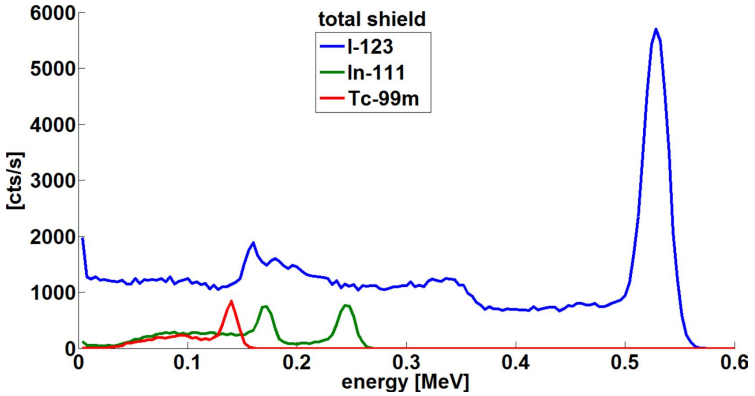

Figure 6.29: Energy spectra obtained for simulations with ^{99m}Tc, ^{111}In and ^{123}I and the final shielding design.

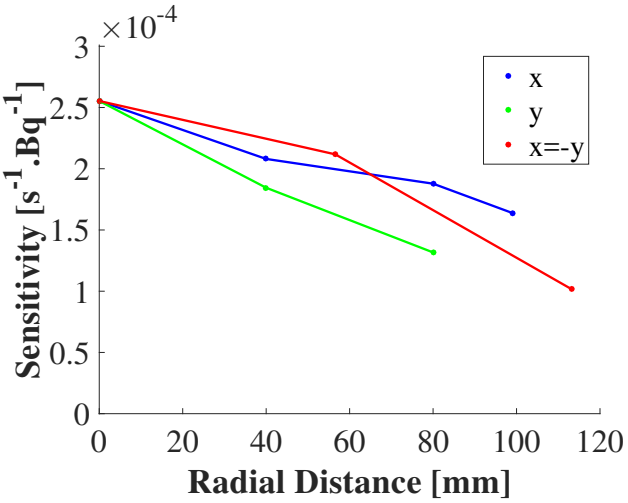

Figure 6.30: Sensitivity of each point source simulation as a function of the radial distance from the centre of the FOV, along x (blue), y (green) and $x = -y$ (red) directions within the transaxial plane.

to the ^{99m}Tc and ^{111}In photopeaks have good definition, but the one of ^{123}I has a high background.

6.3.3 Investigation on System Performance

Point-sensitivity values for the last simulations with the final INSERT and shielding design and off-centre point sources are shown in Figure 6.30 as a function of the radial distance from the centre of the FOV. For the three estimated directions within the transaxial plane, sensitivity decreases from the centre to the edge of the FOV. For the simulation with a cylindrical phantom, the calculated sensitivity is 1.31×10^{-4} $s^{-1}Bq^{-1}$.

Figure 6.31 shows the calculated transaxial and axial resolutions of planar projections from the point-source simulations. Note that the point source located at (-80,-80) is outside the FOV, and some of the detectors do not see this point source, which explains the very poor resolution. For each point source positioned off-centre in the FOV, results show resolution changes for each camera of the INSERT ring, whilst for the point source at the centre, resolution is approximately the same across cameras, as expected. For the simulated point sources, transaxial resolution varies between 8 and 12.5 mm and axial resolution between 6 and 8.5 mm.

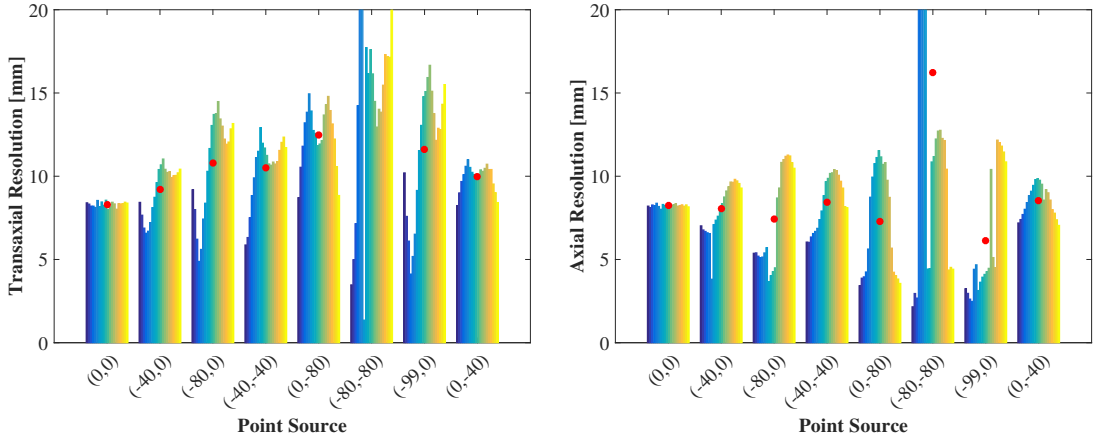

Figure 6.31: Transaxial (left) and axial (right) resolutions of the point-source projection data. Each column corresponds to a different camera of the INSERT partial ring, and the red dot, to the average resolution.

6.4 Discussion

6.4.1 Investigation on System Design

Preliminary results comparing the simulations with the 8+4·½-pinhole and MSS collimators showed that sensitivity for the MSS collimator is approximately twice of the 8+4·½-pinhole collimator, for the same achieved resolution, which is close to the target of 10 mm. These results are in line with the theoretical estimations.

In addition, these first simulations with a point source and a cylindrical phantom helped understanding the structure of the projection data and to develop a method of analysis.

As regards the analysis of the reconstructed images, there is degraded resolution in the part of the FOV where there are no detectors, in comparison to the full ring geometry simulations. The intrinsic resolution of the detectors plays an important role in the final achievable resolution. Results suggest that for a target resolution of 10 mm at the centre of the FOV, an intrinsic resolution up to 1.2 mm is still acceptable. The results for the simulations with the MSS collimator show comparable performance in terms of resolution, with increased sensitivity.

6.4.2 Investigation on Shielding Design

Analysing the plots of Figure 6.16-6.17, both energy spectra show a reduction of counts with thicker FE shielding. Considering the simulations with $t_F = 6$ mm and $t_E = 2$ mm, the accumulation of counts at the front and back edge of the detectors is reduced for the first peak of ^{123}I, but not for the second high energy peak, when compared to the no FE shielding case (Figure 6.20). However, the shielding weight required to stop these photons would overload the system. For ^{111}In (Figure 6.21), the count-distribution along the detectors is

uniform, as opposed to the absence of FE shielding case.

For the B shielding, a thickness of 2 mm reduces the accumulation of ^{123}I counts at the back of the detector (Figure 6.22). However, in the energy spectrum, the peak at 159 keV is broadened by scatter from the high energy peak (Figure 6.18), making $t_{\mathrm{B}} = 3$ mm a better option. This shielding thickness is also suitable in the case of ^{111}In (Figure 6.19 and Figure 6.23).

When comparing the simulations with variable L shield thickness, the energy spectra are not affected by the thickness, so it is important to check the count-distribution. The edge effects in the edges-detectors of the partial ring disappear with $t_{\mathrm{L}} = 5$ mm for both ^{123}I and ^{111}In (Figure 6.24 and Figure 6.25).

We observed no differences in the energy spectra obtained for different thicknesses of the base plates (Figure 6.26 and Figure 6.27), so the best option for patient support should be considered.

Based on these results, the suggested shielding for the SPECT insert is $t_{\mathrm{F}} = 6$ mm, $t_{\mathrm{E}} = 2$ mm, $t_{\mathrm{B}} = 3$ mm, and $t_{\mathrm{L}} = 5$ mm. With this shielding, the photopeak count rate per detector reduces by a factor of 94 for ^{111}In (171 keV) and 39 for ^{123}I (159 keV). The activity in the FOV is representative of the activity in the brain, but not outside the FOV, where it will accumulate only in some organs of the patient. Therefore, the high contribution from the high energy photons in the case of ^{123}I is likely to be overestimated compared to practice, due to the use of the NEMA phantom in the simulations. The estimated weight of the total shielding is 5.4 kg, which is not a limitation for the system.

Regarding the effects of the PET LSO crystals, without shielding, there is a relatively high contribution of ^{176}Lu photons in the range of 100-200 keV. When simulating with the total shielding selected previously, the effect of the LSO intrinsic activity is negligible for the energies of interest (Figure 6.28).

6.4.3 Investigation on System Performance

The calculated volume sensitivity is approximately half of that estimated for the MSS-based system in the first investigation. However, in that simulation, the INSERT system consisted of a complete ring with 24 detectors, instead of the partial ring geometry with 20 detectors of the final design, and with appropriate shielding in place. Similarly, sensitivity is lower in comparison to the one estimated analytically in Chapter 5, but the same geometry differences apply.

Regarding the resolution figures in the projection space, transaxial resolution degrades from the centre of the FOV to the edge, because the point sources are positioned in the direction of the detector gap in the partial ring. Comparing the resolution in the two evaluated directions, axial resolution is better than the transaxial one, and it is more uniform

across the tested positions. These results suggest that the target resolution of 10 mm at the centre of the FOV is achievable for the final INSERT system design, and they are in line with the analytical predictions.

6.5 Conclusion

The objective in this chapter was to further refine the INSERT system geometry and design, and to evaluate the final system performance with realistic simulations using GATE.

A framework for performing and analysing GATE simulations of the INSERT system was developed. This allowed for a flexible testing of different system designs and geometries using parametrizable macros of the simulations. With this framework in place, three important investigations were performed.

First, the system design was evaluated comparing results from simulations with the 8+4·½-pinhole and MSS collimators, and with the complete and partial ring geometry. The main conclusion was that the INSERT system with the MSS collimator achieves similar performance in terms of estimated resolution, but with higher sensitivity, which is a priority for the design of this system. In relation to the ring geometry, simulations for the partial ring configuration confirm degradation of resolution for the region of the detector gap, however this could be partly compensated during reconstruction as was shown in the previous chapter. Therefore, the partial ring is a good compromise between performance and patient comfort.

Second, a design of gamma shielding for the INSERT detector ring was devised. Gamma shielding of the SPECT detectors plays an important role in image quality, specially when considering the installation of this system inside PET/MRI system. The PET crystals have intrinsic activity, which can interfere with the INSERT gamma detection. Results suggest that a lead shielding configuration with thickness of 6 mm-front, 2 mm-end, 3 mm-back, and 5 mm-lateral is appropriate for the INSERT.

Finally, with the appropriate shielding in place and the final INSERT system design, performance evaluation simulations indicate a volume sensitivity of 1.3×10^{-4} $s^{-1}Bq^{-1}$ and a resolution in the projection space in line with the target resolution of 10 mm. The next logical step would be to validate these simulations with measurements using the INSERT system. However, the INSERT system is not available.

Chapter 7

Installation of the Single-Detector Prototype INSERT System

This chapter gives an overview of the prototype system installation at UCL, and related software, in order to perform tomographic experiments.

7.1 Introduction

Geometrical calibration procedures, data processing and collimator design validation can only be fully accomplished in the presence of a SPECT system to test and obtain experimental data. However, due to the accumulated delays within the INSERT project, it was uncertain whether the final clinical system would be available in time for testing. As an alternative, a prototype MSS collimator and prototype detector were made available with the purpose of setting-up a prototype INSERT system that could be used to assess the previous points.

The objective of this chapter is therefore to present the different steps followed during the installation of the INSERT prototype, from components to system, and from planar to tomographic acquisitions. Ultimately, this prototype system will set the basis for the development of calibration procedures, collimator design comparison and validation, and evaluation of the clinical usability of the INSERT camera.

All the physical components were shipped to UCL: electronics and pre-clinical detector (5×5 cm) were sent from POLIMI, where they had been previously characterised, and the prototype 8+4·½-pinhole and MSS collimators, from NUCFI, where they had been assembled. The acquisition software was shared by a joint-effort of POLIMI and MEDISO. The prototype camera was firstly physically assembled with the help of POLIMI, who provided useful and essential INSERT electronics training.

Figure 7.1 shows the set-up of the overall prototype system. In the following sections, each installation step is described in more detail.

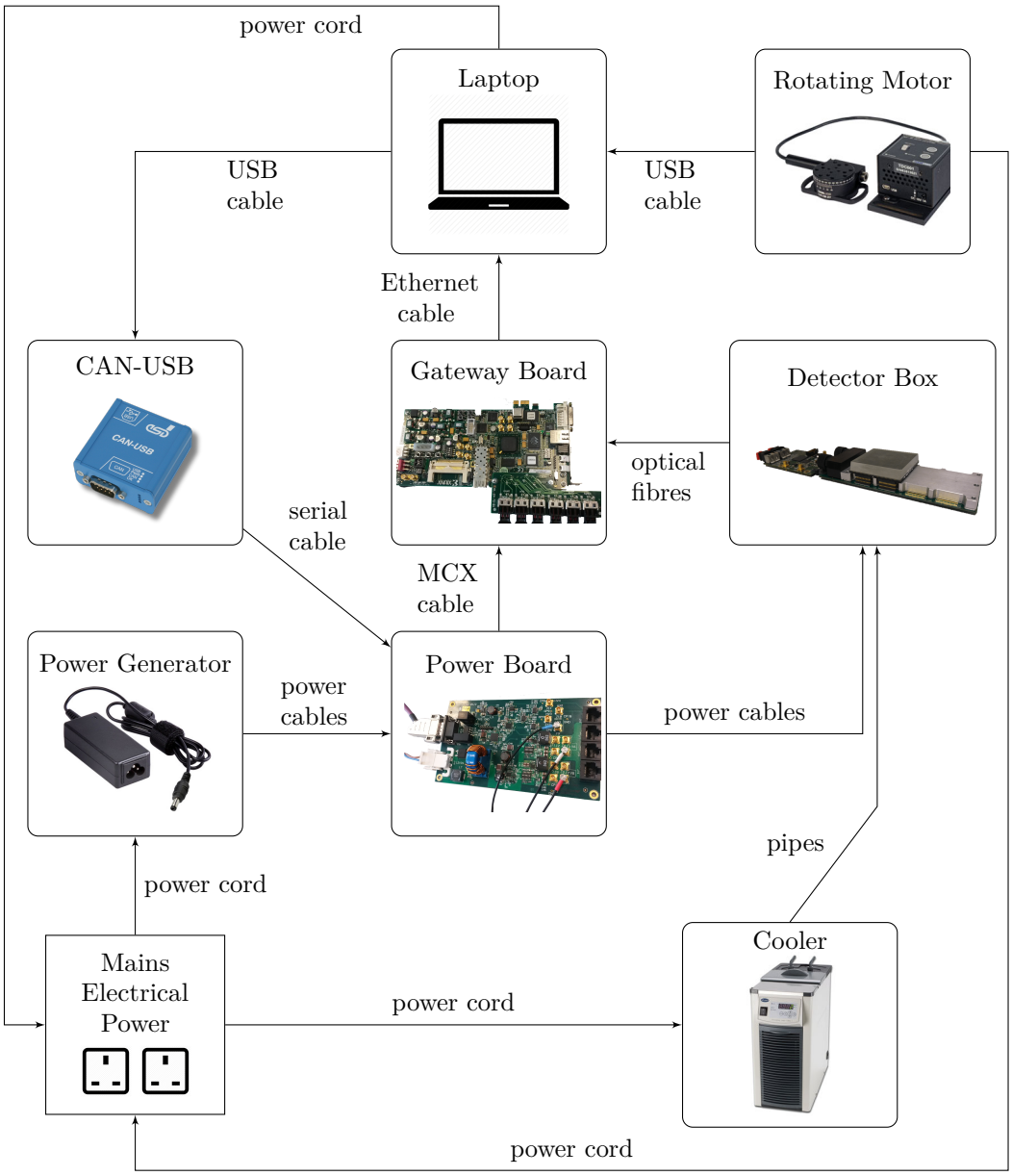

Figure 7.1: Schematic block-diagram of the overall prototype system set-up.

In this chapter, although different software is described, my role was to understand and integrate the different software/hardware platforms, in order to have a working pipeline able to perform SPECT measurements with phantoms.

7.2 Hardware Set-Up

There are two main electronic devices in the INSERT set-up: the detector and the power boxes.

The detector box contains the 5×5 cm CsI:Tl scintillation crystal coupled with four SiPM tiles, which connect to the ASIC board to read out 36 channels. This board is only

populated with one ASIC, because it has the preclinical configuration. The crystal is wrapped in PTFE tape and black tape to isolate the detector and to insulate from spurious light. Between the SiPM tiles and the ASIC board sits the aluminium cooling block, that maintains the low temperature of the SiPMs low for improved detector performance. Finally, the DAQ board connects to the ASIC board: the two boards have to be well aligned for the connection to work properly. In order to prevent condensation, small bags of silica gel crystals are added to the free space inside the box, to absorb any moisture that can damage the electronics.

The detector box has five outlets: two for the cooling pipes – in and out circulation –, two for the six optical fibres, and one for the three power cables – high, mid and low voltage. The power cables connect to the power board and the optical fibres to the gateway board. These two boards are connected via micro coaxial (MCX) cable and they sit in the power box. The connection from the power board to the laptop is established via serial cable to CAN-USB hardware and USB cable to the laptop; together with the CANreal software, they enable communication with LabVIEW for the SiPMs biasing. The gateway board is connected to the laptop via Ethernet cable, for data transfer. The laptop is equipped with Jumbo frame communication, which allows data transfer with frames larger than a standard Ethernet frame, increasing the effective bandwidth.

In order to simulate the operation of a SPECT camera, the crystal side of the detector box is closely aligned with a collimator and tungsten slabs/blocks are positioned around it to shield the crystal from unwanted gamma photons. The available collimators are the prototype MSS, the prototype 8+4·½-pinhole and a section of parallel-hole collimator.

An acrylic rotating platform is positioned in front of the SPECT camera, which holds the phantom. The rotating motor (CR1-Z7, Thorlabs Inc., Newton, New Jersey, USA) is connected to the computer via USB cable and it can be precisely controlled using a LabVIEW GUI. The interface allows for the set up of the number of rotations, angle of rotation in degrees, and time between rotations in milliseconds. However, there is no synchronization between the rotation and the acquisition interfaces. Therefore manual time-sync is always needed for the first acquired frame: for example, the acquisition interface is started and, when the first time frame finishes acquiring, the rotation interface is manually started.

The laptop, recirculating cooler, rotation motor and power generator (12 V, 3 A) are powered up directly by the mains electrical power, whereas the detector is powered by the power generator through the power board.

Regarding the cooling supply, the cooling block provides a cold surface to lower the SiPMs temperature, thus it is in close proximity to the detector tiles. This block connects to the recirculating cooler (SRC4, Stuart, UK) through thermally insulated plastic tubes and pipes, which circulate a mixture of water and glycol. This mixture is cooled down to -5 ^{o}C to reach 0 ^{o}C at the SiPMs. Zip ties and Teflon tape are wrapped around the tube-to-pipe

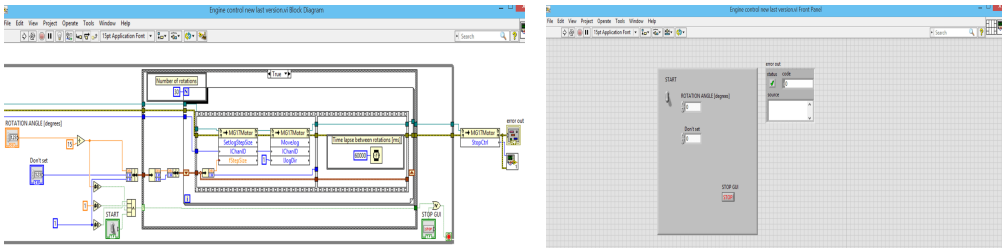

Figure 7.2: LabVIEW interface for the rotating motor. The number of rotations and the time between rotations are defined in the block diagram and the angle in the front panel, because the interface has not been fully optimised. [Courtesy of POLIMI]

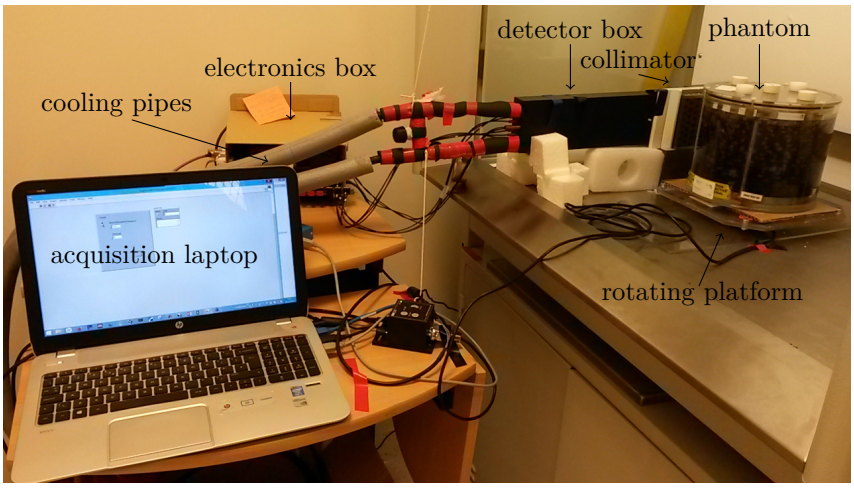

Figure 7.3: Example of one full experimental set-up of the prototype system at UCL.

connectors in order to prevent leaks. An additional pressure valve was installed to monitor the liquid pressure and prevent leakage problems, which could interfere with the normal operation of the detector electronics.

Finally, with all components fully functional, Figure 7.3 shows how in practice the INSERT prototype system is installed in the department's hot laboratory – a room in which radiopharmaceuticals or radioactive diagnostic tracers are prepared.

7.3 Acquisition Software

The acquisition software comprises the Bulma interface (Figure 7.5) and the CANreal interface (Figure 7.6), both provided by MEDISO. The latter allows communication with the ASIC board. The first, the Bulma interface, is part of MEDISO's Nucline software platform, it allows programming of the ASIC board and recording of the gamma events. The name of the output file and the acquisition time can be set in this interface. Acquired data are saved in list-mode format, in a `.data` file, which stores event information in packets of data. Therefore, these files need to be further processed into projection data files (see Section 7.5).

For the SiPMs to work with high gain, they have to be biased above the ideal high

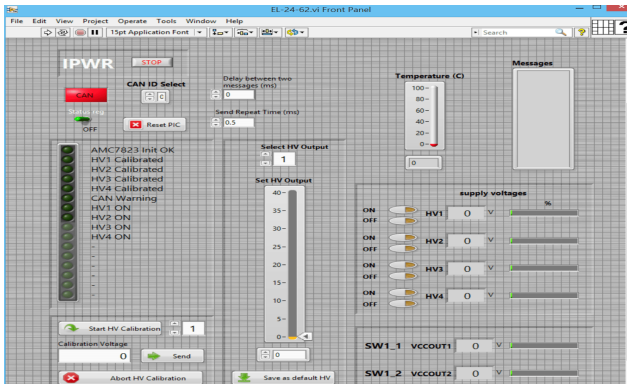

Figure 7.4: LabVIEW interface for the biasing of the SiPMs. [Courtesy of POLIMI]

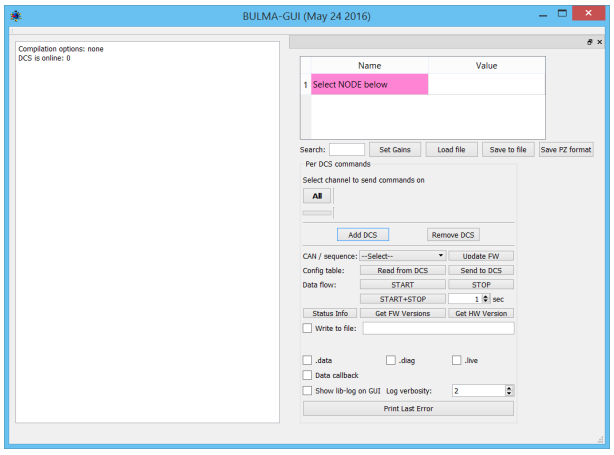

Figure 7.5: Bulma interface for data acquisition. [Courtesy of MEDISO]

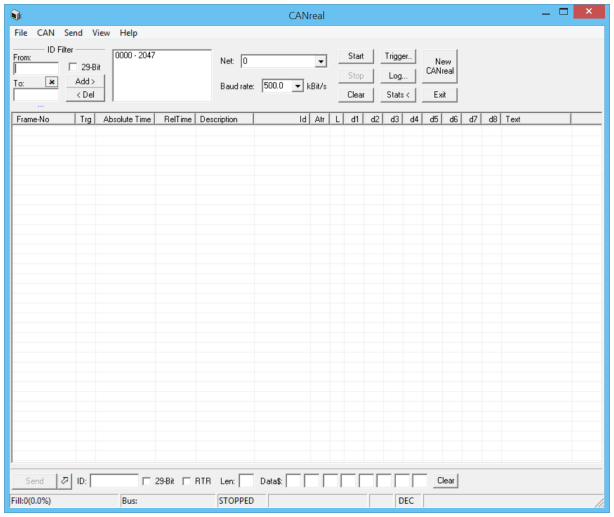

Figure 7.6: CANreal interface for the communication with the ASIC board.

voltage of 34.9 V at 0 ^{o}C. Therefore a LabVIEW interface for SiPM biasing was provided by POLIMI (Figure 7.4). In the case of this detector, the high voltage is set to 35.4 V.

7.4 Detector Calibration

Detector calibration involves generating a light model that corresponds to the detector response to gamma irradiation. The light model is generated by the `LRF_main` MATLAB function, which correlates the coordinates of the absorbed gamma photons with the expected amount of light collected by the detector (Occhipinti et al., 2016). The process is summarized in Figure 7.7: it consists of acquiring data from a uniform irradiation of the detector, without gamma shielding or collimator, for 10 minutes and at a distance of 50 cm, such that the data rate in the acquisition interface is around 100 kB.s^{-1}. These data are converted from BULMA file format `.data` to MATLAB formatted data `.mat`, and reconstructed with the Centre of Gravity (CoG) method to obtain a first estimation of the planar gamma events coordinates; then a 2D Gaussian Light Response Function (LRF) is fitted to each of the detector channels and the event positions are estimated with an ML algorithm. The light model is updated iteratively based on the work of Solovov et al. (2012), until all position estimates are uniformly distributed within the detector FOV (Figure 7.8). In contrast to most common methods of detector calibration that are long and require a precise set-up, for example, in Bouckaert et al. (2014) a robotic stage moves a collimated point source within a grid of points in the detector FOV for a total of 11 hours, this method is a fast and practical procedure.

This calibration method is based on experimental measured data, therefore the model has to be generated from time to time, to ensure a correct correspondence between model and detector response. The same applies for different radionuclides, due to the energy dependence. However, this method of calculation has some limitations. First, the light model can only be applied to thin crystals, because this is a planar position estimation method. In addition, there is no DOI information, which has been shown to affect image quality (see chapter 4). Note that there is ongoing work from POLIMI to extend the method to 3D, in order to obtain DOI information for each event. Second, the Gaussian fit is not the most appropriate fit of the light distribution at the edges of the detector. Finally, the number of ML iterations needs to be tuned and parameters determined for regularization of the input dataset, e.g. parameter η. This parameter evaluates the difference between the planar images at the present and previous iteration, and acts as a stopping condition during the event data processing.

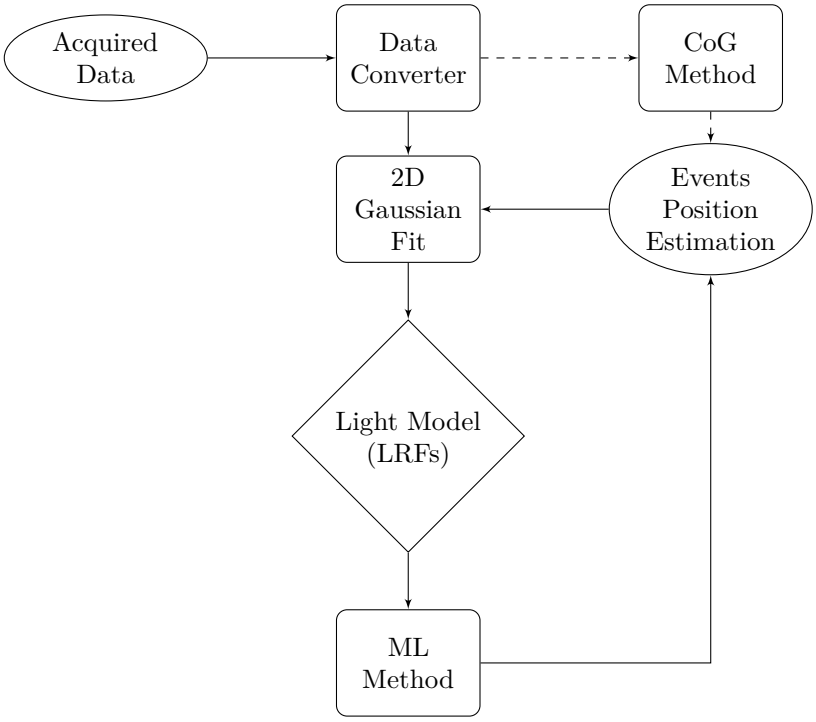

Figure 7.7: Diagram of the light model estimation method for detector response. [Adapted from Occhipinti et al. (2016)]

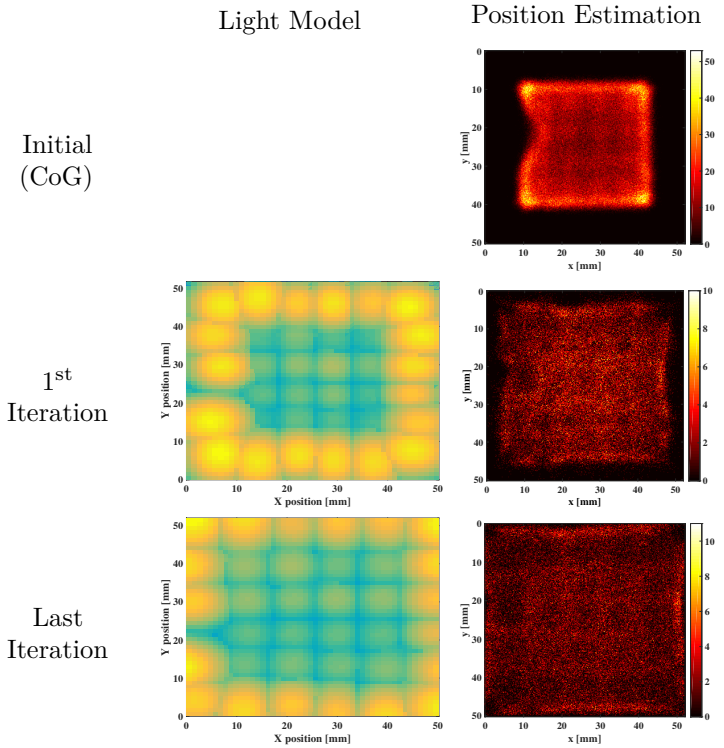

Figure 7.8: Graphical representation of the light model fit at the first and last iterations of the calibration procedure (left column), for a 5 minute uniform irradiation of the detector with a ^{99m}Tc point source of 1 MBq at a distance of 28.5 cm. Events positions are also shown at each stage of the calibration (right column). Note that one channel is not working fully.

7.5 Gamma-Event Reconstruction

Acquired data are processed into projection data using the gamma-event reconstruction software provided by POLIMI. This software allows two different types of event reconstruction: analytical and statistical. Both methods are implemented in MATLAB functions, the first is `Main_Gamma_Elab` and the latter `RECONSTRUCTION_main`. Prior to using these functions, acquired data have to be converted to MATLAB formatted data using the `Data_Converter` function.

The analytical method uses a CoG algorithm that computes the planar position of the gamma-event as the average central position of hit-photodetectors within the detection module, weighted by the signal collected by each channel. Therefore, one of the limitations of this method is the fact that all events will be reconstructed within a region of the detector, delimited by the centre of the edge channels. However, this method provides a fast reconstruction, which can be used as a first check of the acquired projection data.

The statistical method uses the ML algorithm to compute the position and energy of detected events by maximizing the likelihood of obtaining the acquired data, given the previously-generated light model. Due to the iterative nature of the algorithm, this method requires parallel computing to speed up the calculations. In contrast to the CoG reconstruction, the ML method is less limited at the edges of the detector, due to the modelling of the each channel as Gaussian LRFs. Also, the ML method provides increased linearity and uniformity, because the use of the light model directly compensates for different channel gains.

However, there was a practical problem with this software, the entire acquired data file was read into memory and only then processed to calculate the event positions. Because the computation time depends on the number of events, longer acquisitions would result in memory errors. Therefore, the reconstruction software had to be modified to read and process data files iteratively, using packets of data (`Data_Converter_bigFiles_projections`). Until it reaches the end of the raw data file `.data` and for each data packet, this routine reads in the data directly, applies the ML method, and concatenates each position result and adds each energy result. In addition, the timing of each event is also read out, which allows data framing. This is especially helpful when acquiring data at different angles with the rotating motor, during one single acquisition. For each time frame, data acquired during the phantom rotation are discarded and the remaining are processed into one projection image.

In order to validate the framing process, data were acquired at nine angles over 360 ^{o}, 60 seconds per viewing angle. Figure 7.9 shows the event reconstruction for the total acquired data (unframed) and for frames of 60 seconds. The summed-frame image is in good agreement with the unframed projection. In addition, the number of counts also supports a correct

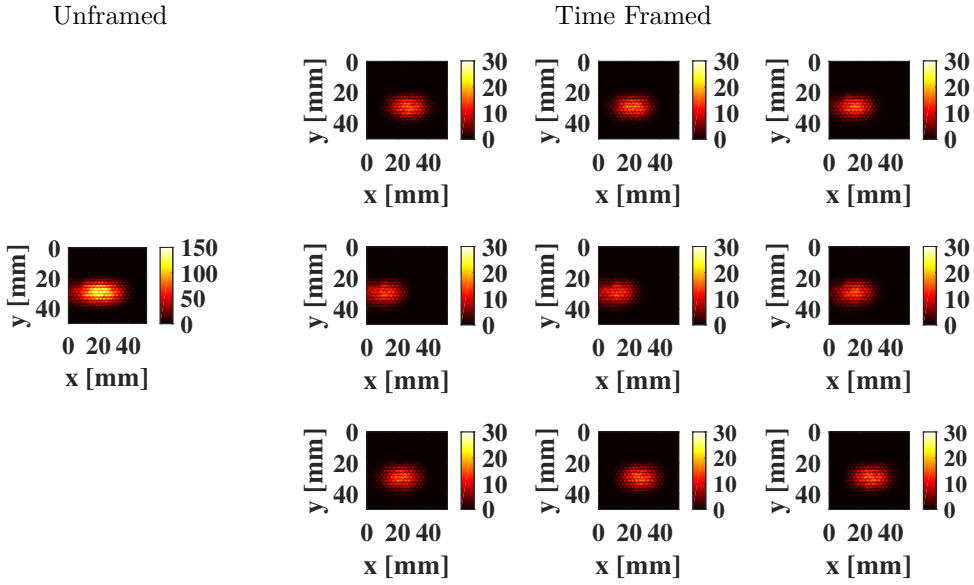

Figure 7.9: Comparison between unframed (left) and framed (right) projection data for an acquisition of 9 viewing angles.

modification of the code.

7.6 Intrinsic Corrections of Projection Data

7.6.1 Decay Correction

In the case of tomographic experiments, all time frames of the projection data are decay corrected in relation to the counts of the first frame. This is implemented in a MATLAB script `counts_decay` by applying Equation 7.1 to the projection data, which is a re-arrangement of the decay equation.

$$C_{\text{corr}} = \frac{C_{\text{uncorr}}}{e^{-\lambda \Delta t}} \tag{7.1}$$

where λ is the decay constant specific to the radioisotope, Δt is the time between the frame to correct and the first acquired frame, and C_{uncorr} is the uncorrected projection data.

7.6.2 Linearity Correction

In order to obtain the linearity transformation matrix to correct for detector linearity problems, data were acquired for one hour with a ^{99m}Tc point source, 26.5 MBq, at around 50 cm from the detector. A segment of a parallel-hole collimator, with 2 mm hole diameter and 0.25 mm septa thickness, was positioned in front of the detector to act as a grid. The set-up of the experiment and the corresponding planar projection image are shown in Figure 7.10. Due to the high intrinsic resolution of the prototype detector, it is possible to distinguish each hole of the collimator in the corresponding projection image. The idea is that the

Figure 7.10: Set-up of the experiment to obtain the linearity transformation matrix.

transformation can be obtained from controlled pairs of points, as one would do by scanning a point source through the detector's FOV, with only one acquisition.

However, the projection data for each hole is not separate from each other, so the acquired data were processed in the following manner to estimate the hole position (Figure 7.11):

- deconvolution with a Gaussian kernel to enhance the projection data for each hole;
- intensity threshold;
- morphological erosion and dilation operation with a small disk, followed by calculation of the centre of mass and area for each separate object, and selection of objects with area smaller than 90 pixels but bigger than 3 to obtain position estimates for the central collimator holes;
- re-dilation, followed by the same calculations and selection criteria to obtain position estimates for holes closer to the edge of a detector area of 40×40 mm.

Finally the linearity transformation matrix can be inferred from the spatial transformation between estimated and true hole positions of the parallel-hole collimator, using the `cp2tform` MATLAB function. To actually then correct for linearity, the inferred transformation is applied to planar projection data using `imtransform` MATLAB function.

Figure 7.12 compares the projection image for linearity corrected and uncorrected projection data. Even though the use of a point source at a distance is not the ideal representation of a flood source, the corrected image shows less distortions when compared to the uncorrected one, specially closer to the edges of the detector FOV. Both images show cold regions throughout, which could indicate that uniformity correction of the detector is needed. Further exploration of this issue is presented in Chapter 9.

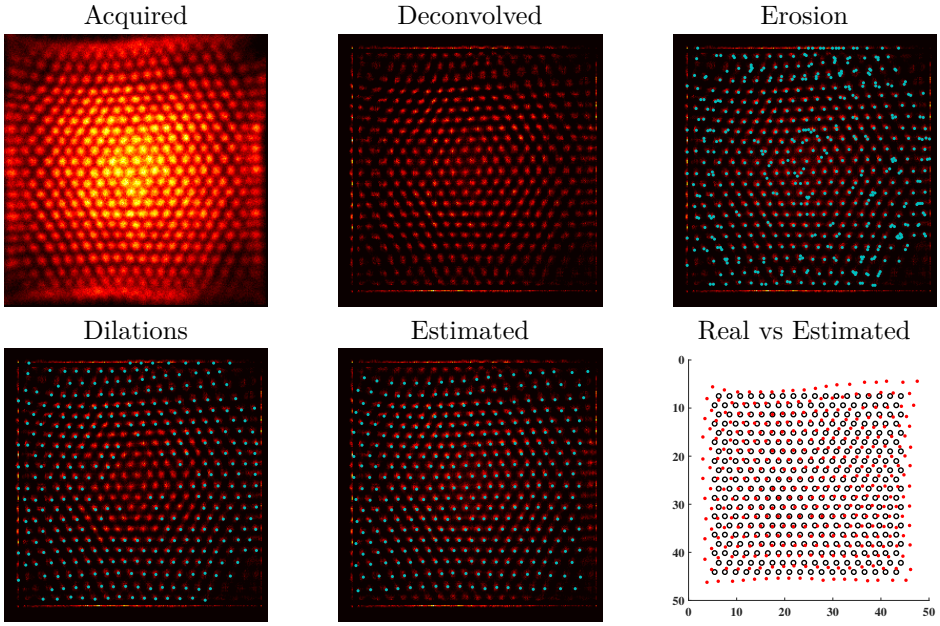

Figure 7.11: Different stages of the hole position estimation from parallel-hole projection data and comparison between real and estimated hole positions.

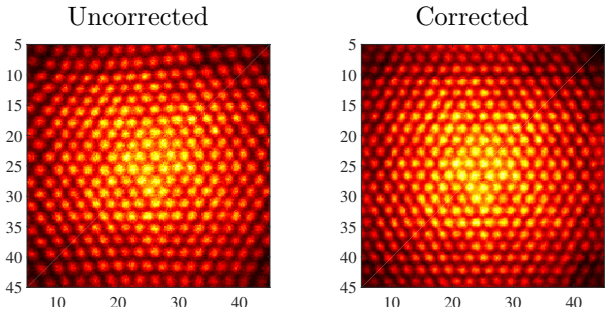

Figure 7.12: Comparison between linearity corrected and uncorrected projection data.

7.7 Image Reconstruction

The tomographic reconstruction software is based on the concept of angular blurring (Bousse et al., 2013a,b).

To compute the system matrix, the algorithm assumes each voxel is a 3D Gaussian kernel and calculates an analytical blurring of the line integrals within the possible azimuthal and polar angles. This angular blurring contains the line of response geometry and the PSF, which can vary according to the system design. Due to this feature, the (back-)projector can also be used for evaluation of different collimator designs (Erlandsson et al., 2013; Salvado et al., 2014, 2015).

In a post-processing step, the system matrix is multiplied by the appropriate sensitivity factors, depending on the collimator apertures, and blurred according to the angle of incidence to incorporate parallax effects.

Finally, the reconstructed image is obtained by running an implementation of the MAP-EM algorithm, based on the previously described (back-)projector and appropriate collimator calibration. Extrinsic calibration will be discussed in the next chapter.

7.7.1 Advanced Features

In order to profit from the design characteristics of the INSERT system and the simultaneous acquisition of SPECT and MRI data, the reconstruction software includes a number of advanced features: anatomically-guided reconstruction, motion correction, partial volume correction and kinetic modelling. All these methods improve SPECT quantification, especially important in a clinical context.

For the anatomically-guided reconstruction, a smoothing prior is incorporated into the MAP-EM algorithm, which can be restricted by anatomical boundaries using MR-based anatomical data. Unlike SPECT, MR images have high-resolution structural information. Therefore, the use of MR-based anatomical information has the potential to improve the spatial resolution of the SPECT images. Furthermore, this high-resolution structural information can also be utilised for partial volume correction, during or post-reconstruction.

In addition to high spatial resolution, MR data can provide high temporal-resolution information. High temporal resolution is important for motion correction. After the acquisition of structural MR images at a sufficient high rate to track motion, a six-parameter rigid-body transformation is derived and applied to the SPECT data. Note that in the case of brain imaging, a rigid motion model is sufficient. Motion-corrected images have improved image quality, with reduction of motion-related artefacts.

Finally, as the INSERT system is stationary, dynamic acquisition and kinetic modelling of SPECT data are possible. Specific analysis methods are incorporated in the reconstruction software for the estimation of kinetic parameters, which allow the extraction of clinically-relevant information. However, these methods are beyond the scope of this thesis.

7.8 Conclusion

The main goal here was to install the prototype system, taking into account its different components and software platforms, to ensure appropriate integration and operation as a SPECT camera.

Assembly of the prototype system at UCL was carried out as planned, with a successful installation of the overall system. Test experiments were performed to assess the functioning, interaction, and integration of the different components and software platforms.

Despite experiencing some technical problems, such as cooling leaks, these problems were solved and an independent operation of the prototype system was achieved.

In order to overcome practical issues of data handling, the software for event reconstruc-

tion was further refined. Methods for intrinsic correction of projection data were developed, implemented and tested with the use of experimental data.

In conclusion, the installation of this prototype system will allow development and refinement of geometrical calibration procedures and experimental comparison of different collimator designs.

Chapter 8

Geometrical Calibration of the Prototype INSERT System

This chapter discusses the geometrical calibration of a SPECT system, specially for small cameras and slit-slat collimation.

8.1 Introduction

Precise geometric calibration of SPECT cameras is essential to obtain a good reconstructed image (Nuyts et al., 2009). Calibration can be achieved by measuring directly the system matrix, scanning a point source through the whole FOV, with enough counts to obtain the PSF for each aperture of the collimator (Furenlid et al., 2004). Variations of this method include measuring the PSF in a limited number of points that samples the FOV and interpolating for the remaining positions (van der Have et al., 2008; Miller et al., 2012). These methods are highly accurate and well-suited for stationary systems. However, the duration of the scanning process and the need for sophisticated positioning tools, that might not be compatible with the magnetic field of the MR, make them impractical in a clinical setting.

The alternative method is to model the system matrix as a function of geometric parameters. It has been shown that a pinhole aperture can be fully described by seven parameters (Bequé et al., 2003), and that geometric calibration can be achieved by minimizing the square distances between estimated and measured projections of at least three non-collinear point sources. This method is well suited for standard pinhole SPECT cameras that benefit from the magnification of a small FOV (Metzler and Accorsi, 2005). In addition, this is also a suitable calibration method for SPECT cameras that are still in the development phase, as the camera is not available for test measurements and the design is in constant refinement.

With the latest advances in detector technology and the need for compact systems - e.g. the INSERT SPECT/MRI (Busca et al., 2015; Salvado et al., 2014), small cameras can be used to image large FOVs, trading off minification with high intrinsic resolution to achieve a system resolution similar to that of a standard SPECT system. However, with minification, precise measurement in the projection space, required for calibration purposes, may be compromised.

In this chapter, the goal is to investigate the impact of the magnification factor in a model-based calibration procedure, which has direct relevance to the geometrical calibration of the clinical INSERT camera. A second objective is to implement and refine a model-based calibration procedure for the INSERT prototype system, that can be easily adapted for the calibration of the final INSERT system.

8.2 Impact of the Magnification Factor

Typically pinhole cameras are used to image small organs in order to profit from the magnification of these into the detectors. In this case, magnification occurs because the distance between the detector and the aperture of the collimator is bigger than the distance between the latter and the source. Therefore the magnification factor is higher than 1.

When compactness is needed and small cameras are used to image large FOVs, the distance between the source and the aperture becomes big in relation to that between the latter and the detector, hence minification occurs, i.e. magnification factor lower than 1.

This section aims to investigate the impact of the magnification factor in the model-based geometrical calibration of SPECT cameras.

8.2.1 Methods

Model-based calibration was performed for simulated and measured data of systems with different values of the magnification factor M. Details for each experiment are described in the following sections.

8.2.1.1 Simulations

Seven calibration parameters (Table 8.1) were defined for a single pinhole collimator with magnification factor M of 4 and 0.25, referred to as PH_{mag} and PH_{min}, respectively. The detector size, FOV and intrinsic resolution were matched accordingly: 20 cm, 5 cm and 3 mm for the magnification case, and 5 cm, 20 cm and 1 mm for the minification case.

Simulated data were generated from ideal projections of three non-collinear point sources, blurred according to the system resolution and the parallax effects. Data were then scaled for different count levels and Poisson noise added. This procedure was repeated for 100 noise realizations and three count levels: 10^3, 10^5 and 10^7.

The geometric calibration parameters were estimated using a constrained nonlinear

Table 8.1: Description of the seven geometrical calibration parameters for a single pinhole system. [Adapted from Bequé et al. (2003)]

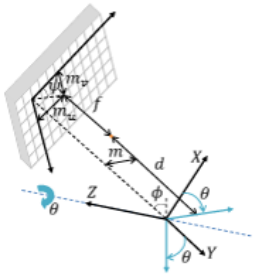

Variable	Parameter Description
x_1	Focal length f
x_2	Focal point to centre of rotation distance d
x_3	Mechanical offset m
x_4	Tilt between detector and rotation axis ϕ
x_5	Twist of the pixel grid in relation to detector ψ
x_6	Electrical shift in transverse direction e_u
x_7	Electrical shift in axial direction e_v

optimization algorithm in MATLAB, that minimises the sum of the square distances between true and simulated projection data from the three point sources (Bequé et al., 2003). Bias and standard deviation (SD) of the parameter estimates were obtained for each calibration parameter.

For a slit-slat collimator, the calibration problem in the transaxial direction is similar to that of a pinhole system, but it is assumed that the number of parameters is reduced to five for the slit component: f, d, m, ϕ and e_u. These geometrical parameters were evaluated for a single slit-slat collimator SS_{min} with minification M=0.25. The same projection and calibration procedure were performed as described previously, and repeated for 100 noise realizations and three count levels.

For each collimator, PH_{mag}, PH_{min} and SS_{min}, the set of geometric calibration parameters with highest deviation from the true parameters was identified from the two lower noise datasets, and used to reconstruct simulated data corresponding to a Derenzo hot-rod phantom. The diameter of the rods in the phantom varied from 7 to 12 mm. Reconstruction was also performed with the true calibration parameters. Profiles along x and y directions of the reconstructed images were obtained for each collimator and calibration case.

8.2.1.2 Measurements

Projection data were acquired for 30 angles covering 360^o with the INSERT prototype detector (Busca et al., 2015) of size 5×5 cm and the MSS prototype collimator – details about this camera are given in the previous chapter. Four ^{99m}Tc line sources were placed on a rotating stage at different radial locations within the FOV: 69.00, 51.75, 34.50 and 17.25 mm, measured from the centre of rotation (CoR), at 90^o intervals. The procedure was repeated for three distances from the collimator to the CoR, 165.00 mm, 106.78 mm, and 48.57 mm (Figure 8.1), adjusting the radial positions accordingly, in order to get different magnification factors.

Model-based geometric calibration was performed as described in Figure 8.2: raw projection data p are corrected for detector-shift and sensitivity, and rebinned with the Sino method (Erlandsson et al., 2016), according to given calibration parameters $\mathbf{x}$; each curve is

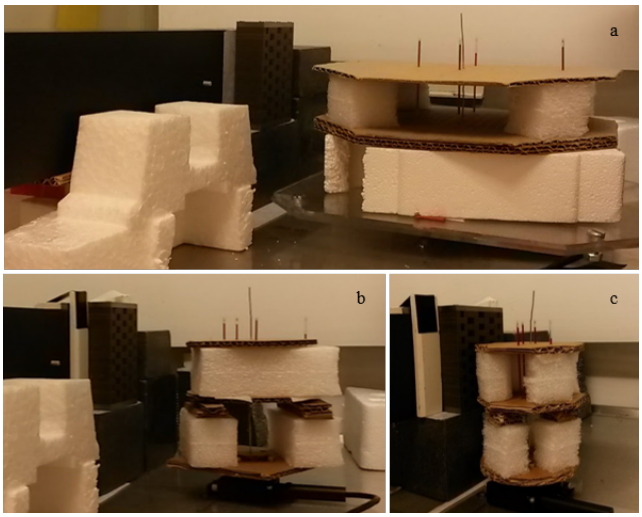

Figure 8.1: Experimental setup: detector (black box), MSS collimator and 4-line-source phantom placed on a rotating stage. The distance between collimator and CoR is 165.00 mm (a), 106.78 mm (b), and 48.57 mm (c).

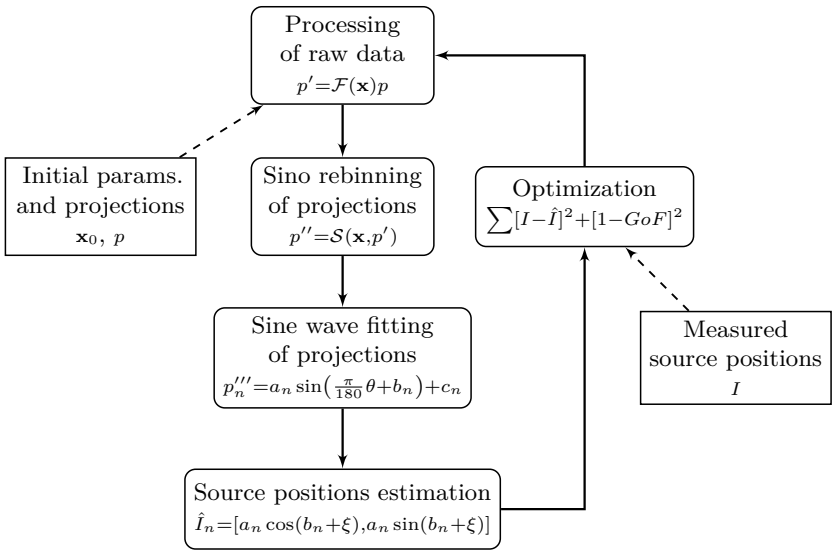

Figure 8.2: Framework of the applied model-based geometrical calibration method. $\mathbf{x}$ corresponds to the set of geometrical parameters $[f, d, m, \phi, \psi, e_u, e_v]$, p to the projection data, and GoF to the sine-wave goodness of fit of Sino-rebinned projection data.

then fitted with a sine wave, and the fitted parameters used to estimate the corresponding source position; optimization of the calibration parameters is achieved by minimising the sum of the squared distances between true I and estimated $\hat{I}$ source positions, with an extra term for the goodness of fit GoF of the sine waves.

Note that the *Sino* is a rebinning method that transforms raw projection data acquired with the MSS collimator, which are difficult to interpret visually, into the traditional sinogram format (Figure 8.3). An added advantage is that these data can then be reconstructed using standard parallel-beam reconstruction algorithms, taking into account that there is missing

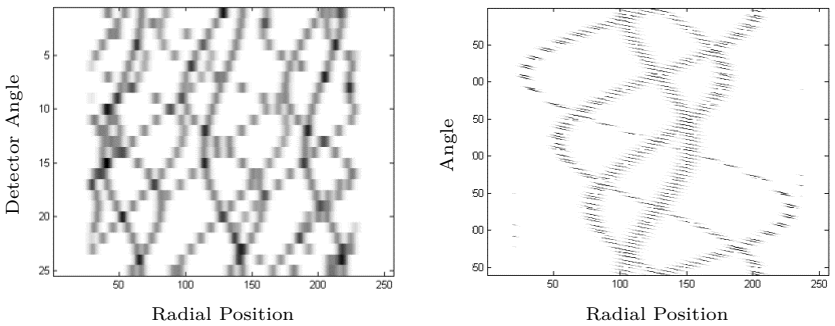

Figure 8.3: Raw projection data (a) and Sino projection data for an acquisition of four line sources with the MSS prototype collimator.

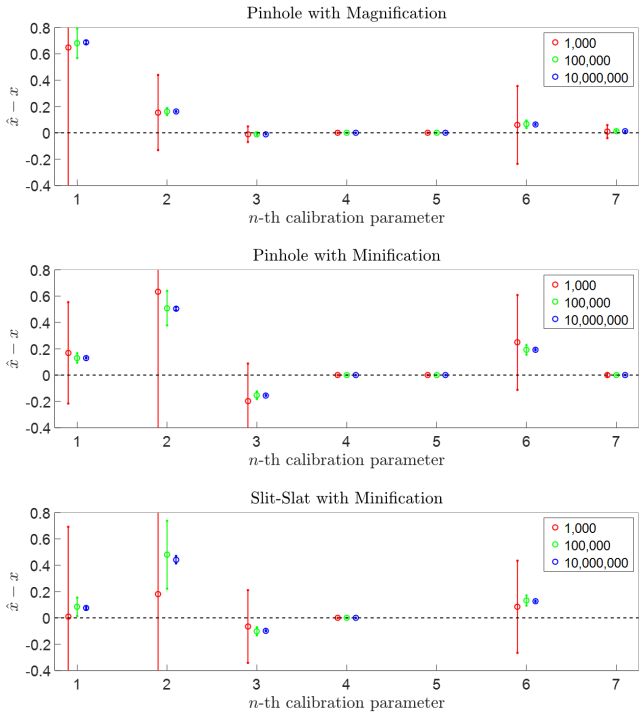

Figure 8.4: Relative bias and SD of the estimated calibration parameters for the PH_{mag}, PH_{min} and SS_{min} collimators. Each colour corresponds to a different count level. SD bars of parameters x_1, x_2 and x_3, and x_1 and x_2 exceed the displayed range, top-bottom respectively.

data due to the absence of detector rotation.

For each experiment with a specific magnification factor, estimated parameters were compared against the true values.

8.2.2 Results

8.2.2.1 Simulations

For each simulated collimator, Figure 8.4 shows the estimated geometrical calibration parameters. Comparing results for the two pinhole collimators, x_2, x_3 and x_6 parameters

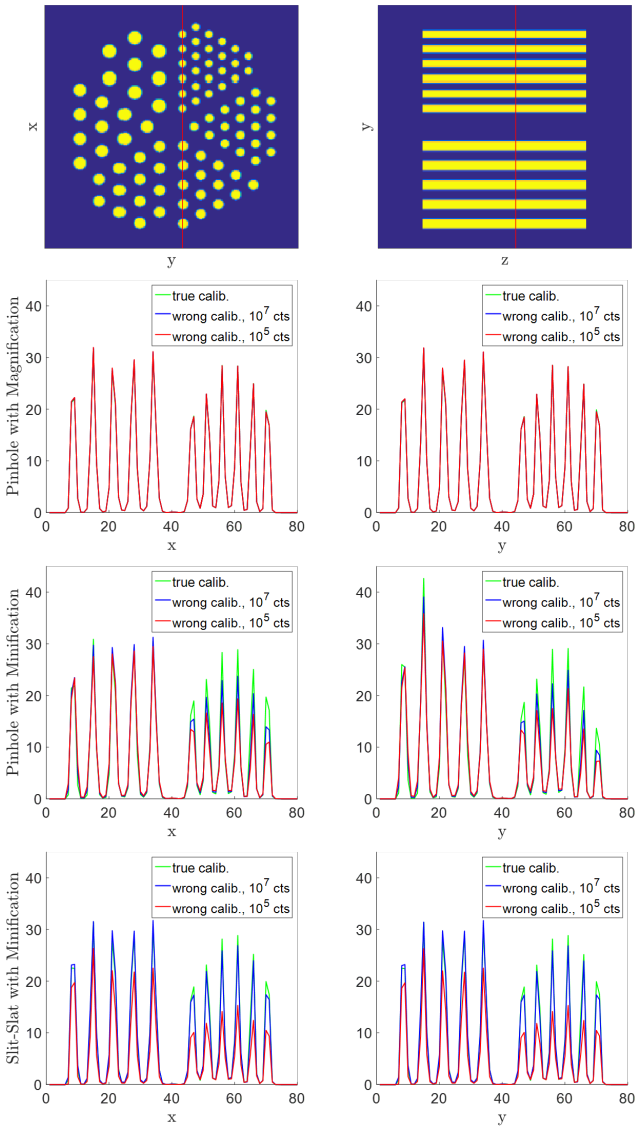

Figure 8.5: Derenzo phantom (top) and profiles along x (left) and y (right) of the reconstructed images with true (green) and incorrect (blue - 10^7 total counts, red - 10^5 total counts) calibration parameters for the $\mathrm{PH_{mag}}$, $\mathrm{PH_{min}}$ and $\mathrm{SS_{min}}$ collimators, top-bottom respectively.

show higher relative bias and SD for $\mathrm{PH_{min}}$ than $\mathrm{PH_{mag}}$, while for x_1 the reverse is true. Comparing the estimates for the collimators with minification, $\mathrm{SS_{min}}$ parameters show lower relative bias than $\mathrm{PH_{min}}$, but higher SD. For all the simulated collimators, SD is reduced for a higher number of counts, i.e. lower noise.

Taking the worst-case calibration scenario of each collimator at the two lower noise levels, Figure 8.5 shows profiles along the x and y directions of the reconstructed Derenzo phantom, together with profiles obtained with the correct calibration parameters. When reconstructed with incorrect compared to correct calibration parameters at the lowest noise level, profiles for the collimators with minification show marginally wider FWHM of the

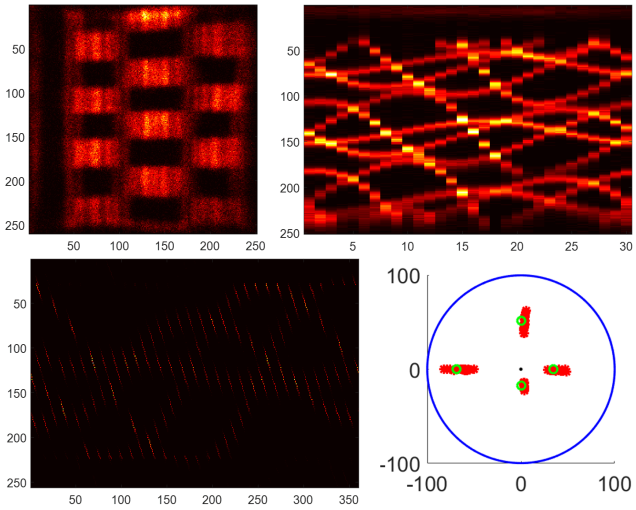

Figure 8.6: Planar projection of the measured raw data (top left), sinogram (top right), sinogram after Sino rebinning with initial calibration parameters (bottom left), and plot of the optimization method (bottom right) for the acquisition at a distance of 165 mm. The FOV is represented in blue, the true line source positions in green, and the iteratively estimated positions in red.

phantom rods and activity underestimation. When increasing the noise, the peak height decreases even more, especially for the SS_{min} collimator. No visible difference is observed for the PH_{mag} collimator at the two noise levels.

8.2.2.2 Measurements

Figure 8.6 shows the measured projection data for experiment 1, at 165 mm distance, in the form of a planar projection and as a function of the detector angle. The corresponding Sino-rebinned sinogram for the first iteration of the calibration process is also shown. Each curve corresponds to data acquired from each line source. The line source positions estimated during the calibration optimisation are shown in the plot.

For the three experiments, Table 8.2 shows the focal length, radius of rotation (RoR), average line source location errors estimated with the proposed geometric calibration framework and a plot of the source locations within the FOV. The mean error of the estimated line source positions improved with a higher magnification factor, for experiments 2 and 3 compared to experiment 1.

8.2.3 Discussion

8.2.3.1 Simulations

Comparing the PH_{min} calibration parameter estimates to the ones from the PH_{mag} collimator, the higher bias and SD observed suggests that calibration is less robust when minification is present. When calibrating the SS_{min} collimator, the fact that only five parameters are estimated reduces the bias introduced by the minification, however precision is compromised

Table 8.2: Experimental geometric parameters estimated with the proposed model-based calibration framework. Distance to CoR, focal length, RoR and source position errors shown in millimetres.

	Experiment 1	**Experiment 2**	**Experiment 3**
Coll.–CoR [mm]	165.00	106.78	48.57
$\hat{f}$ [mm]	24.66	23.33	21.93
$\widehat{RoR}$ [mm]	166.41	124.11	68.19
$\overline{I-\hat{I}}$	1.67	0.83	1.03
$\widehat{M}$	0.15	0.19	0.32
FOV	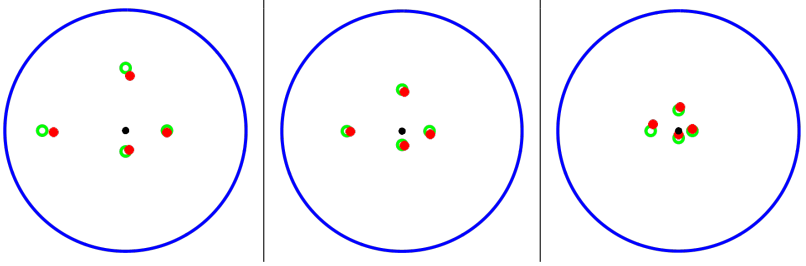		

at low counts. For all simulated collimators, the estimated parameters are more stable with higher counts, which corresponds to longer acquisitions.

At the lowest noise level, the profiles of the reconstructed images show that the deviation in the estimated calibration parameters result in small quantitative differences when minification is present, even for the SS_{min} collimator, which has low-bias parameter estimates compared to the other collimator geometries. However, when noise increases, activity underestimation becomes problematic with the SS_{min} collimator.

8.2.3.2 Measurements

Results for the experimental data obtained with the prototype INSERT camera are in line with the ones from simulated data, although the mean error of the source positions are slightly higher for experiment 3 compared to experiment 2. This is due to the fact that sine-fitting of Sino-rebinned projection data are difficult for the source closest to the CoR (flat curve). Furthermore, the sine-fitting of the data with the four sources at the same time adds an extra complication in the process. Therefore the separate acquisition of each source should improve results.

Regarding the focal length, the estimated values should have been the same across the three experiments, as they were performed with the same collimator. This can be explained by the fact that the focal length and the ROR are highly correlated, which introduces a high bias in their estimation. If one of these two parameters can be fixed, i.e. measured separately, accuracy of the results should improve.

Geometrical calibration of SPECT cameras is more sensitive to minification as opposed to magnification, and requires high precision estimation of the model parameters, in order to avoid deterioration in image quality.

8.3 Practical Calibration of the INSERT Prototype

In this section, the aim is to develop and refine a practical calibration procedure for the single-detector INSERT prototype camera equipped with the MSS prototype collimator. As described in Chapter 7, this camera consists of a 5×5 cm detector based on SiPM readout and a CsI:Tl scintillation crystal.

For the MSS collimator, in the transaxial direction, the mini-slits provide collimation similar to that of a pinhole collimator, whereas the slats provide collimation resembling that of the parallel-hole collimator in the axial direction. Taking advantage of these design characteristics of the collimator, the approach to the geometric calibration of the camera was to have separate measurements to estimate the calibration parameters for the different directions independently.

8.3.1 Methods

A practical framework was developed for detector response correction and geometric calibration of the INSERT camera with a single prototype detector and MSS prototype collimator.

The calibration framework consists of four main steps, in which a particular phantom has to be scanned in order to estimate calibration parameters. Each acquisition is described below. Estimated parameters are then incorporated in the system matrix used by the reconstruction algorithm, providing accurate correspondence between the model and the actual system.

Parallel-hole Collimator

Data acquired from an irradiation through a parallel-hole collimator allows for the linearity correction of the detector. The spatial transformation is derived from pairs of control points, the centroids of parallel-hole collimator projection and the true hole positions. Note that the MSS prototype collimator is not utilised in this acquisition, as this correction relates only to the detector response. Also, this is a one-off correction, as long as the detector is set-up with the same operation conditions, namely temperature and high voltage.

Planar Phantom

Data acquired with a planar phantom allows for uniformity correction and determination of the electronic shifts and pixel size (Figure 8.7). Note that this phantom has to be wider than the prototype collimator in the transaxial direction to cover the FOV of the half-mini-slits. The sensitivity profile of the detector FOV across the different sections along the axial direction is determined from the planar projection data to correct for non-uniformities. The electronic shifts are computed from the difference between the projected data centre and the centre of the detector FOV.

Horizontal Line Source Phantom

Data acquired with a horizontal line source phantom allows for the determination of the detector's axial resolution, and twist and tilt parameters. The horizontal line source

Figure 8.7: Uniformity correction data acquisition set-up with the prototype detector, the MSS prototype collimator and a planar phantom.

Figure 8.8: Data acquisition set-up with a horizontal line source phantom for axial calibration of the MSS prototype collimator.

phantom consists of a structure where a capillary tube, filled with activity, can be placed parallel to the slats at several distances from the detector (Figure 8.8). Axial resolution is then computed as the FWHM of the projection data Gaussian fit in the axial direction. The twist is determined from the deviation from the horizontal orientation of the line source projection on the detector, and the tilt from the apparent up-down motion of the projection as the capillary moves away from the detector.

Vertical Line Source Phantom

Data acquired with a vertical line source phantom allows for the determination of the remaining transaxial parameters: focal length, mechanical shift and slit positions. These are estimated based on Bequé et al. (2003) by iteratively optimizing the squared difference between the measured projection data and analytically estimated projections, assuming the radius of rotation is known, i.e. can be measured independently. Acquisition of the vertical line source is performed for four non-collinear positions within the FOV, and for a number of views equally distributed over 360^o (Figure 8.9). In contrast to the calibration of pinhole collimation, for the MSS collimator, line sources can be utilised instead of point sources due to the different collimations in the transaxial and axial directions.

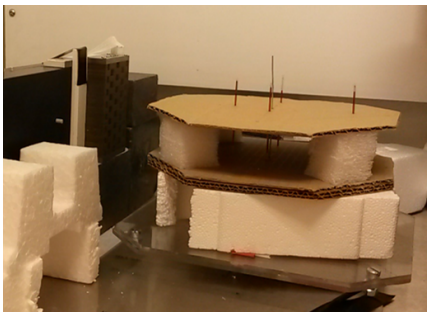

Figure 8.9: Data acquisition set-up with a vertical line source phantom for transaxial calibration of the MSS prototype collimator.

Table 8.3: Acquisition parameters for each calibration phantom: planar, parallel-hole collimation, horizontal line source and vertical line source phantoms. The acquisition time corresponds to the total scan time.

Phantom	Activity [MBq]	Acquisition Time [s]	No. of Views over 360^o [#]
planar	68.3	18000	1
parallel-hole coll.	26.5	3600	1
horiz. line source	15.0	150 (×11)	1
vert. line source	17.5	1800	30

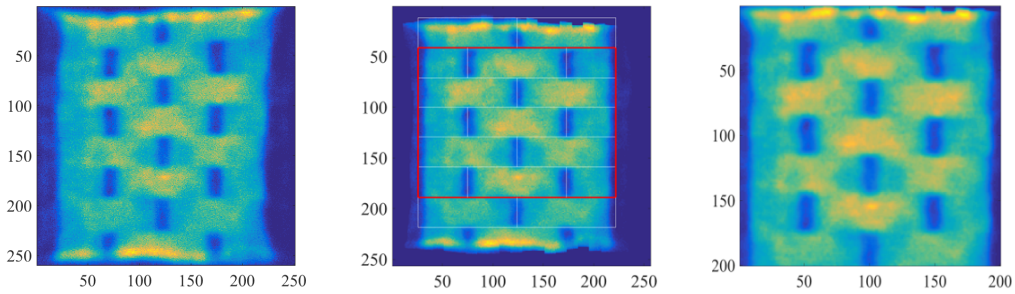

Figure 8.10: Planar projection data for the acquisition with the planar phantom: raw data (left) and linearity corrected data (centre). The red square denotes the detector FOV, which has an area of 4×4 cm (zoom on the right).

8.3.2 Results

Table 8.3 summarises the acquisition parameters for each of the calibration phantoms, and the corresponding projection data are shown in Figures 8.10, 8.12 and 8.14. Projection data for the parallel-hole collimator were already mentioned in the previous chapter.

Figure 8.10 shows the planar projection data for the scan with the planar phantom, before and after linearity correction of the raw data. The corresponding sensitivity profiles for uniformity correction of the prototype collimator are shown in Figure 8.11.

Regarding the axial calibration, Figure 8.12 shows the planar projection data for the acquisitions with the horizontal line source phantom at different distances from the collimator. Axially, resolution degrades as the distance to detector increases, as also shown in Figure 8.13

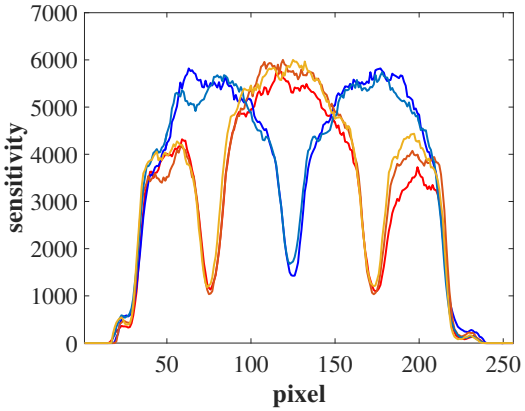

Figure 8.11: Sensitivity profiles obtained for each section of the MSS prototype collimator by scanning a planar phantom.

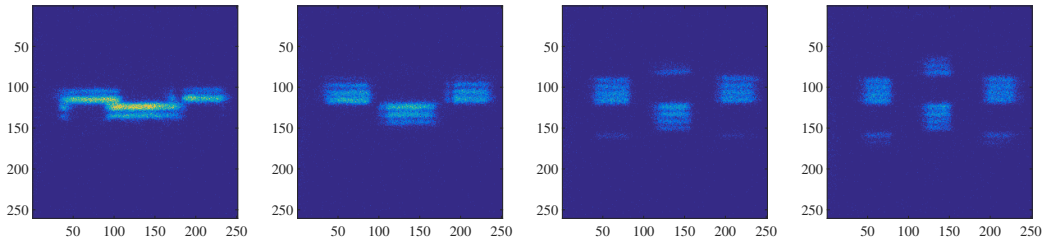

Figure 8.12: Planar projection data of the horizontal line source phantom acquired at four increasing distances from the detector (left to right).

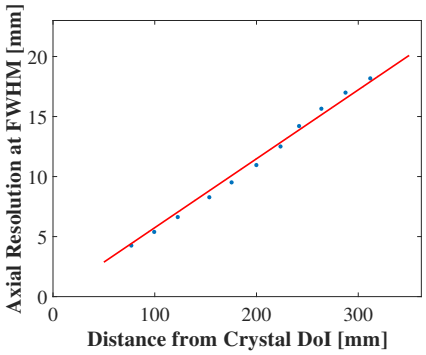

Figure 8.13: Axial resolution determined from the acquisition with the horizontal line source phantom as a function of the source distance to the crystal DOI. The red line indicates the linear fit of the resolution estimates.

with the plot of the estimated axial resolution for each performed scan. Transaxially, it is possible to observe the effect of the different magnification factors of the mini-slit apertures with distance.

Finally, Figure 8.14 compares the measured projection data with the analytically calculated data, as a result of the optimisation procedure to compute the last transaxial calibration parameters from the vertical line source acquisitions. These images indicate a good agreement between the two projections.

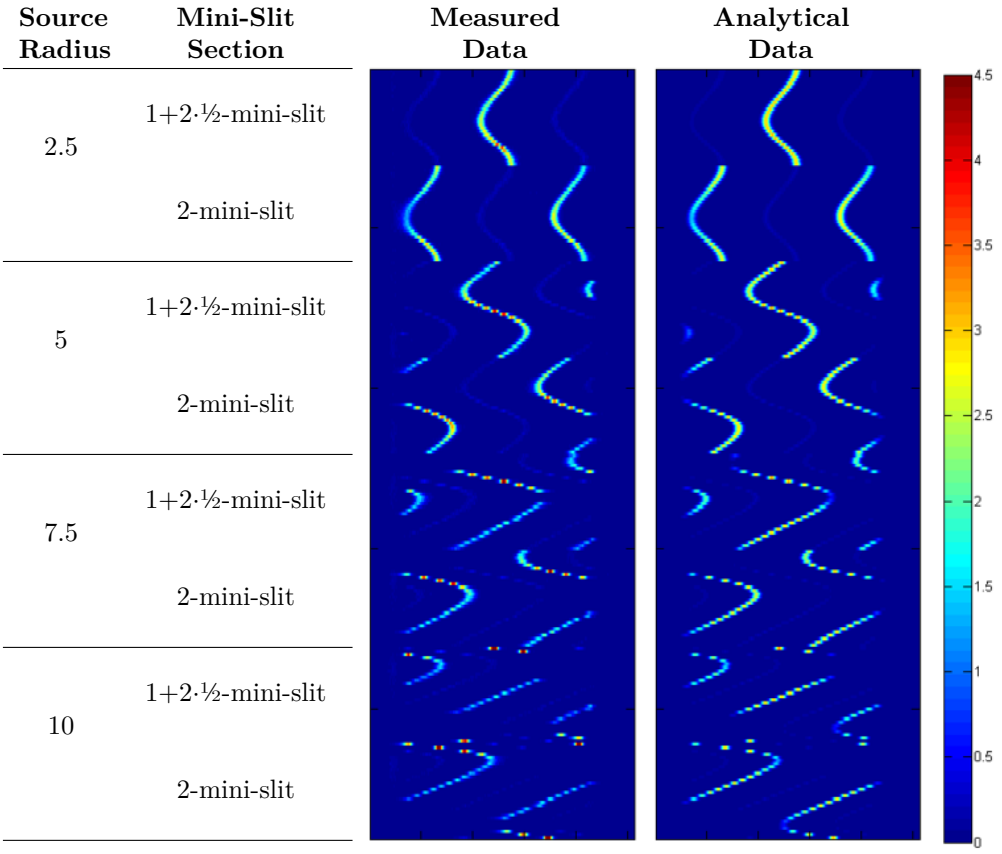

Figure 8.14: Projection data measured with the vertical line source phantom and corresponding analytically calculated projection data, for the four line sources positioned at different radius from the centre of rotation.

8.3.3 Discussion

Results obtained for each calibration phantom showed that geometrical calibration parameters can be estimated from the acquired projection data, to calibrate the MSS prototype collimator. Ultimately, these parameters need to be integrated in the reconstruction algorithm to be able to reconstruct data from tomographic acquisitions of different phantoms. In the next chapter, this framework will be applied to calibrate the prototype system and reconstruct tomographic data.

Analysing the scanning times, it suggests that calibration data can be acquired within seven hours. In practice, due to the different set-ups for each calibration phantom, this procedure takes about two days to complete. Taking into consideration that the final INSERT system has 20 detectors, calibration will take considerably longer than for the prototype system. However, some of the measurements, such as the acquisitions with the line sources, can be performed in simultaneous for all detectors, reducing the calibration time.

Furthermore, the use of a rotating platform is essential in order to obtain different views of the calibration phantom, since the system is stationary. Therefore, the final INSERT

system cover had to be adapted to accommodate the installation of a rotating stage. This requires that calibration is performed outside the MR room.

8.4 Conclusion

The main objective in this chapter was to develop a framework for the geometrical calibration of the INSERT prototype system.

First, as there is minification of the projection data for this system, the impact of the magnification factor in the calibration procedure was investigated. Results indicate that minification, as opposed to magnification, limits the precision of the estimated parameters in a model-based geometric calibration. This study also provided the implementation of tools that were then refined for the calibration of the prototype system.

Second, a practical framework for the calibration of the MSS prototype collimator was developed based on the estimation of geometrical parameters from four separate main measurements. This method takes advantage of the independent types of collimation along the transaxial and axial directions of the prototype collimator.

Finally, this calibration procedure can be easily adapted for the final INSERT system, as the calibration phantoms are the same and the estimated parameters are integrated in the reconstruction process.

Chapter 9

Experimental Evaluation of the Prototype INSERT System

This chapter presents the first results of planar and tomographic experiments with a single prototype detector and two different prototype collimators, comparing their experimental performance.

9.1 Introduction

Experimental validation of the design features of the INSERT system is an essential step in determining the clinical utility of the developed system. In the absence of the final INSERT system, a prototype camera can provide evidence of the achievable system performance and clinical applicability.

The main objective is to perform phantom experiments with a prototype detector equipped with the MSS prototype collimator to confirm the design concept, calibration procedure and reconstruction algorithm.

This chapter is divided into three main topics: detector evaluation, collimator design comparison and tomographic performance.

First, the prototype detector is characterised in order to evaluate clinical capability of the camera, e.g. regarding multi-radionuclide imaging.

Second, physical performance of the MSS prototype collimator is estimated, and contrasted with that of the 8+4·½-pinhole prototype collimator to verify the chosen design options for the final INSERT system.

Finally, tomographic phantom experiments are performed and analysed to provide preliminary evidence of tomographic performance and realistic imaging capability.

9.2 Detector Performance Evaluation

In this section, the goal is to evaluate the performance of the INSERT prototype detector. The main properties that will be tested are uniformity, linearity, count rate and energy resolution. These features are important due to their impact on the system performance.

9.2.1 Methods

The majority of the measurements were performed without collimator, unless indicated otherwise, and with the 5×5 cm prototype detector. The set-up for the single-detector prototype system and related software have already been introduced in Chapter 7.

Every measurement was performed with an applied high voltage of 35.4 V, and after temperature stabilisation of the recirculating cooler at -5 ^{o}C. Acquired data were processed into planar projections, before assessment of the aforementioned properties.

9.2.1.1 Uniformity

In order to obtain uniform planar projection data, parameters of the ML event-reconstruction algorithm were tested for a uniform flood acquisition with a small source at 50 cm distance. The source of activity was a syringe with 1 MBq of ^{99m}Tc.

Acquired data were processed into planar projections for different values of the change parameter η=[0.06,0.05,0.04,0.03]. This parameter evaluates the difference between the planar images at the present and previous iteration, and acts as a stopping condition during the event data processing.

9.2.1.2 Linearity

As regards the detector linearity, the correction method developed in Chapter 7 was validated against the following experiment. With the help of a manual linear positioning stage – precision of 0.5 mm per rotation, a point source was scanned every 2 mm along the central axis of the detector, in the x and y directions, from 0 to 50 mm.

The geometry of the source was obtained collimating a capillary tube filled with ^{99m}Tc by positioning it on top of one of the apertures of the prototype 8+4·½-pinhole collimator, as shown in Figure 9.1.

For the x direction, each scan lasted 120 seconds and the activity was 10.4 MBq; for the y direction, 180 seconds and 3.7 MBq, respectively.

Acquired data were corrected with the linearity transformation matrix obtained previously. The position of the source at each scan was estimated as the centre of mass of the activity distribution in the planar projection data. Then the estimated source positions were compared against the true position of the measurement, by applying a linear fit to the data.

(a) (b)

Figure 9.1: Experimental set-up for the testing of the linearity correction. The collimated point source is attached to a manual linear stage that moves the source along the x (a) and y (b) directions of the detector's central axis.

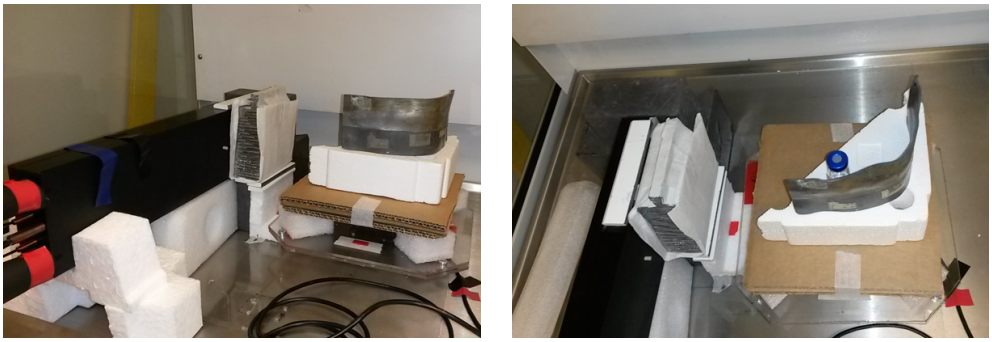

Figure 9.2: Acquisition set-up for the decaying source experiment: side view (left) and top view (right). The source corresponds to the blue vial.

9.2.1.3 Count Rate

This was evaluated by scanning a decaying source. The apparatus is shown in Figure 9.2. A 20 ml-vial filled with 115.8 MBq of ^{99m}Tc was positioned in front of the detector and data were acquired for intervals of 60 seconds in a total span of 32 hours.

Acquired data were processed into projections and the total counts were estimated for the photopeak window, for each acquired scan.

Assuming that for low count rates the observed count rate of the detector is the same as its true count rate, the latter was estimated. Given the true and observed count rates, data were fitted to both a paralyzable and non-paralyzable count rate model. Finally, dead time was estimated from the best fitted model and the photopeak count rate for the final INSERT system was extrapolated assuming that a 20 % loss is acceptable.

9.2.1.4 Energy Resolution

Assessment of the energy resolution of the prototype detector was performed through the scanning of five different radionuclides: ^{99m}Tc, ^{57}Co, ^{75}Se, ^{177}Lu and ^{111}In. For each scan, data were acquired from a small source with low activity, positioned at around 50 cm from the detector, without any shielding or collimator (Figure 9.3). A blank scan was also

Figure 9.3: Example of one acquisition set-up for the evaluation of the detector's energy resolution.

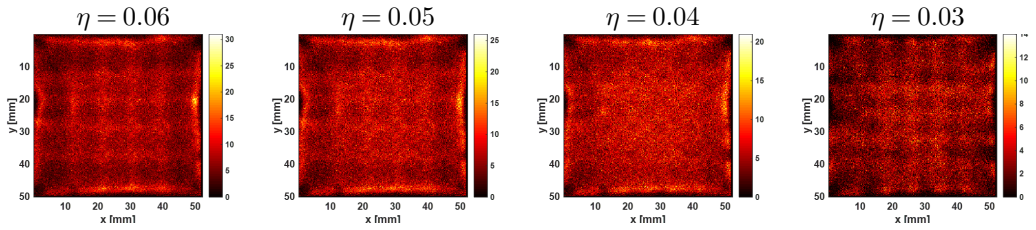

Figure 9.4: Planar projection data obtained for an event reconstruction with different values of the parameter η for the same acquired data.

performed with and without the MSS prototype collimator in front of the detector to check for background noise, and its impact in the acquisitions. For all experiments, data were acquired for 10 minutes and the data rate in the acquisition interface was maintained between 104 and 208 kBit.s^{-1}.

The energy spectrum was obtained for each scanned radionuclide and background scans. These spectra are given as a function of the detector's cumulative channel signal, instead of energy.

For each scan, the spectrum was blurred with a Gaussian function with a sigma proportional to the square root of the photopeak energy, and each photopeak was fitted to a Gaussian function in order to estimate peak location and FWHM. The energy-channel calibration curve for this detector was then derived. With the calibration curve in place, the energy spectrum for each experiment was analysed.

In addition, energy resolution was calculated as the ratio between the estimated FWHM and the photopeak energy.

9.2.2 Results

Figure 9.4 shows the planar projection data for the same experiment – uniform irradiation of the detector with a point source, but processed with different values of the parameter η. The image is more uniform for smaller values of η, whilst for higher values, more events are positioned in the centre of the read out channel. However, for η=0.03, uniformity is degraded.

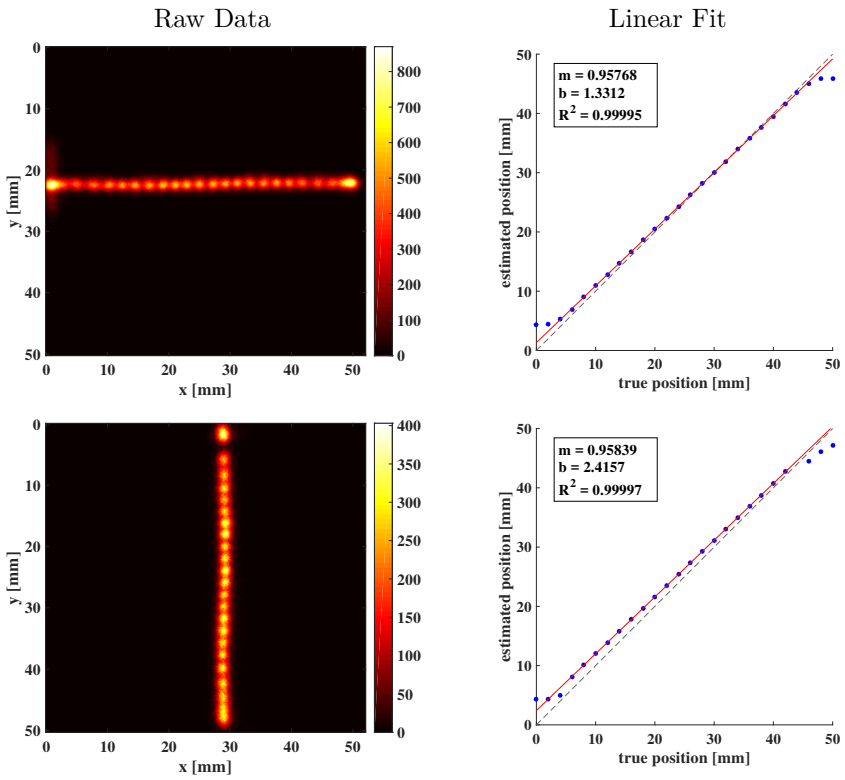

Figure 9.5: Planar projection data for all acquired positions along the x and y directions of the detector plane (left column). Linear fit of the centroid position of each point source projection (right column). The dashed line corresponds to the identity line.

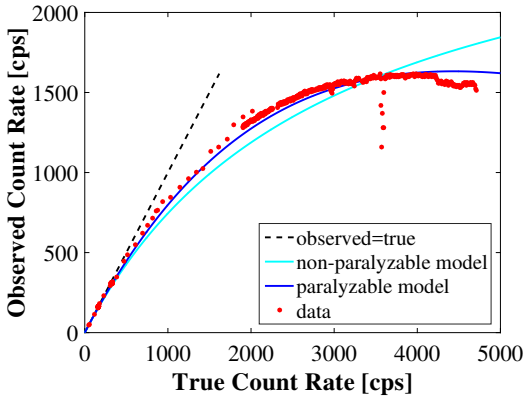

Figure 9.6: Observed count rate from the acquisition with a decaying source. The black and blue curves correspond to a paralyzable and non-paralyzable model fit, respectively.

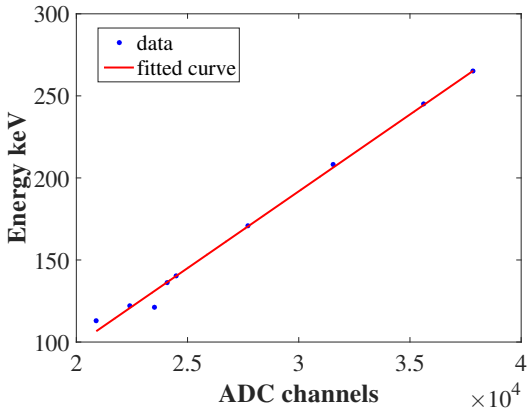

Figure 9.7: Energy-channel calibration curve obtained by fitting the photopeaks of the energy spectrum acquired with different radionuclides.

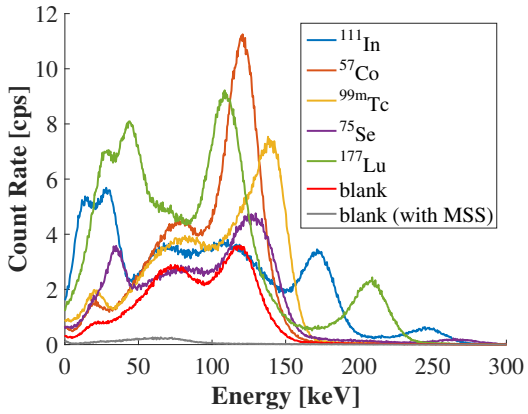

Figure 9.8: Energy spectra obtained for five different radionuclides. The energy spectrum for two blank scans is also shown, with and without the collimator in place.

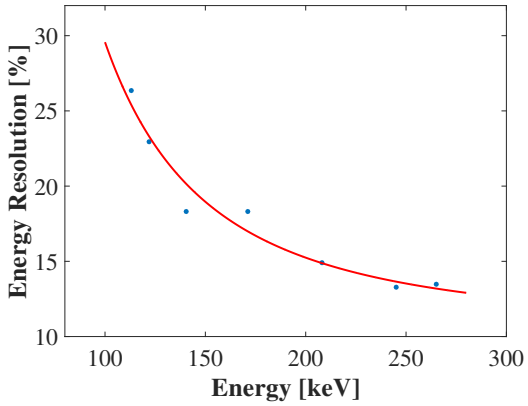

Figure 9.9: Estimated energy resolution as a function of the photopeak energy. The red line indicates the trend of all the estimates.

Regarding the linearity experiments, Figure 9.5 shows the summed planar projection data for all the scans along the x and y directions of the detector plane. For the y direction, there is a data gap at 4 mm due to a missing measurement. The corresponding point source estimated positions are also shown in the adjacent plot. Each plot shows a high linear relationship between the true and estimated point source positions for a central area of 40×40 mm. Outside this area, however, there is a high bias. In addition, analysing the linear fit, the experimental pixel size can be estimated multiplying the theoretical pixel size, 0.2 mm, by the slope of the linear fit. Thus the real pixel size is 0.19 for both x and y directions.

Figure 9.6 shows the calculated count rate at different time points for a decaying source, as a function of the true count rate of the detector. At a rate of 4 kcps, the observed count rate was lower than expected, suggesting a problem with the detector. Later time points indicate this was a non-persistent problem. Assuming a 20 % loss, the detector's count rate is 990 cps.

Furthermore the plot of Figure 9.6 also shows the data fit for a paralyzable and non-paralyzable count rate model. The best fit is for a paralyzable model with a dead time of 2.3×10^{-4} s.

Figure 9.7 shows the energy-channel calibration curve obtained from the scans with different radionuclides. The coefficient of determination is very close to 1, demonstrating a good fit between the cumulative channel signal and the energy, i.e. good energy linearity.

Utilising the energy-channel calibration curve, Figure 9.8 shows the energy spectra for all the scanned radionuclides. Most photopeaks are easily identified: 113 and 208 keV for ^{177}Lu, 122 keV for ^{57}Co, 140.5 keV for ^{99m}Tc, and 171 and 245 keV for ^{111}In. For ^{75}Se, there is a big peak at around 130 keV, which corresponds to the two lower photopeaks at 121 and 136 keV, a very small peak corresponding to the 265 keV photopeak, and the remaining photopeaks are not visible. Comparing the two blank acquisitions, there is a very low observable count rate when the MSS collimator is in place.

Finally Figure 9.9 shows the relationship between energy and energy resolution. At 140.5 keV, the energy resolution of the prototype detector is 18.31 %. Energy resolution improves as the energy of the photopeak increases.

9.2.3 Discussion

Regarding the detector uniformity, results suggest that η=0.04 is optimal for measurements with ^{99m}Tc. However, event-positioning is dependent on the gamma photon's energy, therefore the impact of this parameter for other radionuclides should be further investigated.

For the linearity measurements, there is a high bias outside the central projected area of the detector. This is an expected result, as the linearity correction matrix was only

determined for that same area, which also corresponds to the usable detector FOV.

In regards to the count rate, extrapolating the estimated photopeak count rate for the final INSERT system with 20 detectors, a figure of 40,000 cps is obtained at a 20 % loss.

In the case of the experiments to evaluate energy resolution, channel-to-energy calibration was achieved, allowing for the visualisation and analysis of the energy spectra. These suggest that at low energies, e.g. below 50 keV, there is event pile-up due to noise or high background activity. At high energies, such as for the high-energy photopeaks of ^{75}Se, there is detection efficiency loss, thus these peaks are not visible. Spectra for the blank acquisitions demonstrate that the background is negligible when acquiring data with the MSS collimator.

The calculated energy resolution, around 20 % at 140 keV, is worse than expected, which might impact the capability of system to perform dual-radionuclide imaging. For example, the two low-energy photopeaks of ^{75}Se were indistinguishable due to the detector's insufficient energy resolution.

The final INSERT system will have improved detector technology in comparison to the prototype detector utilised for these experiments. Clinical detectors have better excess noise factor and dark count rate, which impacts the detector's best achievable energy resolution and noise. Therefore overall performance is expected to improve.

9.3 Collimator Performance Comparison

In Chapter 5, the prototype designs for the 8+4·½-pinhole and MSS collimators were introduced, assuming an INSERT system geometry with 25 detectors distributed in a complete ring. These collimators were manufactured by NUCFI.

The objective in this section is to compare the achievable experimental performance of the INSERT system, utilising the 5×5 cm prototype detector equipped with both prototype collimators.

9.3.1 Methods

In the case of the prototype MSS collimator, data were acquired from vertical line sources, i.e. capillary tubes filled with ^{99m}Tc activity, positioned at different radial distances from the centre of rotation, namely 25, 50, 75 and 100 mm, at intervals of 90 ^{o}. For the prototype 8+4·½-pinhole collimator, data were acquired from ^{99m}Tc point sources, placed in the same positions inside the FOV as for the previous experiment. The general set-up for both acquisitions is summarised in Figure 9.10.

In addition, a tomographic acquisition of a cylinder phantom of diameter 184 mm was performed utilising the rotating stage to rotate the phantom for 25 views equally distributed over the 360^{o}. The phantom was filled with ^{99m}Tc up to a height of 20 mm, to ensure the imaging object was within the axial detector FOV. Data were acquired with the MSS and

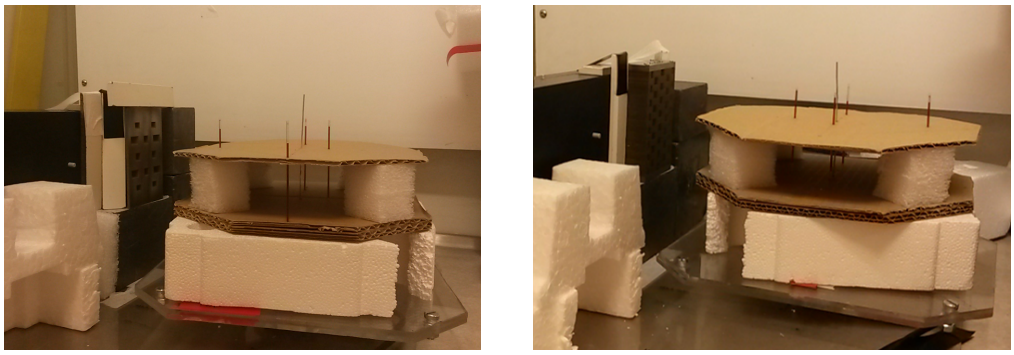

(a) (b)

Figure 9.10: Experimental set-up for the acquisition of the point source phantom with the detector prototype equipped with the 8+4·½-pinhole collimator (a) and the line source phantom with the MSS collimator (b).

the 8+4·½-pinhole prototype collimators (Figure 9.11).

Acquired data were energy windowed for the ^{99m}Tc photopeak and processed into planar projections.

Point and line source projection data were analysed to calculate resolution in the projection space, for both collimator designs. Resolution was estimated as the FWHM of the summed projections in the x and y of the transaxial plane. Point/line sensitivity was also estimated from these data, as the total detected counts divided by the activity and scanning time.

Cylinder phantom projection data were utilised to calculate volume sensitivity of both collimators, for the same source of activity. Projection data were decay–, scatter– and attenuation–corrected. For the scatter correction, acquired data were processed into planar projections for an energy window of 100-110 keV, scaled according to the scatter and photopeak energy windows, divided by two, and finally subtracted from the photopeak planar projection data (Hutton et al., 2011; Jaszczak et al., 1984). For the attenuation correction, a cylindrical phantom was forward-projected with and without attenuation, assuming an attenuation factor of 0.15 cm^{-1}. The ratio between the total number of counts obtained with and without attenuation was utilised as the mean attenuation factor for the attenuation correction. After all corrections, sensitivity was calculated as the total detected counts divided by the activity and the scanning time.

9.3.2 Results

Figure 9.12 shows the estimated resolution for point/line sources at four positions within the FOV. Note that the prototype detector is positioned at [-215, 0] mm. Resolution varies from approximately 7 to 16 mm for the MSS collimator, and from 9 to 15 mm for the 8+4·½-pinhole collimator.

In regards to sensitivity, point/line source sensitivity estimates are shown in Figure 9.13.

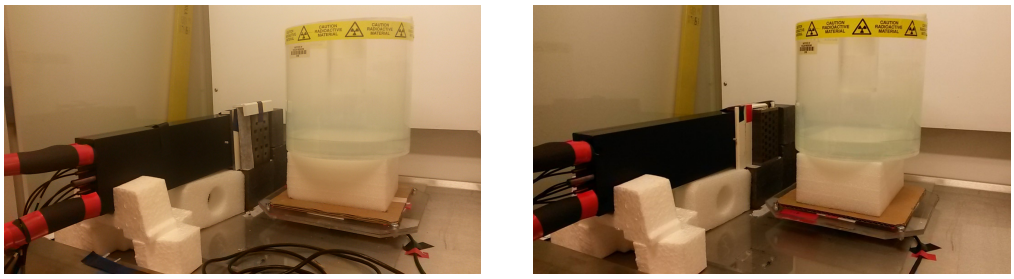

(a) (b)

Figure 9.11: Experimental set-up for the tomographic acquisition of the uniform cylindrical phantom with the detector prototype equipped with the 8+4·½-pinhole (a) and the MSS (b) prototype collimators.

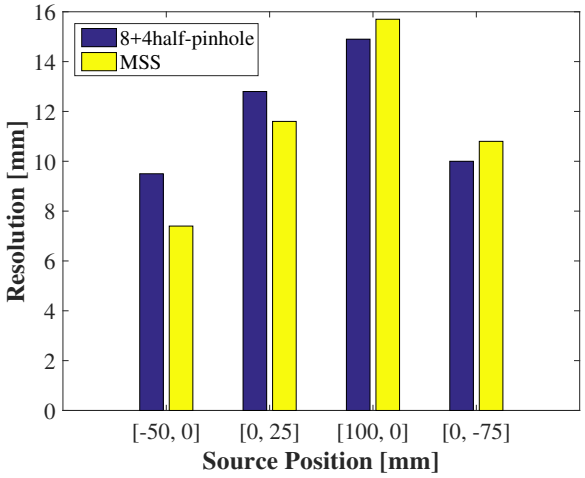

Figure 9.12: Estimated resolution from the point/line source planar projections, for both prototype collimators.

These estimates range from 2×10^{-6} to 3×10^{-6} $s^{-1}Bq^{-1}$ for the experiments with the 8+4·½-pinhole collimator and from 3.5×10^{-6} to 6×10^{-6} for the MSS collimator. For the experiments with the cylindrical phantom, the calculated volume sensitivity figures are 1.45×10^{-6} and 7.11×10^{-6} $s^{-1}Bq^{-1}$, for the 8+4·½-pinhole and MSS prototype collimators, respectively.

9.3.3 Discussion

Regarding the resolution results, both collimators achieve similar resolution at the four tested positions. As the calibration and reconstruction procedures were not optimised for the 8+4·½-pinhole geometry, this evaluation had to be carried out in the projection space.

For the point and volume sensitivity estimates, the MSS collimator achieves higher sensitivity in comparison to the 8+4·½-pinhole collimator, as expected.

Using the sensitivity result for the experiment with the MSS prototype collimator and the uniform phantom, the sensitivity for the final INSERT system can be extrapolated. Since the final system consists of 20 detectors, the sensitivity should be approximately twenty times

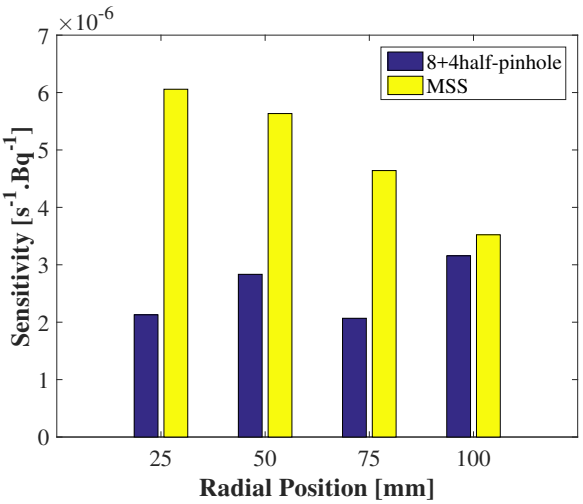

Figure 9.13: Estimated point sensitivity from the point/line source planar projections, for both prototype collimators.

higher, i.e. 1.42×10^{-4} $s^{-1}Bq^{-1}$. This sensitivity figure is close to the one estimated from the GATE simulations, but lower than the analytical one. Given these results, sensitivity measurements should be confirmed with more experiments to assess the source of error.

These results also suggest that the MSS design provides higher sensitivity than the 8+4·½-pinhole, at a similar level of achievable resolution.

9.4 Evidence of Tomographic Performance

This section will focus on the single-detector system equipped just with the prototype MSS collimator.

Experimental validation of the INSERT prototype system will be performed with the purpose of investigating its tomographic performance.

9.4.1 Methods

Experiments were performed with the 5×5 cm prototype detector equipped with the prototype MSS collimator for a set of imaging phantoms: line source phantom, uniform phantom, sphere phantom, Hoffman brain phantom and Alderson brain phantom. The specific set-up for each phantom is given in the following subsections.

The general experimental and software set-up were already described in detail in Chapter 7. A high voltage of 35.4 V was applied to the SiPMs, and the temperature in the recirculating cooler was set to -5 ^{o}C. Shielding was positioned around the prototype MSS collimator to shield the crystal from spurious gammas. Finally, the phantom was positioned in the centre of the rotating platform, at 215 mm from the back of the crystal. This allowed for the simulation of a tomographic acquisition from a 25-detector full-ring system, but using a single detector. Therefore each experiment took several hours to acquire to compensate for

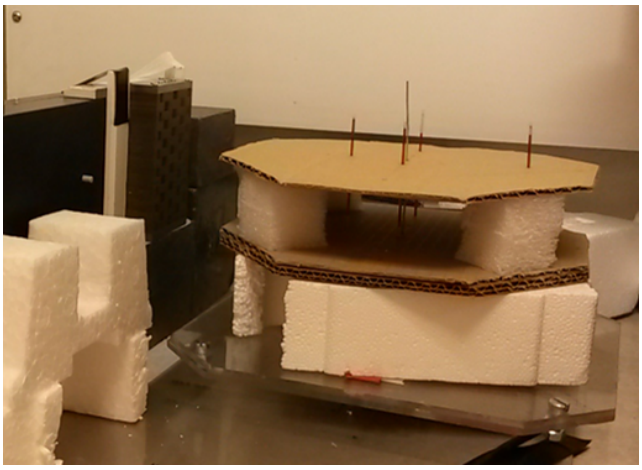

Figure 9.14: Experimental set-up for the tomographic acquisition of the line source phantom with the detector prototype equipped with the MSS collimator.

the low sensitivity.

Prior to the scanning of each phantom, geometrical calibration was performed as described in Chapter 8, using a planar and a vertical/horizontal line source phantoms to determine the calibration parameters.

Acquired data were windowed for the corresponding photopeak energies, processed into planar projections, decay-corrected and finally reconstructed with 40 iterations of MAP-EM with a 3 mm Gaussian smoothing prior. Images were then analysed for different features of tomographic relevance.

9.4.1.1 Line Source Phantom Experiment

The line source phantom consisted of a platform with four fillable capillary tubes positioned vertically at four radial distances from the centre of the FOV (Figure 9.14).

Each capillary was filled with ^{99m}Tc and acquired for 30 views equally distributed over 360^o. Note these data were also utilised for the transaxial calibration of the collimator, therefore more views were acquired.

Reconstruction was performed for 10, 20, 30, 40 and 50 iterations, and the resolution was estimated from the reconstructed images.

9.4.1.2 Uniform Phantom Experiment

The uniform phantom consisted of an acrylic cylinder with a diameter of 184 mm.

The phantom was filled with 69.1 MBq of ^{99m}Tc distributed over a height of 20 mm. Acquisition was performed after positioning the phantom in the centre of the rotating platform, in alignment with the detector (Figure 9.15).

Coefficient of variation (CoV) was calculated from the reconstructed images, for circles of different radii from the centre of the phantom, to assess uniformity.

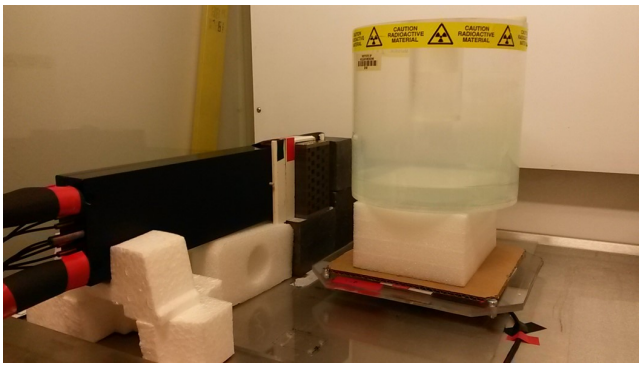

Figure 9.15: Experimental set-up for the tomographic acquisition of the uniform cylindrical phantom with the detector prototype equipped with the MSS collimator.

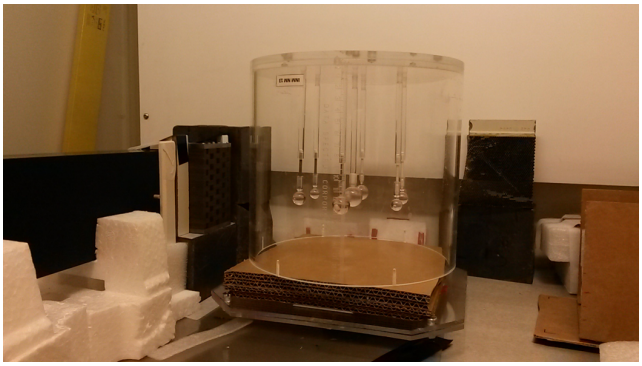

Figure 9.16: Experimental set-up for the tomographic acquisition of the spheres phantom with the detector prototype equipped with the MSS collimator.

9.4.1.3 Spheres Phantom Experiment

The spheres phantom consisted of seven fillable spheres in air with different sizes: two sets of spheres with external diameters of 17, 14 and 11 mm, and one sphere with a diameter of 21 mm.

Each set was filled with a relative ^{99m}Tc activity concentration of 2, 1 and 0.5, respectively. Acquisition was performed after alignment of the phantom in the centre of the FOV and the spheres in the centre of the detector FOV (Figure 9.16).

Activity distribution was evaluated from the reconstructed images, to verify the relative activity concentrations in the spheres.

9.4.1.4 Hoffman Brain Phantom Experiment

The Hoffman brain phantom consisted of a cylindrical phantom with a series of independent plates that, when stacked together, represent the 3D anatomy of the human brain. The activity distribution within the brain is accurately simulated with relative activity concentrations of 3, 1 and 0 for grey matter, white matter and cerebrospinal fluid, respectively.

This phantom was filled with ^{99m}Tc, positioned in the rotating platform and scanned (Figure 9.17).

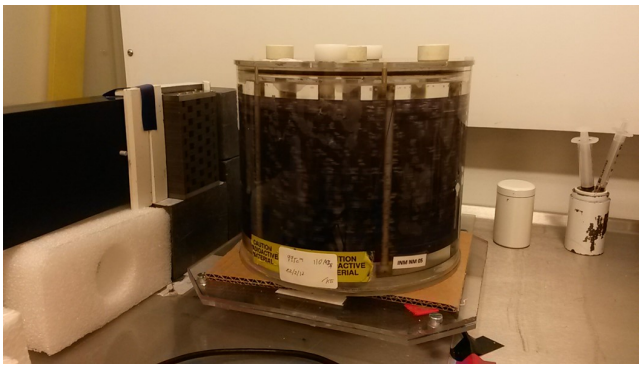

Figure 9.17: Experimental set-up for the tomographic acquisition of the Hoffman brain phantom with the detector prototype equipped with the MSS collimator.

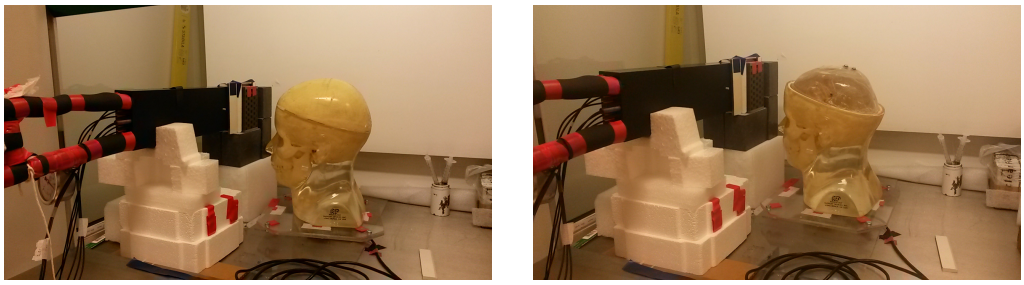

Figure 9.18: Experimental set-up for the tomographic acquisition of the Alderson brain phantom with the detector prototype equipped with the MSS collimator. On the right, detail of the fillable brain compartment.

Realistic activity distribution was visually assessed from the reconstructed images.

9.4.1.5 Alderson Brain Phantom Experiment

The Alderson brain phantom consisted of a perspex head, bone-equivalent skull and a brain with five fillable compartments: right and left nucleus caudate, right and left putamen, and the rest of the brain. The nucleus caudate and the putamen constitute the dorsal striatum. This is a fully tissue-equivalent anthropomorphic phantom of the human striatum and head.

Although striatal imaging has special clinical relevance for brain dysfunctions, it was utilised here to simulate tumour imaging, each small compartment representing a tumour. Each striatal compartment was filled with ^{123}I with an activity concentration ratio relative to the background, i.e. brain compartment, of 4.5, except for the left putamen compartment, which had a ratio of 2.2. Scanning of the phantom was performed after alignment of the striatum with the detector FOV (Figure 9.18).

Activity concentration ratios were estimated from the reconstructed images for each compartment of the striatum in relation to the background, and compared to the true ratios.

9.4.2 Results

Figure 9.19 shows the reconstructed image for the tomographic acquisition of the line source phantom. Analysing the transaxial plane, Figure 9.20 shows the estimated resolution as the

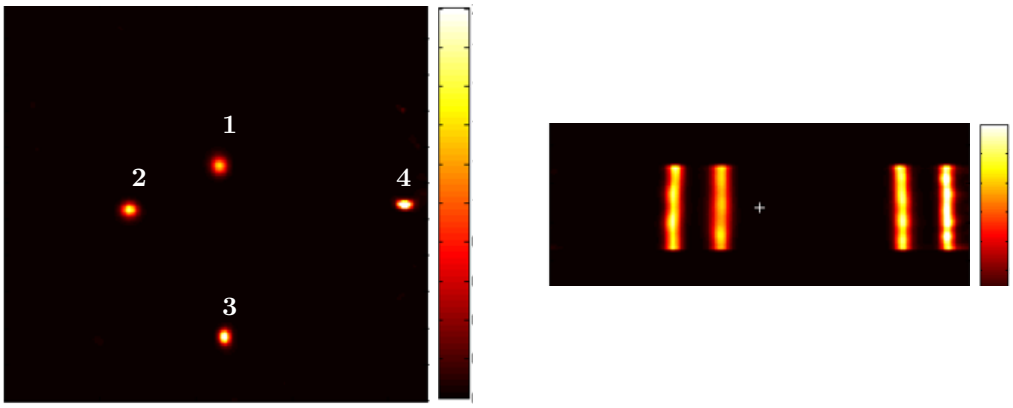

(a) (b)

Figure 9.19: Reconstructed image of the tomographic acquisition with the line source phantom: transaxial (a) and axial (b) views.

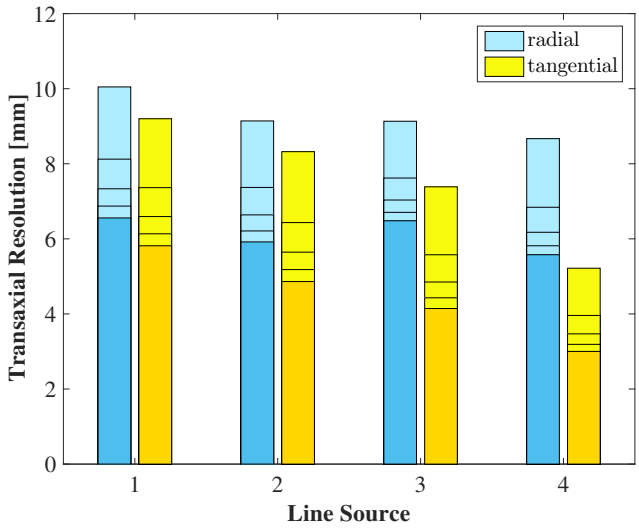

Figure 9.20: Estimated resolution for the radial and tangential directions of the transaxial plane of the line source reconstructed images, with increasing distance from the centre. The variability in each plotted bar represents a reconstruction with a different number of iterations from 10 to 50. The darker coloured bars correspond to 50 iterations.

FWHM in the radial and tangential summed profiles for each source.

Figure 9.21 shows the reconstructed image for the tomographic acquisition of the cylindrical uniform phantom. In order to evaluate uniformity of the reconstructed image, Figure 9.22 shows the calculated CoV for a circle centred in the centre of the detector FOV with varying radii.

For the tomographic acquisition of the spheres phantom, Figure 9.23 shows the corresponding reconstructed image. For each sphere, Figure 9.24 shows the activity concentration estimated from the reconstructed data. Spheres 1 to 3 have values close to 6; spheres 4 to 6, close to 3; and sphere 7, close to 1.5.

For the tomographic acquisition of the Hoffman brain phantom, Figure 9.25 shows the

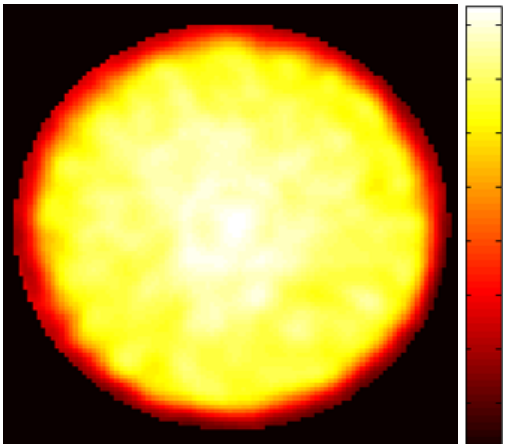

Figure 9.21: Reconstructed image of the tomographic acquisition with the uniform phantom.

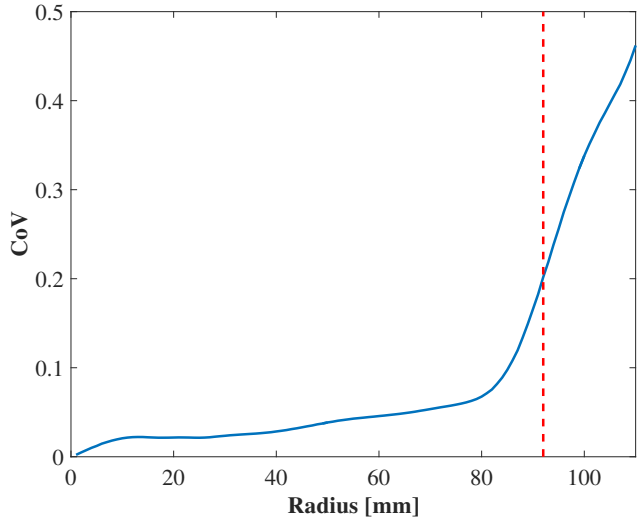

Figure 9.22: CoV calculated from the reconstructed images of the uniform phantom, for a circle region aligned with the centre of the FOV with increasing radius. The dashed line corresponds to the phantom radius.

corresponding reconstructed images. These images show some ring artefacts. However, the activity distribution in the brain is similar to that obtained with a standard SPECT.

Finally, Figure 9.26 shows the reconstructed images for the tomographic acquisition of the Alderson brain phantom. The estimated compartment-to-background activity concentration ratios are shown in Figure 9.27.

9.4.3 Discussion

Analysing the results for the experiments with the line source phantom, resolution improves with a higher number of iterations, but even for the lowest number of iterations utilised, the estimated resolutions are better than the target resolution of 10 mm at the centre of the FOV. As expected from the simulation work, resolution in the radial direction varies less than the one in the tangential direction, as the distance from the centre of the FOV

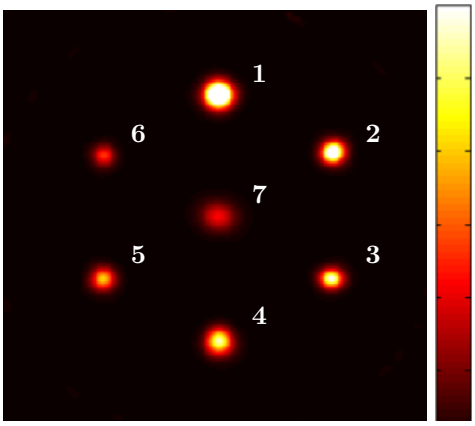

Figure 9.23: Reconstructed image of the tomographic acquisition with the spheres phantom. Spheres 1 to 7 have diameters 17, 14, 11, 17, 14, 11, 21 mm, respectively.

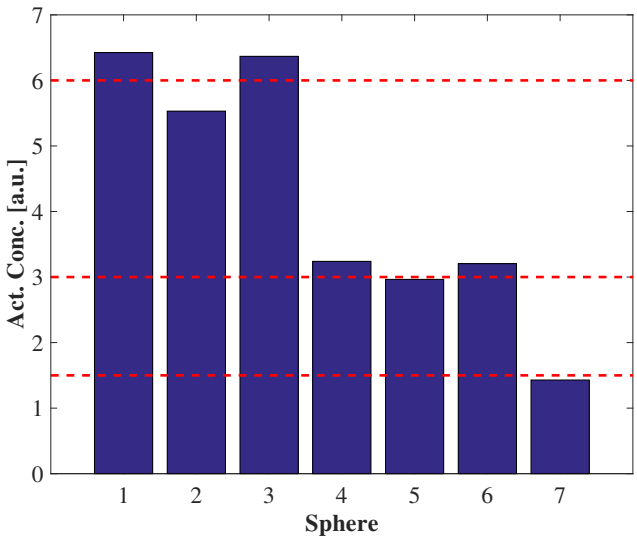

Figure 9.24: Activity concentration estimated from the reconstructed images, for each of the seven spheres. The dashed lines correspond to the true activity concentration: 1.5 for sphere 7, 3 for spheres 4 to 6, and 6 for spheres 1 to 3.

increases.

For the uniform phantom, the estimated CoV is relatively constant up to a radius of 85 mm, measured from the centre of the data. Uniformity then degrades at the edge of the FOV.

In the case of the spheres phantom experiment, each reconstructed sphere has a round shape and it is placed in the corresponding position. Quantification of the activity concentration for each sphere is in good agreement with the relative set activity concentrations.

Reconstructed images of the Hoffman brain phantom indicate the system's ability to image a realistic activity distribution. Note that the whole brain is not shown in the reconstructed images because it is larger than the detector's FOV in the axial direction. Although there are some ring artefacts present in the reconstructed images, these could be

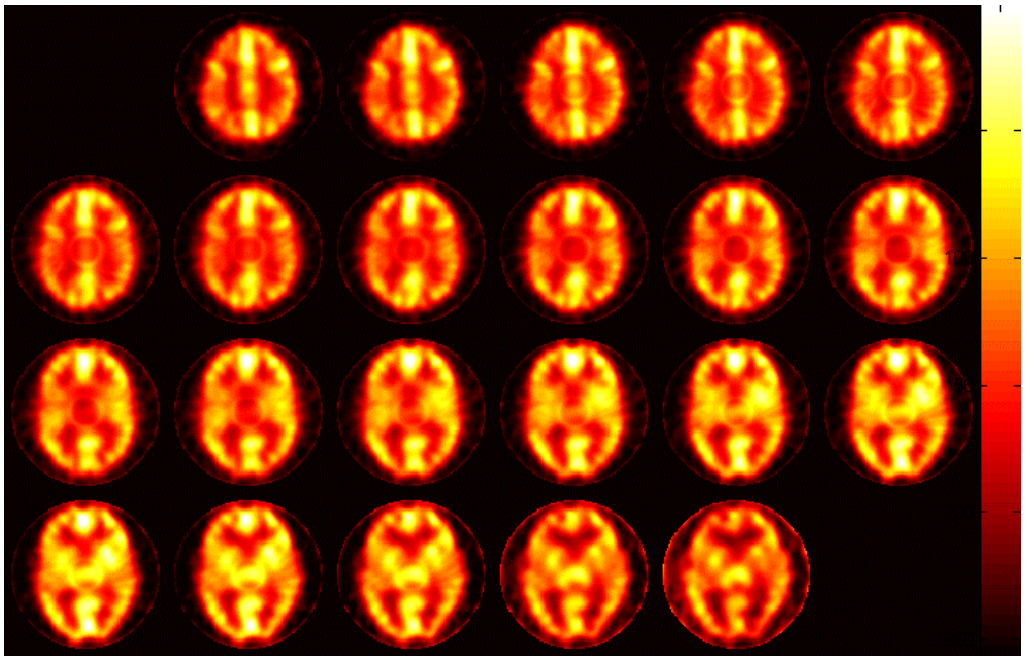

Figure 9.25: Reconstructed image of the tomographic acquisition with the Hoffman brain phantom.

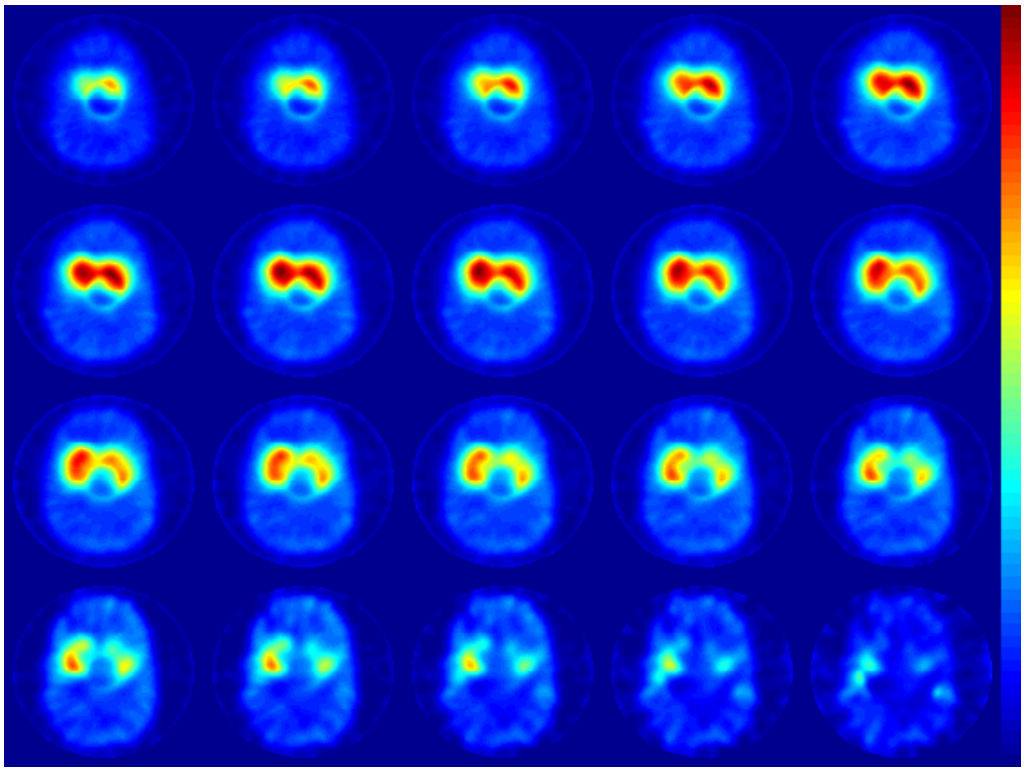

Figure 9.26: Reconstructed image of the tomographic acquisition with the Alderson brain phantom.

due to the fact the phantom is rotated. However, the final INSERT system is stationary, so the image quality could improve.

For the Alderson brain phantom experiment, the striatum is visible, as well as some ring

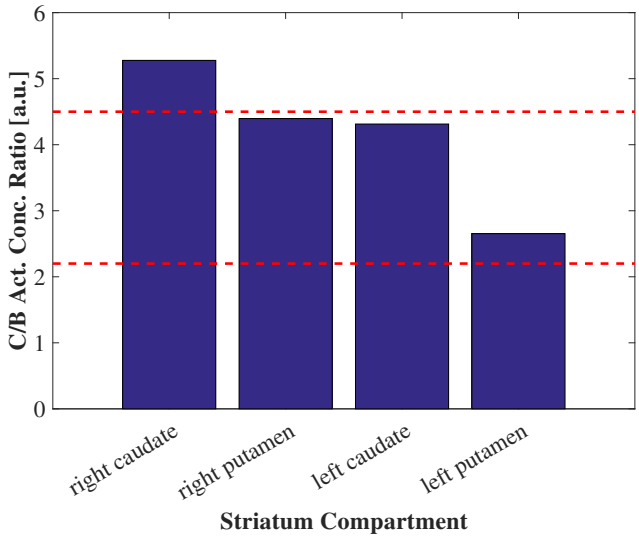

Figure 9.27: Compartment-to-Background (C/B) activity concentration ratio for the four striatal compartments in the Alderson brain phantom.

artefacts. The calculated compartment-to-background ratios correspond to the set activity concentrations. However, this correspondence is slightly worse for the right nucleus caudate and left putamen, as the outline of the regions is difficult. This is due to the poor resolution in the reconstructed images. Resolution could be improved including the detector's intrinsic resolution in the reconstruction process.

Moreover, these tomographic reconstructions also validate the calibration procedure devised in the previous chapter.

9.5 Conclusion

Experimental assessment of the prototype system was performed with a single-detector set-up, which has direct relevance to the final clinical INSERT system.

The prototype detector was evaluated for uniformity, linearity, count rate and energy resolution. Projection data show a good uniformity of the event-positioning, as well as a working linearity correction. The estimated photopeak count rate is 990 cps at a 20 % loss for the prototype detector, suggesting a count rate of around 40,000 cps for the final system. Energy resolution is close to 20 %, which is worse than expected, limiting the prototype camera ability to perform dual-radionuclide imaging. However, the clinical detectors have improved detector technology in comparison to the prototype detector, resulting in improved overall performance.

Regarding the performance comparison with the two prototype collimators, measurements of resolution and sensitivity indicate that the MSS collimator design achieves better sensitivity than the 8+4·½-pinhole collimator for similar resolution. Therefore further tomographic performance evaluation was performed with the prototype MSS collimator.

Reconstructed images of the phantom measurements confirm the calibration procedure and reconstruction algorithm. For the experiments with the line source and uniform phantom, reconstructed resolution is better than the target one and good uniformity is achieved, respectively. Measurements with the spheres and the Alderson brain phantoms provide evidence of correct quantification from the reconstructed images. In addition to the acquisition with the Hoffman brain phantom, these images show an activity distribution similar to that obtained with a standard SPECT system, with visible brain structures. Although ring artefacts are present, these are expected to improve for the final INSERT system.

In summary, these experiments validate the proposed collimator design concept and its improved performance.

Chapter 10

Conclusion

10.1 Summary of Main Conclusions

There has been an increasing interest in the development of multi-modality medical imaging systems, especially those providing simultaneous acquisitions. These systems have the potential to obtain different types of information within the setting of a single examination, towards a more comprehensive diagnostic and/or follow-up of the patient.

The main goal of this thesis was to design adequate collimation for a SPECT insert system, in order to perform simultaneous SPECT/MR imaging of the human brain, based on high-resolution detectors and prioritising high sensitivity over high spatial resolution.

In **Chapter 4**, collimator design issues for a SPECT insert were addressed, namely the restricted space in the MRI bore and the limited angular sampling.

Different types of multi-pinhole and multi-slit slit-slat collimators were designed according to initial expected detector performance, and analytically compared in terms of performance. Additionally new concepts of collimation and system design were proposed to improve angular sampling, such as the half-pinhole and half-slit, and the rotation of one detector ring in regards to the other for the case of multi-pinhole systems. The impact of the use of minimal DOI information during reconstruction was also investigated.

When comparing the multi-pinhole and multi-slit slit-slat collimators, the former gives better reconstructed uniformity and transaxial resolution, while the latter gives better axial resolution and sensitivity. Moreover, the use of DOI information has the potential to improve the reconstructed image quality. Regarding the individual collimator configurations, the 2×2-pinhole and 2-slit slit-slat designs achieve the highest sensitivity, but have the disadvantage of a sub-optimal utilisation of the detector area. With these collimator configurations, the central region of the FOV would be imaged by the edges of the detector, where the intrinsic resolution degrades. As a result, the 5+2·½-pinhole and 1+2·½-slit slit-slat collimator designs

are preferable.

In **Chapter 5**, the design considerations of the previous chapter were further explored and a new concept of collimation was proposed: the multi-mini-slit slit-slat (MSS) collimator. The mini-slit is a short section of the slit component, and therefore arrays of mini-slits can be used to cover the object FOV with one detector, in contrast to the normal continuous slit in a standard slit-slat collimator. In order to improve angular sampling, each mini-slit array is also misaligned with the adjacent one. Additionally, the mini-slit aperture is located within the slats, allowing these to extend beyond the slit plane. As the resolution is fixed in both transaxial and axial directions, the slat spacing can be increased, resulting in a sensitivity gain. So the main advantage is allowing minification without compromising the slat length and maximising the use of space to optimise sensitivity. Finally, this design includes the half-apertures introduced in the previous chapter. An equivalent multi-pinhole design was devised, the 8+4·½-pinhole collimator.

Three main topics of investigation were performed. First, the proposed designs were analytically compared to other multi-pinhole and multi-slit slit-slat colllimator designs. Second, single-module prototype tungsten collimators were designed, in order to develop manufacturing techniques, test MR-compatibility and perform measurements with a single prototype detector. Third, collimation and system geometry were refined for the final INSERT system, based on a partial detector ring. This new geometry was suggested to allow more space for the MR head coil and patient opening, and to relax the space constraints for the system's components in general.

For each type of collimation, the MSS and 8+4·½-pinhole collimators show the best performance in analytical simulations, with the MSS collimator achieving higher efficiency compared to the 8+4·½-pinhole collimator at the same resolution level. Hence, these collimators were re-designed as single-module prototype collimators. Due to the high efficiency, uniform axial coverage, high compactness, negligible interference with the MR operation, and easy manufacture, the MSS collimator was the selected design of choice for the final INSERT system. Finally, investigation on the effects of the partial ring geometry in the system performance showed that mainly transaxial resolution was reduced in the lower part of the FOV, where the detectors are missing, but axial resolution was not affected. As the main objective of the INSERT system is not lesion detection, but treatment follow-up, the tumour position is known and the patient's head can be positioned into the FOV accordingly. Hence the partial ring geometry is a good compromise in terms of patient comfort, space for the components, and system performance. Taking this into consideration, the MSS collimator design was finalised for production.

In **Chapter 6**, a framework for performing and analysing Monte Carlo simulations of the INSERT system was developed using GATE. This allowed for the flexible testing of

different system designs and geometries with realistic SPECT data.

With the framework in place, three investigations were performed. Firstly, the system design was evaluated comparing results from simulations with the 8+4·½-pinhole and MSS collimators, and with the complete and partial ring geometry. Secondly, the gamma shielding design was devised for the INSERT detector ring, considering possible interference due to the intrinsic activity of PET crystals from the PET/MR system and out-of-FOV activity. Finally, the final INSERT system design was simulated to assess performance.

When equipped with the MSS collimator, the INSERT system achieves similar estimated resolution as with the 8+4·½-pinhole collimator, but with higher sensitivity. In relation to the ring geometry, simulations for the partial ring configuration confirm degradation of resolution for the region of the detector gap, however this can be partly compensated during reconstruction as shown in the previous chapter. Results for simulations with different shielding designs suggest that a lead shielding configuration with thickness of 6 mm-front, 2 mm-end, 3 mm-back, and 5 mm-lateral is ideal for the INSERT system, compromising penetration and weight/space limitations. With the appropriate shielding in place, performance evaluation of the final INSERT system design shows a volume sensitivity of 1.3×10^{-4} $s^{-1}Bq^{-1}$ and a resolution in the projection space close to 10 mm.

In **Chapter 7**, practical considerations regarding the installation of the single-detector prototype INSERT system at UCL were addressed.

The main actions carried out were assembly, integration and testing. In order to set-up a platform for SPECT acquisitions, the detection module and corresponding electronics, recirculating cooler, laptop and rotating stage were assembled in the laboratory. The different software platforms were integrated, and the processing of the acquired data into projections refined with experimental data. Test experiments were performed to assess the functioning, interaction, and integration of the different components and software, and to utilise the prototype system independently.

In **Chapter 8**, the impact of projection data minification in the calibration procedure, as opposed to magnification, was investigated and a practical framework for the geometrical calibration of the INSERT prototype system was developed using the prototype system previously introduced.

Simulated and experimental data of single pinhole and slit-slat systems with different magnification factors indicate that minification limits the precision of the estimated parameters in a model-based geometric calibration. Adapting this model-based geometric calibration for the calibration of the prototype system, a practical framework for the calibration of the MSS prototype collimator was developed and implemented. This framework takes advantage of the independent types of collimation along the transaxial and axial directions of the MSS prototype collimator. Calibration is achieved performing a number of independent

measurements with calibration phantoms, in order to estimate geometrical parameters that fully model the geometry of the system.

In **Chapter 9**, experimental assessment of the prototype system was performed with planar and tomographic measurements. First, the prototype detector was evaluated for uniformity, linearity, count rate and energy resolution. Then, the 8+4·½-pinhole and MSS prototype collimators were compared in terms of experimental performance. Lastly, tomographic phantom experiments were performed to provide preliminary evidence of the prototype system's tomographic performance.

For the detector evaluation, projection data showed a good uniformity of the event-positioning, as well as a working linearity correction. The estimated photopeak count rate was 990 cps at a 20 % loss for the prototype detector, suggesting a count rate of around 40,000 cps for the final INSERT system. Energy resolution was close to 20 %, which is worse than expected, limiting the prototype camera ability to perform dual-radionuclide imaging. However, the clinical detectors will have improved detector technology in comparison to the prototype detector, resulting in improved overall performance. Regarding the performance comparison with the two prototype collimators, measurements of resolution and sensitivity indicate that the MSS collimator design achieves better sensitivity than the 8+4·½-pinhole collimator for similar resolution. For the tomographic experiments with the MSS prototype collimator, the reconstructed images confirm the calibration procedure and reconstruction algorithm. For the experiments with the line source and uniform phantom, reconstructed resolution is better than the target one and good uniformity is achieved, respectively. Measurements with the spheres and the Alderson brain phantoms provide evidence of correct quantification from the reconstructed images. In addition to the acquisition with the Hoffman brain phantom, these images show an activity distribution similar to that obtained with a standard SPECT system, with visible brain structures. Although ring artefacts are present, these artefacts are expected to improve for the final INSERT system. Finally, these experiments validate the proposed collimator design concept and its improved performance in relation to equivalent pinhole collimation.

Overall, whilst the resolution figures are consistent across the analytical, simulated and experimental estimations, there is a discrepancy for the sensitivity figures. Scaling the analytical sensitivity result to 20 detectors instead of 25 gives 2.24×10^{-4} $s^{-1}.Bq^{-1}$. For the GATE simulations, sensitivity was 1.31×10^{-4} $s^{-1}.Bq^{-1}$. For the tomographic experiment with a uniform phantom, sensitivity was 1.42×10^{-4} $s^{-1}.Bq^{-1}$. Given these results, sensitivity measurements should be confirmed with more experiments to assess the source of error.

In summary, this thesis describes the development of a clinical brain SPECT insert for simultaneous operation inside a commercially available MRI system. Based on small high-resolution detectors and novel multi-slit-slat collimation, the clinical system design has

direct contribution to the European-funded INSERT project. The final collimator design, the MSS collimator, provides a suitable compromise between compactness, limited angular sampling, performance and patient comfort. Experimental measurements with a prototype system demonstrate the applicability of the new collimation concept, confirming the trend of the analytical and simulation findings. Finally, the output of this work will influence future SPECT system designs and contribute to progress in the field of molecular imaging.

10.2 Suggested Future Work

In this thesis, a novel collimation and system design were proposed for the development of a clinical brain SPECT insert able to operate inside an MRI system, for simultaneous SPECT/MR imaging. Therefore, the main limitation of the work presented here is the absence of the final INSERT system for validation of the research findings.

It is expected that the final clinical INSERT system will be fully assembled soon after the submission of this thesis. By that point, the INSERT system will be a compact bench-top SPECT system, but still far from being ready to be utilised in a clinical environment. Therefore there is scope for further technical developments.

Considerations on the translation of the SPECT INSERT to clinical use and final system validation are addressed below as suggested future work.

Firstly, the performance of the INSERT system should be evaluated as a standalone SPECT system. This requires the refinement of the practical calibration procedures proposed in Chapter 8 and development of corresponding calibration phantoms for the final INSERT system, the development of standard quality control procedures that can be utilised for routine measurement, and the integration of associated software platforms for tomographic data acquisition, reconstruction and analysis. With these in place, phantom studies should be performed to determine system sensitivity, reconstructed spatial resolution, energy resolution, system count rate and reconstructed uniformity, as well as reproducibility of these results over time, in a similar fashion to the work presented in Chapter 9.

Secondly, the INSERT system's MR-compatibility should be verified with measurements of SPECT performance with and without simultaneous MRI operation. On the other hand, MRI performance should be verified in the working presence of the INSERT system and compared to MR-only measurements.

In order to ensure meaningful simultaneous SPECT/MR data, both systems need to have the same frame of reference, thus specific multi-modality quality control should be developed with spatial alignment techniques.

Along with documentation showing compliance with safety regulations for ethics approval of human studies, a number of technical developments should be arranged for the clinical operation of the INSERT system. These include the manufacturing of a support system

and a customised chair or bed for the use of the INSERT with patients, as a standalone SPECT. In the context of simultaneous SPECT/MR imaging, these developments include the manufacturing of a lifting system for installation of the INSERT system on the PET/MRI system, and a head rest for patient comfort. In addition, adaptation of the existing PET/MR bed should allow accurate manual positioning of the patient's head inside the INSERT system.

Finally, the INSERT system should undergo clinical verification, with the performance of patient studies using the INSERT system as a standalone SPECT and as a simultaneous SPECT/MR system. Clinical performance of the INSERT system should also be compared to conventional brain SPECT, and a feasibility study should be designed to evaluate the INSERT's ability to assess early response to treatment in brain tumour patients.

Other possible future work, in the context of multi-modality system development, relate to full system design integration for whole-body SPECT/MR imaging.

10.3 Original Contributions

The main contributions of this thesis to the INSERT project and the field of Nuclear Medicine imaging can be summarised as follows:

- Development of a simple analytical model for multi-slit-slat and pinhole collimator optimisation, that addresses the trade-off between system resolution and sensitivity, and the geometrical and angular sampling constraints of a stationary insert SPECT system.
- Proposal of a novel collimation design and determination of collimator parameters based on sensitivity maximisation for a fixed system resolution.
- Design of prototype collimators for experimental testing.
- Confirmation of the analytical findings and refinement of system design using Monte Carlo simulations.
- Development and implementation of a framework for experimental validation of the collimator design and development of practical calibration procedures.
- Assessment of the geometrical calibration of the collimator and development of a practical calibration procedure using a prototype system.
- Experimental comparison and validation of the proposed collimation.
- Contribution to the design of the world's first clinical SPECT/MRI system.

10.4 List of Published Papers and Presentations

10.4.1 Publications

D. Salvado, K. Erlandsson, A. Bousse, M. Occhipinti, P. Busca, C. Fiorini and B. F. Hutton, "Collimator Design for a Brain SPECT/MRI Insert", *IEEE Transactions on Nuclear Science*, vol. 62, no. 4, pp. 1716–24, 2015. DOI: 10.1109/TNS.2015.2450017.

B. F. Hutton, M. Occhipinti, A. Kuehne, D. Máthé, N. Kovács, H. Waiczies, K. Erlandsson, **D. Salvado**, M. Carminati, G. L. Montagnani, S. C. Short, L. Ottobrini, P. van Mullekom, C. Piemonte, T. Bukki, Z. Nyitrai, Z. Papp, K. Nagy, T. Niendorf, I. de Francesco and C. Fiorini, "Development of Clinical Simultaneous SPECT/MRI", *The British Journal of Radiology*, 90:20160690, pp. 1–13, 2017. DOI: 10.1259/bjr.20160690.

10.4.2 Published Proceedings

K. Erlandsson, **D. Salvado**, A. Bousse, and B. F. Hutton, "Design Optimization and Evaluation of a Human Brain SPECT-MRI Insert based on High-Resolution Detectors and Slit-Slat Collimators", *Nuclear Science Symposium and Medical Imaging Conference (NSS/MIC) 2013 IEEE*, pp. 1–4, 2013. DOI: 10.1109/NSSMIC.2013.6829144.

A. Bousse, K. Erlandsson, N. Fuin, **D. Salvado**, B. F. Hutton, "Variance Prediction in SPECT Reconstruction based on the Fisher Information using a Novel Angular Blurring Algorithm for Computation of the System Matrix", *Nuclear Science Symposium and Medical Imaging Conference (NSS/MIC) 2013 IEEE*, pp. 1–6, 2013. DOI: 10.1109/NSSMIC.2013.6829221.

D. Salvado, K. Erlandsson, A. Bousse, P. van Mullekom and B. F. Hutton, "Novel Collimation for Simultaneous SPECT/MRI", *Nuclear Science Symposium and Medical Imaging Conference (NSS/MIC) 2014 IEEE*, pp. 1–5, 2014. DOI: 10.1109/NSSMIC.2014.7430894.

D. Salvado, K. Erlandsson and B. F. Hutton, "Shielding Requirements of a SPECT Insert for Installation in a PET/MRI System", *Nuclear Science Symposium and Medical Imaging Conference (NSS/MIC) 2015 IEEE* , pp. 1–5, 2015. DOI: 10.1109/NSSMIC.2015.7582068.

D. Salvado, K. Erlandsson and B. F. Hutton, "Effects of the Collimator Magnification Factor in the Geometrical Calibration of SPECT Systems", *Nuclear Science Symposium and Medical Imaging Conference (NSS/MIC) 2016 IEEE*, 2016. (in press)

K. Erlandsson, **D. Salvado** and B. F. Hutton, "A Novel Approach to Image Reconstruction and Calibration for a Multi-Slit-Slat SPECT System", *Nuclear Science Symposium and Medical Imaging Conference (NSS/MIC) 2016 IEEE*, 2016. (in press)

10.4.3 Abstracts

D. Salvado, K. Erlandsson, A. Bousse, M. Occhipinti, P. Busca, C. Fiorini and B. F. Hutton, "Collimator Design for a Clinical Brain SPECT/MRI Insert", *EJNMMI Physics*, vol. 1, suppl. 1:A21 Proceedings of the 3rd PSMR Conference on PET/MR and SPECT/MR, 2014. DOI: 10.1186/2197-7364-1-S1-A21.

K. Erlandsson, P. Busca, T. Bukki, A. Gola, **D. Salvado**, A. Butt, G. Nemeth, C. Piemonte, B. F. Hutton and C. Fiorini, "Design Considerations for INSERT: a New Multi-Modality SPECT/MRI System for Preclinical and Clinical Imaging", *Journal of Nuclear Medicine*, vol. 55, suppl. 1:2139, 2014.

K. Erlandsson, **D. Salvado**, A. Bousse and B. F. Hutton, "Evaluation of a Partial Ring Design for the INSERT SPECT/MRI System", *EJNMMI Physics*, vol. 2, suppl. 1:A47 Proceedings of the 4rd PSMR Conference on PET/MR and SPECT/MR, 2015. DOI: 10.1186/2197-7364-2-S1-A47.

D. Salvado, K. Erlandsson, M. Occhipinti, C. Fiorini, J. Willems, P. van Mullekom, Z. Papp, M. Czeller, K. Nagy and B. F. Hutton, "Use of a Single INSERT Prototype Detector to Validate a Practical Calibration Procedure for a Clinical SPECT-MRI System Incorporating a Multi-Mini Slit-Slat Collimator", in *6th PSMR Conference on PET/MR and SPECT/MR*, Lisbon 2017. (in press)

10.4.4 Other Presentations

D. Salvado, K. Erlandsson and B. F. Hutton, "Using GATE for Collimator and Shielding Design of a SPECT/MRI Insert", in *GATE Users Meeting*, San Diego 2015.

D. Salvado, "Design of a Simultaneous Clinical SPECT/MRI Insert", in *XXV Congreso de ALASBIMN*, Punta del Este 2015.

D. Salvado, "INSERT: Challenges in Developing SPECT/MR", in *UCL PET/MRI Methodology Symposium*, London 2016.

K. Erlandsson, **D. Salvado**, I. De Francesco, F. Fraioli, N. Fersht, M. Gaze, S. Short, A. Groves and B. F. Hutton, "INSERT: The World's 1st Clinical Simultaneous SPECT/MRI Brain Scanner", in *UCL Division of Medicine Research Retreat*, London 2017.

Appendix A

GATE Diagrams

This appendix shows the hierarchy of the volumes defined in GATE to simulate the INSERT system based on the 8+4·½-pinhole or MSS collimator.

For each of the two diagrams presented below, the arrows point from the *parent* volume to the *child* volume, using GATE jargon.

The `LSOnotcoldAreaBlock`*i* volumes correspond to the simulation of each PET crystal in the PET/MR system – simulated by the `MRIbore` volume.

Each photodetector of the INSERT ring corresponds to the `SPECThead` volume, where the detection module `detector` is simulated by a water volume `cooling` and a silicon volume `SiPMlayer` and the crystal by a CsI volume `crystal`.

Each collimator module of the INSERT ring corresponds to the `SPECThead` volume, which is divided into two volumes `topPlate` and `bottomPlate`, to be able to simulate different aperture angulations. Detail on the apertures is given in the legend of each collimator diagram.

The gamma shielding of the INSERT system is simulated by six different volumes:

- `basePlate` corresponds to BP shield;
- `backshield` corresponds to B shield;
- `lateralShield1` and `lateralShield2` correspond to the L shields of each edge-detector of the partial ring;
- `frontShield` corresponds to F shield;
- `endShield` corresponds to E shield.

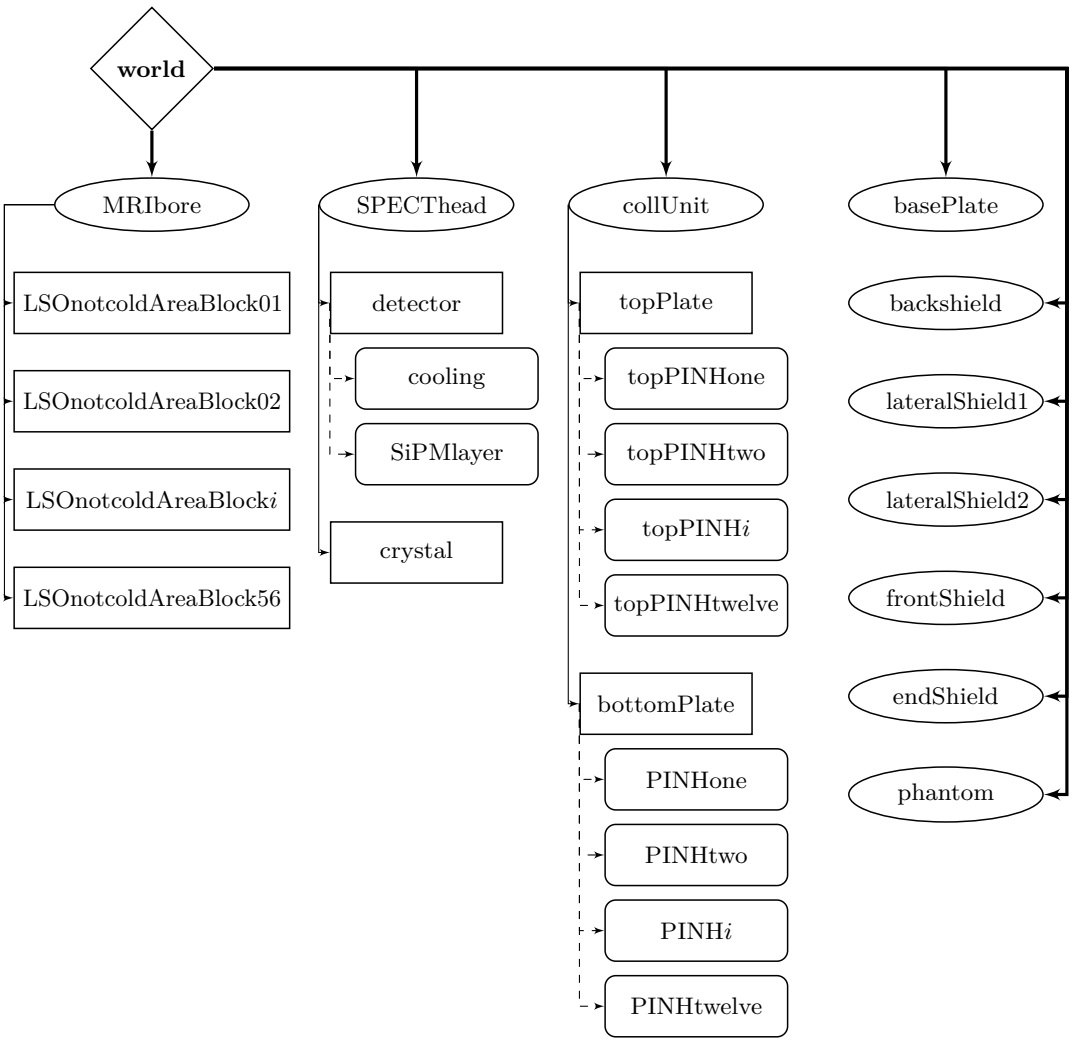

Figure A.1: Diagram of the GATE volumes hierarchy for the INSERT system geometry based on the 8+4·½-pinhole collimator. Each pinhole aperture is defined by two trapezoidal volumes, one for the aperture opening to the detector (e.g. topPINHone) and one for the imaging FOV (e.g. PINHone).

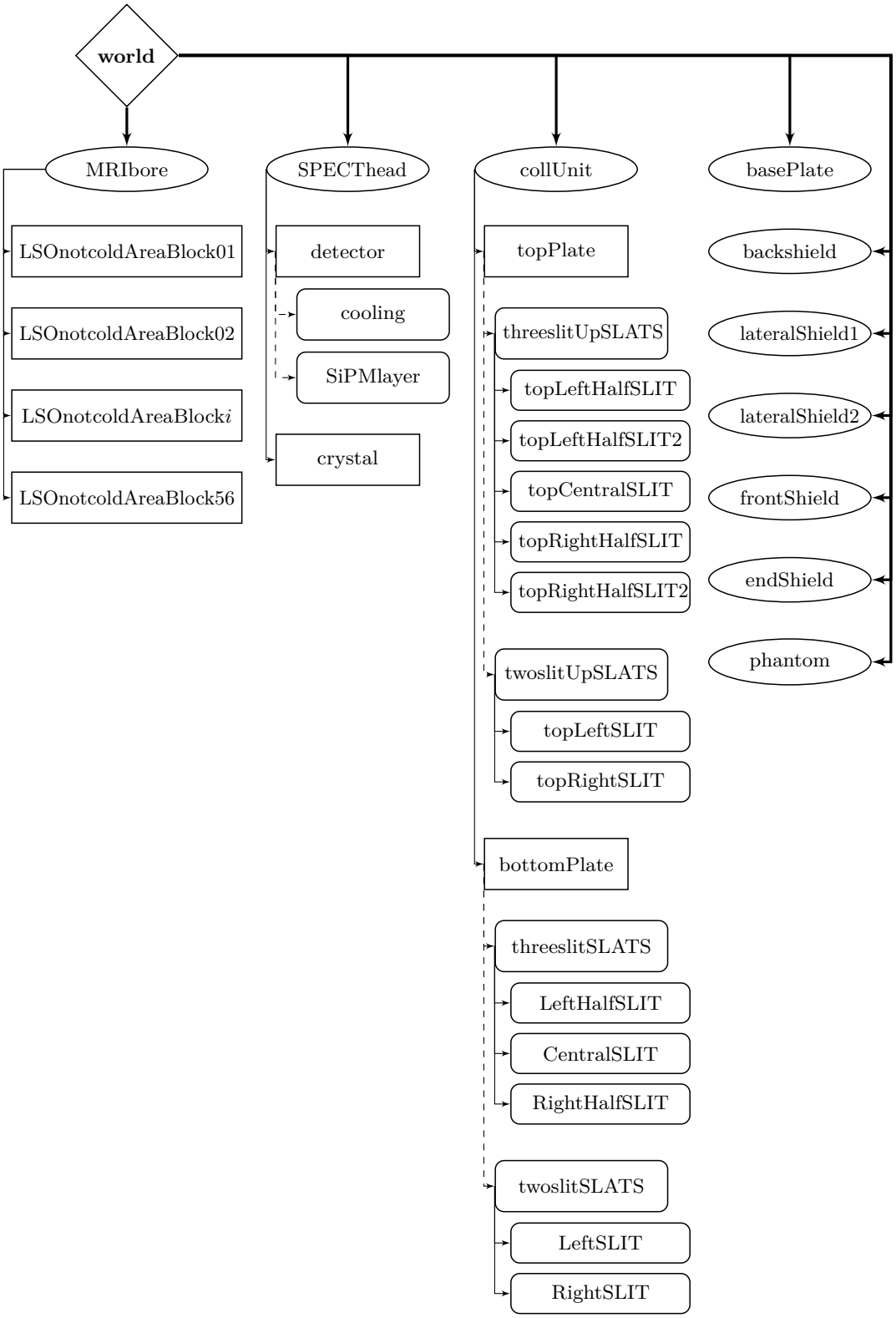

Figure A.2: Diagram of the GATE volumes hierarchy for the INSERT system geometry based on the MSS collimator. Each slit aperture is defined by two trapezoidal volumes, one for the aperture opening to the detector (e.g. topCentralSLIT) and one for the imaging FOV (e.g. CentralSLIT). These apertures are repeated along the mini-slit, for the two different axial sections containing two (e.g. twoslitSLATS) or 1+2·½(e.g. twoslitSLATS) mini-slits.

Bibliography

R. Accorsi and S. D. Metzler. Analytic Determination of the Resolution-Equivalent Effective Diameter of a Pinhole Collimator. *IEEE Transactions on Medical Imaging*, 23(6):750–63, June 2004. ISSN 0278-0062. doi: 10.1109/TMI.2002.803129.

R. Accorsi, J. R. Novak, A. S. Ayan, and S. D. Metzler. Derivation and Validation of a Sensitivity Formula for Slit-Slat Collimation. *IEEE Transactions on Medical Imaging*, 27 (5):709–22, May 2008. ISSN 1558-254X. doi: 10.1109/TMI.2007.912395.

S. Agostinelli, J. Allison, K. Amako, J. Apostolakis, H. Araujo, P. Arce, M. Asai, D. Axen, S. Banerjee, G. Barrand, F. Behner, L. Bellagamba, J. Boudreau, L. Broglia, A. Brunengo, H. Burkhardt, S. Chauvie, J. Chuma, R. Chytracek, G. Cooperman, G. Cosmo, P. Degtyarenko, A. Dell'Acqua, G. Depaola, D. Dietrich, R. Enami, A. Feliciello, C. Ferguson, H. Fesefeldt, G. Folger, F. Foppiano, A. Forti, S. Garelli, S. Giani, R. Giannitrapani, D. Gibin, J.J. Gómez Cadenas, I. González, G. Gracia Abril, G. Greeniaus, W. Greiner, V. Grichine, A. Grossheim, S. Guatelli, P. Gumplinger, R. Hamatsu, K. Hashimoto, H. Hasui, A. Heikkinen, A. Howard, V. Ivanchenko, A. Johnson, F.W. Jones, J. Kallenbach, N. Kanaya, M. Kawabata, Y. Kawabata, M. Kawaguti, S. Kelner, P. Kent, A. Kimura, T. Kodama, R. Kokoulin, M. Kossov, H. Kurashige, E. Lamanna, T. Lampén, V. Lara, V. Lefebure, F. Lei, M. Liendl, W. Lockman, F. Longo, S. Magni, M. Maire, E. Medernach, K. Minamimoto, P. Mora de Freitas, Y. Morita, K. Murakami, M. Nagamatu, R. Nartallo, P. Nieminen, T. Nishimura, K. Ohtsubo, M. Okamura, S. O'Neale, Y. Oohata, K. Paech, J. Perl, A. Pfeiffer, M.G. Pia, F. Ranjard, A. Rybin, S. Sadilov, E. Di Salvo, G. Santin, T. Sasaki, N. Savvas, Y. Sawada, S. Scherer, S. Sei, V. Sirotenko, D. Smith, N. Starkov, H. Stoecker, J. Sulkimo, M. Takahata, S. Tanaka, E. Tcherniaev, E. Safai Tehrani, M. Tropeano, P. Truscott, H. Uno, L. Urban, P. Urban, M. Verderi, A. Walkden, W. Wander, H. Weber, J.P. Wellisch, T. Wenaus, D.C. Williams, D. Wright, T. Yamada, H. Yoshida, and D. Zschiesche. Geant4 - A Simulation Toolkit. *Nuclear Instruments and Methods in Physics Research Section A: Accelerators, Spectrometers, Detectors and Associated Equipment*, 506(3):250 – 303, 2003. ISSN 0168-9002. doi: http://dx.doi.org/10.1016/S0168-9002(03)01368-8. URL `//www.sciencedirect.com/science/article/pii/S0168900203013688`.

P. Aguiar, F. Pino, J. Silva-Rodríguez, J. Pavía, D. Ros, A. Ruibal, and Z. El Bitar. Analytical, Experimental, and Monte Carlo System Response Matrix for Pinhole SPECT Reconstruction. *Medical Physics*, 41(3):032501:1–10, mar 2014. ISSN 0094-2405. doi: 10.1118/1.4866380. URL `http://www.ncbi.nlm.nih.gov/pubmed/24593739`.

H. O. Anger. Use of a Gamma-Ray Pinhole Camera for in Vivo Studies. *Nature*, 170(4318): 200–1, 1952.

H. O. Anger. Scintillation Camera. *Review of Scientific Instruments*, 29(1):27–33, 1958. ISSN 00346748. doi: 10.1063/1.1715998. URL `http://scitation.aip.org/content/aip/journal/rsi/29/1/10.1063/1.1715998`.

H. O. Anger and D. J. Rosenthal. Scintillation Camera and Positron Camera. In *Medical Radioisotope Scanning*, pages 59–82, Vienna, 1959. International Atomic Energy Agency.

H. Babla, C. Bai, and R. Conwell. A Triple-Head Solid State Camera for Cardiac Single Photon Emission Tomography (SPECT). *Proceedings of SPIE*, 6319:63190M1–5, August 2006. doi: 10.1117/12.683765. URL `http://proceedings.spiedigitallibrary.org/proceeding.aspx?articleid=1291007`.

H. H. Barrett and W. C. J. Hunter. Detectors for Small-Animal SPECT I: Overview of Technologies. In M. A. Kupinski and H H Barrett, editors, *Small-Animal SPECT Imaging*, chapter 2, pages 9–48. Springer-Verlag New York Inc., 2005.

F. J. Beekman and F. van der Have. The Pinhole: Gateway to Ultra-High-Resolution Three-Dimensional Radionuclide Imaging. *European Journal of Nuclear Medicine and Molecular Imaging*, 34(2):151–61, February 2007. ISSN 1619-7070. doi: 10.1007/s00259-006-0248-6. URL `http://www.ncbi.nlm.nih.gov/pubmed/17143647`.

F. J. Beekman and B. Vastenhouw. Design and Simulation of a High-Resolution Stationary SPECT System for Small Animals. *Physics in Medicine and Biology*, 49(19):4579–92, October 2004. ISSN 0031-9155. doi: 10.1088/0031-9155/49/19/009. URL `http://stacks.iop.org/0031-9155/49/i=19/a=009?key=crossref.2907ff6852836eb2dda5db66366f56ad`.

D. Bequé, J. Nuyts, G. Bormans, P. Suetens, and P. Dupont. Characterization of Acquisition Geometry of Pinhole SPECT. *IEEE Transactions on Medical Imaging*, 22:599–612, 2003.

D. Bequé, J. Nuyts, P. Suetens, and G. Bormans. Optimization of Geometrical Calibration in Pinhole SPECT. *IEEE Transactions on Medical Imaging*, 24(2):180–90, 2005. ISSN 02780062. doi: 10.1109/TMI.2004.839367.

T. Beyer, D. W. Townsend, T. Brun, P. E. Kinahan, M. Charron, R. Roddy, J. Jerin, J. Young, L. Byars, and R. Nutt. A Combined PET/CT Scanner for Clinical Oncology.

Journal of Nuclear Medicine, 41(8):1369–79, August 2000. ISSN 0161-5505. URL http://www.ncbi.nlm.nih.gov/pubmed/10945530.

R. Bitar, G. Leung, R. Perng, S. Tadros, A. R. Moody, J. Sarrazin, C. McGregor, M. Christakis, S. Symons, A. Nelson, and T. P. Roberts. MR Pulse Sequences: What Every Radiologist Wants to Know but Is Afraid to Ask. *RadioGraphics*, 26(2):513–37, 2006. ISSN 0271-5333. doi: 10.1148/rg.262055063. URL http://pubs.rsna.org/doi/10.1148/rg.262055063.

S. C. Blankespoor, X. Wu, K. Kalki, J. K. Brown, H. R. Tang, C. E. Cann, and B. H. Hasegawa. Attenuation Correction of SPECT Using X-Ray CT on an Emission-Transmission CT System: Myocardial Perfusion Assessment. *IEEE Transactions on Nuclear Science*, 43(4): 2263–74, 1996. ISSN 00189499. doi: 10.1109/23.531891.

W. E. Bolch. The Monte Carlo Method in Nuclear Medicine: Current Uses and Future Potential. *Journal of Nuclear Medicine*, 51(3):337–9, March 2010. ISSN 1535-5667. doi: 10.2967/jnumed.109.067835. URL http://www.ncbi.nlm.nih.gov/pubmed/20150264.

C. Bouckaert, S. Vandenberghe, and R. Van Holen. Evaluation of a Compact, High-Resolution SPECT Detector Based on Digital Silicon Photomultipliers. *Physics in Medicine and Biology*, 59(23):7521–39, nov 2014. ISSN 1361-6560. doi: 10.1088/0031-9155/59/23/7521. URL http://www.ncbi.nlm.nih.gov/pubmed/25401505.

A. Bousse, S. Pedemonte, D. Kazantsev, S. Ourselin, S. Arridge, and B. F. Hutton. Weighted MRI-Based Bowsher Priors for SPECT Brain Image Reconstruction. In *2010 IEEE Nuclear Science Symposium and Medical Imaging Conference (NSS/MIC)*, pages 3519–22, 2010. ISBN 9781424491056.

A. Bousse, K. Erlandsson, N. Fuin, D. Salvado, and B. F. Hutton. Variance Prediction in SPECT Reconstruction Based on the Fisher Information Using a Novel Angular Blurring Algorithm for Computation of the System Matrix. In *2013 IEEE Nuclear Science Symposium and Medical Imaging Conference (NSS/MIC)*, pages 1–6, 2013a.

A. Bousse, K. Erlandsson, S. Pedemonte, S. Ourselin, S. Arridge, and Hutton B. F. Angular Rebinning for Geometry Independent SPECT Reconstruction. In *Fully Three-Dimensional Image Reconstruction in Radiology and Nuclear Medicine*, pages 308–311, 2013b.

W. Branderhorst, B. Vastenhouw, F. van Der Have, E. L. A. Blezer, W. K. Bleeker, and F. J. Beekman. Targeted Multi-Pinhole SPECT. *European Journal of Nuclear Medicine and Molecular Imaging*, 38(3):552–61, 2011. ISSN 16197070. doi: 10.1007/s00259-010-1637-4.

E. Breton, P. Choquet, C. Goetz, J. Kintz, P. Erbs, R. Rooke, and A. Constantinesco. Dual SPECT/MR Imaging in Small Animal. *Nuclear Instruments and Methods in Physics Research Section A: Accelerators, Spectrometers, Detectors and Associated Equipment*, 571(1-2):446–8, February 2007. ISSN 01689002. doi: 10.1016/j.nima.2006.10.131. URL `http://linkinghub.elsevier.com/retrieve/pii/S0168900206019292`.

P. P. Bruyant. Analytic and Iterative Reconstruction Algorithms in SPECT. *Journal of Nuclear Medicine*, 43(10):1343–58, 2002. URL `http://jnm.snmjournals.org/content/43/10/1343.full.pdf+html`.

P. Busca, C. Fiorini, A. D. Butt, M. Occhipinti, R. Quaglia, P. Trigilio, K. Nagy, T. Bukki, M. Czeller, Z. Nyitrai, C. Piemonte, A. Ferri, A. Gola, and J. Rieger. Development of a SiPM-Based Anger Camera for INSERT, a New Multi-Modality SPECT/MRI System for Preclinical and Clinical Imaging. In *2014 IEEE Nuclear Science Symposium and Medical Imaging Conference (NSS/MIC)*, Nov 2014a.

P. Busca, C. Fiorini, A. D. Butt, M. Occhipinti, R. Quaglia, P. Trigilio, G. Nemeth, P. Major, T. Bukki, K. Nagy, C. Piemonte, A. Ferri, A. Gola, J. Rieger, and T. Niendorf. Development of a High-Resolution Detection Module for the INSERT SPECT/MRI System. In *EJNMMI Physics*, volume 1(Suppl 1):A24, 2014b. doi: 10.1186/2197-7364-1-S1-A24.

P. Busca, M. Occhipinti, P. Trigilio, G. Cozzi, C. Fiorini, C. Piemonte, A. Ferri, A. Gola, K. Nagy, T. Bukki, and J. Rieger. Experimental Evaluation of a SiPM-Based Scintillation Detector for MR-Compatible SPECT Systems. *IEEE Transactions on Nuclear Science*, 62 (5):2122–8, Oct 2015. ISSN 0018-9499. doi: 10.1109/TNS.2015.2481184.

L. Cai, Z. M. Shen, J. C. Zhang, C. T. Chen, and L.-J. Meng. First Imaging Result with an Ultrahigh Resolution Stationary MR Compatible SPECT System. *IEEE Nuclear Science Symposium and Medical Imaging Conference Record*, M18(44):3568–71, 2012.

L. Cai, X. Lai, Z. Shen, C.-T. Chen, and L.-J. Meng. MRC-SPECT: a Sub-500μm Resolution MR-Compatible SPECT System for Simultaneous Dual-Modality Study of Small Animals. *Nuclear Instruments and Methods in Physics Research Section A*, 734(B):147–51, 2014. ISSN 01689002. doi: 10.1016/j.nima.2013.08.080.

L. Cao, T. Kriesche, W. Semmler, and J. Peter. Geometric Co-Calibration of an Integrated Small Animal SPECT-CT System for Intrinsically Co-Registered Imaging. *IEEE Transactions on Nuclear Science*, 56(5):2759–68, 2009. ISSN 00189499. doi: 10.1109/TNS.2009.2025589.

C. Chan, R. Fulton, D. D. Feng, and S. Meikle. Regularized Image Reconstruction with an

Anatomically Adaptive Prior for Positron Emission Tomography. *Physics in Medicine and Biology*, 54(24):7379–7400, 2009. ISSN 0031-9155. doi: 10.1088/0031-9155/54/24/009.

Y.-C. Chen, L. R. Furenlid, D. W. Wilson, and H. H. Barrett. Calibration of Scintillation Cameras and Pinhole SPECT Imaging Systems. In M. A. Kupinski and H H Barrett, editors, *Small-Animal SPECT Imaging*, chapter 12, pages 195–201. Springer US, 2005. doi: 10.1007/b107067.

S. R. Cherry. Multimodality Imaging: Beyond PET/CT and SPECT/CT. *Seminars in Nuclear Medicine*, 39(5):348–53, 2009. doi: 10.1053/j.semnuclmed.2009.03.001. MULTIMODALITY.

G. Delso, S. Furst, B. Jakoby, R. Ladebeck, C. Ganter, S. G. Nekolla, M. Schwaiger, and S. I. Ziegler. Performance Measurements of the Siemens mMR Integrated Whole-Body PET/MR Scanner. *Journal of Nuclear Medicine*, 52:1–9, 2011.

X. Deng, T. Ma, R. Lecomte, and R. Yao. Optimization and Calibration of Slat Position for a SPECT with Slit-Slat Collimator and Pixelated Detector Crystals. *IEEE Transactions on Nuclear Science*, 58(5):2234–43, October 2011. ISSN 0018-9499. doi: 10.1109/TNS.2011.2163418. URL `http://ieeexplore.ieee.org/lpdocs/epic03/wrapper.htm?arnumber=6019036`.

K. Deprez, L. R. V. Pato, S. Vandenberghe, and R. van Holen. Characterization of a SPECT Pinhole Collimator for Optimal Detector Usage (the Lofthole). *Physics in Medicine and Biology*, 58(4):859–85, feb 2013. ISSN 1361-6560. doi: 10.1088/0031-9155/58/4/859. URL `http://www.ncbi.nlm.nih.gov/pubmed/23337658`.

F. P. DiFilippo. Geometric Characterization of Multi-Axis Multi-Pinhole SPECT. *Medical Physics*, 35(1):181–94, 2008. ISSN 00942405. doi: 10.1118/1.2821703. URL `http://link.aip.org/link/MPHYA6/v35/i1/p181/s1&Agg=doi`.

F. P. DiFilippo, M. J. Riffe, K. M. Harsch, N. P. McCabe, and W. D. Heston. Detached Multipinhole Small Animal SPECT Device With Real-Time Calibration. *IEEE Transactions on Nuclear Science*, 53(5):2605–12, 2006. ISSN 00189499. doi: 10.1109/TNS.2006.882748.

A. Drzezga, M. Souvatzoglou, M. Eiber, A. J. Beer, S. Fürst, A. Martinez-Möller, S. G. Nekolla, S. Ziegler, C. Ganter, E. J. Rummeny, and M. Schwaiger. First Clinical Experience with Integrated Whole-Body PET/MR: Comparison to PET/CT in Patients with Oncologic Diagnoses. *Journal of Nuclear Medicine*, 53(6):845–55, June 2012. ISSN 1535-5667. doi: 10.2967/jnumed.111.098608. URL `http://www.ncbi.nlm.nih.gov/pubmed/22534830`.

P. Eckert, H.-C. Schultz-Coulon, W. Shen, R. Stamen, and A. Tadday. Characterisation Studies of Silicon Photomultipliers. *Nuclear Instruments and Methods in Physics Research A*, 620:217–26, 2010.

Z. El Bitar, R. H. Huesman, R. Boutchko, V. Bekaert, D. Brasse, and G. T. Gullberg. A Detector Response Function Design in Pinhole SPECT Including Geometrical Calibration. *Physics in Medicine and Biology*, 58(7):2395–411, 2013. ISSN 1361-6560. doi: 10.1088/0031-9155/58/7/2395. URL `http://www.pubmedcentral.nih.gov/articlerender.fcgi?artid=4017081{&}tool=pmcentrez{&}rendertype=abstract`.

K. Erlandsson, D. Salvado, A. Bousse, and B.F. Hutton. Design Optimization and Evaluation of a Human Brain SPECT-MRI Insert Based on High-Resolution Detectors and Slit-Slat Collimators. In *Proceedings IEEE Nuclear Science Symposium Medical Imaging Conference 2013 (in press)*, pages 1–4, Oct 2013. doi: 10.1109/NSSMIC.2013.6829144.

K. Erlandsson, D. Salvado, and B. F. Hutton. A Novel Approach to Image Reconstruction and Calibration for a Multi-Slit-Slat SPECT System. In *2016 IEEE Nuclear Science Symposium and Medical Imaging Conference (NSS/MIC)*, Nov 2016.

M. Freed, M. A. Kupinski, L. R. Furenlid, D. W. Wilson, and H. H. Barrett. A Prototype Instrument for Single Pinhole Small Animal Adaptive SPECT Imaging. *Medical Physics*, 35(5):1912–25, 2008. ISSN 00942405. doi: 10.1118/1.2896072. URL `http://scitation.aip.org/content/aapm/journal/medphys/35/5/10.1118/1.2896072`.

L. Furenlid, D. Wilson, Y. Chen, H. Kim, P. Pietraski, M. Crawford, and H. Barret. FastSPECT II : a Second-Generation High-Resolution Dynamic SPECT Imager. *IEEE Transactions on Nuclear Science*, 51(3):631–35, 2004.

KETEK GmbH. SiPM Technology, 2017. URL `http://www.ketek.net/products/sipm-technology/`.

C. Goetz, E. Breton, P. Choquet, V. Israel-Jost, and A. Constantinesco. SPECT Low-Field MRI System for Small-Animal Imaging. *Journal of Nuclear Medicine*, 49(1):88–93, January 2008. ISSN 0161-5505. doi: 10.2967/jnumed.107.044313. URL `http://www.ncbi.nlm.nih.gov/pubmed/18077535`.

M. L. Goodenberger and R. B. Jenkins. Genetics of Adult Glioma. *Cancer Genetics*, 205 (12):613–21, December 2012. ISSN 2210-7762. doi: 10.1016/j.cancergen.2012.10.009. URL `http://www.ncbi.nlm.nih.gov/pubmed/23238284`.

M. C. Goorden, M. C. M. Rentmeester, and F. J. Beekman. Theoretical Analysis of Full-Ring Multi-Pinhole Brain SPECT. *Physics in Medicine and Biology*, 54(21):6593–

610, November 2009. ISSN 1361-6560. doi: 10.1088/0031-9155/54/21/010. URL http://www.ncbi.nlm.nih.gov/pubmed/19826198.

M. C. Goorden, F. van der Have, R. Kreuger, R. M. Ramakers, B. Vastenhouw, J. P. H. Burbach, J. Booij, C. F. M. Molthoff, and F. J. Beekman. VECTor: A Preclinical Imaging System for Simultaneous Submillimeter SPECT and PET. *Journal of Nuclear Medicine*, 54(2):306–313, 2013. ISSN 0161-5505. doi: 10.2967/jnumed.112.109538.

H. Graf, G. Steidle, P. Martirosian, U. A. Lauer, and F. Schick. Metal Artifacts Caused by Gradient Switching. *Magnetic Resonance in Medicine*, 54(1):231–4, 2005. ISSN 07403194. doi: 10.1002/mrm.20524.

M. J. Hamamura, S. Ha, W. W. Roeck, L. T. Muftuler, D. J. Wagenaar, D. Meier, B. E. Patt, and O. Nalcioglu. Development of an MR-Compatible SPECT System (MRSPECT) for Simultaneous Data Acquisition. *Physics in Medicine and Biology*, 55(6):1563–75, mar 2010. ISSN 1361-6560. doi: 10.1088/0031-9155/55/6/002. URL http://www.ncbi.nlm.nih.gov/pubmed/20164533.

V. Hartwig, G. Giovannetti, N. Vanello, M. Lombardi, L. Landini, and S. Simi. Biological Effects and Safety in Magnetic Resonance Imaging: A Review. *International Journal of Environmental Research and Public Health*, 6(6):1778–98, 2009. ISSN 16604601. doi: 10.3390/ijerph6061778.

D. J. Herbert, V. Saveliev, N. Belcari, N. D'Ascenzo, Alberto Del Guerra, and A. Golovin. First Results of Scintillator Readout with Silicon Photomultiplier. *IEEE Transactions on Nuclear Science*, 53(1):389–94, 2006.

H. M. Hudson and S. Larkin. Accelerated Image Reconstruction Using Ordered Subsets of Projection Data. *IEEE Transactions on Medical Imaging*, 13:601–609, 1994.

B. F. Hutton. New SPECT Technology: Potential and Challenges. *European Journal of Nuclear Medicine and Molecular Imaging*, 37(10):1883–6, October 2010. ISSN 1619-7089. doi: 10.1007/s00259-010-1550-x. URL http://www.ncbi.nlm.nih.gov/pubmed/20644927.

B. F. Hutton, H. Hudson, and F. Beekman. A Clinical Perspective of Accelerated Statistical Reconstruction. *European Journal of Nuclear Medicine*, 24(7):797–808, 1997.

B. F. Hutton, I Buvat, and F. J. Beekman. Review and Current Status of SPECT Scatter Correction. *Physics in Medicine and Biology*, 56(14):R85–R112, 2011. doi: 10.1088/0031-9155/56/14/R01.

L. C. Hygino da Cruz, I. Rodriguez, R. C. Domingues, E. L. Gasparetto, and A. G. Sorensen. Pseudoprogression and Pseudoresponse: Imaging Challenges in the Assessment of Post-treatment Glioma. *American Journal of Neuroradiology*, 32(11):1978–85, 2011. doi: 10.3174/ajnr.A2397. URL `http://www.ajnr.org/content/32/11/1978.abstract`.

E. F. Jackson, L. E. Ginsberg, D. F. Schomer, and N. E. Leeds. A Review of MRI Pulse Sequences and Techniques in Neuroimaging. *Surgical Neurology*, 47(2):185–99, 1997. ISSN 00903019. doi: 10.1016/{S}0090-3019(96)00375-8.

S. Jan, G. Santin, D. Strul, S. Staelens, K. Assié, D. Autret, S. Avner, R. Barbier, M. Bardiès, P. M. Bloomfield, D. Brasse, V. Breton, P. Bruyndonckx, I. Buvat, A. F. Chatziioannou, Y. Choi, Y. H. Chung, C. Comtat, D. Donnarieix, L. Ferrer, S. J. Glick, C. J. Groiselle, D. Guez, P.-F. Honore, S. Kerhoas-Cavata, A. S. Kirov, V. Kohli, M. Koole, M. Krieguer, D. J. van der Laan, F. Lamare, G. Largeron, C. Lartizien, D. Lazaro, M. C. Maas, L. Maigne, F. Mayet, F. Melot, C. Merheb, E. Pennacchio, J. Perez, U. Pietrzyk, F. R. Rannou, M. Rey, D. R. Schaart, C. R. Schmidtlein, L. Simon, T. Y. Song, J.-M. Vieira, D. Visvikis, R. van de Walle, E. Wieërs, and C. Morel. GATE: A Simulation Toolkit for PET and SPECT. *Physics in Medicine and Biology*, 49(19):4543–61, October 2004. ISSN 0031-9155. doi: 10.1088/0031-9155/49/19/007. URL `http://stacks.iop.org/0031-9155/49/i=19/a=007?key=crossref.be1d0bbaf1d502515584e510c77393cb`.

R. J. Jaszczak, L. T. Chang, and P. H. Murphy. Single Photon Emission Computed Tomography using Multi-Slice Fan Beam Collimators. *IEEE Transactions on Nuclear Science*, NS-26(1):610–8, 1979.

R. J. Jaszczak, K. L. Greer, C. E. Floyd, C. C. Harris, and R. E. Coleman. Improved SPECT Quantification Using Compensation for Scattered Photons. *Journal of Nuclear Medicine*, 25(8):893âĂŞ900, 1984.

M. S. Judenhofer, H. F. Wehrl, D. F. Newport, C. Catana, S. B. Siegel, M. Becker, A. Thielscher, M. Kneilling, M. P. Lichy, M. Eichner, K. Klingel, G. Reischl, S. Widmaier, M. Röcken, R. E. Nutt, H.-J. Machulla, K. Uludag, S. R. Cherry, C. D. Claussen, and B. J. Pichler. Simultaneous PET-MRI: a New Approach for Functional and Morphological Imaging. *Nature Medicine*, 14(4):459–65, April 2008. ISSN 1546-170X. doi: 10.1038/nm1700. URL `http://www.ncbi.nlm.nih.gov/pubmed/18376410`.

A. Kangarlu and P.-M. L. Robitaille. Biological Effects and Health Implications in Magnetic Resonance Imaging. *Concepts in Magnetic Resonance*, 12(5):321–59, 2000. ISSN 10437347. doi: 10.1002/1099-0534(2000)12:5⟨321::aid-cmr4⟩3.0.co;2-j.

D. Kau and S. D. Metzler. Finding Optimized Conditions of Slit-Slat and Multislit-Slat Collimation for Breast Imaging. *IEEE Transactions on Nuclear Science*, 59(1):1–27, 2012. doi: 10.1109/TNS.2011.2177912.Finding.

D. Kazantsev, S. R. Arridge, S. Pedemonte, A. Bousse, K. Erlandsson, B. F. Hutton, and S. Ourselin. An Anatomically Driven Anisotropic Diffusion Filtering Method for 3D SPECT Reconstruction. *Physics in Medicine and Biology*, 57(12):3793–3810, 2012. ISSN 1361-6560. doi: 10.1088/0031-9155/57/12/3793.

M. N. Khan, A. M. Sharma, M. Pitz, S. K. Loewen, H. Quon, A. Poulin, and M. Essig. High-Grade Glioma Management and Response Assessment âĂŤ Recent Advances and Current Challenges. *Current Oncology*, 23(4):e383–91, 2016. doi: 10.3747/co.23.3082.

M. King, S. Glick, P. Pretorius, R. Wells, H. Gifford, M. Narayanan, and T. Farncombe. Attenuation, Scatter, and Spatial Resolution Compensation in SPECT. In J. A. Sorenson and M. E. Phelps, editors, *Emission Tomography: Fundamentals of PET and SPECT*, chapter 22, pages 473–77. Elsevier Academic Press, 2004.

C. S. Levin, S. H. Maramraju, M. M. Khalighi, T. W. Deller, G. Delso, and F. Jansen. Design Features and Mutual Compatibility Studies of the Time-of-Flight PET Capable GE SIGNA PET/MR System. *IEEE Transactions on Medical Imaging*, 35(8):1907–14, Aug 2016. ISSN 0278-0062. doi: 10.1109/TMI.2016.2537811.

J. Lin and S. R. Meikle. SPECT Using Asymmetric Pinholes with Truncated Projections. *Physics in Medicine and Biology*, 56(13):4103–18, jul 2011. ISSN 1361-6560. doi: 10.1088/0031-9155/56/13/023. URL `http://www.ncbi.nlm.nih.gov/pubmed/21693792`.

A. Lipton. Safety in Magnetic Resonance Imaging. Technical report, Society and College of Radiographers and the British Association of Magnetic Resonance Radiographers, 2013. URL `http://www.sor.org/`.

H. Lu, L. M. Nagae Poetscher, X. Golay, D. Lin, M. Pomper, and P. C. M. Van Zijl. Routine Clinical Brain MRI Sequences for Use at 3.0 Tesla. *Journal of Magnetic Resonance Imaging*, 22(1):13–22, 2005. ISSN 10531807. doi: 10.1002/jmri.20356.

T. Ma, R. Yao, and Y. Shao. Determination of Geometrical Parameters for Slit-Slat SPECT Imaging on MicroPET. *IEEE Nuclear Science Symposium Conference Record*, 6(2):4285–8, 2007. ISSN 10957863. doi: 10.1109/NSSMIC.2007.4437063.

T. Ma, R. Yao, Y. Shao, and R. Zhou. A SVD-Based Method to Assess the Uniqueness and Accuracy of SPECT Geometrical Calibration. *IEEE Transactions on Medical Imaging*, 28 (12):1929–39, 2009. ISSN 02780062. doi: 10.1109/TMI.2009.2025696.

S. T. Mahmood, K. Erlandsson, and B. F. Hutton. Improved Reconstructed Image Quality in a SPECT System with Slit-Slat Collimation by Combination of Multiplexed and Non-Multiplexed Data. *IEEE Nuclear Science Symposium Conference Record*, M10(30): 4598–603, 2008.

S. T. Mahmood, K. Erlandsson, I. Cullum, and B. F. Hutton. Design of a Novel Slit-Slat Collimator System for SPECT Imaging of the Human Brain. *Physics in Medicine and Biology*, 54(11):3433–49, June 2009. ISSN 0031-9155. doi: 10.1088/0031-9155/54/11/011. URL `http://www.ncbi.nlm.nih.gov/pubmed/19436098`.

S. T. Mahmood, K. Erlandsson, I. Cullum, and B. F. Hutton. The Potential for Mixed Multiplexed and Non-Multiplexed Data to Improve the Reconstruction Quality of a Multi-Slit-Slat Collimator SPECT System. *Physics in Medicine and Biology*, 55(8): 2247–68, April 2010. ISSN 1361-6560. doi: 10.1088/0031-9155/55/8/009. URL `http://www.ncbi.nlm.nih.gov/pubmed/20354282`.

J. R. Mallard and M. J. Myers. The Performance of a Gamma Camera for the Visualization of Radioactive Isotopes in Vivo. *Physics in Medicine and Biology*, 8(2):165–82, 1963.

D. Meier, D. J. Wagenaar, G. Maehlum, B. Sundal, B. E. Patt, S. Chen, J. Xu, J. Yu, B. M. W. Tsui, M. J. Hamamura, W. W. Roeck, S.-H. Ha, and O. Nalcioglu. A SPECT Camera for Simultaneous SPECT/MRI. *IEEE Nuclear Science Symposium Conference Record*, J01(1):2313–8, 2009.

D. Meier, D. J. Wagenaar, S. Chen, J. Xu, J. Yu, and B. M. W. Tsui. A SPECT Camera for Combined MRI and SPECT for Small Animals. *Nuclear Instruments and Methods in Physics Research Section A: Accelerators, Spectrometers, Detectors and Associated Equipment*, 652(1):731–4, October 2011. ISSN 0168-9002. doi: 10.1016/j.nima.2010.09.116. URL `http://www.pubmedcentral.nih.gov/articlerender.fcgi?artid=3181146&tool=pmcentrez&rendertype=abstract`.

L.-J. Meng, J.-W. Tan, and G. Fu. Design Study of an MRI Compatible Ultra-High Resolution SPECT for in Vivo Mice Brain Imaging. *IEEE Nuclear Science Symposium Conference Record*, M13(117):2956–60, 2007. doi: 10.1109/NSSMIC.2007.4436754. URL `http://ieeexplore.ieee.org/lpdocs/epic03/wrapper.htm?arnumber=4436754`.

S. D. Metzler and R. Accorsi. Resolution- Versus Sensitivity-Effective Diameter in Pinhole Collimation: Experimental Verification. *Physics in Medicine and Biology*, 50(21):5005–17, November 2005. ISSN 0031-9155. doi: 10.1088/0031-9155/50/21/004. URL `http://www.ncbi.nlm.nih.gov/pubmed/16237237`.

S. D. Metzler and R. J. Jaszczak. Simultaneous Multi-Head Calibration for Pinhole SPECT. *IEEE Transactions on Nuclear Science*, 53(1):113–20, 2006. ISSN 00189499. doi: 10.1109/TNS.2005.862978.

S. D. Metzler and N. H. Patil. Measuring the Variation in Radius of Rotation as a Function of Gantry Angle for Ultra-High-Resolution Pinhole SPECT. *IEEE Transactions on Nuclear Science*, 52(5 I):1236–1242, 2005. ISSN 00189499. doi: 10.1109/TNS.2005.851417.

S. D. Metzler, J. E. Bowsher, M. F. Smith, and R. J. Jaszczak. Analytic Determination of Pinhole Collimator Sensitivity with Penetration. *IEEE Transactions on Medical Imaging*, 20(8):730–41, August 2001. ISSN 0278-0062. doi: 10.1109/42.938241. URL `http://www.ncbi.nlm.nih.gov/pubmed/11513024`.

S. D. Metzler, K. L. Greer, and R. J. Jaszczak. Helical Pinhole SPECT for Small-Animal Imaging: a Method for Addressing Sampling Completeness. *IEEE Transactions on Nuclear Science*, 50(5):1575–83, October 2003. ISSN 0018-9499. doi: 10.1109/TNS.2003.817948. URL `http://ieeexplore.ieee.org/lpdocs/epic03/wrapper.htm?arnumber=1236969`.

S. D. Metzler, K. L. Greer, and R. J. Jaszczak. Determination of Mechanical and Electronic Shifts for Pinhole SPECT Using a Single Point Source. *IEEE Transactions on Medical Imaging*, 24(3):361–70, 2005. ISSN 02780062. doi: 10.1109/TMI.2004.842456.

S. D. Metzler, R. Accorsi, J. R. Novak, A. S. Ayan, and R. J. Jaszczak. On-Axis Sensitivity and Resolution of a Slit-Slat Collimator. *Journal of Nuclear Medicine*, 47(11):1884–90, November 2006. ISSN 0161-5505. URL `http://www.ncbi.nlm.nih.gov/pubmed/17079823`.

S. D. Metzler, R. Accorsi, A. S. Ayan, J. R. Novak, R. M. Lewitt, and R. J. Jaszczak. Preliminary Assessment of Multislit-Slat Collimation for Cardiac SPECT. *IEEE Nuclear Science Symposium Conference Record*, M18(54):3345–9, 2007.

S. D. Metzler, R. Accorsi, A. S. Ayan, and R. J. Jaszczak. Slit-Slat and Multislit-Slat Collimator Design and Experimentally Acquired Phantom Images from a Rotating Prototype. *IEEE Transactions on Nuclear Science*, 57(1):125–34, 2010. doi: 10.1109/TNS.2009.2033989.Slit-Slat.

S. D. Metzler, S. C. Moore, and M.-A. Park. Design of a New Small-Animal SPECT System Based on Rectangular Pinhole Aperture. *IEEE Nuclear Science Symposium and Medical Imaging Conference*, M21(43):3815–3820, 2012.

B. W. Miller, R. Van Holen, H. H. Barrett, and L. R. Furenlid. A System Calibration and Fast Iterative Reconstruction Method for Next-Generation SPECT Imagers. *IEEE Transactions on Nuclear Science*, 59(5):1990–6, 2012. ISSN 00189499. doi: 10.1109/TNS.2012.2198243.

G. L. Montagnani, M. Occhipinti, M. Carminati, and C. Fiorini. Mapping Tool for Investigation of Component-Level PCB Compatibility in Multimodal MRI/SPECT. In *2016 IEEE Nuclear Science Symposium and Medical Imaging Conference (NSS/MIC)*, Nov 2016.

G. Muehllehner. A Diverging Collimator for Gamma-Ray Imaging Cameras. *Journal of Nuclear Medicine*, 10(4):197–201, April 1969. ISSN 1998-3808. doi: 10.4103/0971-3026.82282. URL `http://www.ncbi.nlm.nih.gov/pubmed/23692638`.

P. Nillius and M. Danielsson. Theoretical Bounds and System Design for Multipinhole SPECT. *IEEE Transactions on Medical Imaging*, 29(7):1390–400, July 2010. ISSN 1558-254X. doi: 10.1109/TMI.2010.2047113. URL `http://www.ncbi.nlm.nih.gov/pubmed/20378465`.

J. R. Novak, A. S. Ayan, R. Accorsi, and S. D. Metzler. Verification of the Sensitivity and Resolution Dependence on the Incidence Angle for Slit-Slat Collimation. *Physics in Medicine and Biology*, 53(4):953–66, 2008.

J. Nuyts. The Use of Mutual Information and Joint Entropy for Anatomical Priors in Emission Tomography. In *2007 IEEE Nuclear Science Symposium and Medical Imaging Conference (NSS/MIC)*, pages 4149–54, 2007. ISBN 1424409233. doi: 10.1109/NSSMIC.2007.4437034.

J. Nuyts, K. Vunckx, M. Defrise, and C. Vanhove. Small Animal Imaging with Multi-pinhole SPECT. *Methods*, 48:83–91, 2009.

M. Occhipinti, P. Busca, A. D. Butt, G. Cozzi, C. Fiorini, I. Perali, F. Acerbi, A. Ferri, A. Gola, and C. Piemonte. A Compact SiPM Photodetector Array for SPECT Applications. In *2014 IEEE Nuclear Science Symposium and Medical Imaging Conference (NSS/MIC)*, Nov 2014.

M. Occhipinti, P. Busca, and C. Fiorini. Light Response Estimation and Gamma Events Reconstruction in Detectors based on Continuous Scintillators Read by SiPMs. In *2016 IEEE Nuclear Science Symposium and Medical Imaging Conference (NSS/MIC)*, Nov 2016.

O. Ott. Photon Emission Probabilities of 176Lu. *International Journal of Radiation Applications and Instrumentation Part A, Applied Radiation and Isotopes*, 70(9):1886–92, 2012.

D. Paix. Pinhole Imaging of Gamma Rays. *Physics in Medicine and Biology*, 12(4):489–500, 1967.

T. E. Peterson and L. R. Furenlid. SPECT Detectors: the Anger Camera and Beyond. *Physics in Medicine and Biology*, 56(17):R145–82, September 2011. ISSN 1361-6560. doi: 10.1088/0031-9155/56/17/R01. URL `http://www.pubmedcentral.nih.gov/articlerender.fcgi?artid=3178269&tool=pmcentrez&rendertype=abstract`.

F. Pino, N. Roé, A. Orero, C. Falcón, S. Rojas, J. M. Benlloch, D. Ros, and J. Pavía. Development of a Variable-Radius Pinhole SPECT System With a Portable Gamma Camera. *Revista Española de Medicina Nuclear*, 30(5):286–91, 2011. ISSN 1578-200X. doi: 10.1016/j.remn.2011.03.004. URL `http://www.ncbi.nlm.nih.gov/pubmed/21640439`.

D. Renker. Geiger-Mode Avalanche Photodiodes, History, Properties and Problems. *Nuclear Instruments and Methods in Physics Research Section A: Accelerators, Spectrometers, Detectors and Associated Equipment*, 567(1):48 – 56, 2006. ISSN 0168-9002. doi: http://dx.doi.org/10.1016/j.nima.2006.05.060. URL `//www.sciencedirect.com/science/article/pii/S0168900206008680`.

W. L. Rogers, N. H. Clinthorne, J. A. Stamos, K. F. Koral, R. Mayans, J. W. Keyes, J. J. Williams, W. P. Snapp, and G. F. Knoll. SPRINT: a Stationary Detector Single Photon Ring Tomograph for Brain Imaging. *IEEE Transactions on Medical Imaging*, MI-1(1): 63–8, 1982.

W. L. Rogers, N. H. Clinthorne, J. A. Stamos, K. F. Koral, R. Mayans, G. F. Knoll, J. Juni, J. W. Keyes, and B. A. Harkness. Performance Evaluation of SPRINT, a Single Photon Ring Tomograph for Brain Imaging. *Journal of Nuclear Medicine*, 25(9):1013–8, 1984.

W. L. Rogers, N. H. Clinthorne, L. Shao, P. Chiao, Y. Ding, J. A. Stamos, and K. F. Koral. SPRINT II: a Second Generation Single Photon Ring Tomograph. *IEEE Transactions on Medical Imaging*, 7(4):291–7, January 1988. ISSN 0278-0062. doi: 10.1109/42.14511. URL `http://www.ncbi.nlm.nih.gov/pubmed/18230481`.

M. M. Rogulski, H. B. Barber, H. H. Barrett, R. L. Shoemaker, and J. M. Woolfenden. Ultra-High-Resolution Brain SPECT Imaging: Simulation Results. *IEEE Transactions on Nuclear Science*, 40(4):1123–9, 1993. ISSN 00189499. doi: 10.1109/23.256722. URL `http://ieeexplore.ieee.org/lpdocs/epic03/wrapper.htm?arnumber=256722`.

R. K. Rowe, J. N. Aarsvold, H. H. Barrett, J.-C. Chen, W. P. Klein, B. A. Moore, I. W. Pang, D. D. Patton, and T. A. White. A Stationary Hemispherical SPECT Imager for Three-Dimensional Brain Imaging. *The Journal of Nuclear Medicine*, 34(3):474–80, 1993.

D. Salvado, K. Erlandsson, A. Bousse, P. van Mullekom, and B. F. Hutton. Novel Collimation for Simultaneous SPECT/MRI. In *2014 IEEE Nuclear Science Symposium and Medical Imaging Conference (NSS/MIC)*, Nov 2014.

D. Salvado, K. Erlandsson, A. Bousse, M. Occhipinti, P. Busca, C. Fiorini, and B. F. Hutton. Collimator Design for a Brain SPECT/MRI Insert. *IEEE Transactions on Nuclear Science*, 62:1716–24, 2015.

A. M. Samoudi, K. van Audenhaege, G. Vermeeren, M. Poole, E. Tanghe, L. Martens, R. van Holen, and W. Joseph. Analysis of Eddy Currents Induced by Transverse and Longitudinal Gradient Coils in Different Tungsten Collimators Geometries for SPECT/MRI Integration. *Magnetic Resonance in Medicine*, 74(6):1780–9, 2015. ISSN 15222594. doi: 10.1002/mrm.25534.

J. F. Schenck. Safety of Strong, Static Magnetic Fields. *Journal of Magnetic Resonance Imaging*, 19:2–19, 2000. ISSN 10531807. doi: 10.1002/1522-2586(200007)12:1⟨2::AID-JMRI2⟩3.0.CO;2-V.

O. Schillaci. Hybrid SPECT/CT: a New Era for SPECT Imaging? *European Journal of Nuclear Medicine and Molecular Imaging*, 32(5):521–4, May 2005. ISSN 1619-7070. doi: 10.1007/s00259-005-1760-9. URL `http://www.ncbi.nlm.nih.gov/pubmed/15747153`.

H.-P. W. Schlemmer, B. J. Pichler, M. Schmand, Z. Burbar, C. Michel, R. Ladebeck, K. Jattke, D. Townsend, C. Nahmias, P. K. Jacob, W.-D. Heiss, and C. D. Claussen. Simultaneous MR/PET Imaging of the Human Brain: Feasibility Study. *Radiology*, 248(3):1028–35, 2008. ISSN 0033-8419. doi: 10.1148/radiol.2483071927.

N. U. Schramm, G. Ebel, U. Engeland, T. Schurrat, M. Béhé, and T. M. Behr. High-Resolution SPECT Using Multipinhole Collimation. *IEEE Transactions on Nuclear Science*, 50(3):315–20, 2003.

L. Shepp and Y. Vardi. Maximum Likelihood Reconstruction for Emission Tomography. *IEEE Transactions on Medical Imaging*, 1(2):113–22, 1982. URL `http://www-stat.wharton.upenn.edu/~shepp/publications/58.pdf`.

M. F. Smith. Recent Advances in Cardiac SPECT Instrumentation and System Design. *Current Cardiology Reports*, 15(8):387:1–11, August 2013. ISSN 1534-3170. doi: 10.1007/s11886-013-0387-x. URL `http://www.ncbi.nlm.nih.gov/pubmed/23832650`.

M. F. Smith and R. J. Jaszczak. The Effect of Gamma Ray Penetration on Angle-Dependent Sensitivity for Pinhole Collimation in Nuclear Medicine. *Medical Physics*, 24(11):1701–9, November 1997. ISSN 0094-2405. URL `http://www.ncbi.nlm.nih.gov/pubmed/9394277`.

V. N. Solovov, V. A. Belov, D. Y. Akimov, H. M. Araujo, E. J. Barnes, A. A. Burenkov, V. Chepel, A. Currie, L. DeViveiros, B. Edwards, C. Ghag, A. Hollingsworth, M. Horn, G. E. Kalmus, A. S. Kobyakin, A. G. Kovalenko, V. N. Lebedenko, A. Lindote, M. I. Lopes, R. Luescher, P. Majewski, A. S. Murphy, F. Neves, S. M. Paling, J. Pinto da Cunha, R. Preece, J. J. Quenby, L. Reichhart, P. R. Scovell, C. Silva, N. J. Smith, P. F. Smith, V. N. Stekhanov, T. J. Sumner, C. Thorne, and R. J. Walker. Position Reconstruction in a Dual Phase Xenon

Scintillation Detector. *IEEE Transactions on Nuclear Science*, 59:3286–93, 2012. doi: 10.1109/TNS.2012.2221742. URL http://dx.doi.org/10.1109/TNS.2012.2221742.

J. A. Sorenson and M. E. Phelps. The Anger Camera: Performance Characteristics. In J. A. Sorenson and M. E. Phelps, editors, *Physics in Nuclear Medicine*, chapter 16, pages 331–345. Saunders, 2nd edition, 1987.

J.-W. Tan, L. Cai, and L.-J. Meng. A Prototype of the MRI-Compatible Ultra-High Resolution SPECT for in Vivo Mice Brain Imaging. *IEEE Nuclear Science Symposium Conference Record*, M05(250):2800–5, 2009.

S. Tong, A. M. Alessio, and P. E. Kinahan. Image Reconstruction for PET/CT Scanners: Past Achievements and Future Challenges. *Imaging in Medicine*, 5(2):529–45, 2010. doi: 10.2217/iim.10.49.

B. M. W. Tsui, J. W. Hugg, J. Xu, S. Chen, D. Meier, W. A. Edelstein, A. El-Sharkaway, D. J. Wagenaar, and B. E. Patt. Design and Development of MR-Compatible SPECT Systems for Simultaneous SPECT-MR Imaging of Small Animals. In Norbert J. Pelc, Ehsan Samei, and Robert M. Nishikawa, editors, *Proceedings of SPIE*, volume 7961, pages 79611Y:1–7. SPIE, March 2011a. doi: 10.1117/12.878903. URL http://proceedings.spiedigitallibrary.org/proceeding.aspx?articleid=723841.

B. M. W. Tsui, J. Xu, A. Rittenbach, S. Chen, A. El-Sharkaway, W. A. Edelstein, X. Guo, A. Liu, and J. W. Hugg. High Performance SPECT System for Simultaneous SPECT-MR Imaging of Small Animals. *IEEE Nuclear Science Symposium Conference Record*, MIC13(6):3178–82, October 2011b. doi: 10.1109/NSSMIC.2011.6153652. URL http://ieeexplore.ieee.org/lpdocs/epic03/wrapper.htm?arnumber=6153652.

K. van Audenhaege, R. van Holen, K. Deprez, J. S. Karp, S. D. Metzler, and S. Vandenberghe. Design of a Static Full-Ring Multi-Pinhole Collimator for Brain SPECT. *IEEE Nuclear Science Symposium Conference Record*, MIC22(1):4393–7, 2011. doi: 10.1109/NSSMIC.2011.6153847.

K. van Audenhaege, S. Vandenberghe, K. Deprez, B. Vandeghinste, and R. van Holen. Design and Simulation of a Full-Ring Multi-Lofthole Collimator for Brain SPECT. *Physics in Medicine and Biology*, 58(18):6317–36, 2013. ISSN 1361-6560. doi: 10.1088/0031-9155/58/18/6317.

K. van Audenhaege, R. van Holen, C. Vanhove, and S. Vandenberghe. Collimator Design for a Multipinhole Brain SPECT Insert for MRI. *Medical Physics*, 42(11):6679–89, 2015. ISSN 0094-2405. doi: 10.1118/1.4934371. URL http://scitation.aip.org/content/aapm/journal/medphys/42/11/10.1118/1.4934371.

F. van der Have and F. J. Beekman. Penetration, Scatter and Ssensitivity in Channel Micro-Pinholes for SPECT: a Monte Carlo Investigation. *IEEE Transactions on Nuclear Science*, 53(5):2635–45, 2006.

F. van der Have, B. Vastenhouw, M. Rentmeester, and F. J. Beekman. System Calibration and Statistical Image Reconstruction for Ultra-High Resolution Stationary Pinhole SPECT. *IEEE Transactions on Medical Imaging*, 27(7):960–71, January 2008. ISSN 1558-254X. doi: 10.1109/TMI.2008.924644. URL `http://www.ncbi.nlm.nih.gov/pubmed/18599401`.

F. van der Have, O. Ivashchenko, M. C. Goorden, R. M. Ramakers, and F. J. Beekman. High-Resolution Clustered-Pinhole 131-Iodine SPECT Imaging in Mice. *Nuclear Medicine and Biology*, 43(8):506–11, 2016. ISSN 18729614. doi: 10.1016/j.nucmedbio.2016.05.015. URL `http://www.sciencedirect.com/science/article/pii/S0969805116300968`.

R. van Holen and S. Vandenberghe. Optimization of a Stationary Small Animal SPECT System for Simultaneous SPECT/MRI. In *2013 IEEE Nuclear Science Symposium and Medical Imaging Conference (NSS/MIC)*, pages 1–4, 2013.

R. van Holen, B. Vandeghinste, K. Deprez, and S. Vandenberghe. *Medical Physics*, 40(11): 112501:1–11, 2013. doi: 10.1118/1.4822621.

B. Vandeghinste, J. De Beenhouwer, R. van Holen, S. Vandenberghe, and S. Staelens. Characterizing the Parallax Error in Multi-Pinhole Micro-SPECT Reconstruction. *IEEE Nuclear Science Symposium and Medical Imaging Conference (NSS/MIC)*, pages 2738–42, 2011.

R. A. Vogel, D. Kirch, M. LeFree, and P. Steele. A new Method of Multiplanar Emission Tomography Using a Seven Pinhole Collimator and an Anger Scintillation Camera. *Journal of Nuclear Medicine*, 19(6):648–54, 1978.

F. M. Vogt, M. E. Ladd, P. Hunold, S. Mateiescu, F. X. Hebrank, A. Zhang, J. F. Debatin, and S. C. Göhde. Increased Time Rate of Change of Gradient Fields: Effect on Peripheral Nerve Stimulation at Clinical MR Imaging. *Radiology*, 233(2):548–54, 2004. ISSN 0033-8419. doi: 10.1148/radiol.2332030428. URL `http://pubs.rsna.org/doi/abs/10.1148/radiol.2332030428`.

K. Vunckx, P. Suetens, and J. Nuyts. Effect of Overlapping Projections on Reconstruction Image Quality in Multipinhole SPECT. *IEEE Transactions on Medical Imaging*, 27(7): 972–83, January 2008. ISSN 1558-254X. doi: 10.1109/TMI.2008.922700. URL `http://www.ncbi.nlm.nih.gov/pubmed/18599402`.

K. Vunckx, A. Atre, K. Baete, A. Reilhac, C. M. Deroose, K. Van Laere, and J. Nuyts. Evaluation of Three MRI-Based Anatomical Priors for Quantitative PET Brain Imaging. *IEEE Transactions on Medical Imaging*, 31(3):599–612, 2012. ISSN 02780062. doi: 10.1109/TMI.2011.2173766.

D. J. Wagenaar, O. Nalcioglu, L. T. Muftuler, M. Szawlowski, M. Kapusta, N. Pavlov, D. Meier, G. Maehlum, and B. E. Patt. Development of MRI-Compatible Nuclear Medicine Imaging Detectors. *2006 IEEE Nuclear Science Symposium Conference Record*, M06(41): 1825–8, 2006. doi: 10.1109/NSSMIC.2006.354248. URL `http://ieeexplore.ieee.org/lpdocs/epic03/wrapper.htm?arnumber=4179361`.

Y. Wang and T. Jiang. Understanding High Grade Glioma: Molecular Mechanism, Therapy and Comprehensive Management. *Cancer Letters*, 331(2):139–46, May 2013. ISSN 1872-7980. doi: 10.1016/j.canlet.2012.12.024. URL `http://www.ncbi.nlm.nih.gov/pubmed/23340179`.

J. Xu, S. Chen, J. Yu, D. Meier, D. J. Wagenaar, B. E. Patt, and B. M. W. Tsui. SPECT Data Acquisition and Image Reconstruction in a Stationary Small Animal SPECT/MRI System. *Proceedings of SPIE*, 7622:1–8, March 2010. doi: 10.1117/12.845504. URL `http://proceedings.spiedigitallibrary.org/proceeding.aspx?articleid=747435`.

R. Yao, T. Ma, and Y. Shao. Lutetium Oxyorthosilicate (LSO) Intrinsic Activity Correction and Minimal Detectable Target Activity Study for SPECT Imaging with a LSO-based Animal PET Scanner. *Physics in Medicine and Biology*, 53:4399–415, 2008.

I. G. Zubal, C. R. Harrel, E. O. Smith, Z. Rattner, G. Gindi, and P. B. Hoffer. Computerized Three-Dimensional Segmented Human Anatomy. *Medical Physics*, 21(2):299–302, 1994.